VTT RESEARCH NOTES 2582

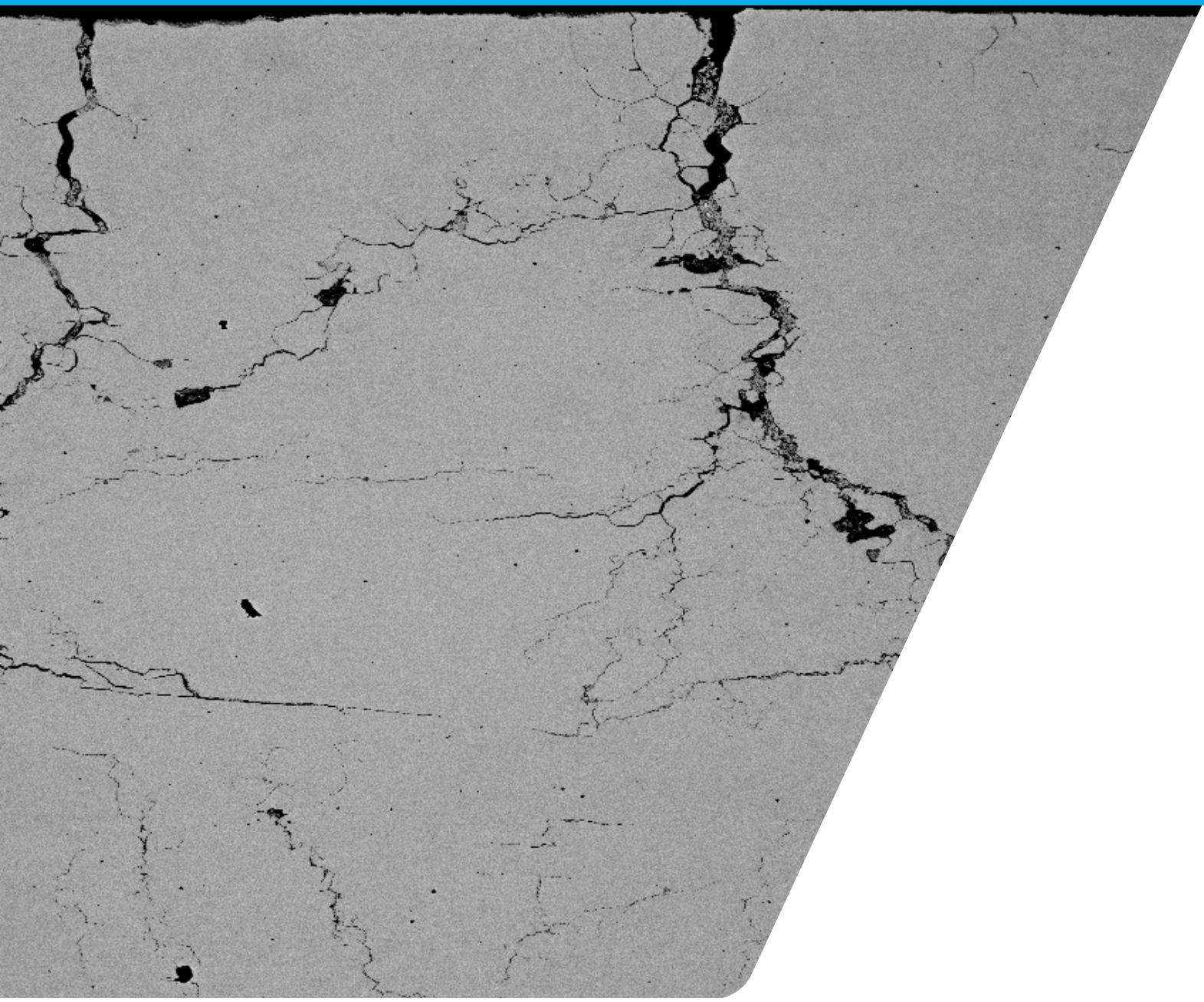

Hannu Hänninen, Anssi Brederholm, Tapio Saukkonen,
Mykola Ivanchenko, Aki Toivonen, Wade Karlsen, Ulla Ehrnstén, &
Pertti Aaltonen

Environment-assisted cracking and hot cracking susceptibility of nickel-base alloy weld metal

VTT TIEDOTTEITA – RESEARCH NOTES 2582

Environment-assisted cracking and hot cracking susceptibility of nickel-base alloy weld metal

Hannu Hänninen, Anssi Brederholm, Tapio Saukkonen & Mykola Ivanchenko

Aalto University School of Science and Technology,
School of Engineering, Finland

Aki Toivonen,Wade Karlsen, Ulla Ehrnstén & Pertti Aaltonen

VTT Technical Research Centre of Finland

ISBN 978-951-38-7709-5 (soft back ed.)
ISSN 1235-0605 (soft back ed.)

ISBN 978-951-38-7710-1 (URL: http://www.vtt.fi/publications/index.jsp)
ISSN 1455-0865 (URL: http://www.vtt.fi/publications/index.jsp)

JULKAISIJA – UTGIVARE – PUBLISHER

VTT, Vuorimiehentie 5, PL 1000, 02044 VTT
puh. vaihde 020 722 111, faksi 020 722 4374

VTT, Bergsmansvägen 5, PB 1000, 02044 VTT
tel. växel 020 722 111, fax 020 722 4374

VTT Technical Research Centre of Finland, Vuorimiehentie 5, P.O. Box 1000, FI-02044 VTT, Finland
phone internat. +358 20 722 111, fax +358 20 722 4374

Kopijyvä Oy, Kuopio 2011

Hannu Hänninen, Anssi Brederholm, Tapio Saukkonen, Mykola Ivanchenko, Aki Toivonen, Wade Karlsen, Ulla Ehrnstén & Pertti Aaltonen. Environment-assisted cracking and hot cracking susceptibility of nickel-base alloy weld metals. Espoo 2011. VTT Tiedotteita – Research Notes 2582. 152 p.

Keywords Nickel-base alloys, weld metal, hot cracking, environment-assisted cracking, electron microscopy, dynamic strain aging, differential scanning calorimetry, residual stress

Abstract

The Tekes project PERDI (Performance and ageing of dissimilar metal joints) was carried out at TKK and VTT during the period 2006 to 2009. It was primarily driven by the needs of the nuclear power plant (NPP) industry, but the oil refining, conventional energy production and the pulp and paper industries also benefitted from the results and expertise developed in the project. The extensive studies carried out in the project on welding technology, microstructural characterization, non-destructive examination (NDE) and environmentally assisted cracking (EAC) revealed a number of open research issues regarding the dissimilar metal welds (DMW) and pure Ni-based weld metals of modern nuclear power plants. Alloy 690 and its associated weld metals Alloy 152 and Alloy 52 are nowadays widely used for repair and replacement of thick-section components and in the construction of new reactors like the European Pressurized Water Reactor (EPR). Some aspects of the project were focused on the repair welding of BWR dissimilar metal welds, where the repair method and the filler material were chosen taking into account the residual stresses produced in the structure, possible material property changes of the remaining materials, and the resistance of the new weld metal (Alloy 82 or 52) to EAC. In addition to examining the materials properties and weldability of DMWs, the studies also covered NDE inspection and residual stress measurement and modelling in DMWs.

The weldability research utilized a modern, versatile Varestraint test system for hot crack susceptibility testing of the Ni-based alloys used for nuclear and oil refinery DMWs. Weld metals and hot cracks were examined using a modern FEG-SEM/EBSD system and by ATEM. Additionally the solidification and precipitation processes were characterized by differential scanning calorimetry (DSC) methods. It was found that hot cracking is generally associated with the segregation of Nb, Si and Mn in the final melt of the solidifying weld. The Varestraint test technique was also used for producing controlled amounts of hot cracking type defects in the test samples for subsequent EAC studies carried out at VTT and at Tohoku University, Japan. A full scale DMW mock-up of a thick-wall weld was prepared for an oil refinery application, and the whole manufacturing procedure was documented on video film. The mock-up was then methodically characterized by both non-destructive and destructive methods. About 2/3 of the pipe weld was then used for a NDE performance demonstration mock-up sample, where all possible defects expected in the oil refinery conditions were present. Extensive NDE studies were made of the mock-up sample, and the sample is now used by Neste Oil for NDE performance demonstrations (separate report [1]).

To assess the relative EAC susceptibilities of various types of Alloy 182, 82, 52 and 152 pure weld metals and DMW configurations with and without hot cracks, four-point bend tests were carried out in a high-temperature steam environment that was doped with impurities to enhance crack initiation. The

results showed a relatively high susceptibility of Alloys 182 and 82 to EAC, while Alloys 152 and 52 showed no crack initiation. The hot cracks and other weld defects present in the samples did not show any signs of extension in the doped steam test, in any of the studied materials. The cracking mechanism of Alloy 182 and 82 weld metals as well as Alloy 600 was studied by FEG-SEM and discussed based on high-temperature electrochemistry and oxidation. The dynamic strain aging (DSA) behaviour of the weld metals was determined. In an international round robin, crack growth rate data obtained by participants for Alloys 600 and 182 were compared. VTT results were found to be like those of the others [2].

Through the PINC project, an international NDE round robin was held using DMW mock-ups provided by NRC, USA. The test results obtained by VTT were analysed and published in the PINC final report (separate report [3]). The roles of the stress state and the accessibility of the DMWs in the inspection results were especially evaluated, and guidance was given on the detectability of various defects by the ultrasonic techniques used for DMWs, as well as on the sizing techniques. The techniques used in the international round robin were also employed for the NDE inspections of the Neste Oil mock-up sample.

DMWs are at present a major research topic in the nuclear industry internationally, because a number of crack indications have been detected in DMWs in both BWR and PWR plants. During the PERDI project cooperation agreements were made and joint research was performed or started with the following international research activities:

- International Cooperative Research Project on Non-destructive Examination for Primary Water Stress Corrosion Cracking in Nickel-base Materials and Dissimilar Metal Welds, PINC, The United States Nuclear Regulatory Commission, 2005–2009.
- Tohoku University, Japan, MIT/CALTECH, USA, and TKK/VTT, Dissimilar Metal Weld Project, 2005–2010 (supported by MEXT, Ministry of Education, Culture, Sports, Science and Technology, Japan).
- EPRI Alloy 690/152/52 Expert Panel Collaboration, 2008–2015.
- EPRI/NRC Weld Residual Stress Program: Phase 1 and 2 (2009–2011).

One purpose of the PERDI project was to transfer the high level knowledge in the field of DMWs and their long-term behavior in operation from the nuclear industry, to conventional industries. In return, the powder metallurgy knowledge from multi-material components was transferred to the nuclear industry. The common goal for all the partners was to develop reliable testing methods and to obtain high-level research results on the new materials and their dissimilar metal joint (thermo)-mechanical testing, their structural evaluation and design, control of residual stresses and performance of NDE.

An extensive study was made on the possible use in nuclear applications of materials/components made by the Hot Isostatic Pressing (HIP) method. The purpose would be to replace the present forged products with HIP-products, but the HIP technique is not at present approved by the codes, such as ASME. The study clarified the requirements for ASME approval and the procedure for obtaining a code case for HIP products. The same aim is under process also elsewhere, and at present it is expected that in a couple of year's time there will be enough data for obtaining the ASME code case for HIP products (separate report [4]).

Separate reports:

1. Ritamäki, P. Non-destructive Inspection of Dissimilar Metal Welds between Stainless Steel and Heat-resisting Steel (Ruostumattoman ja kuumalujan teräksen hitsatun eripariliitoksen mikrorakenne ja ultraäänitarkastettavuus). M.Sc. Thesis, Helsinki University of Technology, Espoo, Finland, 2008. 137 p. + app. 10 p.

2. Morra, M. Personal communication, 2008.

3. Cumblidge, S. E., Doctor, S. R., Heasler, P. G. & Taylor, T. T. Results of the Program for the Inspection of Nickel Alloy Components. NUREG/CR-7019, Revision 1. 2010. U.S. Nuclear Regulatory Commission. Washington DC, USA, 2010. 576 p. http://www.nrc.gov/reading-rm/doc-collections/nuregs/contract/cr7019/r1/cr7019r1.pdf.

4. Aaltonen, P., Toivonen, A. & Hänninen, H. Applicability of HIP for Reactor Components. VTT Technical Research Centre of Finland, Espoo, Finland, 2009. VTT Research Report VTT-R-00714-09. 27 p.

Preface

This research is primarily addressed to the needs of the nuclear power plant (NPP) industry, but conventional energy production, pulp and paper, oil refining and other process industries, and heavy metal and mining industries can also benefit from the results and expertise developed. The PERDI project is based on the earlier ERIPARI project, in which the background research and test method development was carried out. The degradation of dissimilar metal welds in both BWR- and PWR-plants is currently an area of widespread international interest. The PERDI research project was conducted in cooperation with a number of different on-going and planned international cooperative research projects. The research is particularly relevant because indications have been found in the reactor pressure vessel nozzle dissimilar metal welds of BWRs similar to Finnish BWR designs, while the EPR PWR-plant under construction contains a number of different and new types of dissimilar metal welds of which there is no previous experience available.

New materials can offer exceptional performance in conventional energy production, pulp and paper, oil refining and other process industries, as well as heavy metal and mining industry applications. New types of dissimilar metal welds may then be required, and be critical for the performance of the new types of products. Control of the residual stresses in manufacturing is often a critical factor in these applications.

The purpose of the study was to transfer the high level knowledge from the nuclear industry to conventional industries in the field of dissimilar metal welds and their long-term behavior in operation. In return, the powder metallurgy knowledge from multi-material components was transferred to the nuclear industry. The common goal for all the partners was to develop reliable testing methods and to obtain high-level research results on the new materials and their dissimilar metal joint (thermo)-mechanical testing, their structural evaluation and design, control of residual stresses and performance of NDE. The ageing mechanisms of dissimilar metal weld joints in nuclear power plants and their EAC cracking resistance are extremely important, and are also very useful in oil refining and other industry applications.

Contents

List of symbols

AES	Auger Electron Spectroscopy
ATEM	Analytical Transmission Electron Microscopy
BTR	Brittle Temperature Range
BWR	Boiling Water Reactor
°C	Degree Celsius
C(T)	Compact Tension
cc	Cubic Centimetre
CDCB	Countered Double Cantilever Beam
CERT	Constant Extension Rate Test
CGR	Crack Growth Rate
cm	Centimetre
CMTR	Certified Material Test Report
DDC	Ductility Dip Cracking
DMW	Dissimilar Metal Weld
DSC	Differential Scanning Calorimetry
DSA	Dynamic Strain Aging
DTA	Differential Thermal Analysis
EBSD	Electron Backscattering Diffraction
EDS	Energy Dispersive X-ray Spectrometer
EPRI	Electric Power Research Institute
FEA	Finite Element Analysis
FEM	Finite Element Method
FM	Filler Metal
FZ	Fusion Zone
HAGB	High Angle Grain Boundary
HAZ	Heat Affected Zone
IDSCC	Interdendritic Stress Corrosion Cracking
IGA	Intergranular Attack
IGC	Intergranular Corrosion
IGM	Intragranular Misorientation
IGSCC	Intergranular Stress Corrosion Cracking
IPF	Inverse Pole Figure
LAS	Low-alloy Steel
LTCP	Low Temperature Crack Propagation
L-T	Longitudinal-Transverse Direction
LTA	Low Temperature Aging
LWR	Light Water Reactor
M	Moment
mV_{SHE}	Millivolt on Standard Hydrogen Electrode Scale

NDE	Non Destructive Examination
NPP	Nuclear Power Plant
p	Pressure
ppb	Parts Per Billion
ppm	Parts Per Million
PWR	Pressurised Water Reactor
PWHT	Post-Weld Heat Treatment
PWSCC	Primary Water Stress Corrosion Cracking
Q	Activation Energy
RPV	Reactor Pressure Vessel
SMAW	Shielded Metal Arc Welding
SCC	Stress Corrosion Cracking
SEM	Scanning Electron Microscope
SEN(B)	Single Edge Notch Bend (Specimen)
SSRT	Slow Strain Rate Test
STF	Strain-to-Fracture
T	Temperature
t	Time
TCL	Total Crack Length
Tekes	Finnish Funding Agency for Technology and Innovation
TEM	Transmission Electron Microscope
TIG	Tungsten Inert Gas (Welding)
T-S	Transverse-Thickness Direction
TVO	Teollisuuden Voima Oy
VTT	VTT Technical Research Centre of Finland
WEDM	Wire Electric Discharge Machining
XRD	X-ray Diffraction
σ	Stress
$\varnothing$	Diameter

1. Introduction

The increasing demand for better performance of products in applications where the load bearing capacity, higher temperatures and aggressive environments are present results in combinations of different materials being joined together by various techniques in the same product. This is often done by welding, but other advanced new joining methods are applied as well. There is very little public knowledge available regarding demanding dissimilar metal joints, especially for new materials, and therefore extensive testing and research is normally required before they can be more broadly utilization in industrial applications. In general new testing techniques have to be developed for these purposes.

In the nuclear power industry dissimilar metal welding is widely used in many constructions and systems. The operating experience of major nuclear power plant (NPP) pressure boundary components has recently shown that dissimilar metal weld joints can jeopardize the plant availability and safety because of increased incidences of environment-assisted cracking (EAC) of Alloy 600 and its corresponding weld metals (Alloys 182/82). Alloy 690 and its associated weld metals (Alloys 152/52) are widely used for repair and replacement of the affected thick-section components. These are also the main construction materials of such components in new reactors such as the EPR. The selection of new materials relies mainly on laboratory results and short-term service experience. The long-term behavior of these materials and their performance in the plant has still to be demonstrated. At present the problems with dissimilar metal joints in nuclear power plants are a great international challenge. The experience and research results from the nuclear power plant dissimilar metal joint applications can be widely used in other industries and applications such as oil refineries, other energy sectors where elevated temperatures are present (fuel cells, high temperature power plants, etc.) and pulp and paper and other process industries where better energy efficiency is required.

In general the weldability of nickel-base materials is evaluated based on the results obtained with weld metals of different chromium contents. The susceptibility to hot cracking in welding is equally important to the stress corrosion cracking susceptibility in primary water (PWSCC), and both of them are based on the metallurgical properties of the nickel-base alloys. The microchemistry and microstructures in the multi-pass nickel-base alloy welds is very different than that in the wrought and recrystallised nickel-base materials. Additionally, the thermal ageing behavior of various nickel-base weld metals is expected to be quite different from that of wrought base materials. Weld residual stresses and their role in PWSCC is of great importance in the case of dissimilar metal joints. They have been modelled to a certain extent, but results of direct measurements of residual stresses are not

available at present for any of the dissimilar metal welds of NPPs. The application of various surface stress improvement techniques for PWSCC mitigation are being considered at present, but the decision to employ them in plants first requires extensive residual stress measurements and demonstration to be made.

In the international project PINC (Program for the Inspection of Nickel Alloy Components) the application, improvement and qualification of NDE methods for nickel-base alloy weld locations were evaluated with regards to the probes, techniques and scanning devices employed [3]. The need for representative mock-ups for technique development and qualification was identified, and they are currently under development. The technical basis for the development of inspection requirements for dissimilar metal welds, and efforts to qualify inspection procedures and personnel, are emphasized in order to obtain more reliable results.

Maintaining the structural integrity of the main components of NPP, oil refinery and pulp and paper industry throughout the service life in spite of the several possible ageing mechanisms related to the dissimilar metal welds is essential for plant safety and availability. The ERIPARI-project [5, 6] was focused on dissimilar metal structures, both on welds and components. The welds studied were typical mock-up welds for various nuclear power plant applications, but they are also present in modern oil and gas industry applications. The results obtained within the ERIPARI-project encouraged further studies in the area of dissimilar metal welds (DMW), as a vast amount of new questions arose. The research work carried out within the follow-on PERDI project suggests that there are still a large number of important tasks to be clarified further, as described in this report, which concentrates on the properties of Ni-base alloy welds and their dissimilar metal joints.

2. Characterization of the nickel-base alloy weld metals

Several studies have been made to investigate the hot cracking susceptibility of the nickel-based weld filler metals Alloys 82, 182, 52 and 152 and base metal Alloy 690, e.g. [7, 8, 9]. Hood & Lin [7] studied the hot cracking susceptibility of the Ni-base alloy filler metals using the Varestraint and spot-Varestraint tests. The results showed that Alloy 52 exhibited the best resistance to both weld solidification cracking and weld metal liquation cracking, followed by Alloys 82, 152 and 182. Wu & Tsai [8] investigated the hot cracking susceptibility of Alloys 82 and 52 with Alloy 690 by Varestraint tests. Alloy 82 showed greater total crack length (TCL) than Alloy 52. Liquation cracks and ductility dip cracks were found in the heat affected zone (HAZ), but an accurate distinction of the crack type was difficult. These results indicate that the hot cracking susceptibility of Alloy 82 is greater than that of Alloy 52 in Varestraint testing. Recently a Gleeble-based test technique, termed strain-to-fracture (STF), was developed by Nissley et al. [10] and employed for evaluating the strain-to-fracture of ductility-dip cracking (STF DDC) susceptibility curves for filler metals of Alloys 82 and 52 [9, 10]. The filler metal Alloy 52 was more susceptible to DDC than Alloy 82, which also exhibited heat-to-heat variation in susceptibility. Thus, because of the varying observations coming from various tests there is a major need to rank the Ni-base alloy weld metals in terms of their hot cracking susceptibility, and to understand the mechanisms of solidification cracking properly.

2.1 Solidification cracking

Different dissimilar metal weld configurations were studied. The weld geometries contained nickel-base weld metals Alloy 152 (mock-up 1, TU1), 52 (mock-up 2, TU2), both 52 and 152 (mock-up 3, TU3), 182 (mock-up TV), Figure 1 and Table 1. In one case not shown, Alloy 82 was employed in a manner simulating a repair weld.

2.1.1 Microstructures and Varestraint test results

The principle of Varestraint testing is shown in Figure 2.

2. Characterization of the nickel-base alloy weld metals

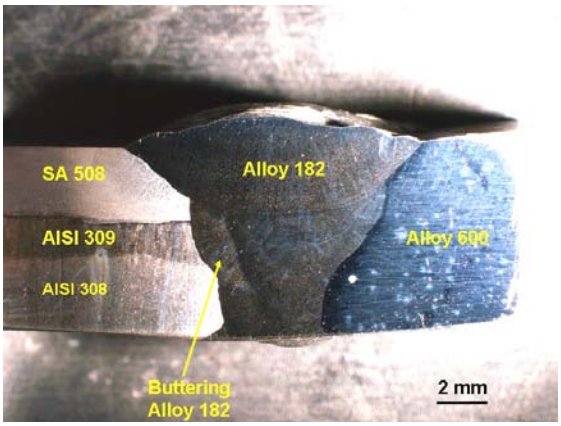

a)

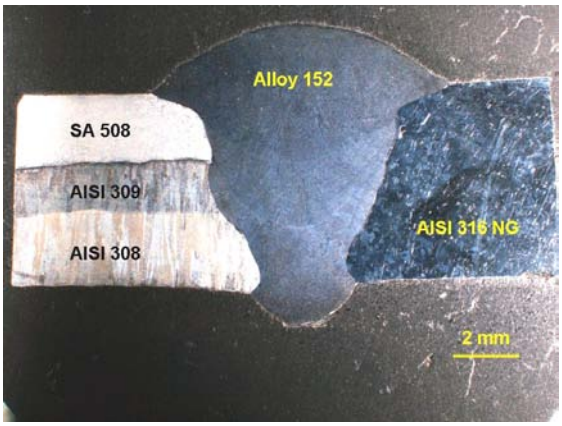

b)

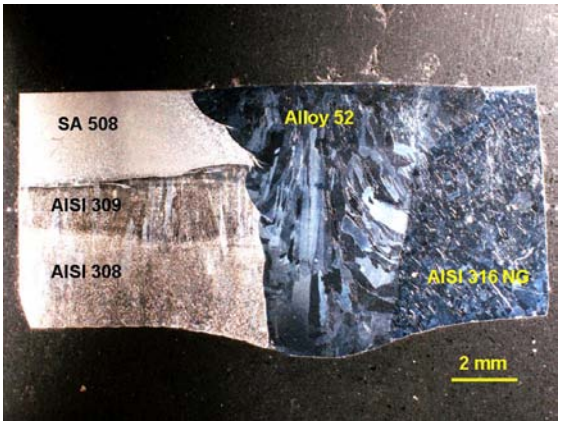

c)

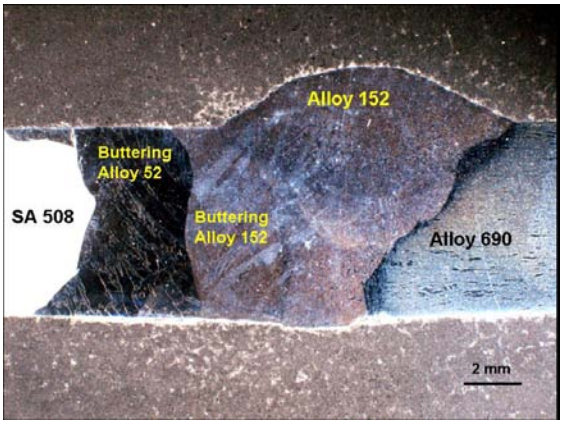

d)

Figure 1. Materials and cross-section of a) mock-up TV, b) mock-up 1, TU1, c) mock-up 2, TU2 and d) mock-up 3, TU3 dissimilar metal welds.

Table 1. The nominal chemical compositions* and CMTR analyses of the base materials and filler metals used in the dissimilar metal welds.

	C	Si	Mn	P	S	Cr	Mo	Ni	Nb	Ti	Fe	Al	Co	Cu
Base materials														
AISI 316 NG	< 0,03					16,5-18,5	2,5-3	11-14						
SA508 (Grade 2)	0,24	0,21	1,38		0,009	0,16	0,54	0,58				0,015		0,12
Alloy 600	0,07	0,19	0,21	0,007	0,001	16,3		72,86	Nb+Ta 0,10	0,28	9,44	0,229	0,076	0,13
Alloy 690	0,02	0,04	0,16		0,001	29,46		59,82		0,33	9,96	0,2		<0,01
Filler metals														
AISI 308L (OK Band 11.61)	< 0,025	0,4	1,8			20		10						
AISI 309L (OK Band 11.65)	< 0,025	0,4	1,8			24		13						
Alloy 182 (OK 92.26)	0,03	0,8	6,5	0,01	0,003	15,7		68	1,8	0,1	6,7			< 0,01
Alloy 82 (OK Tigrod 19.85)	0,039	0,03	2,98	0,001	0,004	19,94		72,6	Nb+Ta 2,47	0,34	1		0,01	0,01
Alloy 52	0,03	0,13	0,24	<0,001	<0,001	29,2	0,03	59,28	Nb+Ta <0,02	0,51	9,8	0,72	0,009	0,04
Alloy 52M	0,02	0,09	0,8	0,003	0,001	30,06	0,01	59,54	Nb+Ta 0,83	0,224	8,22	0,11	0,027	0,02
Alloy 52MS	0,014	0,12	0,68	0,004	0,0007	29,53	0,02	60,14	0,78	0,19	8,33	0,13	0,008	0,03
Alloy 152	0,048	0,41	3,48	0,003	0,003	28,74	0,01	55,2	Nb+Ta 1,54	0,09	10,39	0,06	<0,005	<0,01
Alloy 152M	0,0293	0,3276	3,247	<0,001	0,0042	28,98	<0,005	57	Nb+Ta 1,533	0,039	8,75	<0,005	0,0119	<0,005

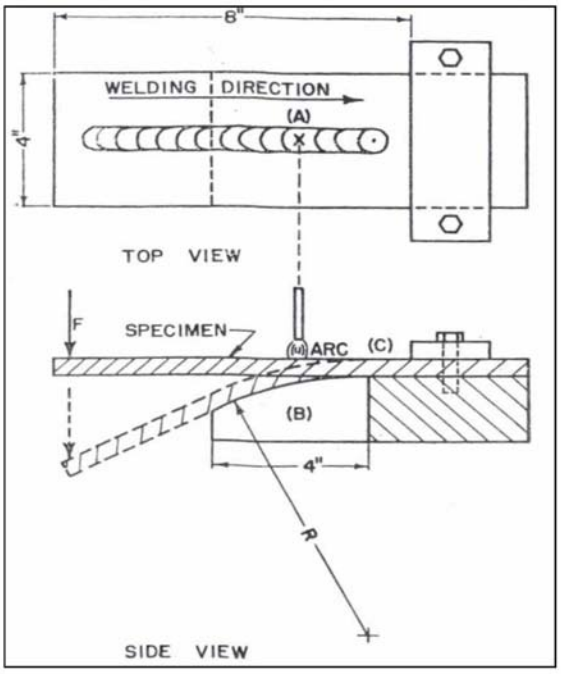

Figure 2. Simplified sketch of the operation of the Varestraint testing device.

The hot cracking susceptibility of Ni-base alloy dissimilar metal welds was studied by using the mock-ups shown in Figure 1. The motivation for the study was the need for repair welding of Alloy 182 welds of safe ends in BWR plants, and identifying possible welding problems with new Alloy 152/52 weld metals. Susceptibility to hot cracking was examined by Varestraint tests, and weld microstructures were studied by optical and field emission gun scanning electron microscopy (FEG-SEM/EDS). Figure 1 presents materials and cross-section of dissimilar metal welds of Alloys 182, 152 and 52. The clad pressure vessel steel SA 508 side of specimen TV (with Alloy 182 buttering) had

been heat treated at 610 °C for 6 h and mock-up 3 (with Inconel 52 and Inconel 152 buttering) had been heat treated at 610 °C for 4 h before welding. Whole welded test specimens of mock-ups 1 and 2 were heat treated at 610 °C for 16 h after welding. Figure 3 presents the test piece geometry for Varestraint testing of pure weld metals, and as an example, the weld pass sequence of the test specimen welded with Alloy 82. The base material in each of those tests was an AISI 304 plate into which a 20 mm wide, 60 mm long and 4 mm deep groove was machined, which was then welded with the filler metal. The surface of the weld was ground to the level of the base metal so that the surface quality was equal in all Varestraint tests. The filler metals used in the pure weld metal tests were Alloy 182 (Esab OK 92.26), 82 (Esab Tigrod 19.85), and Alloys 152, 152M, 52, 52M, and 52MS (Special Metals), Table 1. Table 2 presents the welding parameters used for mock-ups in the Varestraint testing.

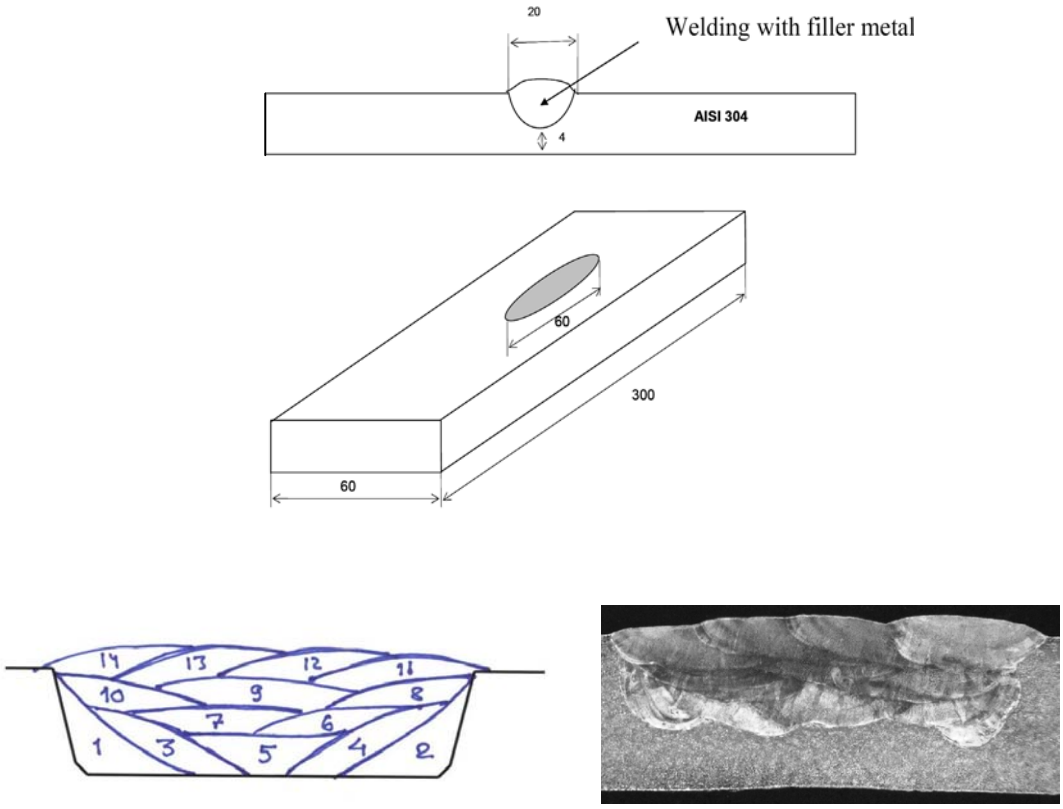

Figure 3. Test piece for Varestraint testing of pure weld metals and weld pass sequence of the test specimen welded with filler metal Alloy 82.

Table 2. Summary of the welding parameters used for Mock-ups in the Varestraint tests.

	Current [A]	Voltage [V]	Welding speed [cm/min]	Heat input [kJ/cm]
Mock-up TV (Alloy 182)	**150**	**10.5**	**12**	**4.7**
Mock-up 1 (Alloy 152)	**150**	**10.5**	**12**	**4.7**
Mock-up 2 (Alloy 52)	**150**	**10.5**	**12**	**4.7**
Mock-up 3 (Alloy 152)	**150**	**10.5**	**12**	**4.7**

Figure 4 a) presents the surface of the Alloy 182 weld test piece with hot cracks after Varestraint testing (augmented strain 4%). Optical micrograph b) of a hot crack (dark areas) in the cross-section of the weld and FEG-SEM micrographs c) and d) of hot crack tips show details of an irregularly shaped white phase associated with the hot cracks of this alloy. The compositions of the white phase areas were examined by energy dispersive X-ray spectroscopy (EDS). Figure 5 presents X-ray element maps and Figure 6 shows a SEM image and EDS analyses of the white phase area in a dendrite boundary region. They show marked Si, Nb, Mn and P enrichment, which is compensated by depletion of Cr, Fe and Ni. Based on the high magnification backscattered electron (BSE) images and the EDS analyses, the phase appearing white in the optical micrograph of Figure 4 b) actually consists of two phases, appearing white and grey in SEM (Figure 4 d), with varying Nb, Si, Mn and Ti contents. Inside and along the dendrite/grain boundaries white Nb-rich particles, Nb(C, N), are present.

a)

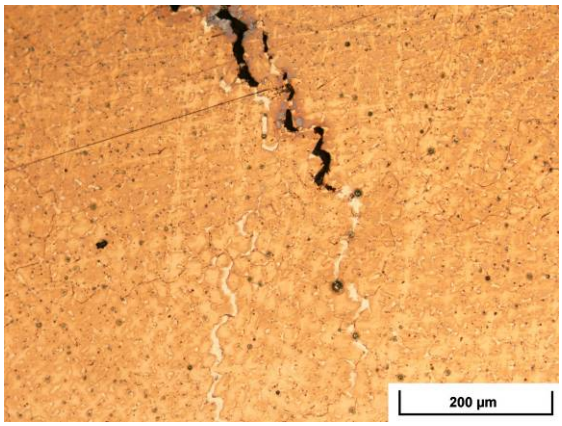

b)

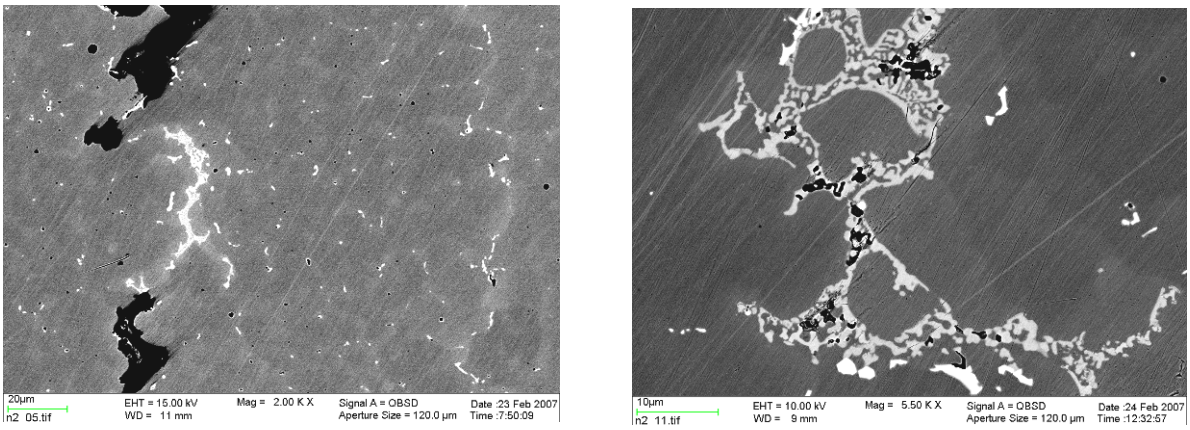

c) d)

Figure 4. a) Surface of Alloy 182 weld test piece with hot cracks after Varestraint test (augmented strain 4%). b) Optical micrograph of the hot cracks (dark areas) in a cross-section of the weld (note the white phase ahead of the hot crack tip). c) and d) SEM micrographs of weld hot crack tips showing details of the irregularly shaped white phase on the dendrite boundaries.

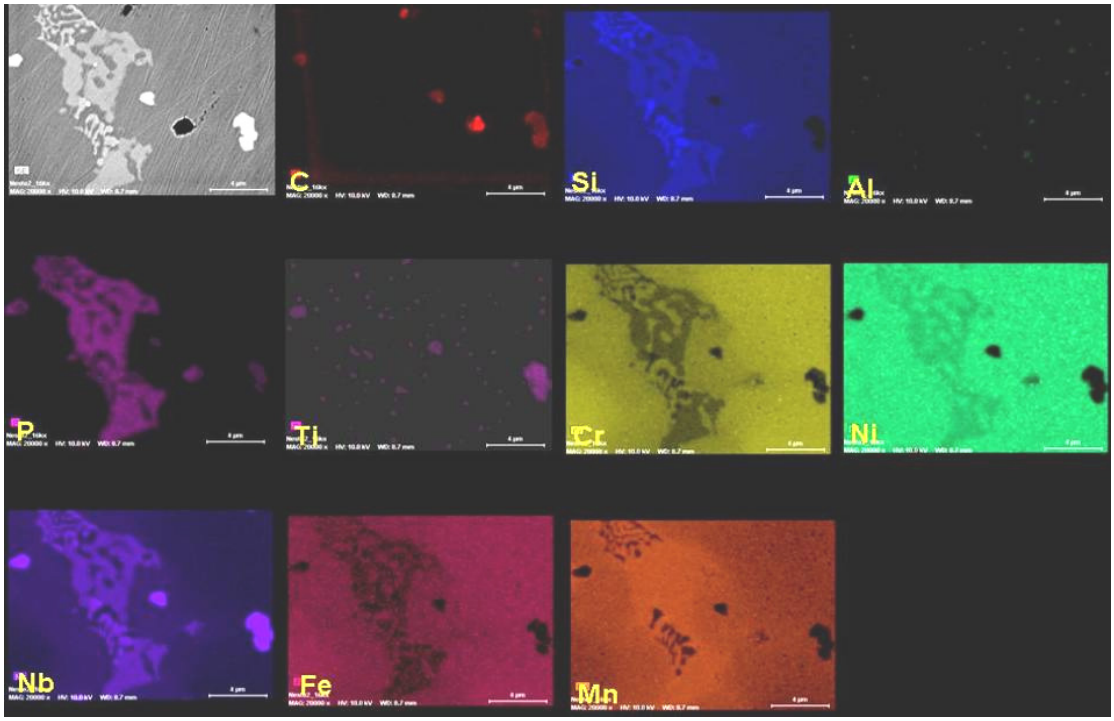

Figure 5. X-ray element maps of the white phase area in Alloy 182 weld in a dendrite boundary region. Note marked Nb enrichment in the white phase and less enrichment in a wider area along the dendrite boundary. Marked Si, Mn and P enrichment compensated by depletion of Cr, Fe and Ni can also be seen.

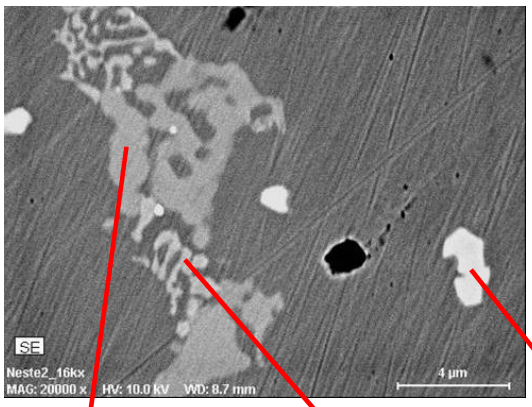

Element	Filler metal wt.%	Grey area wt.%	Enrichment vs. filer metal	Light white area wt.%	Enrichment vs. filer metal	White area wt.%	Enrichment vs. filer metal
Si	0,8	3,4	4,3	6,5	8,1	0	0,0
P	0,01	1,3	130,0	1,3	130,0	0,2	20,0
Ti	0,1	0,04	0,4	0,7	7,0	2,8	28,0
Cr	15,7	5,4	0,3	4,9	0,3	1,4	0,1
Mn	6,5	17,7	2,7	11,8	1,8	1,1	0,2
Fe	6,7	4,7	0,7	4,9	0,7	1,5	0,2
Ni	68	51,4	0,8	49,4	0,7	0	0,0
Nb	1,8	15,2	8,4	20,6	11,4	89,6	49,8

Figure 6. SEM image and EDS analyses of the white and grey phase in Alloy 182 weld showing Nb, Si, Mn and P enrichment and Nb-rich particles, Nb(C, N). The spot size in EDS analysis has an interaction diameter about 1 µm, and therefore the surrounding matrix affects also the result.

Figure 7 shows an opened hot crack fracture surface of Alloy 182 imaged in SEM with a relatively low acceleration voltage of 7 kV, so that the information comes from close to the surface. The wavy morphology of the interdendritic fracture surface indicates that the phase along the dendrite boundaries was still molten during fracture.

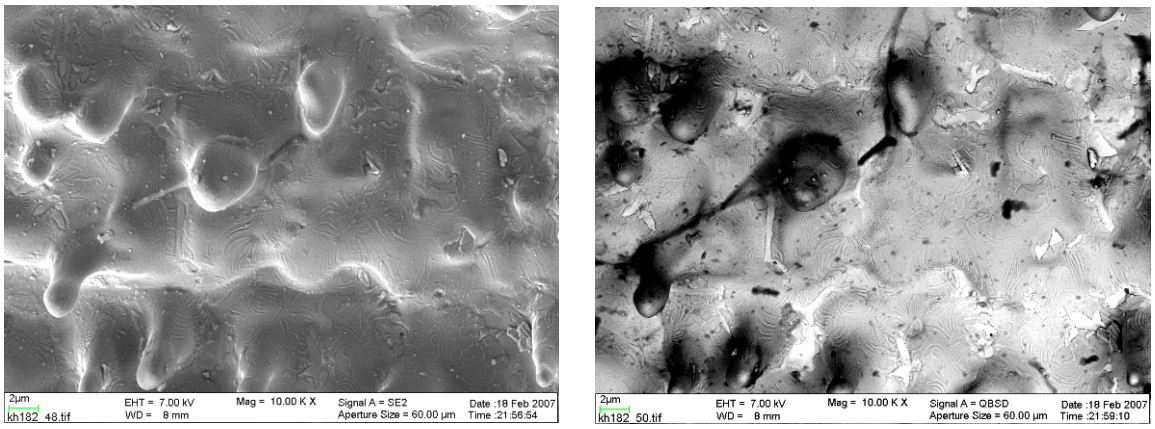

Figure 7. Fracture surface of an Alloy 182 hot crack showing the white phase in the valleys between dendrites.

Study of the fracture surfaces of Alloy 182 weld hot cracks revealed same kind of segregation of Nb, Si, Mn, and P on the fracture surfaces as had been seen in the white phase in the cross-sections of the hot cracks. On the fracture surface Nb-rich particles, probably Nb(C, N), and the lamellar white phase were intermixed in the final microstructure.

Figure 8 presents a SEM image of a cross-section of hot cracks in the Alloy 152 weld metal of mock-up 1, after Varestraint testing (augmented strain 4%). It also shows SEM images of the fracture surface, where the presence of the white phase in the valleys between the dendrites is clearly visible. The X-ray element map of the hot crack fracture surface exhibited high enrichment of Nb to the white phase.

Alloy 152 weld metal shows similar hot cracking tendency as compared to Alloy 182. The Nb-rich white phase is connected to the hot cracks and the phase can be easily found in the cross-sections of the hot cracks as well as on the fracture surfaces (local coverage can be as high as 30%, see Figure 8 c). The dendrite boundaries containing the white phase show in addition to Nb, a marked increase of Si, Mn and P contents both in the white phase, but also in the wider zone along the dendrite boundaries. Simultaneously depletion of Cr, Ni and Fe is observed in these zones. In addition to the white phase both in the cross-section as well as on the fracture surfaces, plenty of small particles, Nb, Ti(C, N), are present.

Figure 9 presents SEM images and EDS results for hot-cracks formed in weld metal Alloy 52 of mock-up 2 after Varestraint testing (augmented strain 4%). Filler metal Alloy 52 also contains Ti (0,51 wt.-%), but does not contain Nb as Alloys 182, 82 and 152, and thus, hot cracks formed along the dendrite boundaries in the absence of the Nb-rich white phase. A lot of small particles (probably TiN) are present along the dendrite boundaries.

Hot cracking of Alloy 52 does not show any indications of the Nb-rich white phase observed with Alloys 182, 82 and 152, since Alloy 52 does not contain Nb. Alloy 52 contains Ti and therefore a lot of precipitation of TiN(C) was observed both in the cross-sections along the dendrite boundaries as well as on the fracture surfaces of the hot cracks, where the coverage of the hot crack fracture surface by TiN(C) can be quite extensive. The large interdendritic TiN(C) phase particles are presumed to have formed in the melt prior to final solidification of the weld. On the fracture surface MnS phase particles are also observed as separate phases. Thus, in Alloy 52 the only marked phase on the hot crack surfaces is TiN(C).

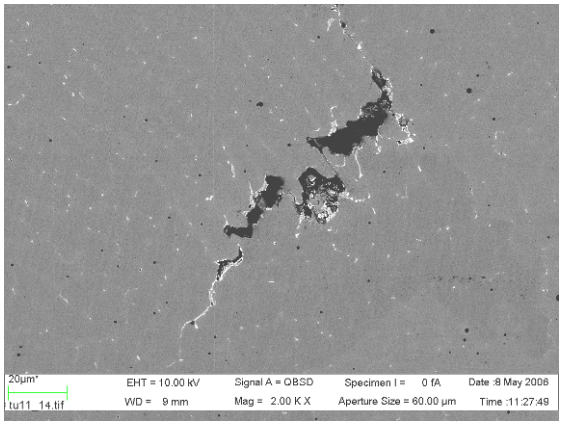

a)

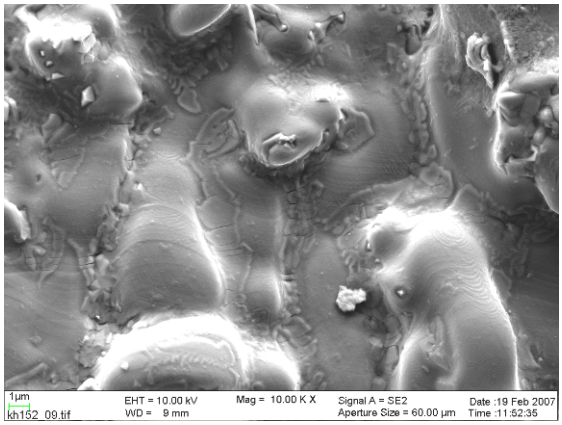

b)

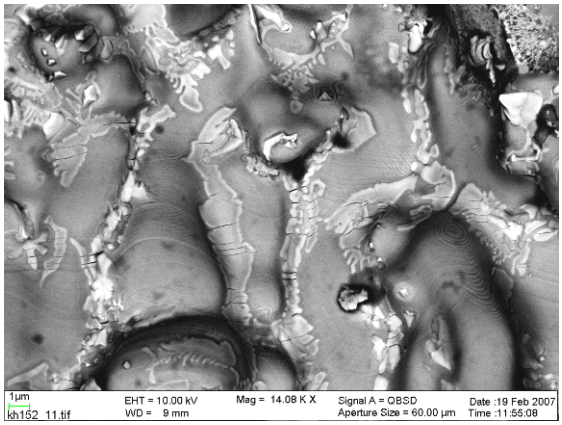

c)

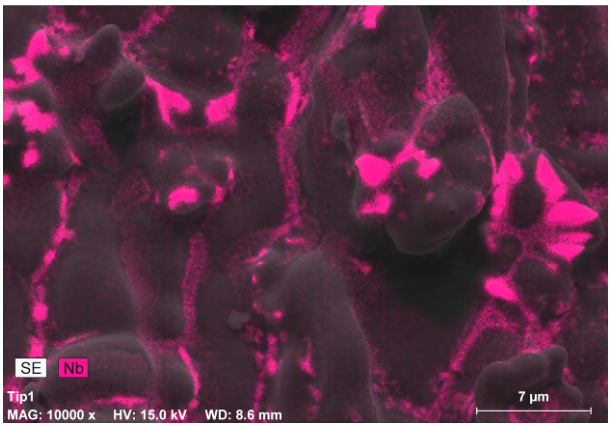

d)

Figure 8. a) SEM image of a cross-section of hot cracks in Alloy 152 weld metal illustrates the relationship of the white phase to hot cracks. b), c), and d) Hot crack fracture surface of Alloy 152 weld metal shows the brittle nature of the lamellar white phase and high enrichment of Nb to the white phase.

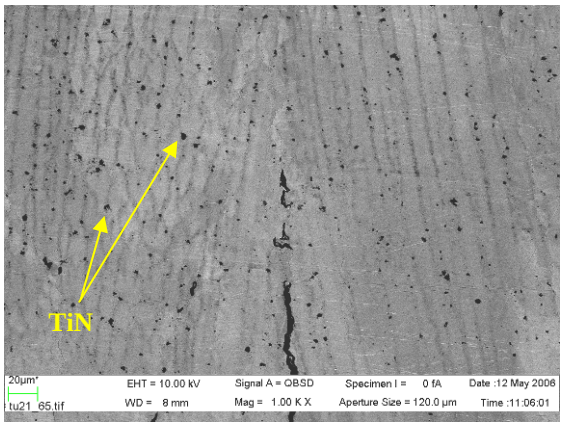

a)

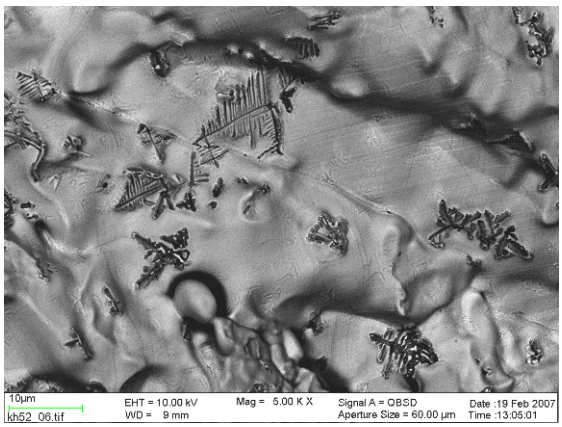

b)

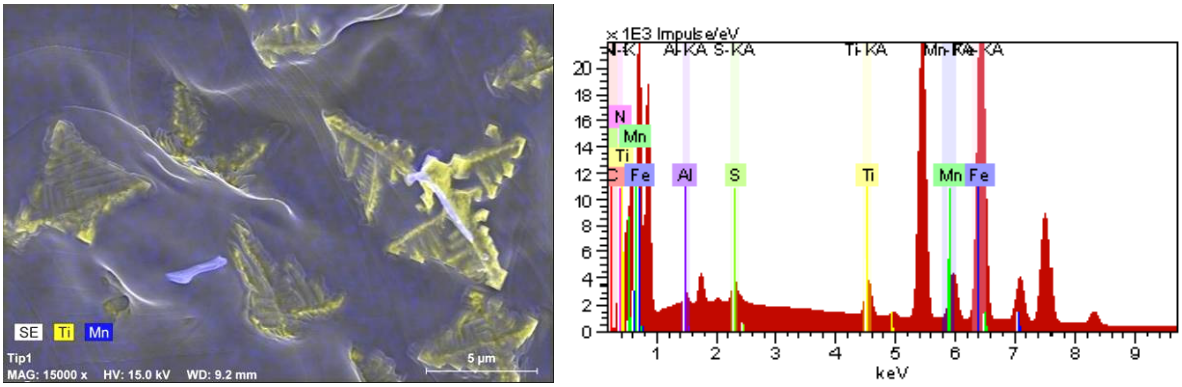

c)

Figure 9. SEM images of weld hot cracking in the Alloy 52 weld metal of mock-up 2 after Varestraint testing with 4% augmented strain; a) crack cross-section b) fracture surface and c) fracture surface X-ray element map and EDS analyses revealing the dendritic phase of TiN(C). Separate MnS particles were also present based on observed elements.

Total crack lengths (TCL) of Alloy 182 of mock-up TV and mock-ups 1, 2 and 3 are shown in Figure 10 a) and maximum crack lengths (MCL) in Figure 10 b), as welded and with augmented strains of 0.5%, 1%, 2%, 3% and 4%. The legend labelling is "Case, tension side, filler metal." Table 3 presents a summary of the Varestraint test results for the pure Ni-base alloy weld metals after 4% augmented strain (see Table 1 and Figure 3).

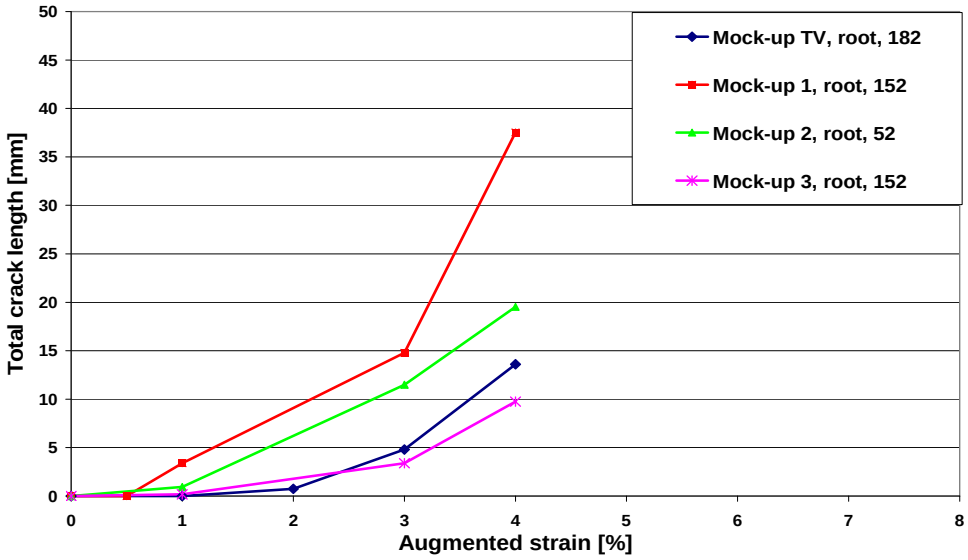

a)

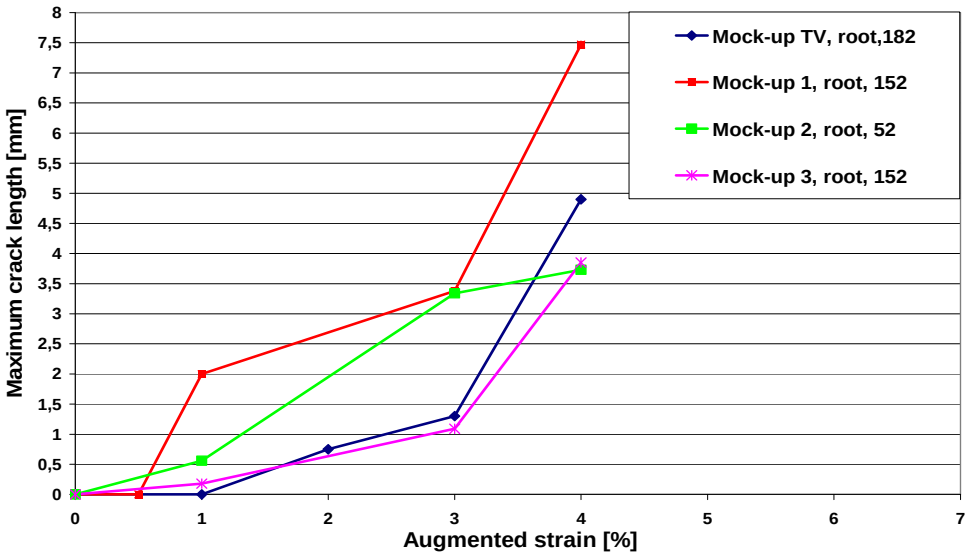

b)

Figure 10. a) Total crack lengths (TCL) and b) maximum crack lengths (MCL) as a function of augmented strain for the four mock-up dissimilar metal weld samples following Varestraint testing.

For comparison, in the ERIPARI project pure Alloy 82 weld metal hot cracking took place only at higher heat input (Q = 9.4 kJ/cm). The hot cracks formed were markedly oxidized, probably because of the high heat input and also because of segregation to the final melt. SEM image and X-ray element maps of cross-sections of hot cracks in that material also exhibited a strong Nb segregation, but less marked Si, P and Ti segregation to the dendrite boundaries at the hot crack tip. Nb- and Ti-rich

particles, Nb, Ti(C, N), were also clearly visible (Ti content of Alloy 82 is 0.34 wt.-%). For more details, see Hänninen et al. [5, 6]

Table 3. Summary of Varestraint tests made for pure Ni-base alloy weld metals using an augmented strain of 4% and heat input of 4.7 kJ/cm. For Alloy 82 a 9.4 kJ/cm heat input was also applied.

Alloy 182	**TCL = 19.3 mm / 2nd test -> cracks**
Alloy 82 (Q=4.7 kJ/cm)	**no cracks / 2nd test -> no cracks**
Alloy 82 (Q=9.4 kJ/cm)	**TCL = 32.9 mm**
Alloy 152	**TCL = 19.7 mm / 2nd test -> cracks**
Alloy 152M	**TCL = 8.1 mm**
Alloy 52	**no cracks / 2nd test -> no cracks**
Alloy 52M	**TCL = 3.1 mm / 2nd test -> no cracks**
Alloy 52MS	**no cracks / 2nd test -> no cracks**

Hot cracking occurred along the dendrite boundaries and the susceptibility to hot cracking in the dissimilar metal weld mock-up samples was observed to follow the order: Alloy 152 > Alloy 52 > Alloy 182 > Alloy 82. In pure weld metal hot cracking tests the susceptibility was observed to follow the order: Alloy 182 ≥ Alloy 152 > Alloy 52 ≥ Alloy 82. The differences between these two test types are thought to be related to dilution effects, because Fe, Si, and C enhance the eutectic phases and expand the solidification temperature range.

2.1.2 Weldability of Ni-base materials

Weldability of the studied Ni-base materials was evaluated based on the results obtained with various mock-up welds of real components or anticipated weld designs of future plants and weld metals of different chromium contents. The susceptibility to hot cracking was examined based on the Varestraint test results by ranking the materials. The mechanistic understanding of the hot cracking susceptibility of Ni-base weld metals is still largely missing and careful metallurgical studies of the solidification mechanisms were carried out by a modern FEG-SEM/EDS instrument. Marked segregation of alloying elements such as Nb, Si, P and Mn to the last liquid to solidify at dendrite boundaries was observed and in Nb-bearing alloys an eutectic Nb-rich Laves phase (white phase), $(Ni, Cr, Fe)_2(Nb, Si, Mn, P, Ti)$, formed in the interdendritic regions containing Nb as much as 15–30 wt.-%. The formation of the Laves phase is probably enhanced by the presence of Si, Mn and P, which are also markedly segregated to the white phase and/or interdendritic areas. Solidification cracking occurs during the terminal stages of solidification, when a liquid film is distributed along the interdendritic regions as a continuous film and the shrinkage strains across these boundaries cannot be accommodated. The solidification temperature range and morphology of the interfacial liquid are the primary factors controlling the solidification cracking susceptibility. Solute redistribution affects the solidification temperature range and amount of terminal liquid (small amount of terminal liquid is most detrimental).

Minor variations in Nb, Si, and C content in Ni-base alloys have a strong influence on the solidification temperature range, type and amount of secondary phases, which form during terminal stages of solidification and affect the solidification cracking susceptibility. These alloy additions decrease the liquidus and solidus temperatures and increase the solidification temperature range, Nb being most effective in this. Of the two types of the eutectic-type constituents, γ/NbC (or TiN(C)) and γ/Laves, known to form as the Ni-base alloy welds solidify, the γ/Laves constituent is more deleterious in terms of hot cracking, as it forms at a lower temperature and thus extends the solidification temperature range. In dissimilar metal welds the studied alloys are used to join low alloy steels to stainless steels and due to dilution the weld metal can become significantly enriched in Fe, Si, P, S and C, which may significantly change the solidification behavior and associated cracking tendency. It is known that Fe additions to Nb-bearing Ni-base alloys promote the formation of γ/Laves constituent and Si addition has similar effect. Niobium addition promotes higher amounts of total eutectic and both eutectic-type structures (Laves and NbC) are highly enriched in Nb [11–14].

2.1.3 ATEM study of solidification cracking

Analytical transmission electron microscopy (ATEM) was carried out on some of the hot cracks found in the Alloy 182 weld metal of mock-up TV after Varestraint testing. The ATEM studies were initiated in order to try to further characterize the white phase ahead of the hot cracks that had been observed in FEG-SEM. The goal was to target the region of the phase in question, preferably at the tip of a hot crack, to better understand the reason for hot cracking.

The crack tip was targeted by utilizing special specimen preparation methods. The cracks were first back-filled with a low-viscosity M-Bond epoxy and then metallographic cross-sections were made of them. Thin slices were made which contained crack cross-sections. Pieces containing individual crack tips were excised from the slices, and then epoxy-bonded to copper supporting rings in order to prevent further crack opening with subsequent material removal. A Gatan Dimpler was used to mechanically pre-thin through the epoxy coating on both sides at the target location. Finally, electropolishing was used to complete thinning of the specimen to electron transparency, utilizing a 20% perchloric acid/methanol solution at -35 ºC and 15 V.

The second phase particles observed in SEM were rather large for proper examination with TEM, particularly for electron diffraction methods. Nonetheless, TEM did enable accurate compositional analyses to be made of the second phases using energy dispersive X-ray spectroscopy (EDS), while also giving important contextual information regarding the microstructure around the particles. Based on ATEM examinations, it would seem that two basic kinds of phases are present in the material. There are particles with a distinctly different crystal structure and a clear boundary with the surrounding matrix, as well as regions having diffuse boundaries, but dramatic compositional variability as compared to the bulk material.

The particles having their own crystal structure and distinct phase boundaries were of two basic types: there were diamond-shaped ones of uniform size of about 1 µm across that were typically high in Mn, Cr, Ti and Al, and there were more rounded, abstractly-shaped ones principally comprised of Nb with some Ti. An example of the latter is shown in Figure 11.

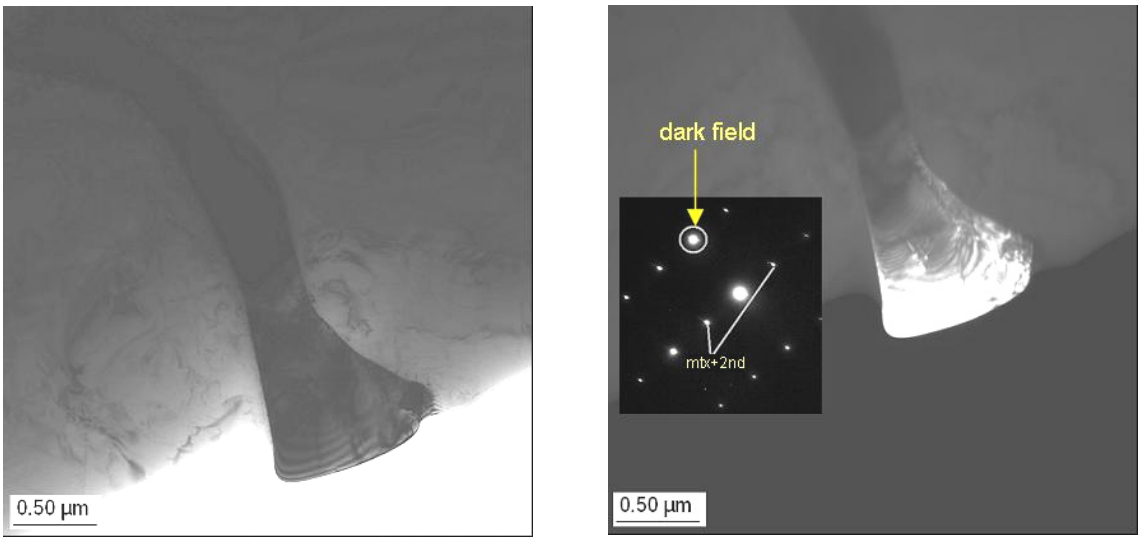

a) b)

Figure 11. a) Rounded-shaped phase ahead of the hot crack tip, with a composition of 90Nb-2Ti-3Ni-3Cr-1Fe (wt.%). b) Diffraction pattern and dark field image of the phase shows that it is a distinctly different phase.

The measured composition of the particle was (wt. %) 90 Nb and 2 Ti, with 3 Ni, 3 Cr and 1 Fe perhaps coming from the matrix contribution to the spectrum. The abstract shape of the particles suggests that they formed from the melt, so they are primary particles. As shown Figure 11 b), the diffraction of the particle was isolated from that of the matrix, enabling dark field imaging. This shows that it is a distinctly different phase. An example of the diamond-shaped particles is shown in Figure 12.

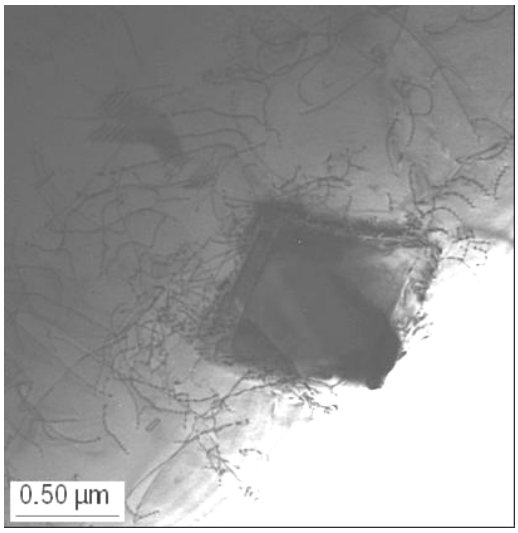

Figure 12. A diamond-shaped phase ahead of the hot crack tip with composition of 51Mn-16Cr-11Ti-6Al-9Fe-4Ni (wt.%). Note the misfit dislocations around the particle.

In the example shown, the measured composition included (wt. %) 51 Mn, 16 Cr, 11 Ti, and 6 Al, with 9 Fe and 4 Ni perhaps coming from the matrix. Noteworthy are the dislocations around the particle, which are due to misfit strains and stresses.

The regions of diffuse dendrite boundaries are large, and their composition varied dramatically. They often included or surrounded one or more of the aforementioned particles. The collages in Figure 13 and Figure 14 show two of these regions, together with compositions in particular locations within them.

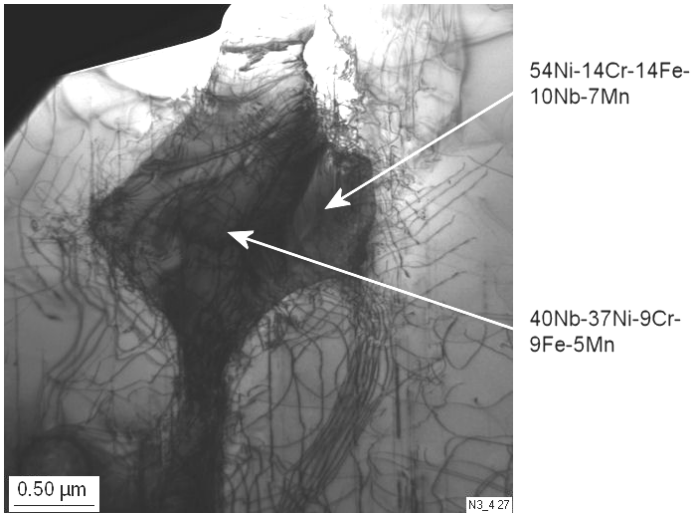

Figure 13. Wide region of the diffuse dendrite boundary ahead of a hot crack tip shows varying composition and these regions include or surround one or more of the particles shown in Figures 11 and 12.

In Figure 14 it is evident that they are significantly enriched in Nb and Mn and possibly Ti and Al. In this case the core is rich in Al and Mn, the interphase is Ti-rich and the outer shell is rich in Nb. The large phase regions also had a high dislocation density within them and around them, which is an indicator of significant residual strains.

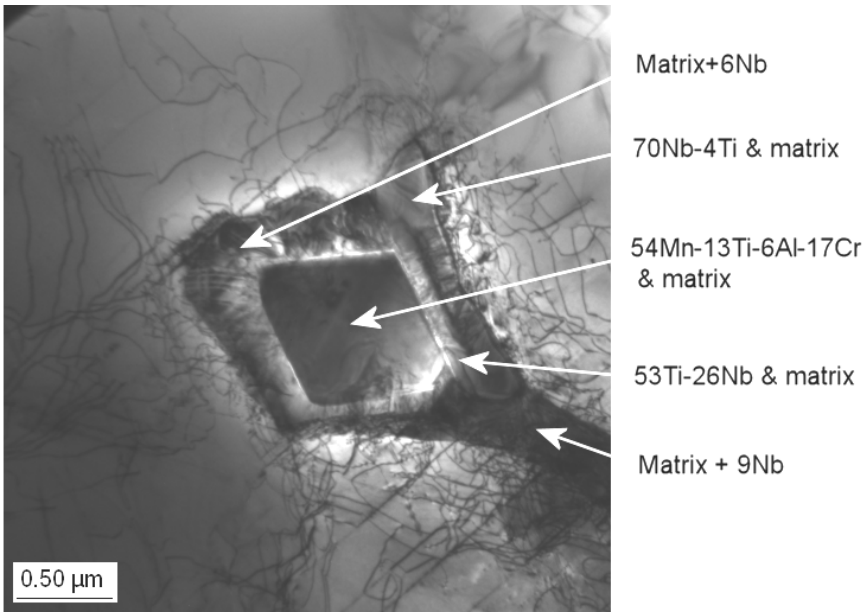

Figure 14. Wide region of the diffuse dendrite boundary ahead of the hot crack tip shows varying composition and these regions include or surround one or more of the particles shown in Figures 11 and 12. Note the high dislocation density on the diffuse dendrite boundary.

Selected area diffraction of the large phases did not show marked difference from the lattice of the matrix. As shown in the images of Figure 15, the boundaries of those regions seem to be principally distinguishable due only to a thickness variation between the boundary region and the matrix.

One possible reason for this would be that the Nb enrichment may alter the electropolishing properties locally. As shown in Figure 15, the dislocations are common to both regions of the boundary and the matrix, meaning that they share the same crystal lattice. The combination of a single lattice but marked composition changes suggests that the diffuse boundary regions most likely represent the eutectic phase.

The results summarized above indicate several things about the Alloy 182 weld metal of the mock-up. Firstly, the Nb- and Mn-rich particles probably formed from the melt, with some being incorporated into the solidifying matrix individually. As dendrites grew, the remaining liquid ahead of the solidification front was enriched in the alloying elements, particularly Nb and Mn, ultimately solidifying as a mixture of Nb-Ti and Mn-Ti-Al phase particles as well as a Nb-rich eutectic. Although Laves phase was not specifically sought in the studied ATEM samples, it was reportedly found in the FEG-SEM examinations that covered much larger volumes of materials, so could conceivably also be a consitutent in regions similar to those studied by ATEM. Perhaps most importantly, a high density of dislocations existed in and around the eutectic/particle mixture, while the eutectic still shared the austenite lattice of the matrix.

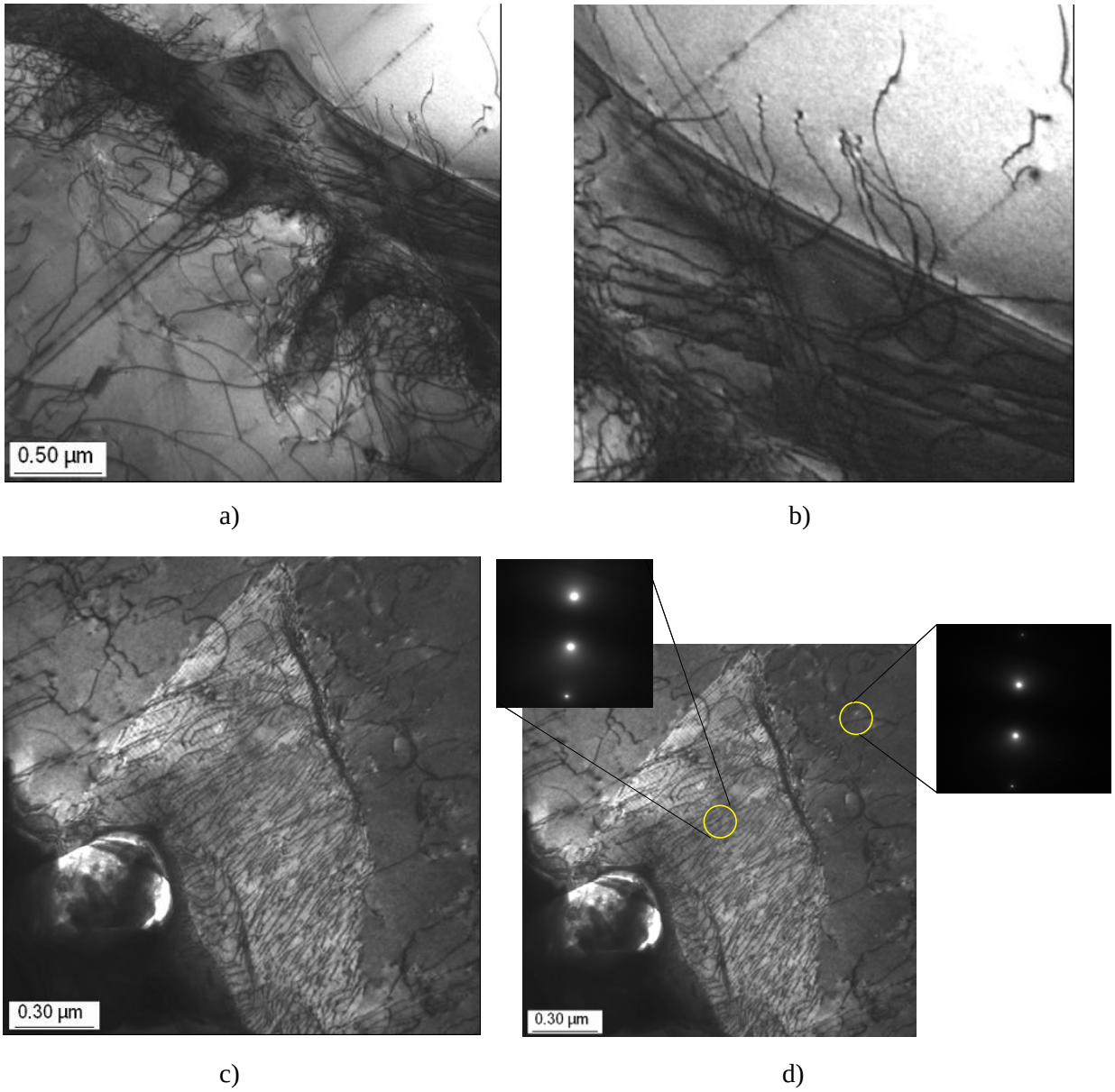

Figure 15. a) Diffuse dendrite boundary ahead of the hot crack tip shows marked compositional changes but no crystallographic lattice differences. The boundaries are distinguishable due to a thickness variation between the boundary region and the matrix. b) Dislocations are common to both matrix and the boundary region so they share their crystal lattice in spite of the Nb enrichment. c) Eutectic regions have a high dislocation density and d) they show the same diffraction pattern with the matrix.

The combination of the TEM results and the SEM results suggests that the hot cracking has occurred in the interdendritic eutectic mixture. The primary Nb- and Mn-rich phase particles within the mixture probably served as stress concentrators, but the separation was most likely occurring within the eutectic itself. The eutectic had similar crystallography to the matrix, but with its more complex composition it probably had a different exact lattice parameter and phase stability, which contributes to the

residual strain accumulation upon further cooling. It would seem conceivable that those residual strains may promote cracking in service, if they are associated with a sufficiently high residual stress component.

2.1.4 Differential scanning calorimetry of weld metals

The pure weld metals of alloys 182, 82, 152 and 52 were studied with differential scanning calorimetry (DSC) (Netzsch Model STA 449 F1 Jupiter) for determining their solidification temperature ranges and precipitation reactions during cooling (40°C/min) to room temperature. The DSC technique involves measurement of the heat absorbed/released during the solidification/melting or during the phase transformation in the solid state depending on whether the transformation reaction is endothermic or exothermic. Figure 16 shows the dynamic DSC curves for cooling from the melt to 400°C for the four studied weld metals. The solidification temperature ranges obtained in these first measurements for the studied alloys are the following:

- Alloy 182 21°C
- Alloy 82 40°C
- Alloy 152 53°C
- Alloy 52 47°C.

Only Alloy 82 (highest Nb content) shows a peak at 1137°C which can be related to Laves phase formation. In the solid state region the low-temperature peaks, 700–765°C, are similar for all alloys and are obviously related to Cr-carbide precipitation (exothermic peak). Other explanation for these peaks is due to the ordering reaction taking place resulting in Ni_2Cr short-range order in the studied alloys. The endothermic peak at 885°C is present only in Alloy 182 and 152 and the other endothermic peak at 945°C is different for Alloy 152 (double peak) but similar for the other weld metals. The origin of these peaks is not clear yet.

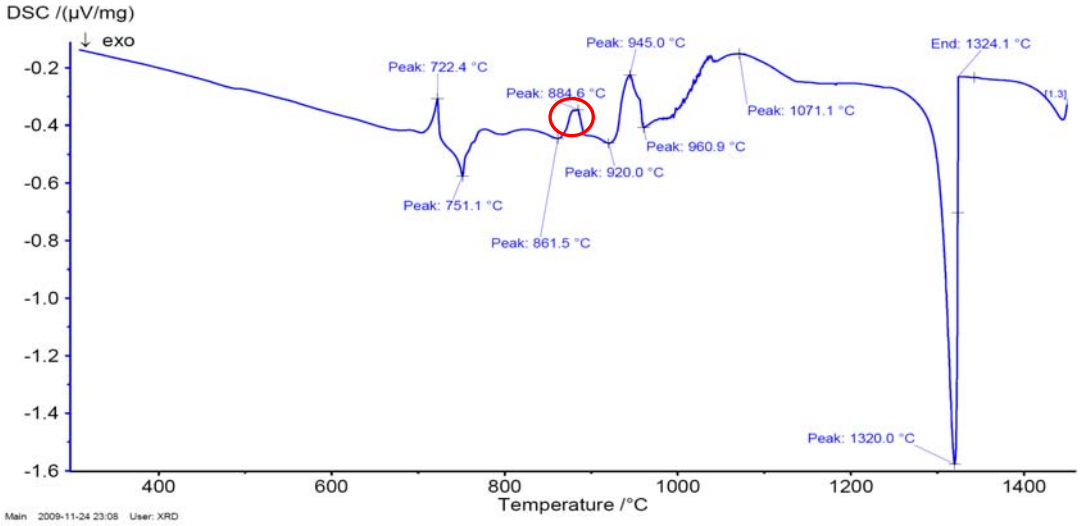

a) Alloy 182

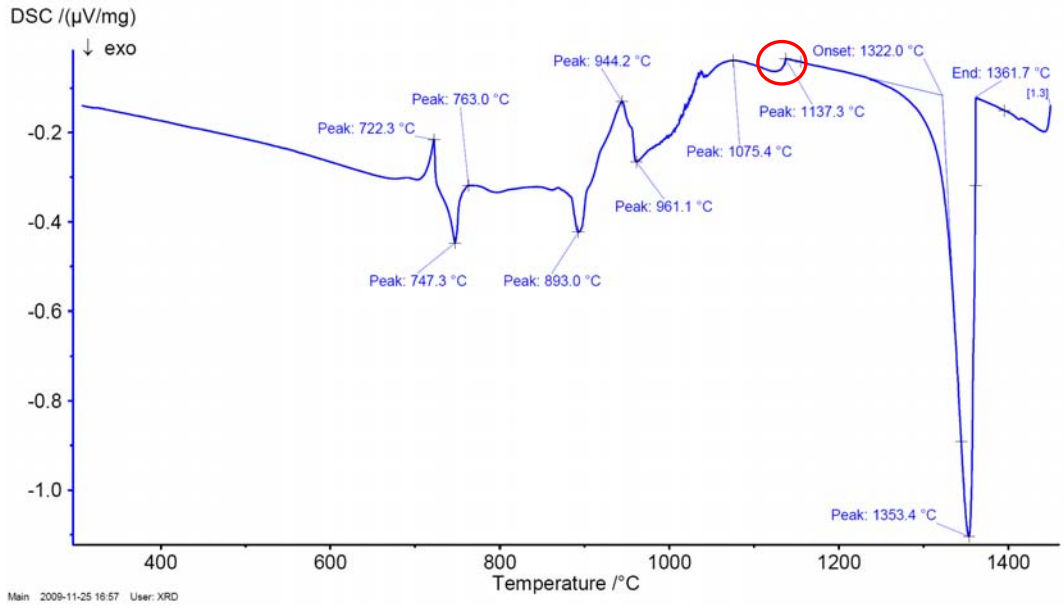

b) Alloy 82

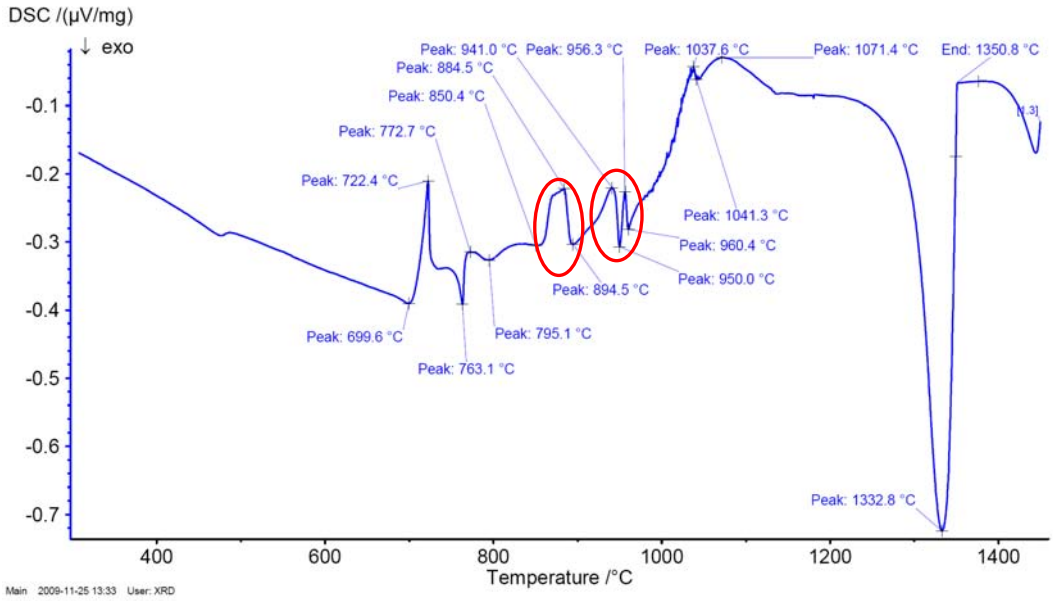

c) Alloy 152

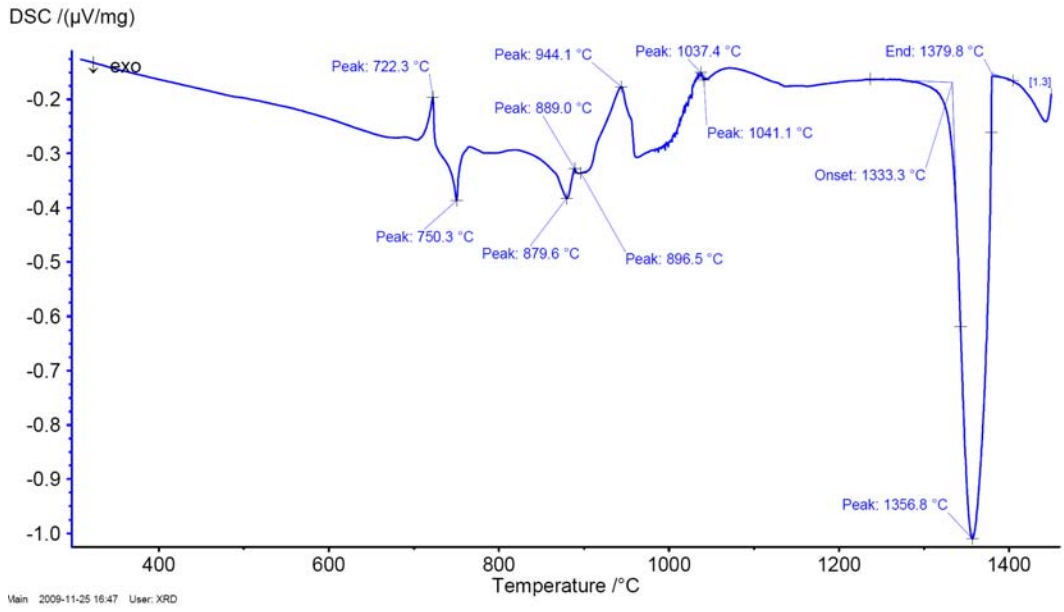

d) Alloy 52

Figure 16. DSC diagrams for cooling (40°C/min) from the melt to below 400°C temperature for the studied weld metals: a) Alloy 182, b) Alloy 82, c) Alloy 152, and d) Alloy 52.

The cooling rate of the real weld metal solidification is much higher than was used in DSC measurements, and in multi-pass welding, re-melting is also important. For understanding the effects of cooling and heating rate as well as liquation cracking in these weld metals, the experiments were also run with other speeds. The samples (weight range 55–95 mg) were heated up in an argon atmosphere to 1450°C at the rate of 40°C/min. The cooling down to 1000°C was made either at 5 or 20°C/min. Then the samples were heated again to 1450°C at the rate of 5 or 20°C/min and finally cooled down to room temperature at the rate of 40°C/min. Figure 17 shows the dynamic DSC curves for cooling (20°C/min) from the melt to 1000°C and heating (20°C /min) back to the melt. The obtained solidification temperature ranges are shown in Figure 18 and the corresponding melting temperature ranges in Figure 19. It is obvious that depending on the cooling rate the solidification temperature ranges vary markedly. Additionally, in heating the melting temperature range is at higher temperatures, and the melting temperature ranges themselves for each allow are narrower than are the solidification temperature ranges during cooling. These findings correlate qualitatively with the hot cracking susceptibility of the pure weld metals in Varestraint testing, i.e., Alloy 182 is more susceptible than Alloy 82 and Alloy 152 is more susceptible than Alloy 52.

In the literature there are some trials to determine the solidification temperature ranges for the studied alloys, and in all studies different cooling or heating rates have been used. For example, Wu et al. [8] measured the solidification temperature ranges for Alloy 82 and 52 as well as Alloy 690 by DTA analysis (cooling rate 5°C/min), and obtained 44°C, 13°C and 12°C, respectively. According to their hot cracking testing results the hot cracking susceptibility for these alloys followed the same decreasing order. Young et al. [15] measured the melting temperature ranges for some alloys and obtained in heating the following results: Alloy 52 (40°C) and Alloy 82 (59°C). Thus, it is obvious that the results are different between different studies because of varying weld metal compositions as well as cooling and heating rates. Also the result is different when measured in either the solidification or melting direction.

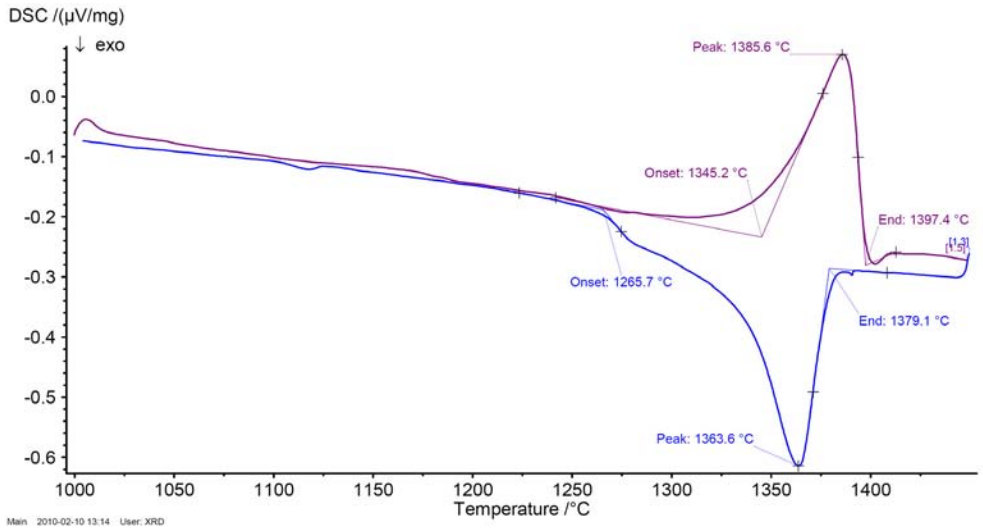

a) Alloy 182

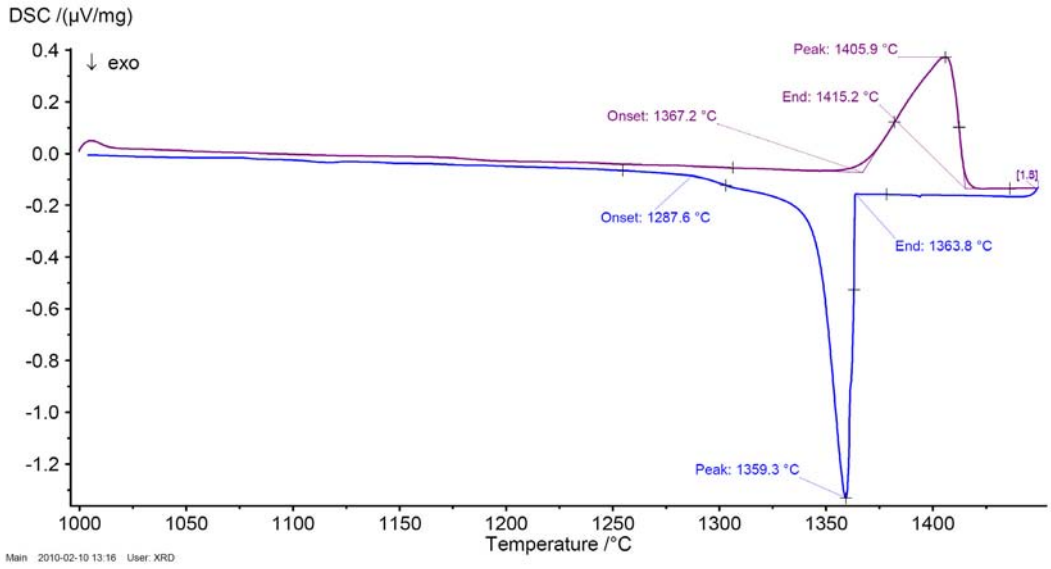

b) Alloy 82

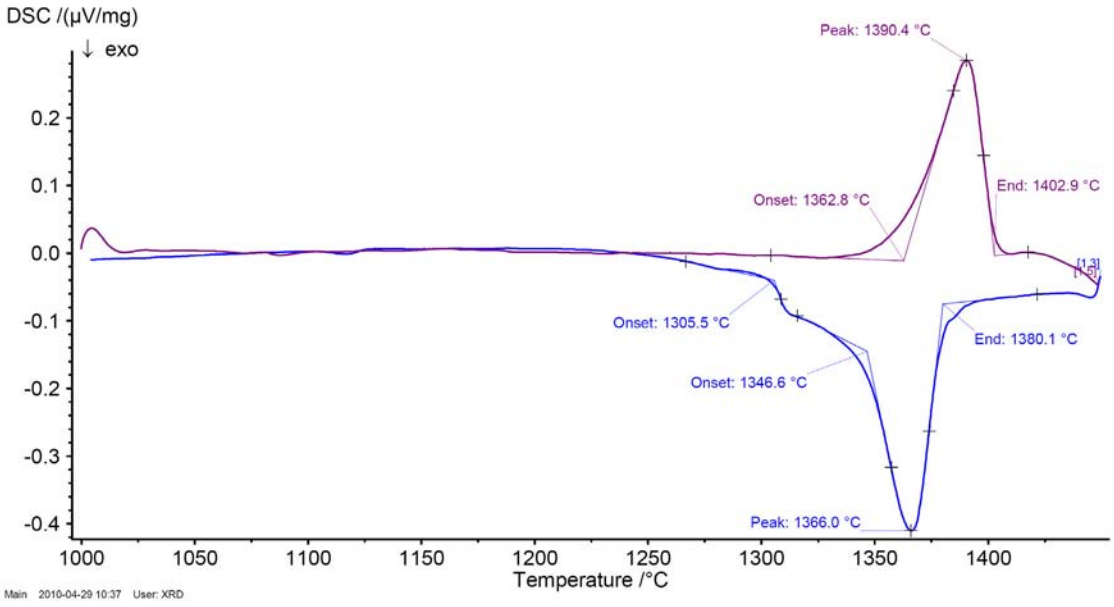

c) Alloy 152

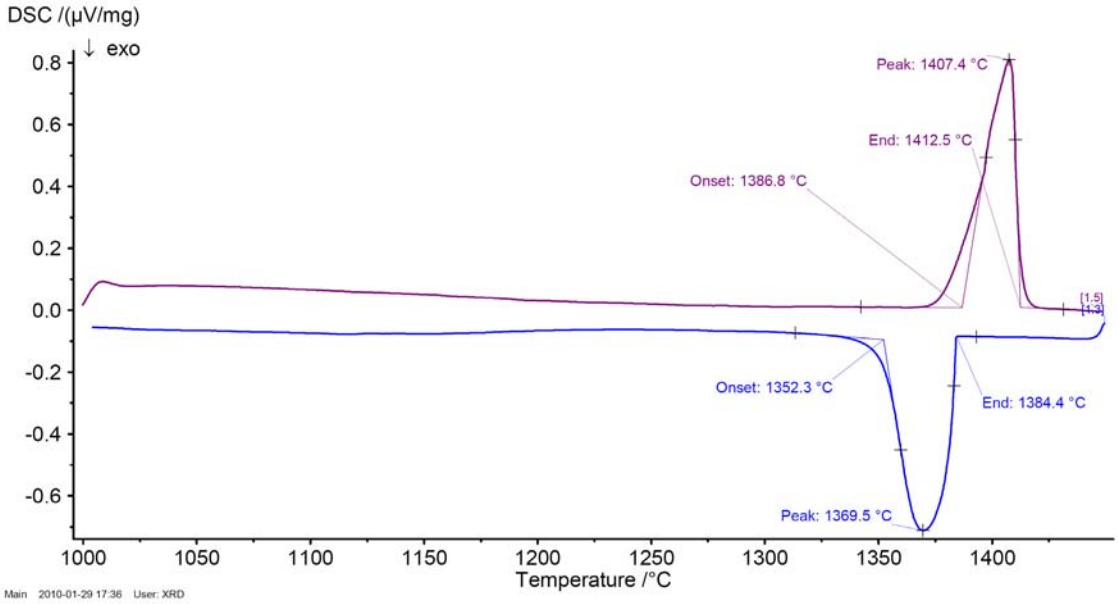

d) Alloy 52

Figure 17. DSC diagrams for cooling (20°C/min) from the melt to 1000°C and subsequent heating (20°C/min) back to the melt for the studied weld metals: a) Alloy 182, b) Alloy 82, c) Alloy 152, and d) Alloy 52.

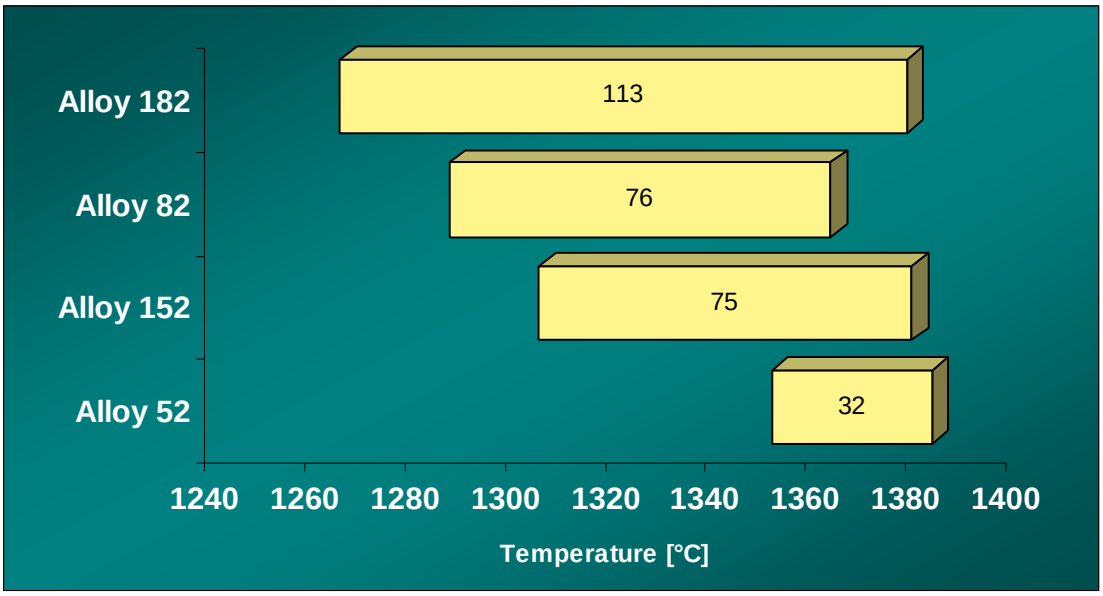

Figure 18. The solidification temperature ranges in cooling (20°C/min) from the melt for the studied weld metals.

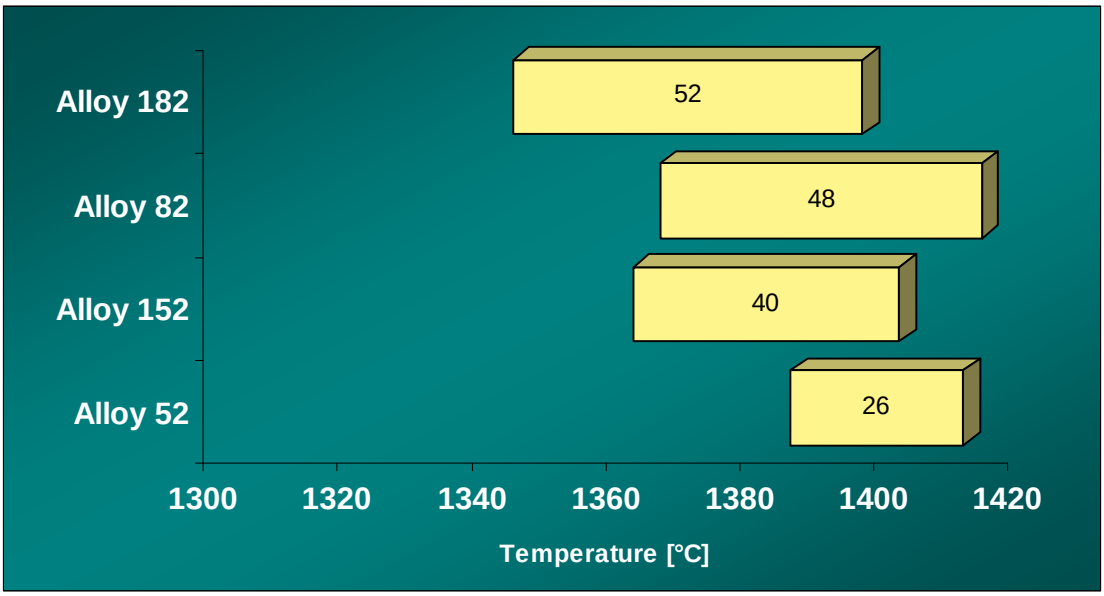

Figure 19. The melting temperature ranges in heating (20°C/min) from 1000°C for the studied weld metals.

2.2 Liquation cracking and ductility dip cracking

Liquation cracking occurs in parent material or in the underlying weld bead adjacent to the fusion boundary when a susceptible material is welded. In multi-pass welds such cracking is called ”micro-fissuring” or “under-bead cracking,” because the cracks are typically small and located adjacent to the inter-pass fusion boundary in the previously deposited weld metal. Such cracking is very similar to solidification cracking, namely that there is a temperature range close to the solidus temperature where the metal has cohesion but it is completely brittle. The cracking takes the form of micro-cracks typically 0,1–0,5 mm in length.

In nickel-base alloys liquation cracks, or fissures, are typically narrow, linear intergranular separations that are perpendicular to weld travel. Grain boundary liquation is the proposed mechanism that causes fissuring. Grain boundary liquation occurs when a phase or particle or segregation causes the grain boundary to melt locally at a temperature below the bulk melting point. Because the liquated grain boundary (liquid film) has practically no strength, separation at the liquated grain boundary can occur, causing the fissure. Constitutional liquation occurs when a second phase particle, (e.g. MC carbide rich in Ti or Nb) begins to dissolve during non-equilibrium, or rapid, heating and forms an intermediate phase with the matrix, which has a solidus temperature that is lower than that of either the second-phase particle or the matrix. Chemical segregation at the grain boundaries can also cause the grain boundary liquation. Elements such as S, B, Mn, P and Nb that form low melting point eutectics can contribute to HAZ fissuring.

In Figures 20–22, transverse sections of cracks found in Varestraint specimens propagating into HAZ are presented. In this study liquation cracking markedly affected the crack depth when hot cracks

were formed in 4-point bend specimens for subsequent crack initiation testing in doped steam conditions. The small hot cracks produced were much larger than intended, and grew below the Varestraint weld bead into the underlying weld metal, negatively affecting the success of the EAC testing. However, no extension of these liquation cracks in any of the test samples was observed following subsequent autoclave EAC testing, Figure 23 (see also Chapter 4.3).

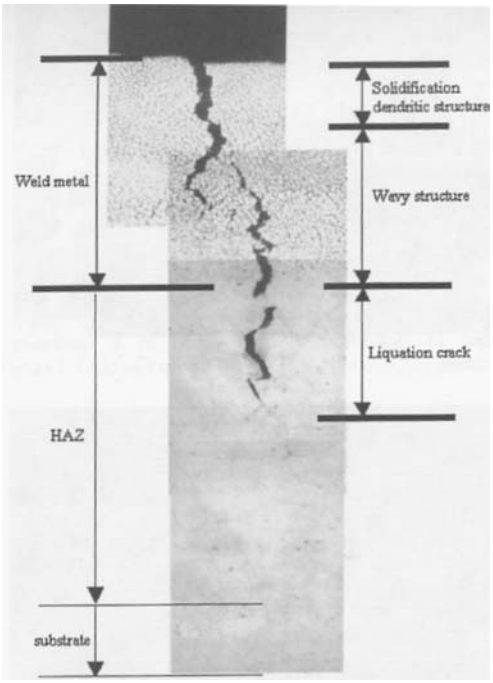

Figure 20. Transverse section of a crack found in a Varestraint specimen propagating into HAZ [16].

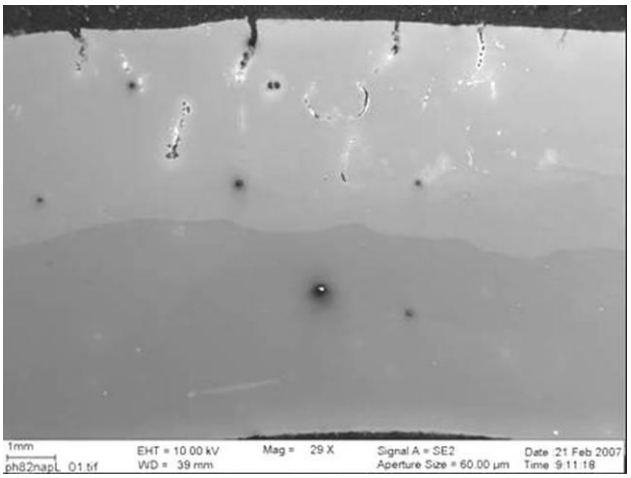

Figure 21. Liquation cracks after Varestraint test in pure Alloy 82 weld metal.

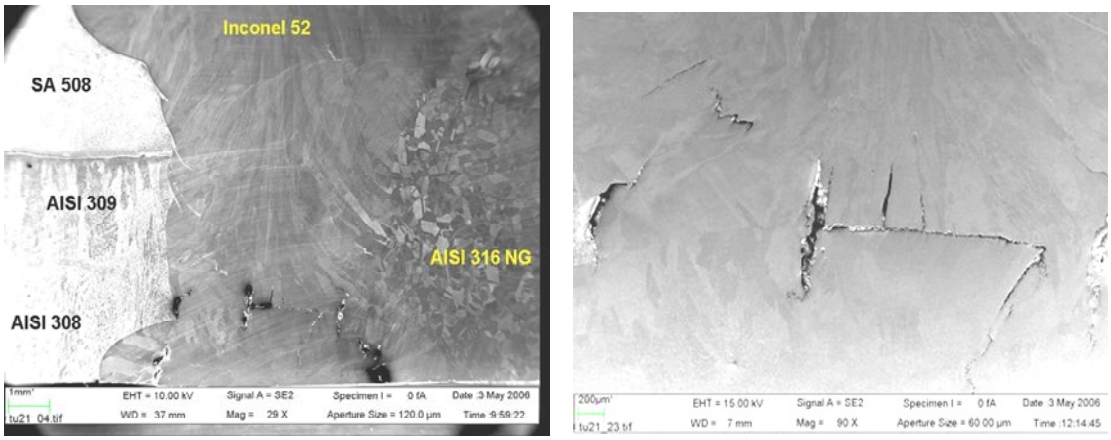

Figure 22. Cross-section of the mock-up 2 weld after Varestraint test showing extensive liquation cracking.

Ductility dip cracking (DDC) is a solid-state phenomenon leading to a situation where a number of alloys may be embrittled (ductility and tensile strength drop sharply) within a specific temperature range. DDC is typically associated with the welding of heavy sections with high restraint conditions and large grain size commonly encountered in critical high-pressure steam, nuclear, and power generation applications. Therefore, welding of susceptible alloys should be limited to welding conditions minimizing shrinkage stresses/strains during cooling. DDC susceptibility is quantified by the ductility dip temperature range (DTR) and the threshold strain (E_{min}) for cracking to occur, Figure 24. DDC occurs intergranularly along the migrated grain boundaries in the weld metal, and does not exhibit a clear dendritic appearance. Thus, the DDC has a different mechanism of formation as compared to liquation cracking. DDC can be thought to be a form of elevated temperature creep failure that occurs rapidly at temperatures above the normal creep regime. Cracking is most prevalent in weld metals where local pinning is not preventing grain boundary sliding. The mechanism for DDC is still not fully understood, but it is believed to be either caused by the grain boundary segregation of P and S or related to partially coherent $M_{23}C_6$ carbide precipitation on grain boundaries, with the large misfit between the carbide and the matrix creating high local stresses/strains between the carbides leading to cracking along the grain boundary.

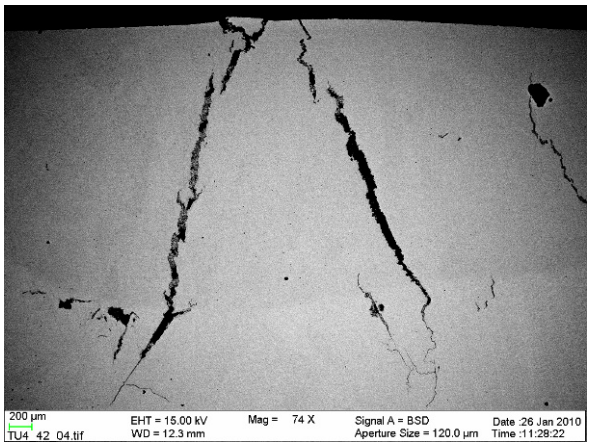

a)

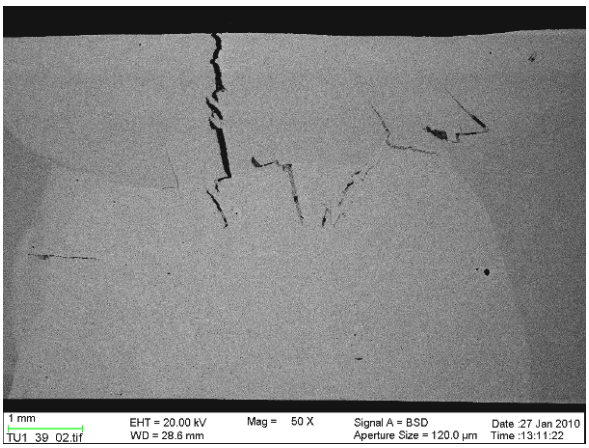

b)

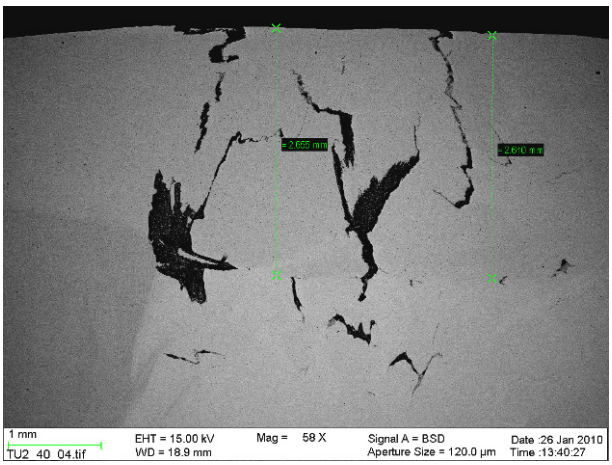

c)

Figure 23. Cross-sections of the mock-ups after Varestraint and doped steam test conducted on the root side of the DMW, a) mock-up TV, b) mock-up 1 and c) mock-up 2. The specimens did not show any crack growth during doped steam tests.

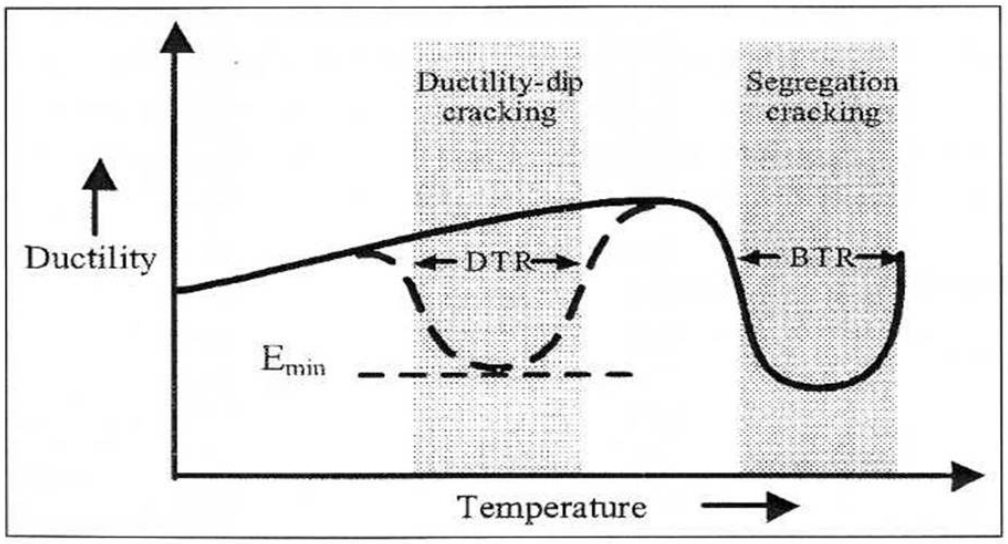

Figure 24. Schematic presentation of elevated temperature cracking susceptibility. Note that the ductility dip cracking temperature range (DTR) is separate and distinct from the brittle temperature range (BTR) where solidification and liquation cracking occur [17].

The weld metal evaluated in this study for DDC susceptibility was Alloy 182, using AISI 304 steel as a base metal. The test samples consisted of a modified "dog bone" tensile specimen design. Prior to cutting the samples from the plate material, welds were made in the groove, Figure 25 a). Once welding was completed the samples were cut from the plate such that the weld was located in the middle of the reduced gauge section of the test specimen (i.e. so it consists fully of the weld metal), Figure 25 b). A cross-section of the weld before machining to the final dimensions is shown in Figure 26 a) and examples of specimens with the final dimensions are shown in Figure 26 b). The use of a modified dog-bone tensile specimen design helped to concentrate both the strain and temperature to the reduced gauge section during the DDC testing. Samples were tested using a 25 kN MTS 858 tensile test machine equipped with a MTS High-Temperature furnace 653.02. Four tensile specimens were tested. The test cycle was made by simulating the Gleeble STF testing procedure of Nissley et al. [17]. Testing was performed in a chamber surrounding 10 cm of the middle section of the sample, Figure 27. For minimizing oxidation of the sample pure argon gas was streamed into the chamber at 10 l/min. A schematic of the test cycle is shown in Figure 28. The sample was first heated up to the testing temperature of 1000 °C at 75 °C/min. After reaching the test temperature the samples were held for 10 seconds, and then strained to 4% target strain at a strain rate of 0,6 mm/s in order to produce DDC. The samples were held at the test temperature under the applied strain for another 10 s before releasing the load and letting the furnace cool back to room temperature. Temperature data was recorded using thermocouples positioned in the reduced gauge section of the sample.

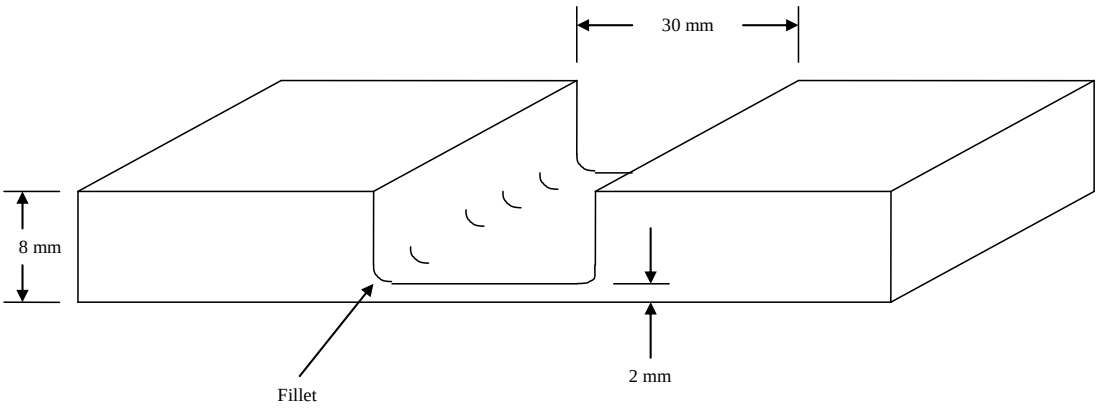

a)

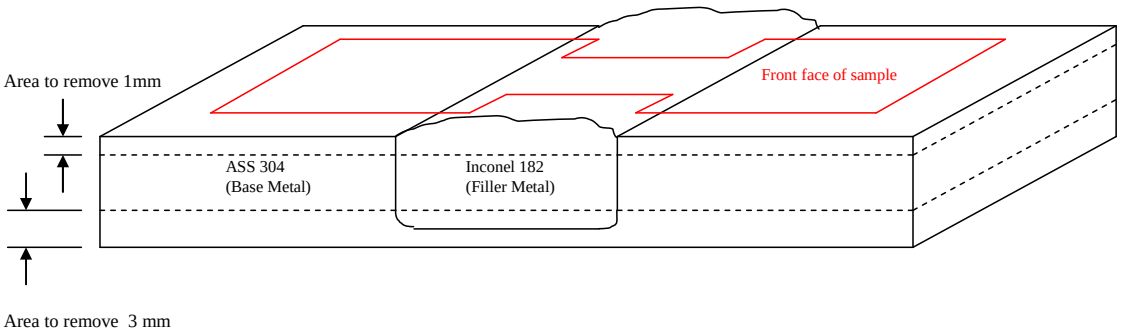

b)

Figure 25. a) Schematic view of the groove in AISI 304 steel plate. b) Schematic view of the plate after welding, and cutting of the tensile test sample.

a)

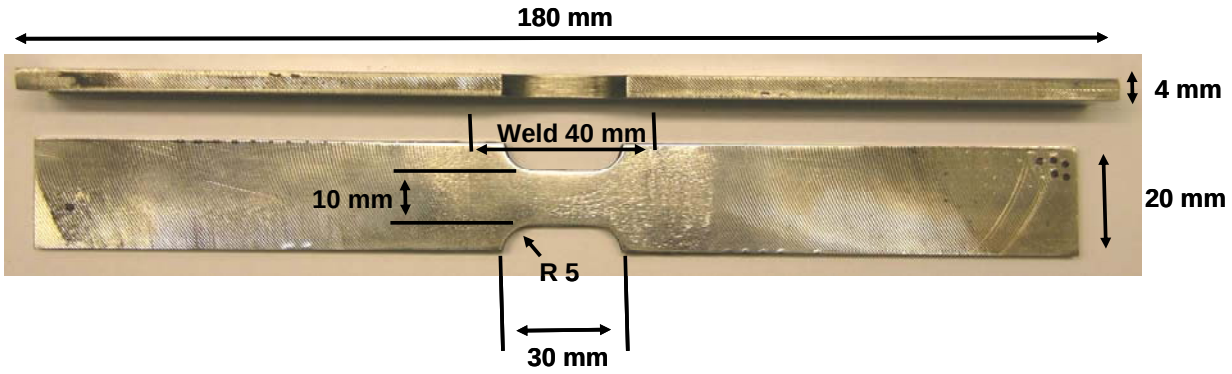

b)

Figure 26. a) Cross-section of the weld, before machining of the tensile specimens. b) As-finished tensile specimen geometry.

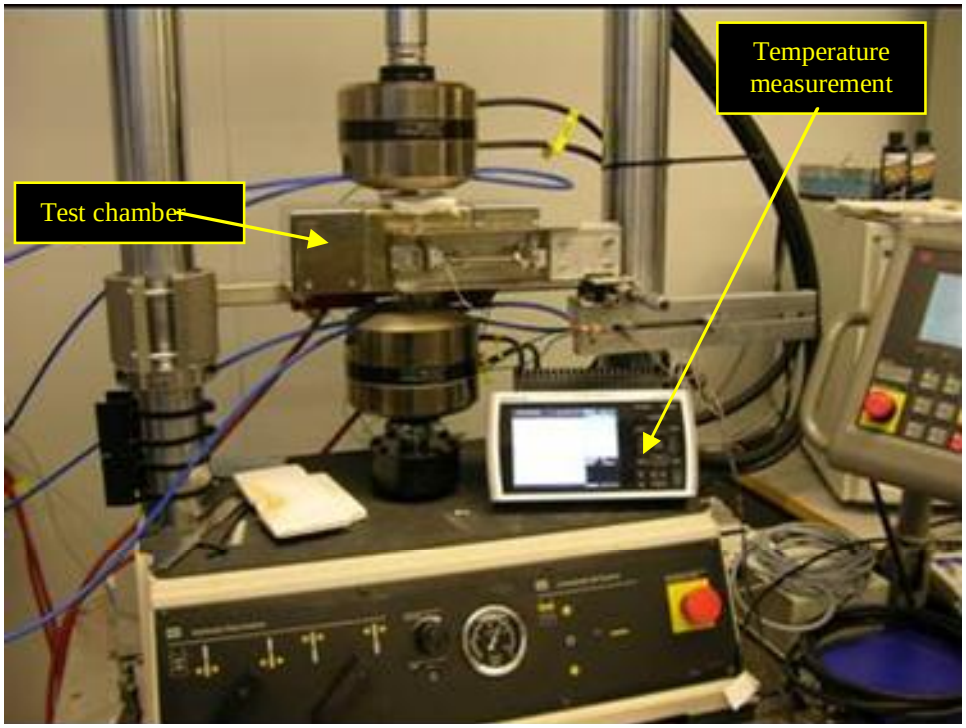

Figure 27. Testing equipment for DDC testing.

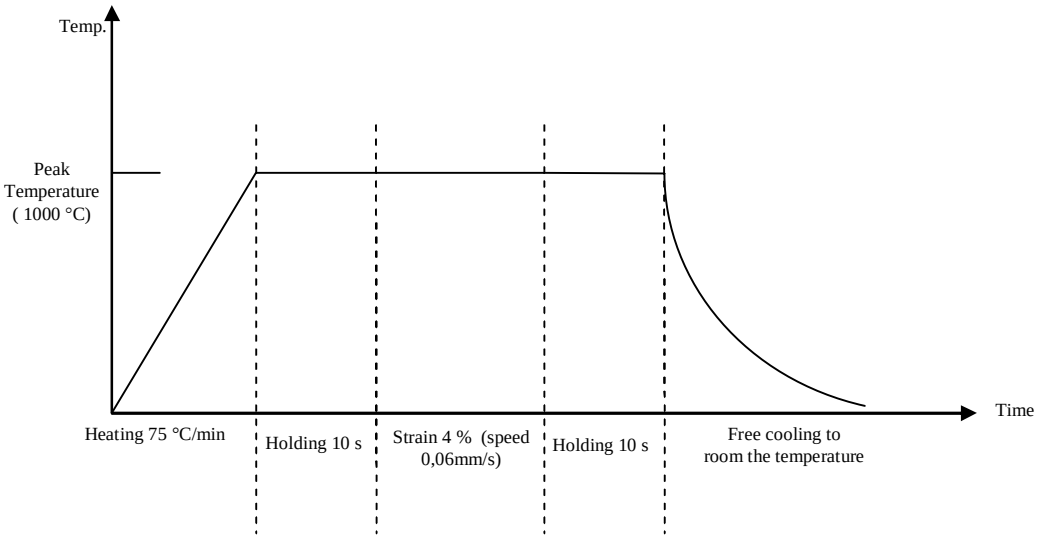

Figure 28. Schematic presentation of the test cycle.

In these tests no indications of ductility-dip cracking of the test specimens were observed at the strain applied, Figure 29. The reason was that part of the strain took place in the AISI 304 steel extension material, so the true amount of strain in the gauge length was less than the desired strain. The argon gas shielding intended to prevent oxidation was also insufficient, and severe oxidation occurred on the surface of the test specimen. Tests are to be continued with revised test specimen geometry and improved gas shielding.

Figure 29. Alloy 182 test specimen surface after a DDC test at 1000°C up to 4% of plastic strain. No indications of DDC cracks are visible.

2.3 Weld defects

Most of the indications of weld defects observed in the metallographic examinations were small pores distributed randomly over the cross-section of the metallographic samples or arranged in lines along the grain boundaries or boundaries between the welding passes (etched secondary phases may also be a possible reason for this), Figures 30 a, b, c. Typical weld defects such as short intergranular cracks and large voids were found only in Alloy 52, along grain boundaries, Figure 30 d.

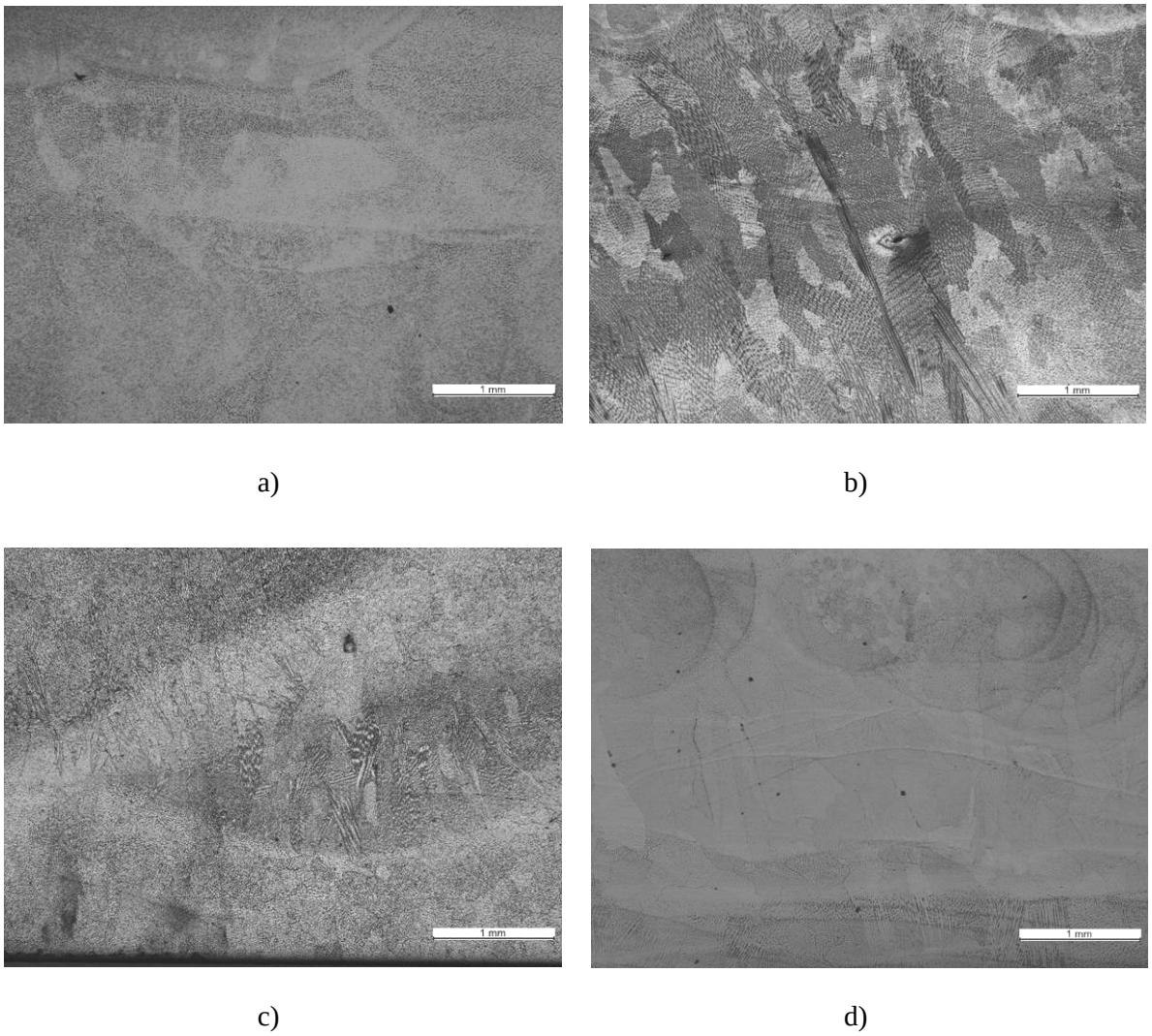

a) b)

c) d)

Figure 30. Microstructures and weld defects of the weld metals of Alloy 182 a), 82 b), 152 c) and 52 d) in as-welded condition.

A remarkable observation was that three specimens (in parenthesis in Table 10) showed large cracks visually after loading within a few days delay in air before exposure to the doped steam. These specimens were not exposed to the doped steam tests and their metallographic study revealed large slag inclusions, which caused the delayed cracking in air after loading, Figure 31 and 32. The outer surfaces and fracture surfaces of these specimens were studied with SEM and details of the larger and smaller slag inclusions are shown in Figures 32 and 33. The composition of the slag shows high amounts of Ca, Si, Al, Mg, Cl, etc. The original idea of the doped steam test was also to simulate the local chemical conditions when a weld metal is exposed to the high purity environment and the slag inclusions of the weld metal dissolve and change locally the chemical conditions on the surface of the material.

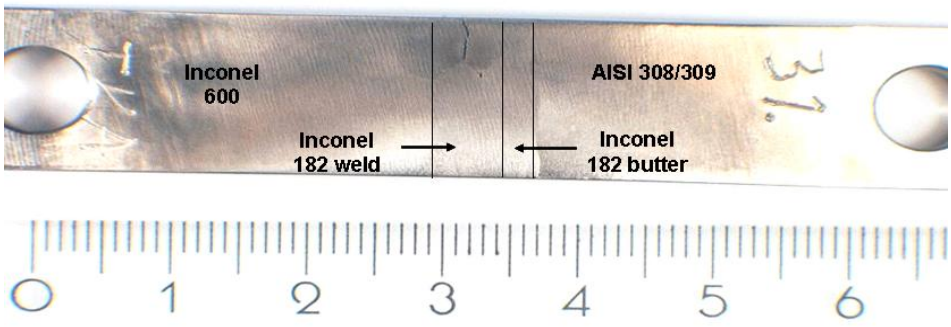

a)

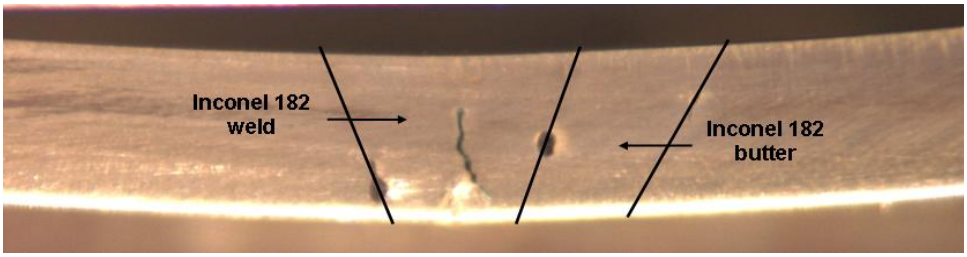

b)

Figure 31. Sample TV (Alloy 182) dissimilar metal weld sample showing delayed fracture in air after loading a) top view, b) side view.

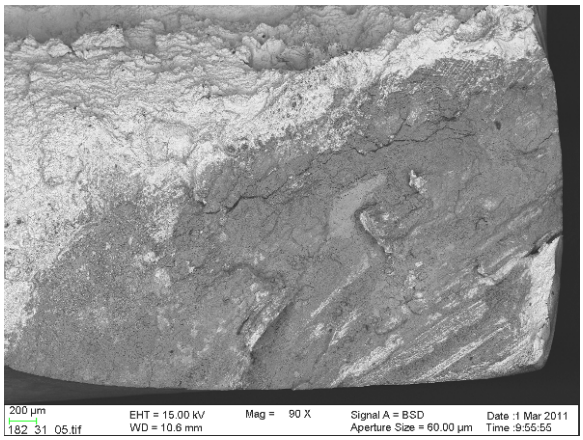

a)

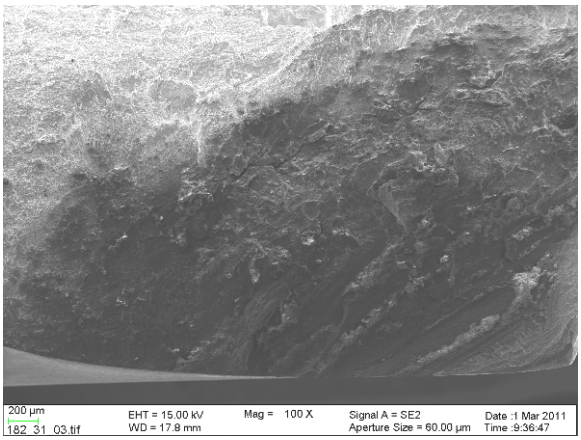

b)

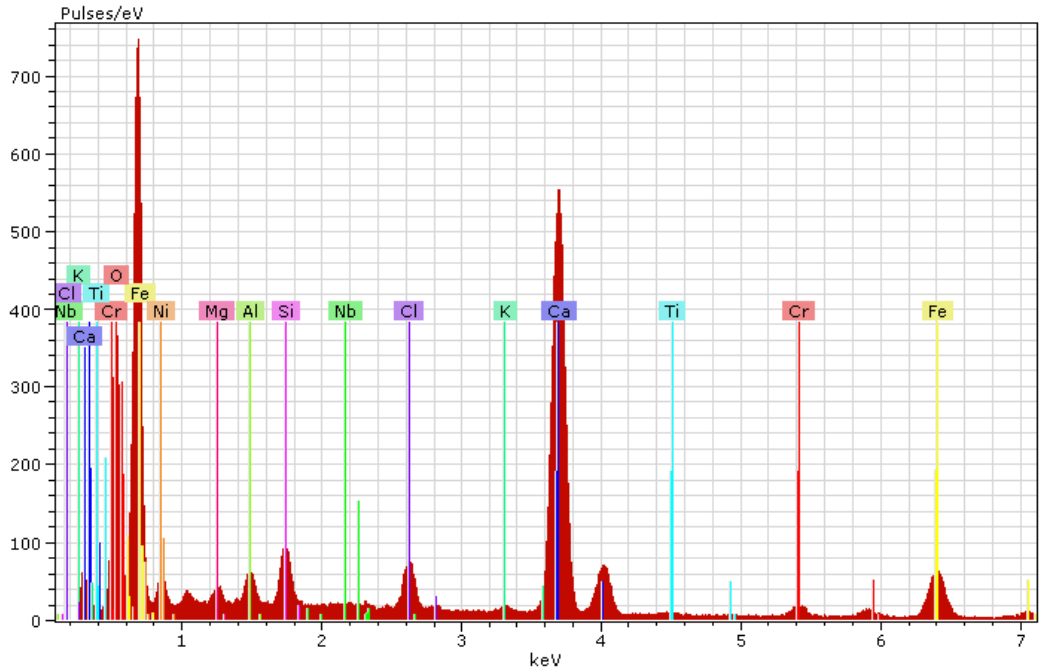

c)

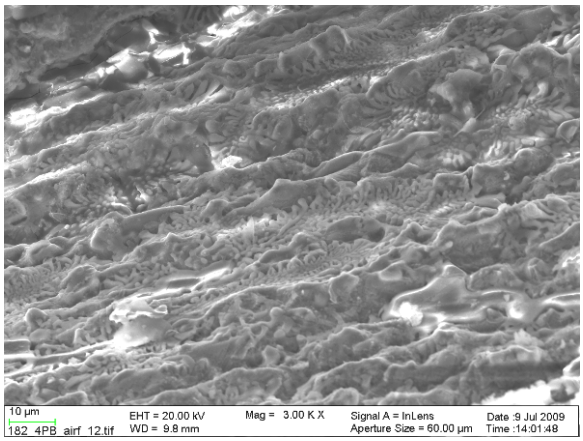

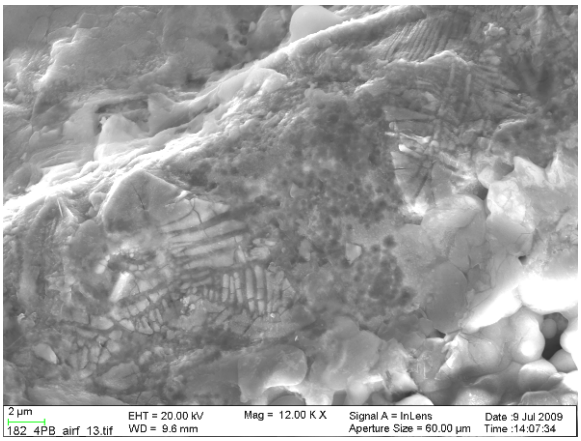

d) e)

Figure 32. Fractography of delayed fracture observed before autoclave testing of Sample TV (Alloy 182) dissimilar metal weld showing that the whole fracture surface consists of slag, a) and b), and the composition of the slag is shown in c). d) and e) show details of the slag covered fracture surface of the delayed fracture sample.

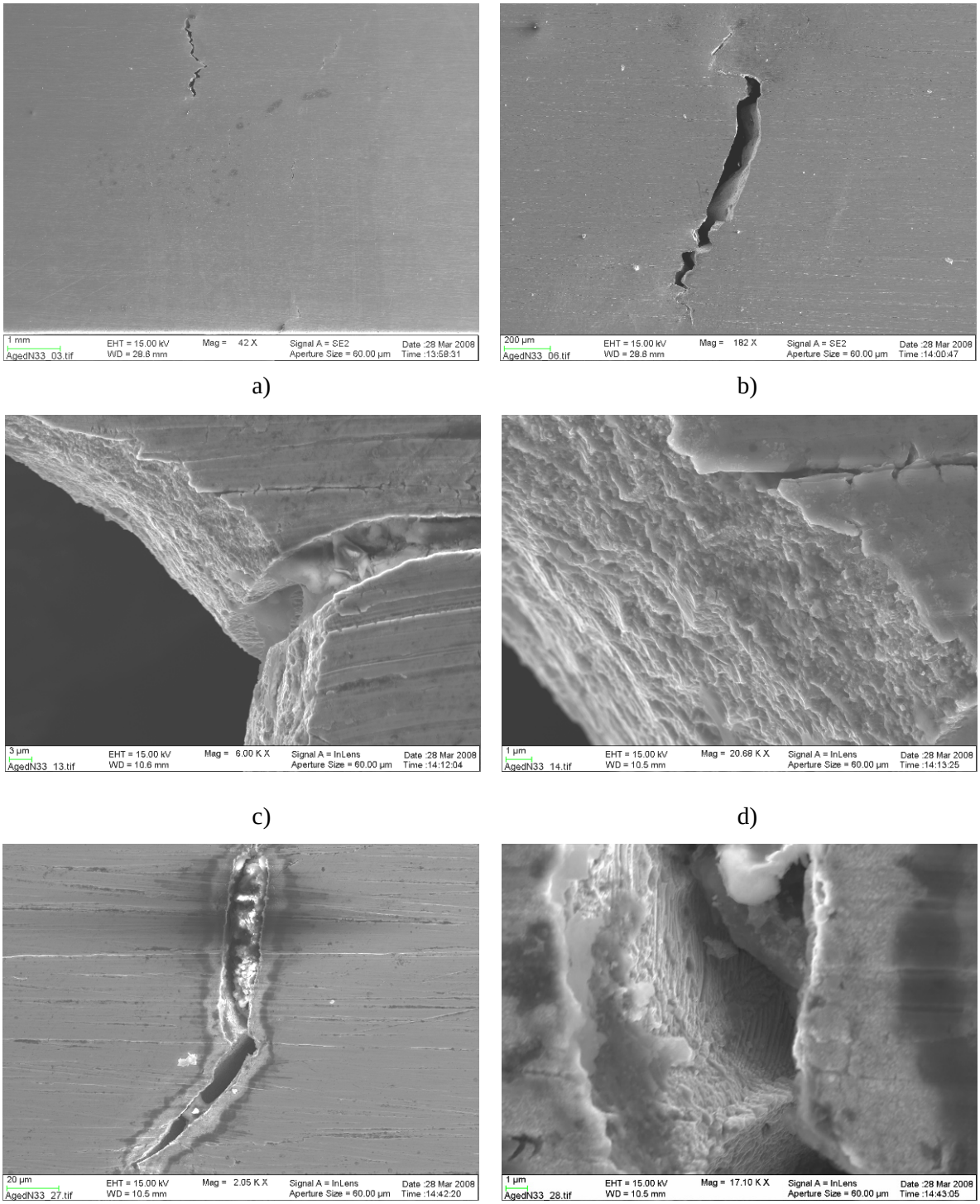

Figure 33. a)–f) Small weld defects (<1 mm) on the outer surface of Sample N33 (AISI 347 and Alloy 82 dilution zone) [5] caused by small slag inclusions show slag inside the defects and the surfaces of the defects are rough consisting of broken slag film.

In most of the specimens after loading in four-point bending to 1–1,1% strain small weld defects became visible but after various exposure times the visible small weld defects did not grow further and the EAC crack initiation and the final fracture always took place in the middle of the specimens without any observable weld defect interaction. Figure 34 shows an example of an Alloy 82 sample (specimen 9) where small weld defects, which opened as a result of initial loading and gave small liquid penetrant test indications, did not grow during the EAC testing intervals. It was concluded that none of these small indications were observed to grow during the EAC testing of any alloy weld metal samples.

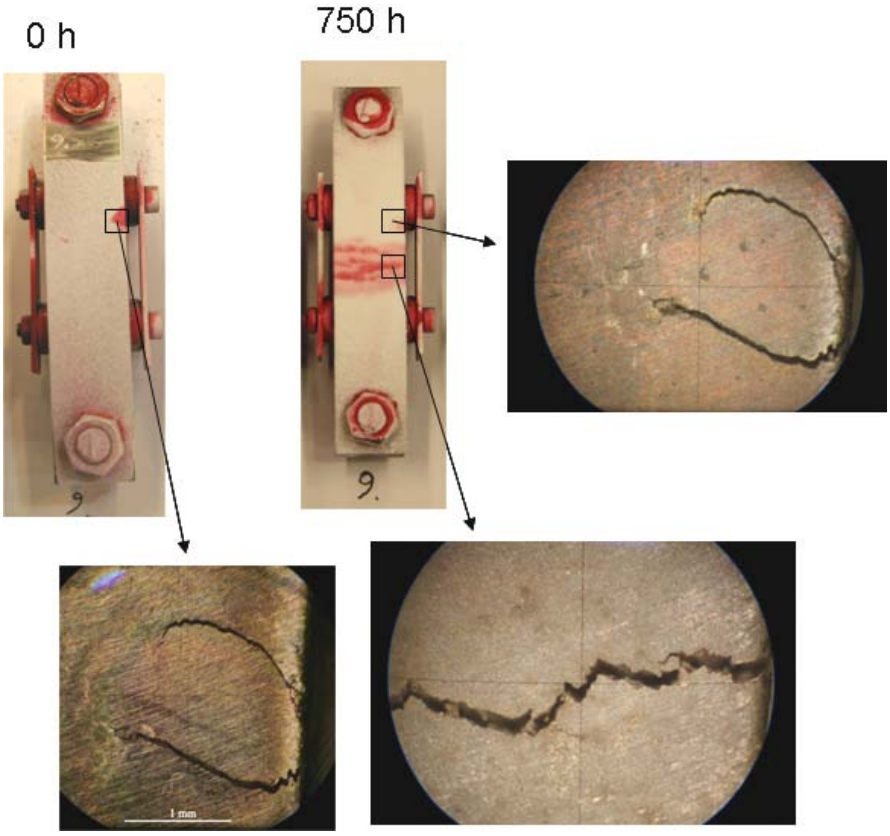

Figure 34. Pure Alloy 82 specimen (specimen No. 9) prior to the exposure and after 750 h exposure to the doped steam. The weld defect opened when the specimen was loaded does not grow further in doped steam and the final fracture takes place in the middle of the specimen without any connection to the weld defect.

In many cases the small weld defects which opened in loading had a rounded form and they did not seem to contain any slag. Figure 35 shows an EBSD study of a common weld defect of the size which corresponds to the weld defect observations on the surfaces of the 4-point bend specimens. EBSD study of such regions showed annealing twins inside the defect microstructure, which do not exist in the solidified weld metal microstructure. Based on this it is concluded that the defect consists of an unmelted welding wire tip. This type of weld defect forms when the TIG filler metal wire is melted behind its tip first and drops into the weld pool, and the tip of the wire stays unmelted. The local misorientation EBSD map on the right side shows that in the region of the defect local elevation of the

residual plastic strain is present, especially on the boundaries between the defect and the solidified weld metal. The boundary shows a welding defect (dark irregular linear feature) and it is expected to be weak, and probably opens when loaded. Many of the small defects observed as liquid penetrant test indications on the surfaces of 4-point bend test samples consisted of opened boundaries of this type of weld defect.

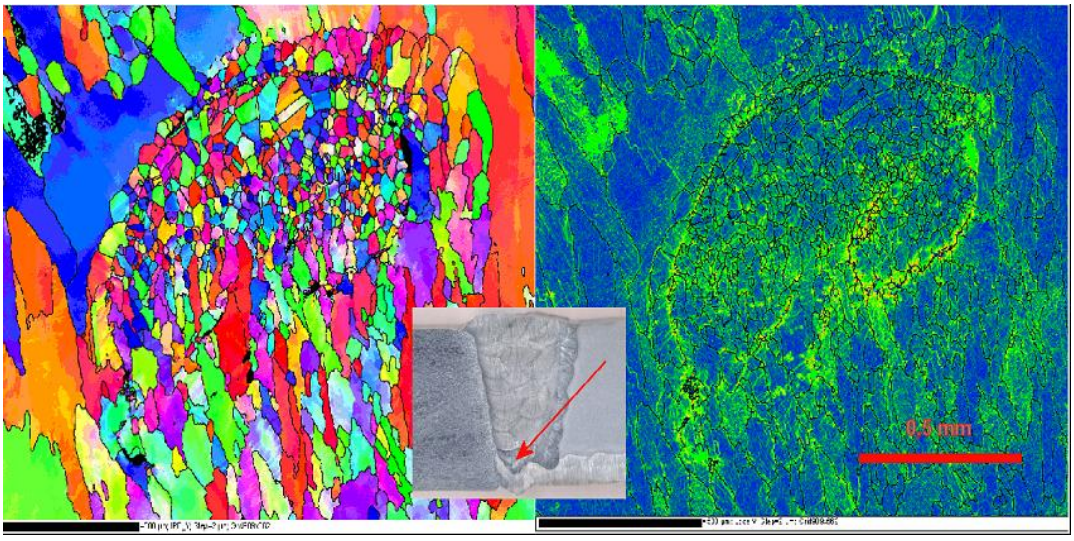

Figure 35. A weld defect in Alloy 82 weld metal of “Neste” mock-up DMW sample [1], where unmelted tip of the TIG filler metal wire is surrounded by the melted and solidified weld metal. On the left is an EBSD IPF map and on the right a local misorientation map. The location of the defect in the DMW is marked by an arrow.

2.4 Effects of dilution on weld metal composition

The chemical compositions across the dissimilar metal weld mock-ups were determined using quantitative SEM/EDS line scan analysis. The line scan analyses were performed with 0.5 mm steps along three lines, i.e., at about 0.5 mm from the weld root, at mid-thickness, and close to the weld crown. Additionally, the composition of the fusion line area at the weld root was determined using 3 µm step line scan analysis. The results are presented in Figures 36–42. A summary of the results of the line scan analyses across the weld root is presented in Table 4. In Table 4, the average of the spot analyses performed within each material, i.e., base material (BM) or cladding, buttering and weld metal is presented. The dilution is also presented, taken as the difference between the measured average and nominal composition for each of the elements. The results show dilution of the elements resulting in a reduced amount of nickel and chromium and an increased amount of iron in the solidified weld metal as compared to the nominal composition of the weld filler material. The largest dilution is observed in welds without buttering. As expected, the amount of dilution is dependent on the difference between the compositions of the materials to be welded. It is highest in mock-up 2, where two stainless steel materials are welded using Alloy 52 filler material.

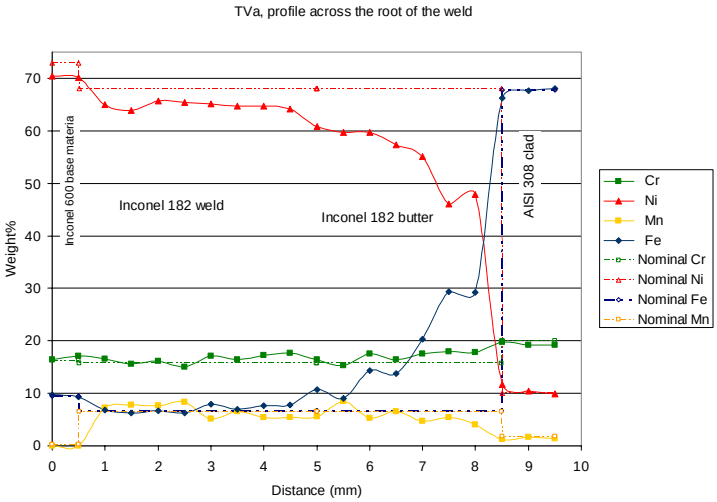

a)

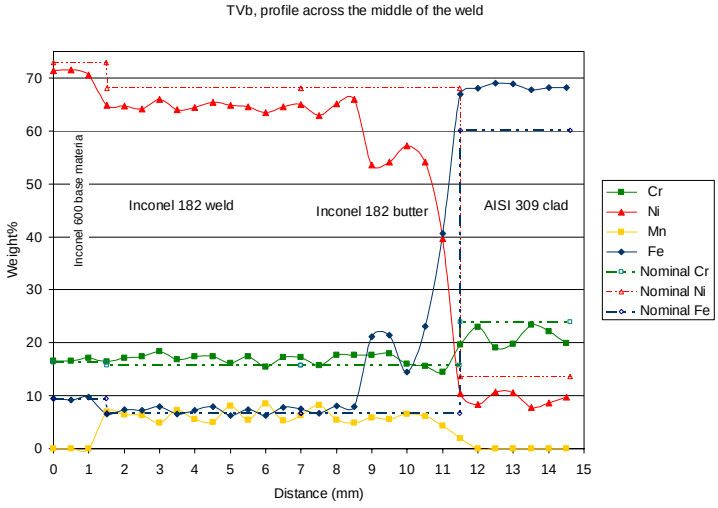

b)

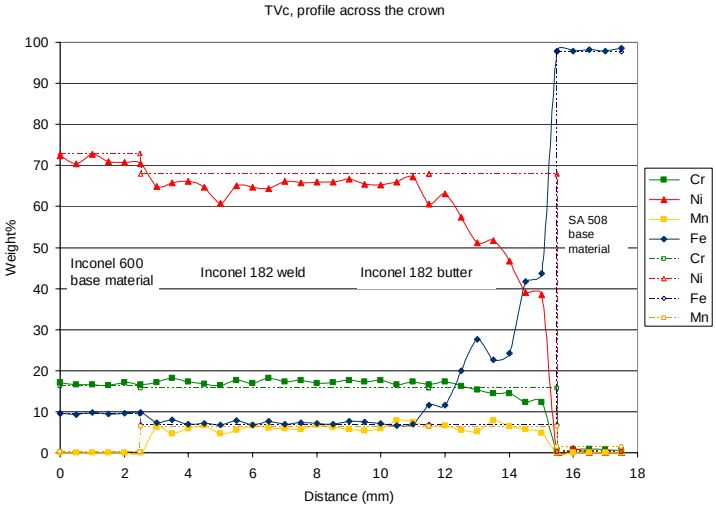

c)

Figure 36. SEM-EDS profile across the weld root at a distance of 0.5 mm from the surface (a), mid-thickness (b) and close to the crown (c) of mock-up TV.

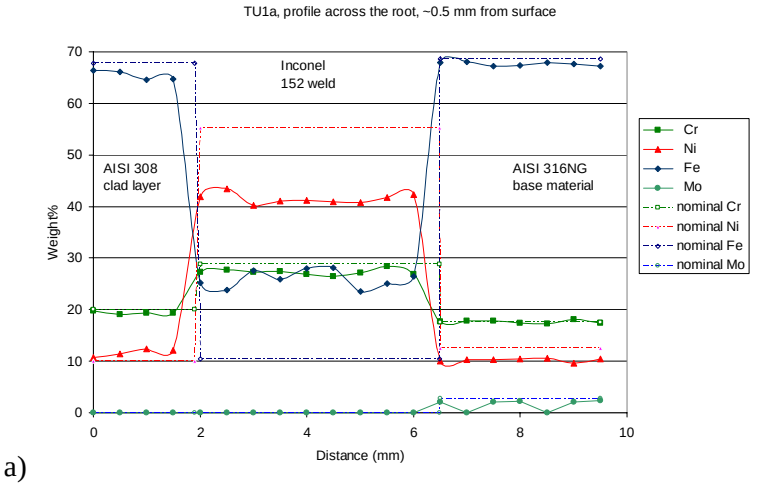

a)

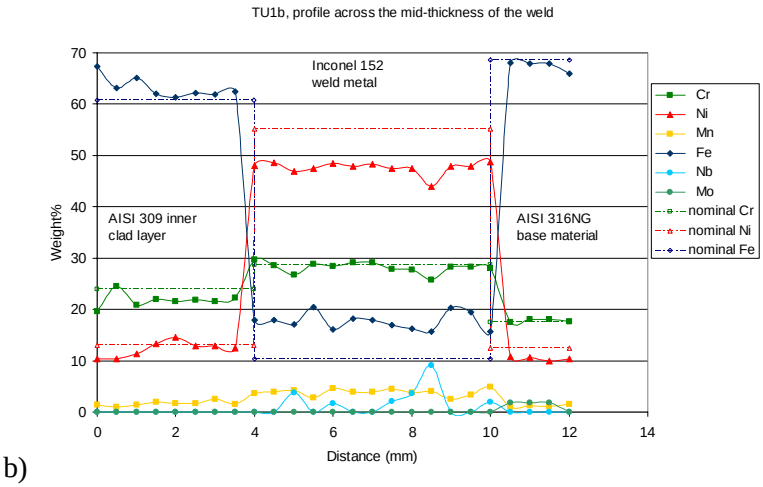

b)

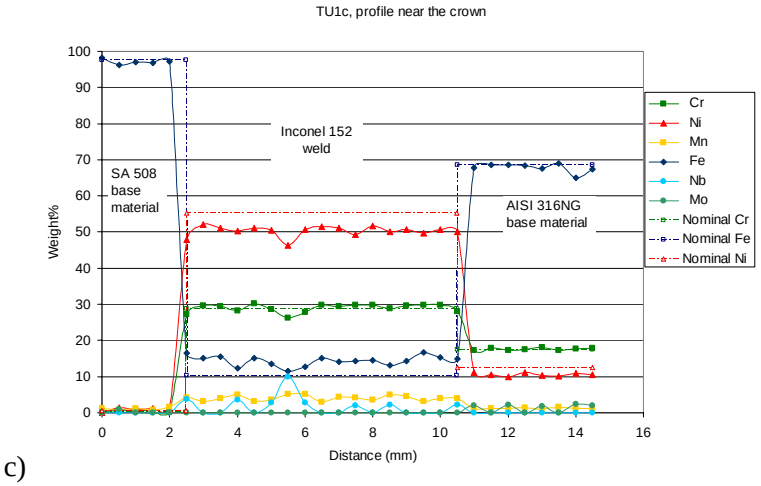

c)

Figure 37. SEM-EDS profile across the weld root at a distance of 0.5 mm from the surface (a), mid-thickness (b) and close to the crown (c) of mock-up 1.

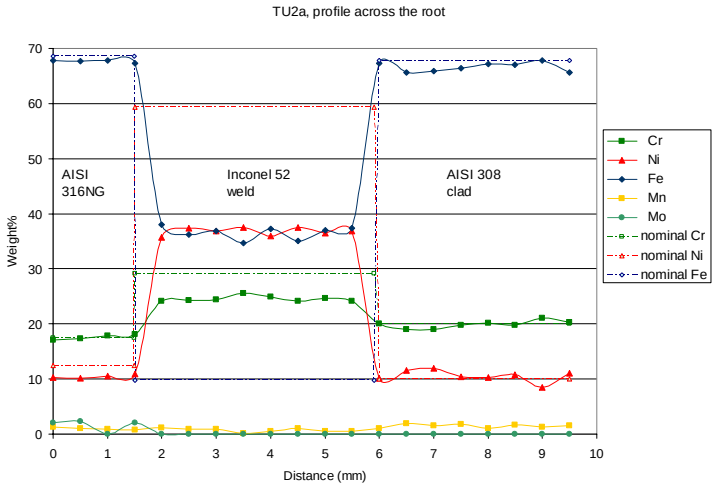

a)

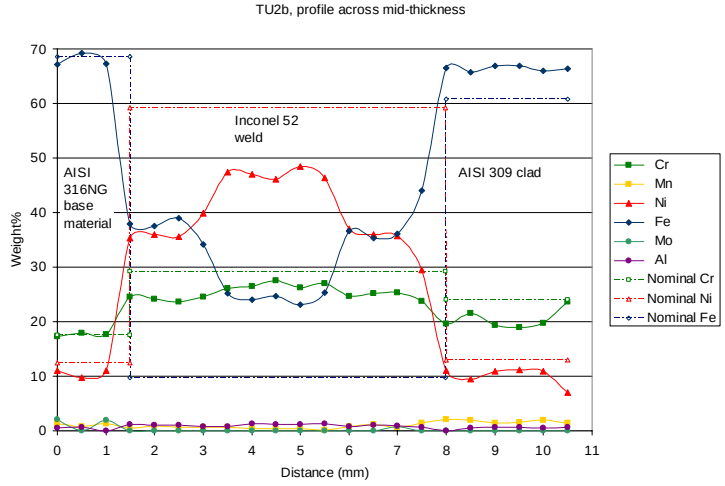

b)

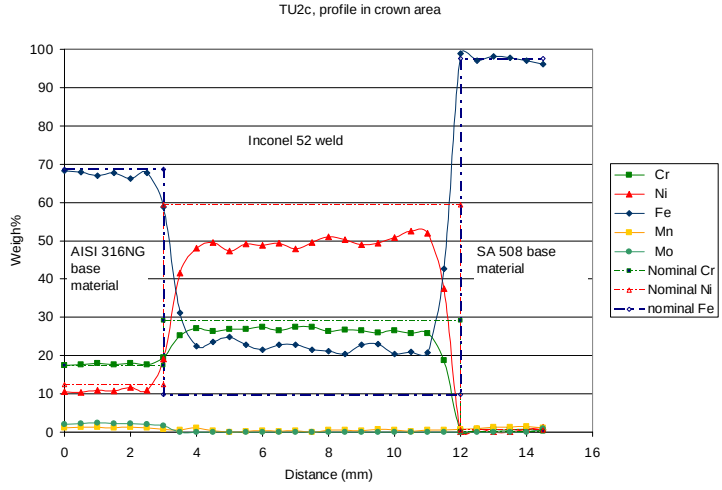

c)

Figure 38. SEM-EDS profile across the weld root at a distance of 0.5 mm from the surface (a), mid-thickness (b) and close to the crown (c) of mock-up 2.

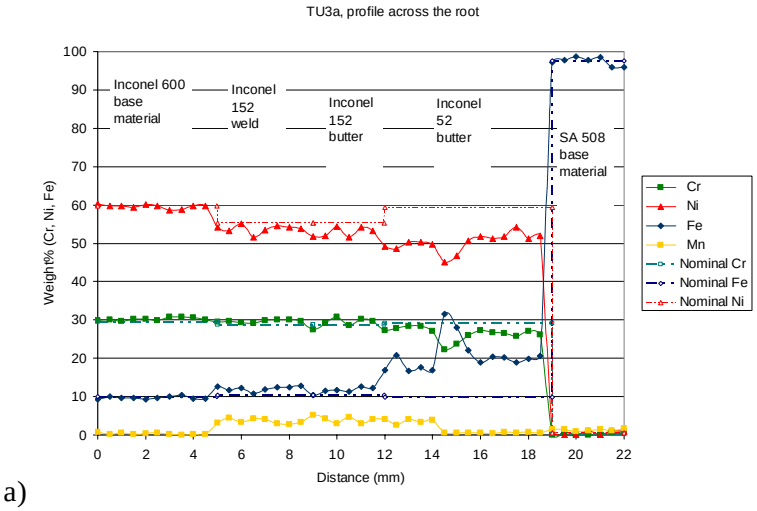

a)

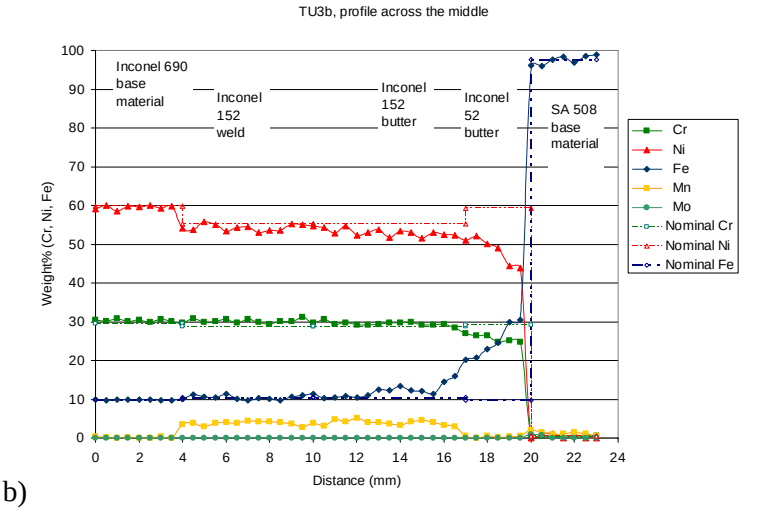

b)

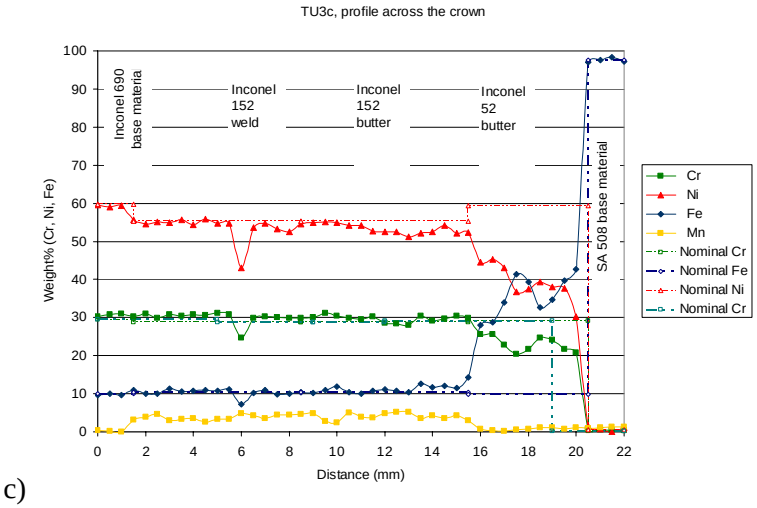

c)

Figure 39. SEM-EDS profile across the weld root at a distance of 0.5 mm from the surface (a), mid-thickness (b) and close to the crown (c) of mock-up 3.

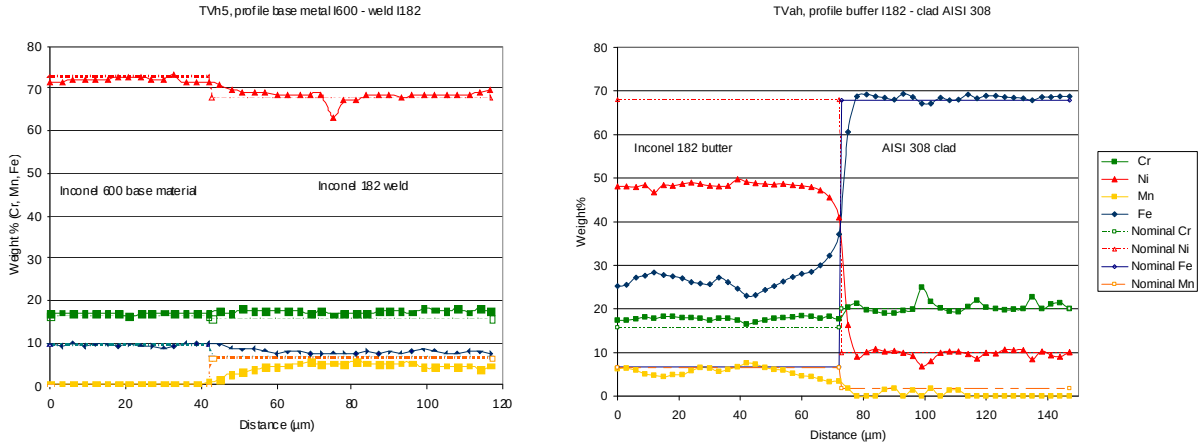

Figure 40. SEM-EDS profile across the fusion line of the weld root at a distance of 0.5 mm from the surface of mock-up TV.

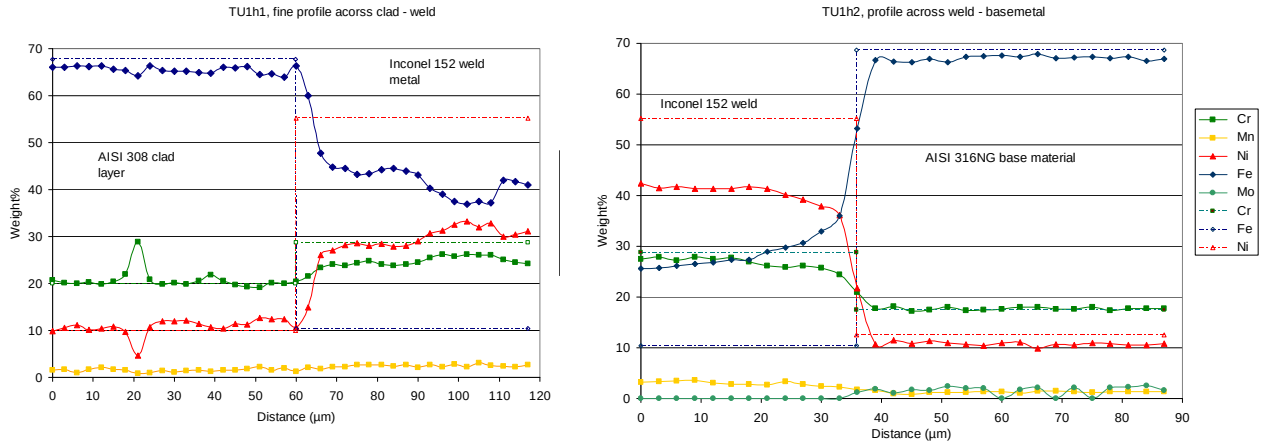

Figure 41. SEM-EDS profile across the fusion line of the weld root at a distance of 0.5 mm from the surface of mock-up 1.

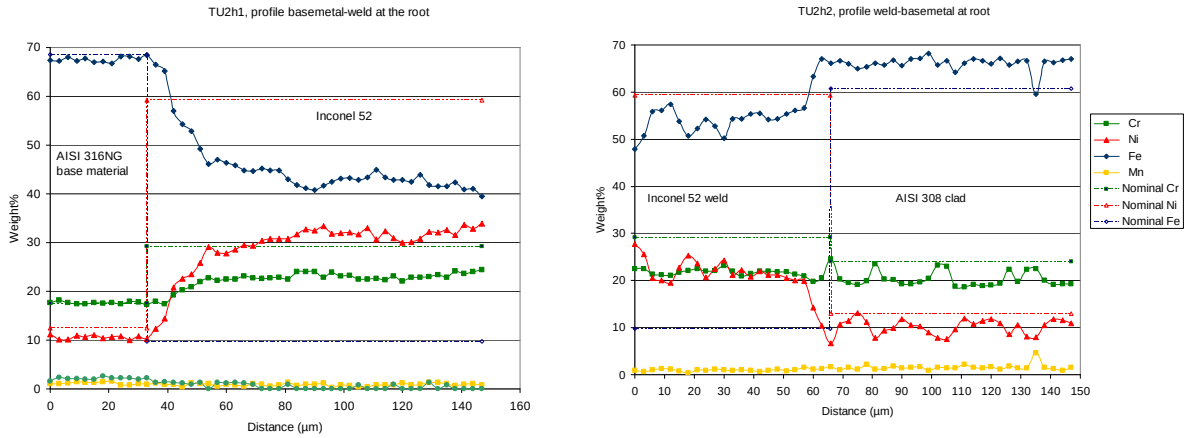

Figure 42. SEM-EDS profile across the fusion line of the weld root at a distance of 0.5 mm from the surface of mock-up 2.

Table 4. Summary of Cr, Ni and Fe in the different weld metals based on results from performed line scan analyses across the weld root. The dilution also presented, taken as the difference between the measured and nominal composition for these elements.

Chromium content					
mock-up TV	Inconel 600 BM	Inconel 182 weld	Inconel 182 butter	AISI 308 clad	
nominal	16.3	15.7	15.7	20.0	
measured av.	16.8	16.5	17.0	19.4	
difference	***1***	***1***	***1***	***-1***	
mock-up 1	AISI 308 clad	Inconel 152	AISI 316NG BM		
nominal	20.0	28.7	17.5		
measured av.	19.4	27.3	17.6		
difference	***-1***	***-1***	***0***		
mock-up 2	AISI 308 clad	Inconel 52	AISI 316NG BM		
nominal	20	29.2	17.5		
measured av.	19.9	24.5	17.6		
difference	***0***	***-5***	***0***		
mock-up 3	Inconel 690	Inconel 152	Inconel 152 butter	Inconel 52 butter	SA 508 BM
nominal	29.5	28.7	28.7	29.2	0.2
measured av.	30.2	29.7	29.3	26.5	0.3
difference	***1***	***1***	***1***	***-3***	***0***

Nickel content					
mock-up TV	Inconel 600 BM	Inconel 182 weld	Inconel 182 butter	AISI 308 clad	
nominal	72.9	68.0	68.0	10.0	
measured ave.	70.2	64.8	52.2	10.7	
difference	***-3***	***-3***	***-16***	***1***	
mock-up 1	AISI 308 clad	Inconel 152	AISI 316NG BM		
nominal	10.0	55.2	12.5		
measured ave.	11.6	41.5	10.3		
difference	***2***	***-14***	***-2***		
mock-up 2	AISI 308 clad	Inconel 52	AISI 316NG BM		
nominal	10.0	59.28	12.5		
measured ave.	10.5	36.8	10.6		
difference	***1***	***-22***	***-2***		
mock-up 3	Inconel 690	Inconel 152	Inconel 152 butter	Inconel 52 butter	SA 508 BM
nominal	59.8	55.2	55.2	59.3	0.6
measured ave.	59.6	53.8	52.9	50.2	1.1
difference	***0***	***-1***	***-2***	***-9***	***1***

Iron content					
mock-up TV	Inconel 600 BM	Inconel 182 weld	Inconel 182 butter	AISI 308 clad	
nominal	9.4	6.7	6.7	67.8	
measured ave.	9.5	7.1	18.1	67.3	
difference	***0***	***0***	***11***	***-1***	
mock-up 1	AISI 308	Inconel 152	AISI 316NG		
nominal	67.8	10.4	68.6		
measured ave.	65.4	26	67.6		
difference	***-2***	***16***	***-1***		
mock-up 2	AISI 308 clad	Inconel 52	AISI 316NG		
nominal	67.8	9.8	68.6		
measured ave.	66.6	35.6	67.7		
difference	***-1***	***26***	***-1***		
mock-up 3	Inconel 690	Inconel 152	Inconel 152 butter	Inconel 52 butter	SA 508 BM
nominal	9.9	10.4	10.4	9.8	97.7
measured ave.	9.7	12.1	11.6	20.7	97.4
difference	***0***	***2***	***1***	***11***	***0***

2.5 FEG-SEM EBSD study of the weld metals

Residual plastic strain is known to increase the susceptibility to stress corrosion cracking (SCC) in austenitic stainless steel power plant pipe welds. The distribution of the residual plastic strain is expected to also be very important in Ni-base alloy weld metals and their HAZ. Studying the amount and distribution of plastic strain in the weld metals produced with different welding procedures using high spatial resolution is essential. Electron backscatter diffraction (EBSD) is an ideal method for that, since it is well accommodated to study relatively large samples and wide areas typically needed when studying welds. When needed, local areas can be examined with high spatial resolution and the results can be related to the local microstructure, which is not generally possible when studying the plastic strain with other methods. EBSD can be used to map the strain qualitatively in the form of different EBSD maps capable of revealing the variation of dislocation density and microstructure in the studied area. The use of EBSD in quantitative strain measurement is still in a development phase. The amount of orientation spread or the average intra-grain misorientations (IGM) can be correlated to the strain via a calibration curve by measuring the IGMs from tensile test samples deformed to various known degrees of strain. Experimental calibration curves have been constructed for strain measurement for austenitic stainless steels, but not yet for Ni-base alloys. The purpose of the present study was to demonstrate the possibilities of EBSD to both characterize the microstructure and to estimate qualitatively the residual plastic strain distribution of the studied Ni-base alloy dissimilar metal welds (DMW), employing the tools readily available in a commercial EBSD software (Oxford Instruments Channel 5). The misorientations present in the grains caused by plastic deformation can be calculated in different ways. Typically, in the EBSD applications misorientation of 10º between the measuring

points is used as the value to separate grains. In the materials forming twin boundaries the grains can be defined either regarding or disregarding the twin boundaries as normal grain boundaries. The intra-grain misorientation measurements of AISI 304 power plant pipe steel have shown that the increase in the intra-grain misorientation (IGM) is almost linear with increasing strain, and this can be qualitatively expected also for Ni-base alloys and their weld metals.

A Zeiss Ultra 55 FEG-SEM equipped with Nordlys II camera and Channel 5 software from Oxford Instruments was used for the EBSD studies. Acceleration voltage was 20 keV. The samples studied by EBSD were polished mechanically to 1 μm diamond paste finish, and as a final step they were polished electrolytically in order to remove the residual strains caused by sample preparation. The electrolyte consisted of 78 ml perchloric acid, 120 ml distilled water, 700 ml ethanol, and 100 ml buthylglycol. The studied materials were the DMWs presented in Figure 1, described in more detail in [5, 6].

In Figures 43–49 the microstructures of the different areas of the weld roots of the DMWs are presented. Plastic strain can be depicted in many different ways using EBSD. Specially designed map components for showing the distribution of strain are typically included in the EBSD software. However, even in the basic kind of maps the signs of different amounts of deformation can be detected. In the figures where the pattern quality in the austenite phase is shown, the grain boundaries are shown black and twin boundaries yellow. The different amounts of deformation can be seen in the local misorientation map figures based on the color key (amount of strain increasing from blue to red). In the areas near the root of the welds and in the HAZ, a high degree of deformation can typically be seen. This can be confirmed from the corresponding local misorientation maps especially designed to show the variation of deformation in the map areas.

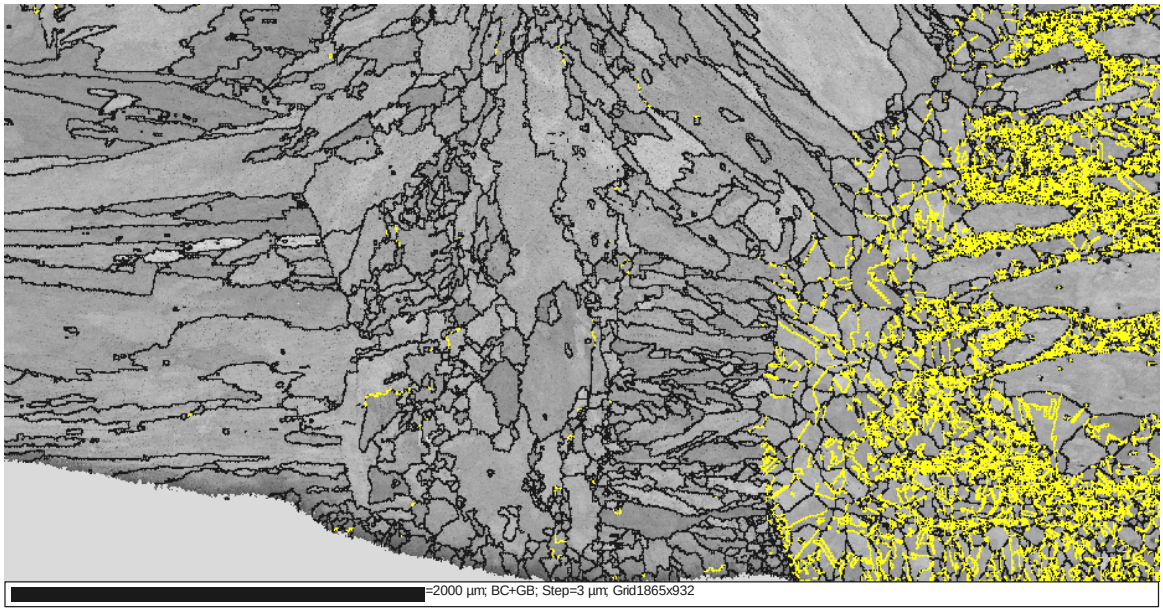
=2000 µm; BC+GB; Step=3 µm; Grid1865x932

a)

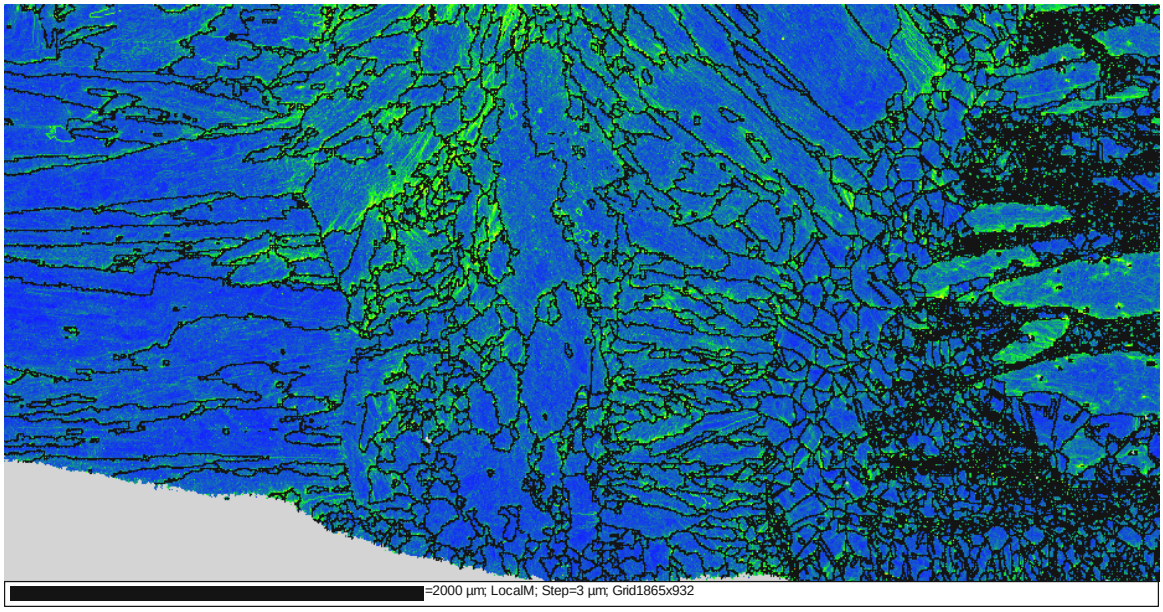
=2000 µm; LocalM; Step=3 µm; Grid1865x932

b)

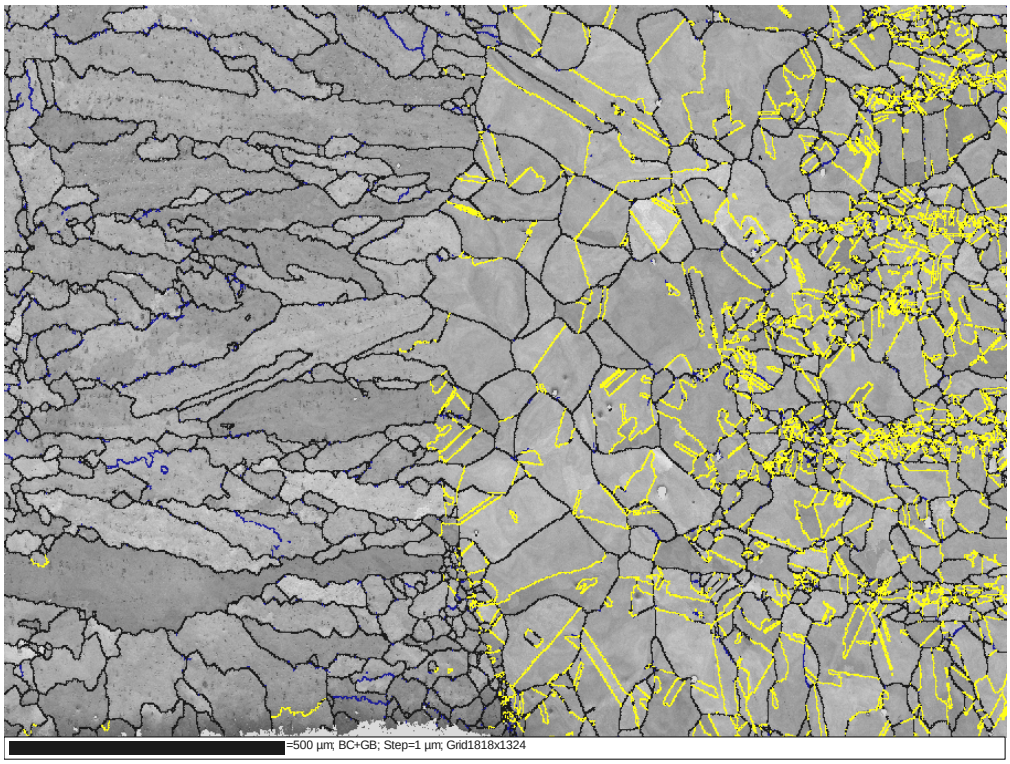

c)

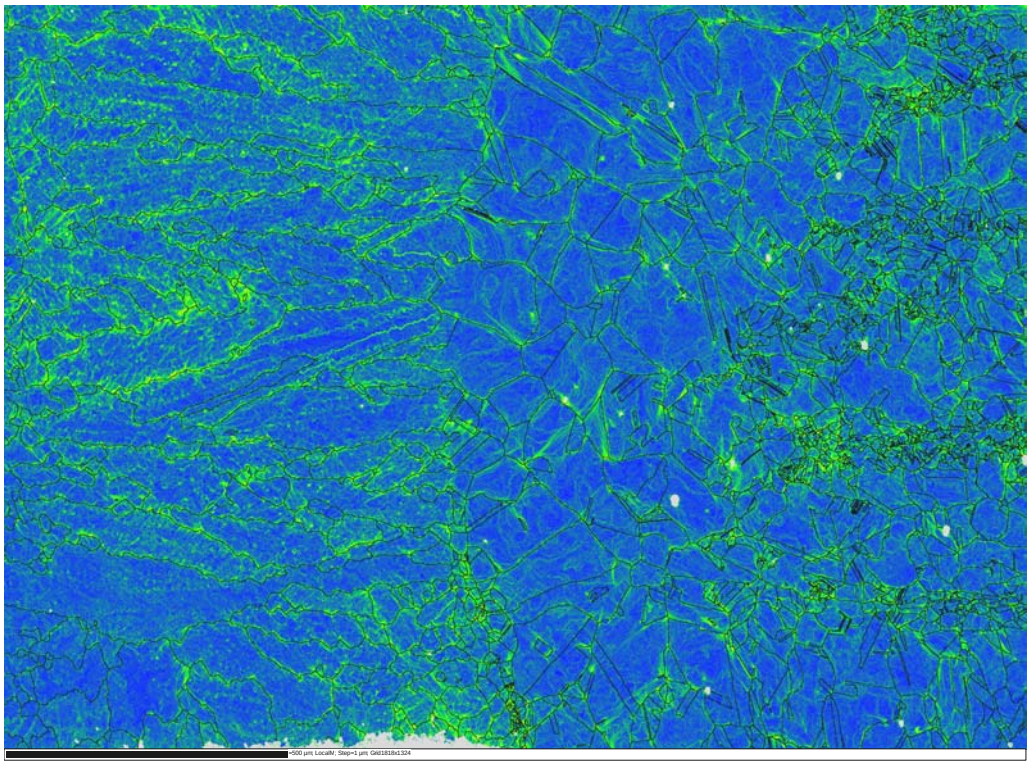

d)

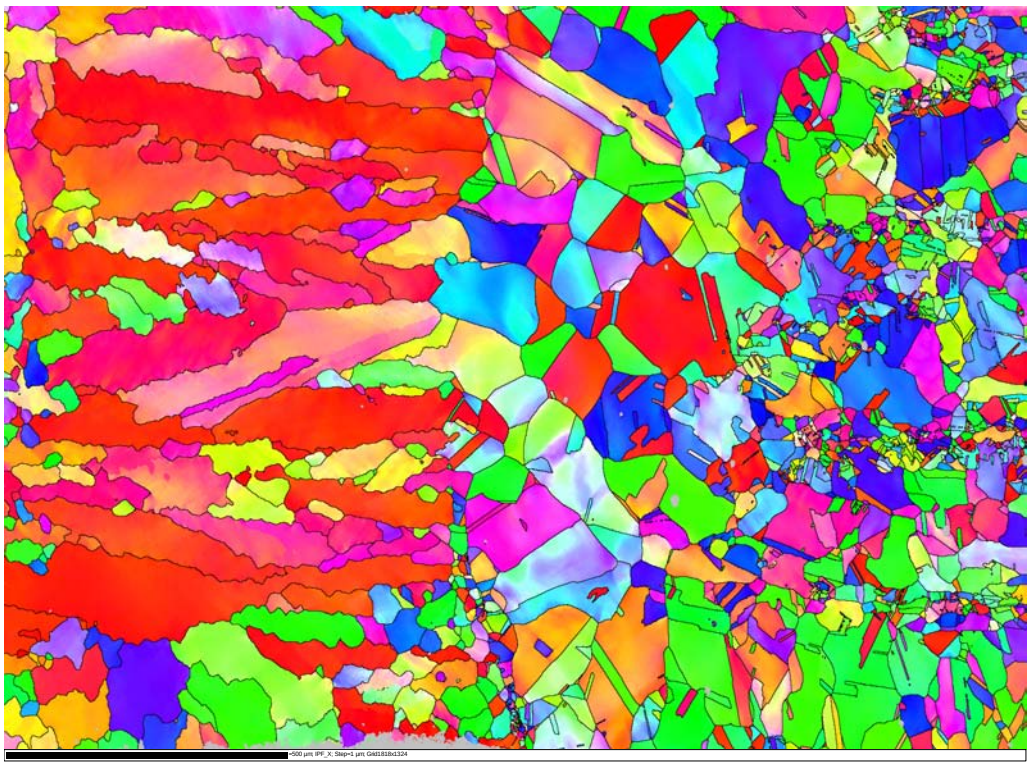

e)

Figure 43. Microstructure of the mock-up TV DMW root, where Alloy 182 weld metal is in the middle, Alloy 600 safe end is on the right, and Alloy 182 buttering is on the left. The pattern quality maps of a) and c) show the distribution of the grain size and grain form. The yellow lines in Alloy 600 show the twin boundaries inside the grains. The local misorientation maps of b) and d) show clearly the local concentration of higher strain (green color) in the areas of dendrite boundaries. In e) the inverse pole figure (IPF) map shows also that inside the large grains, marked orientation differences are present.

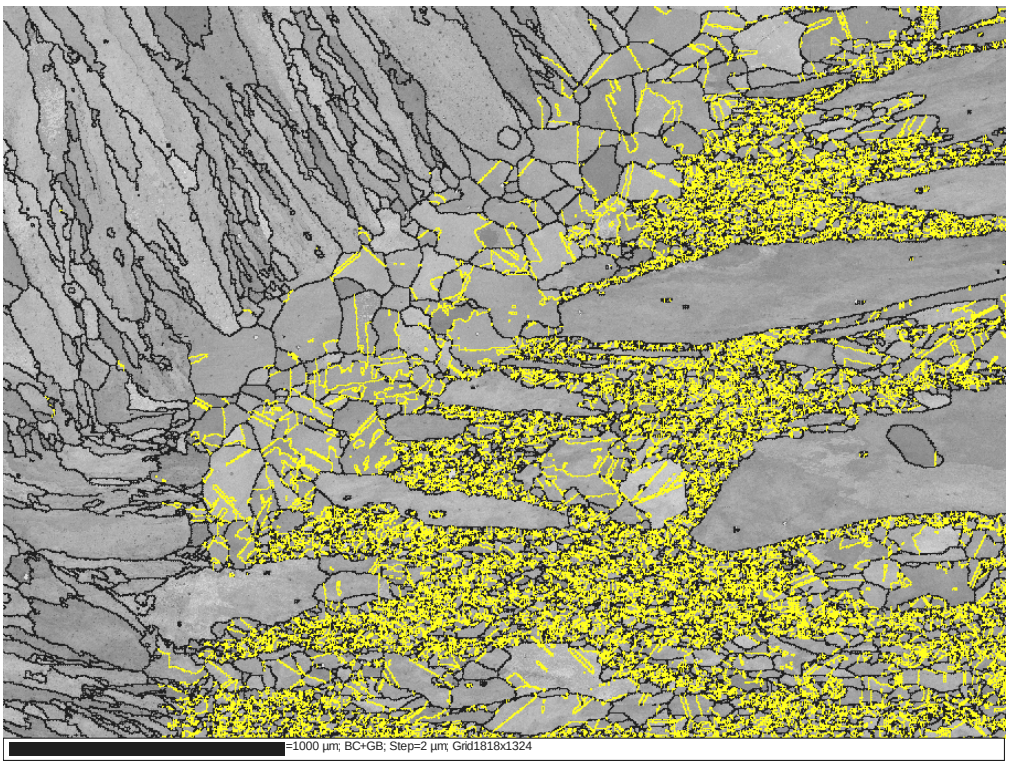

a)

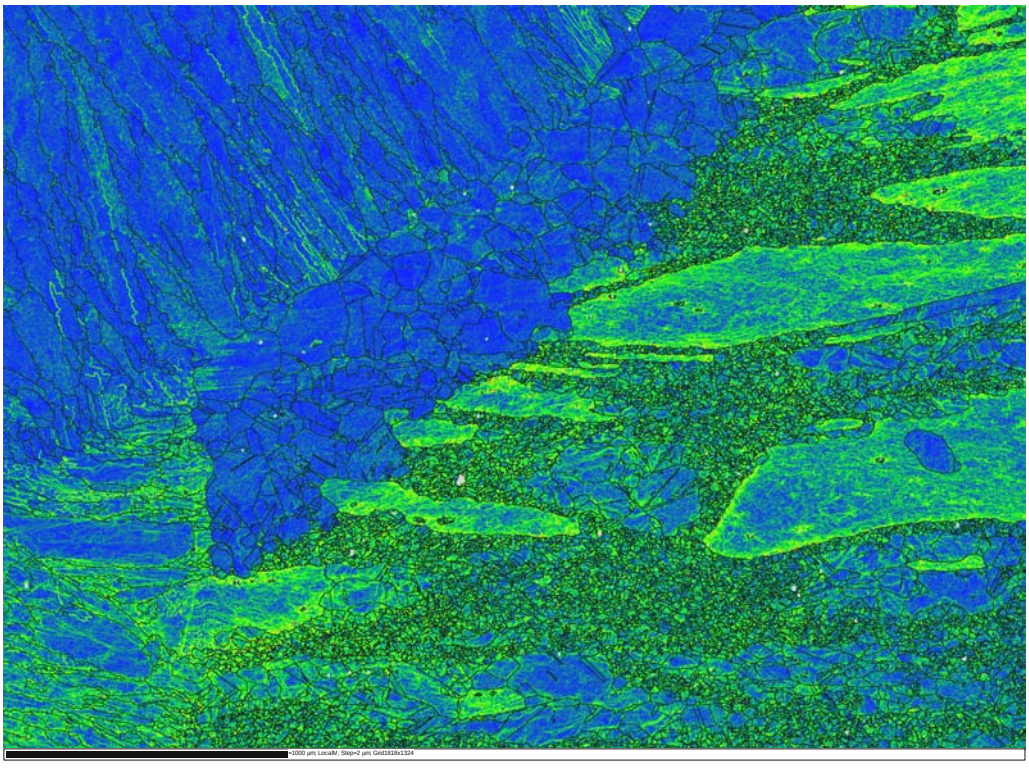

b)

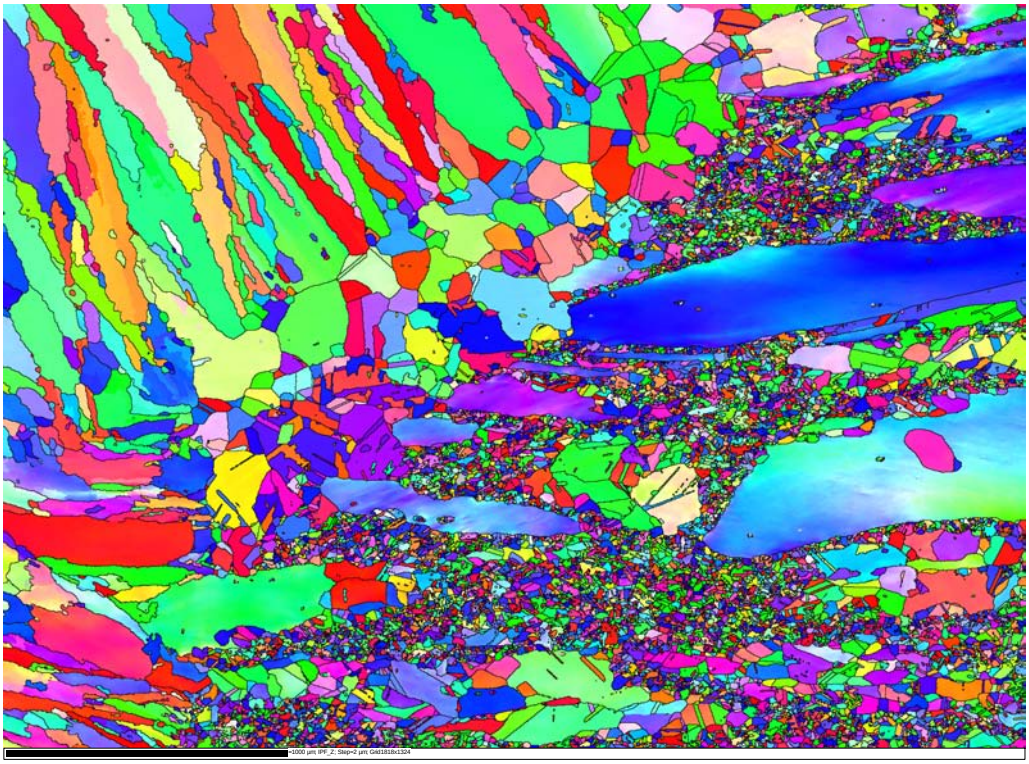

c)

Figure 44. Details of the HAZ of Alloy 600 safe end of mock-up TV DMW are shown. The pattern quality map of a) shows the distribution of the grain size and grain form on both sides of the fusion line. Alloy 600 has recrystallized and locally very small and very large grains are present. The yellow lines in Alloy 600 show the twin boundaries inside the grains. The local misorientation map of b) shows clearly the local concentration of higher strain (green color) in the HAZ and areas of dendrite boundaries in the weld metal. In c) the inverse pole figure map shows also that inside the large grains marked orientation differences are present.

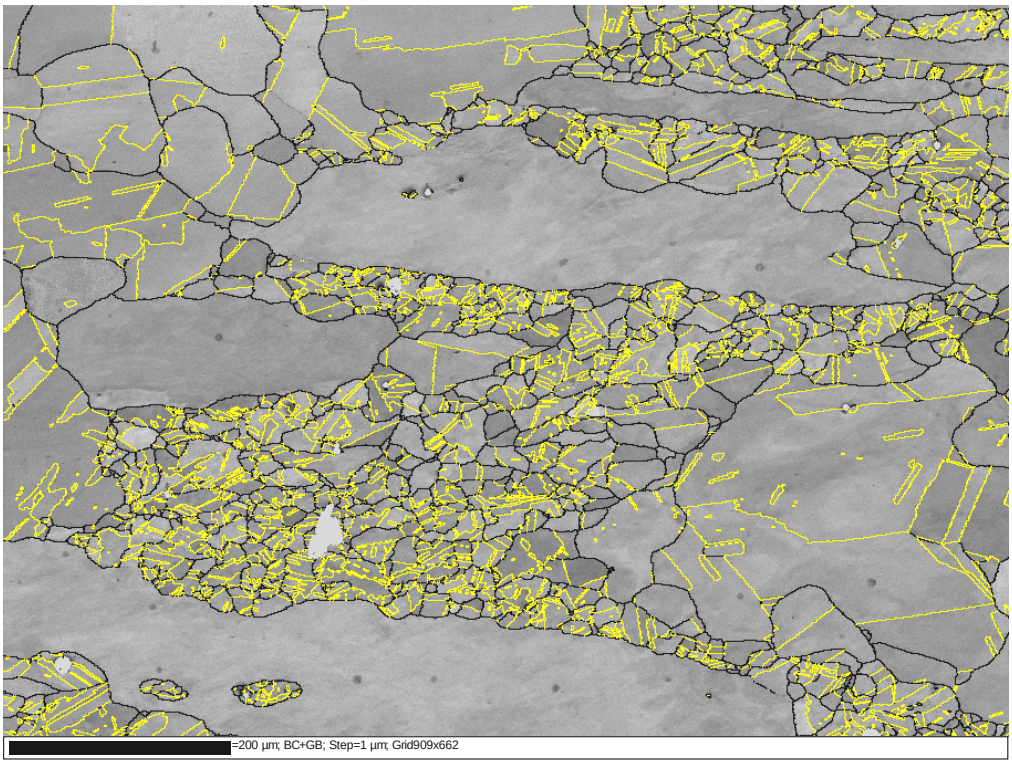
=200 µm; BC+GB; Step=1 µm; Grid909x662

a)

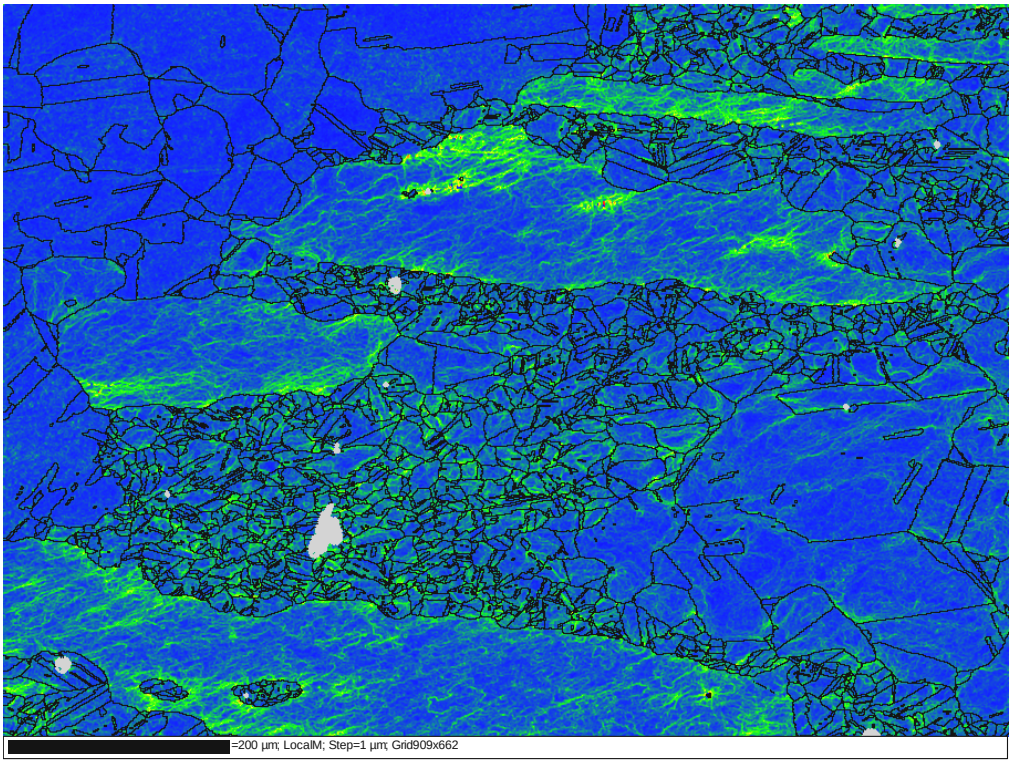
=200 µm; LocalM; Step=1 µm; Grid909x662

b)

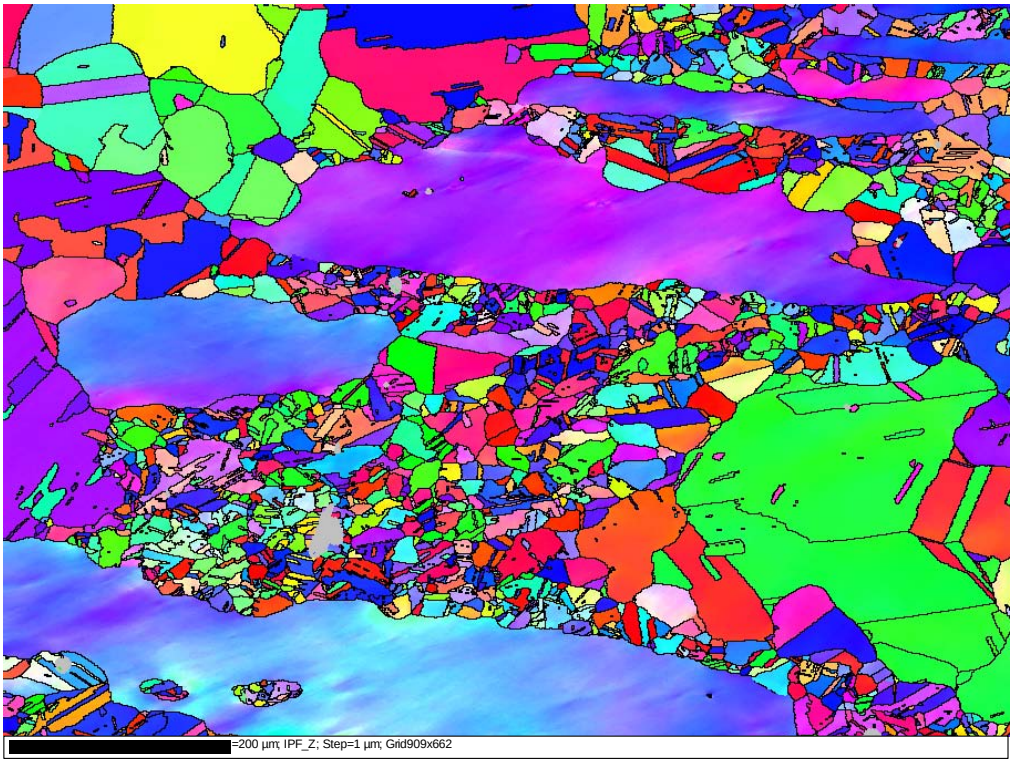

c)

Figure 45. Details of the HAZ of Alloy 600 safe end of mock-up TV DMW are shown at higher magnification. The pattern quality map of a) shows the distribution of the grain size in the HAZ where large and small grains are present. Alloy 600 has recrystallized and locally very small and very large grains are present. The yellow lines show the twin boundaries inside the grains. The local misorientation map of b) shows clearly the local concentration of higher strain (green color) in the HAZ and areas of small and large grains. In c) the inverse pole figure (IPF) map shows also that inside the large grains marked orientation differences are present.

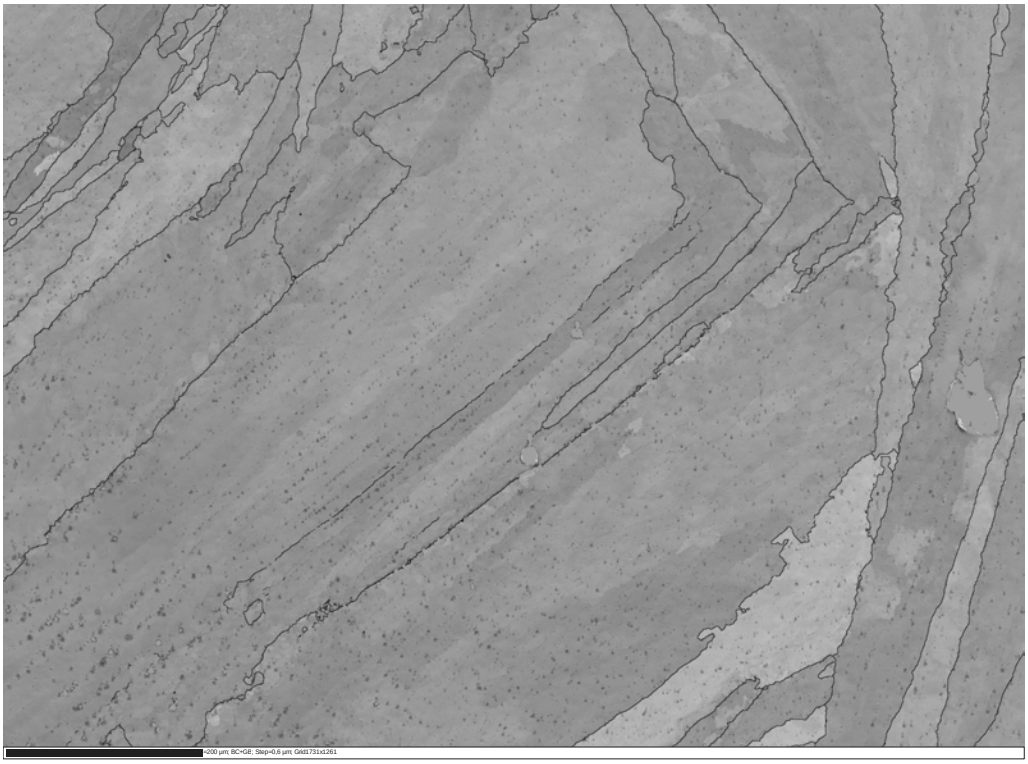

a)

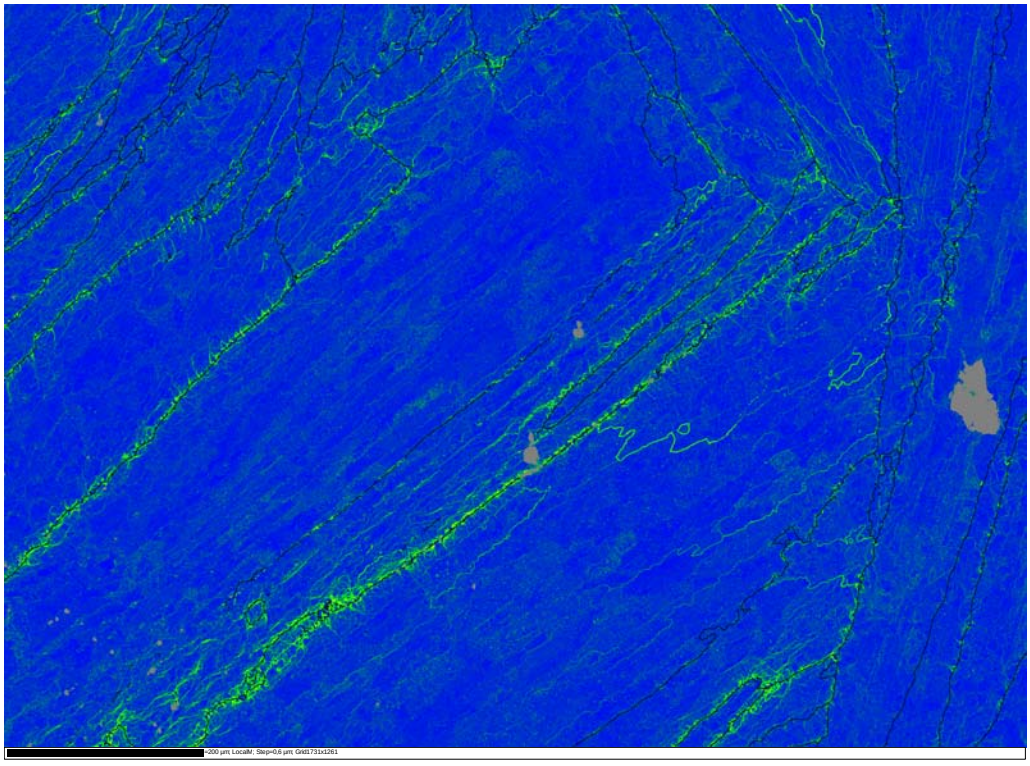

b)

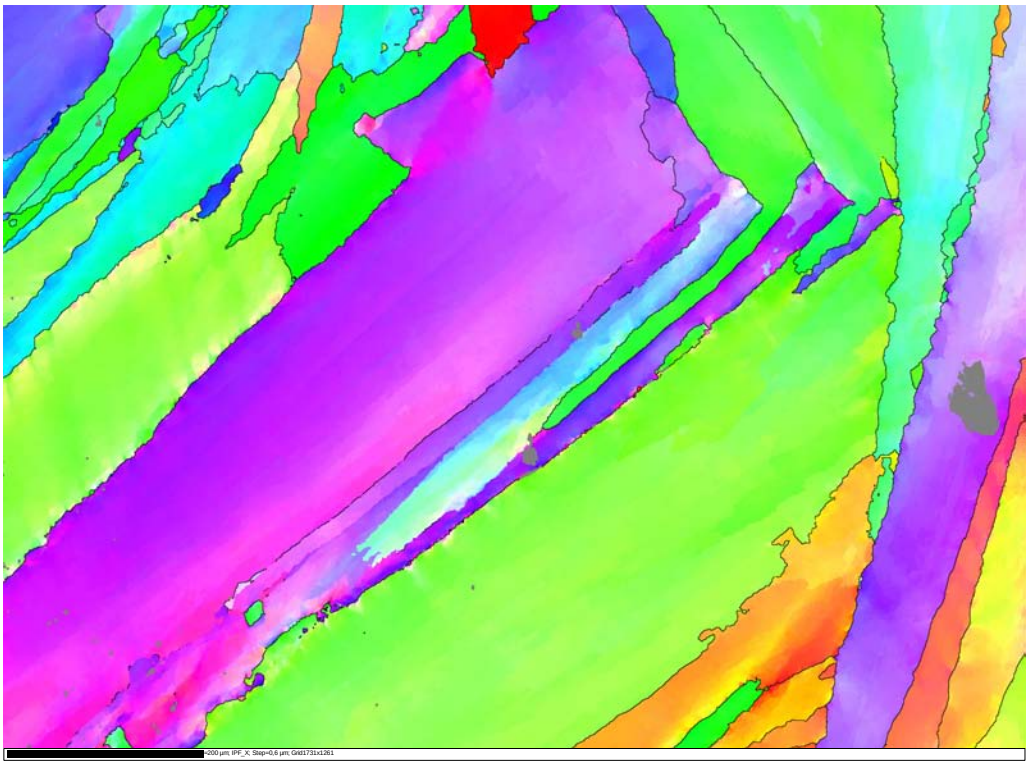

c)

Figure 46. Details of Alloy 182 weld metal of mock-up TV DMW are shown at higher magnification. The pattern quality map of a) shows the distribution of the grain size in the weld metal where very large grains are present. Inside the grains large orientation differences can be seen based on the variation of the grey color. The local misorientation map of b) shows clearly the local concentration of higher strain (green color) close to the grain boundaries in the weld metal. In c) the inverse pole figure (IPF) map shows also that inside the large grains marked orientation differences are present.

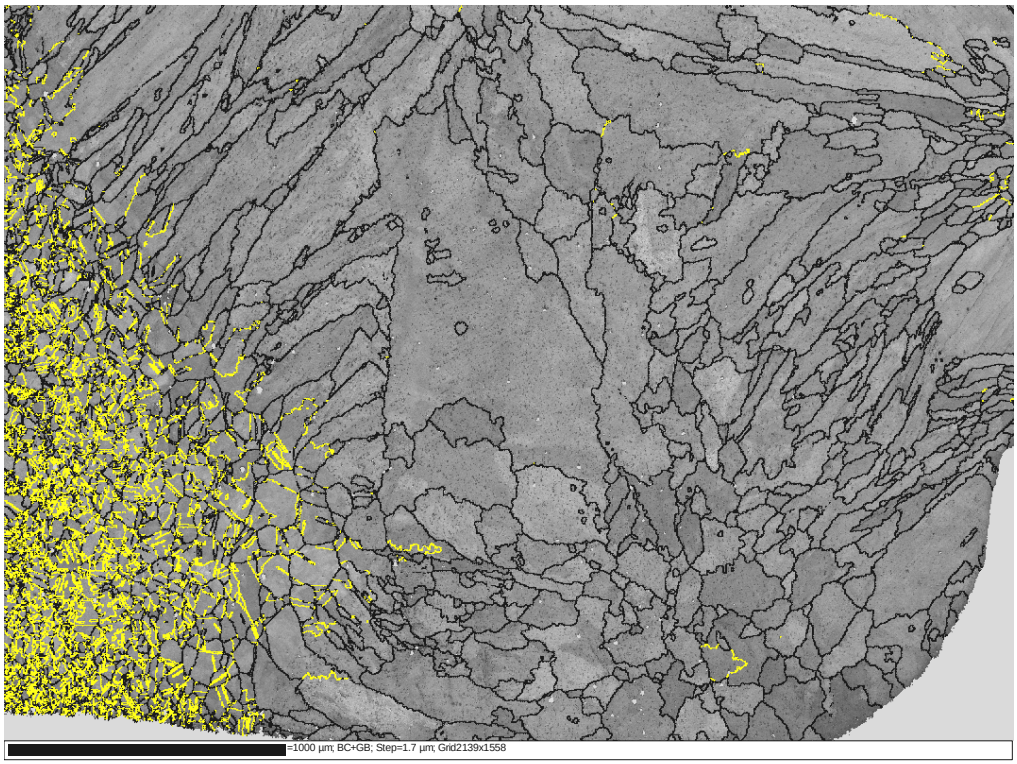
=1000 µm; BC+GB; Step=1.7 µm; Grid2139x1558

a)

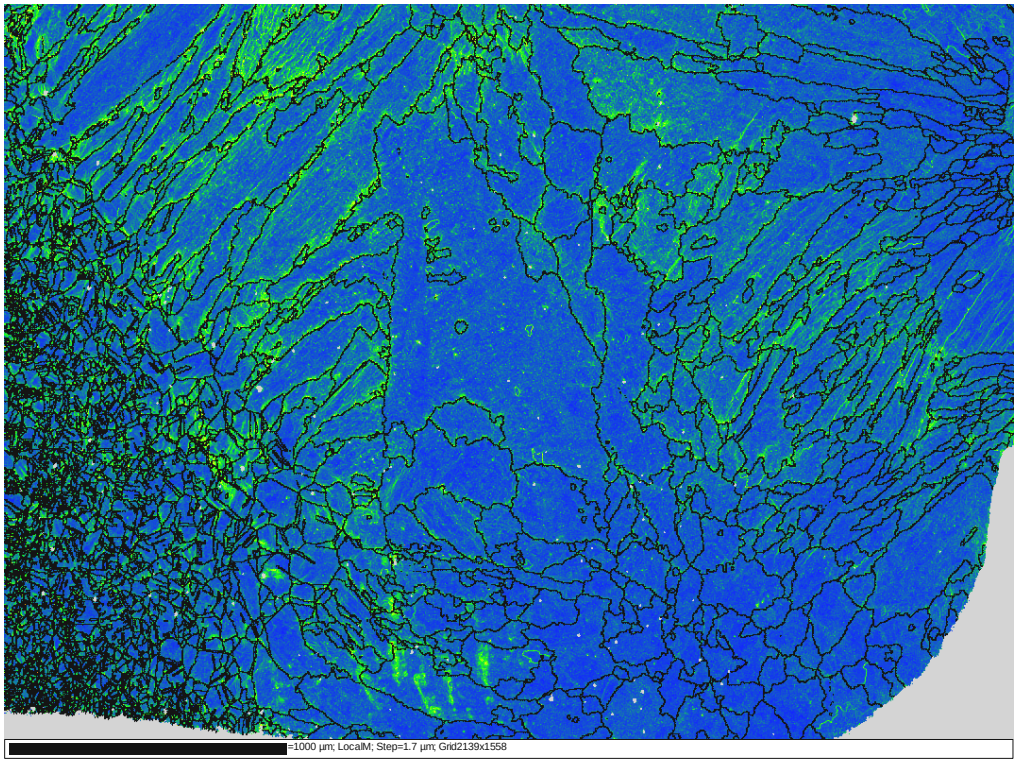
=1000 µm; LocalM; Step=1.7 µm; Grid2139x1558

b)

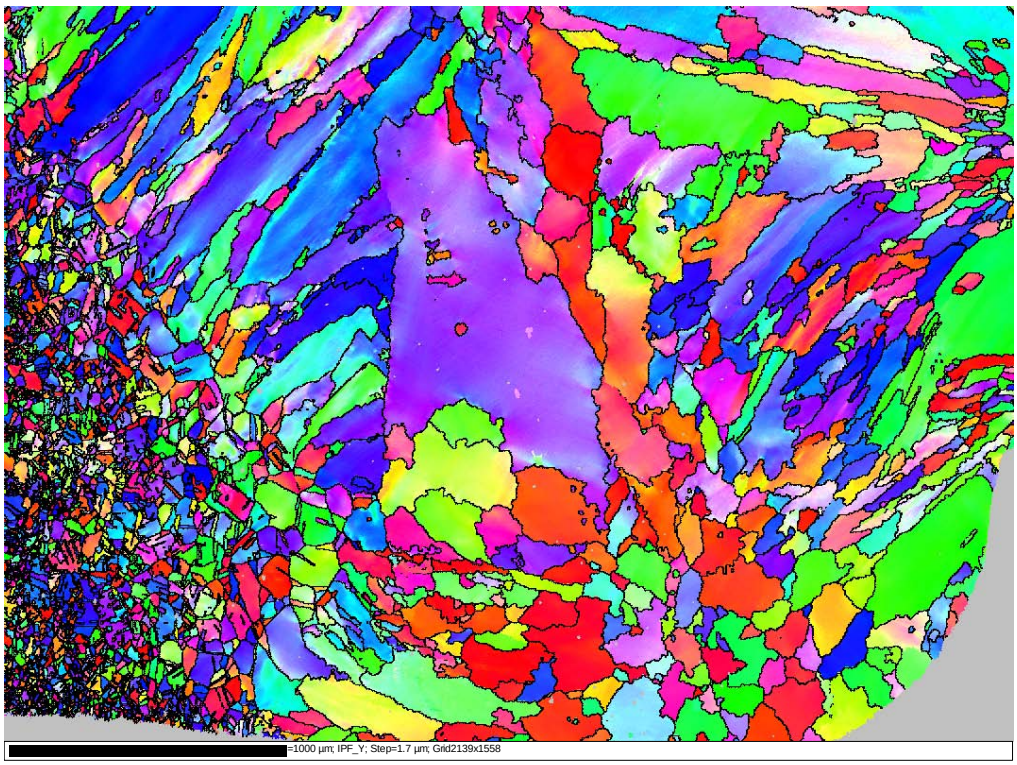

c)

Figure 47. Microstructure of mock-up 1 weld root, where Alloy 152 weld metal is in the middle, AISI 316 NG safe end is on the left, and stainless steel cladding of the LAS is on the right side. The pattern quality map of a) shows the distribution of the grain size and grain form. The yellow lines in AISI 316 NG show the twin boundaries inside the grains. The local misorientation map of b) shows clearly the local concentration of higher strain (green color) in the areas of dendrite boundaries. In c) the inverse pole figure (IPF) map shows also that inside the grains marked orientation differences and small angle boundaries are present.

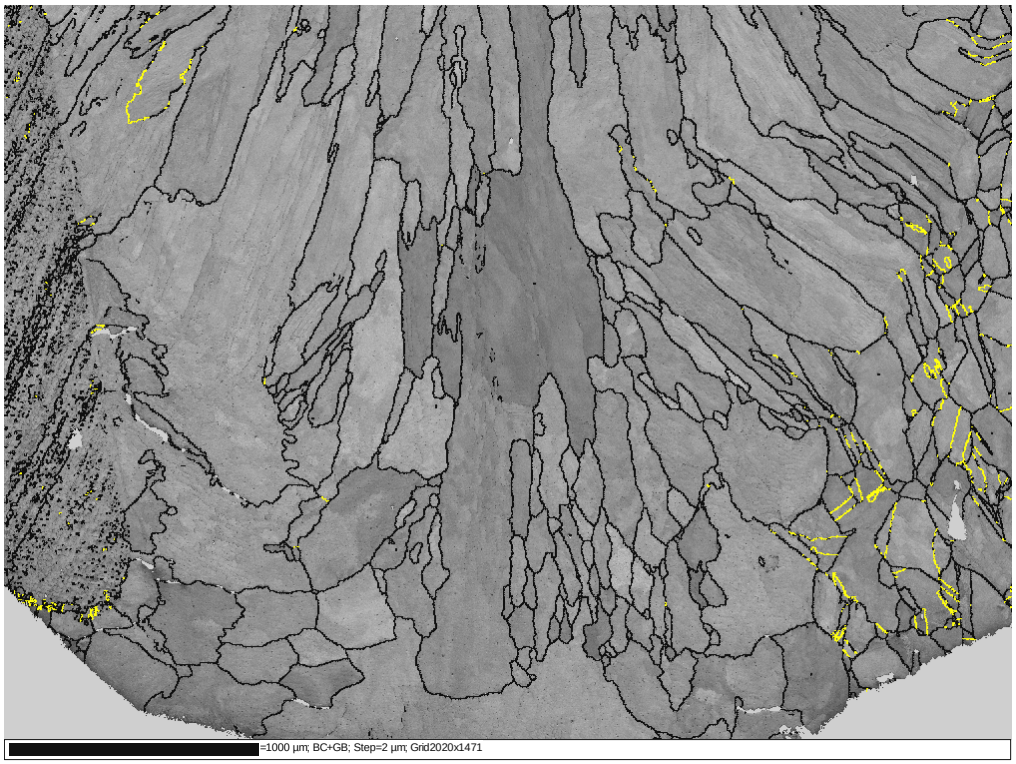
=1000 µm; BC+GB; Step=2 µm; Grid2020x1471

a)

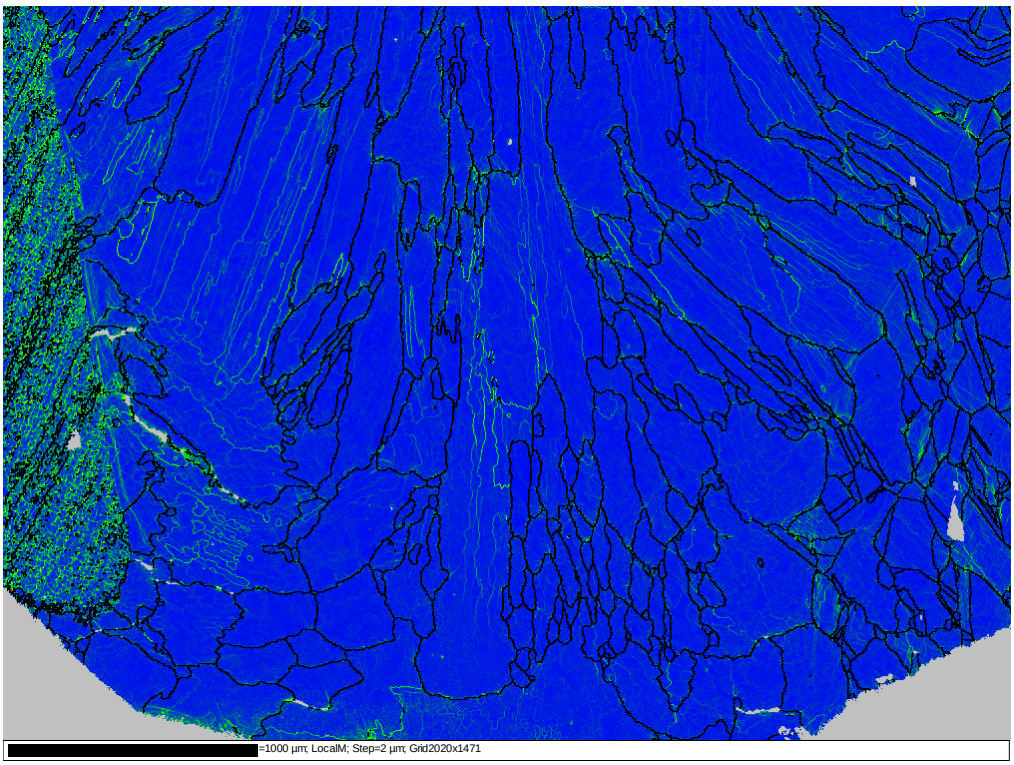
=1000 µm; LocalM; Step=2 µm; Grid2020x1471

b)

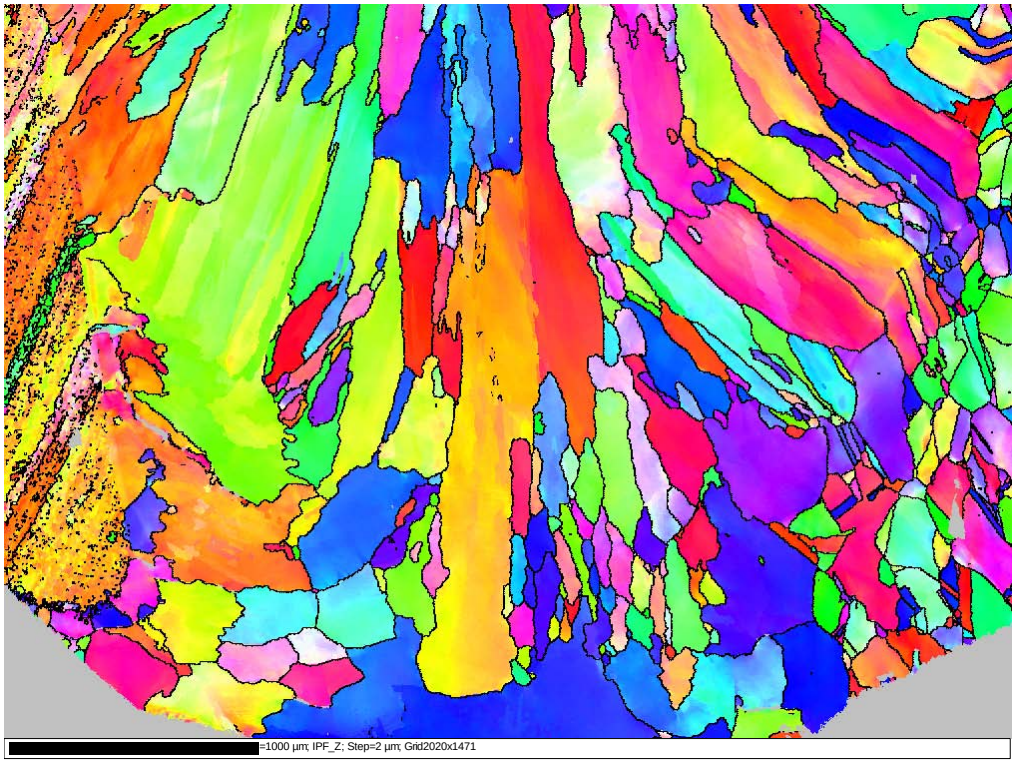

c)

Figure 48. Microstructure of mock-up 2 weld root where the Alloy 52 weld metal is in the middle, the AISI 316 NG safe end in on the right, and the stainless steel cladding of the LAS is on the left. The pattern quality map of a) shows the distribution of the grain size and grain geometry. The yellow lines in AISI 316 NG show the twin boundaries inside the grains. The local misorientation map of b) shows clearly the local concentration of higher strain (green color) in the HAZ in the stainless steel cladding. In c) the inverse pole figure (IPF) map shows that also within the grains marked orientation differences and small angle boundaries are present.

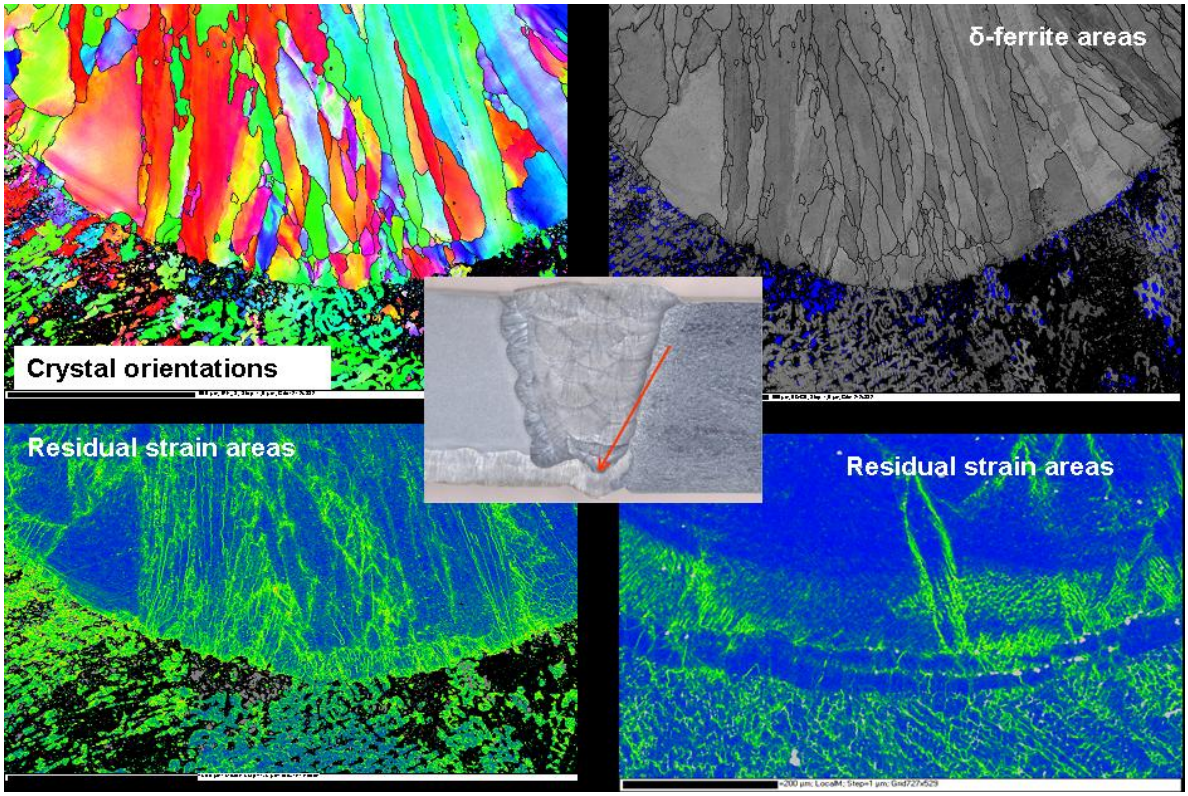

Figure 49. Microstructure of mock-up “Neste” root made for master thesis (see also Figure 54), where AISI 347Si stainless steel cladding of LAS extends up to AISI 321 safe end [1]. Both buttering and weld metal are Alloy 182, except the first two passes of the weld metal, which have been welded with Alloy 82. Alloy 82 weld metal is in the middle and AISI 347Si is below. In addition to pattern quality and local misorientation maps, an inverse pole figure (IPF) map can be seen where various crystal orientations are represented by different colors. The local misorientation maps show clearly the local concentration of higher strain (green color) in the areas of the dendrite boundaries.

Comparison of the EBSD results to the ATEM observations confirms that the residual strains in the weld metal are clearly higher in the grain and dendrite boundary regions. Additionally, residual strain is high in the weld root regions and the HAZs of the dissimilar metal welds. The EBSD technique is very efficient in showing the local misorientation gradients in the material, and in defining the grain size and local differences in the grain size.

EBSD can be used to identify the phase structure of the weld metal. The white phase (e.g., Figure 4) presumed to be a Laves phase in Alloys 182, 152 and 82 was analysed by EBSD. Laves phase compounds AB_2 are formed with A being large ion radius rare-earth or transition metal (Sc, Si, Ti, V, Zr, Nb, Mo Ta, W), while the B atoms with a small ion radius can be simple metal or transition metal (Cr, Mn, Fe, Co, Ni, Mo, Tc, Ru, Rh). The crystal structure can be the cubic C15-$MgCu_2$ type, hexagonal C14-$MgZn_2$ type or dihexagonal C36-$MgNi_2$ type [18, 19]. The size difference is necessary for the stability of a Laves phase. The ideal size ratio of A and B atoms is 1.225. In the weld metal Laves phase A and B atoms are typically not pure elements, but the mixture of several suitable elements of

the weld metal (A = Si, Ti, V, Nb; and B = Cr, Mn, Fe, Ni). The crystal structure is typically either C14 or C15 type. The controlling factors of the C14 or C15 stability are dependent on the average electron concentration factor (e/a) and in which side, A or B rich side, of the stoichiometric composition the Laves phase is formed. The increasing e/a ratio favors the C14 structure. Typical EBSD patterns of the weld metal matrix of Alloy 182 and the white phase can be seen in Figure 50. The EBSD pattern of the matrix is typical for the symmetric cubic FCC structure. The pattern of the white phase in Figure 50 b) is clearly not formed by a cubic crystal structure. Thus, the probable crystal structure of the white phase is the hexagonal crystal type C14. To verify this, the simulated Kikuchi patterns of the studied phase must be created. For this the lattice parameters, the space group and the Wyckoff

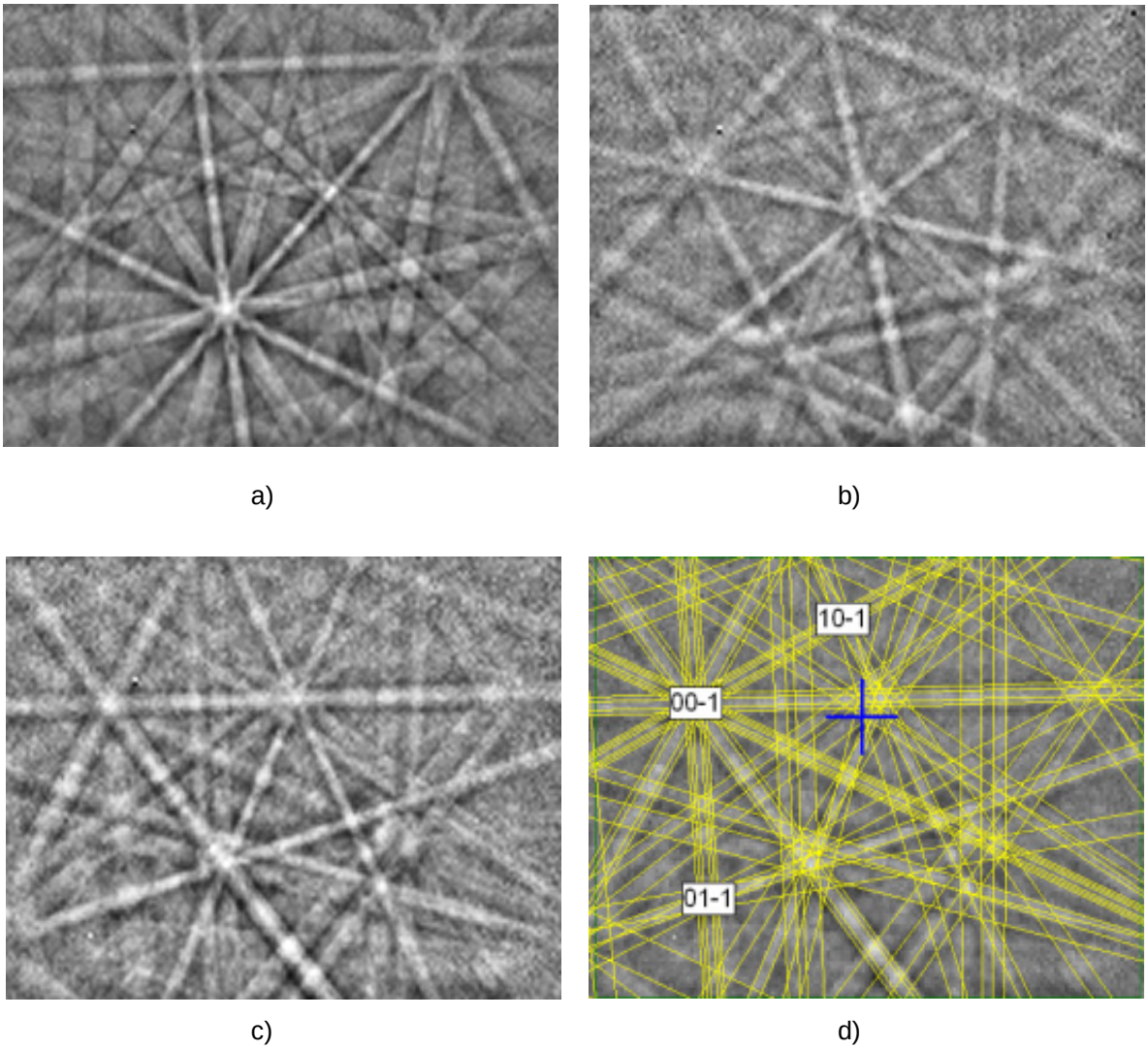

a) b)

c) d)

Figure 50. Laves phase confirmation with EBSD for Alloy 182 hot crack tip (see Figure 4, characterization of the nickel-base alloy weld metals). a) A typical EBSD pattern of the base material. b) An EBSD pattern of the white phase. c) Another EBSD pattern of the white phase. d) The solution with the formed Laves phase simulation.

position of the atoms in the lattice must be known. The cell parameters were approximated by the values (a = 0.476 nm, c = 0.786 nm) taken from a study of Laves phase $(Fe,Ni,Cr)_2(Nb,Si)$ in a stainless steel [20]. The space group and the Wyckoff positions of the atoms were taken from the data of Pearson´s Handbook for the structure type $MgZn_2$. Figures 50 c) and d) show an EBSD pattern of the white phase indexed against the formed simulated pattern. As can be seen the fitting is extremely good. The pattern is indexed as a defined Laves phase even using up to 15 detected bands (not shown in Figure 50 d) for clarity). Thus, the white phase found in the Alloys 182, 152 and 82 is the Laves phase with the C14 type crystal structure.

The formation of the Laves phase results in a high degree of deformation in the base material close to the Laves phase. This can clearly be seen in the SEM channelling contrast image of an area with high concentration of the Laves phase, Figure 51. The cell structure formed by increased dislocation content between the Laves phase strings can be seen. This can be further confirmed by the EBSD map constructed with the identified Laves phase in the area of a high concentration of Laves phase seen in Figure 51. Figure 52 shows an inverse pole figure EBSD map, in which the Laves phase is marked by dark blue colour. It can be seen that along the approximately 2.5 µm long line marked in the image, the cumulative misorientation attains about 20º. The cell structure seen in Figure 51 can also clearly be seen. In some areas even high angle grain boundaries and small grains are formed.

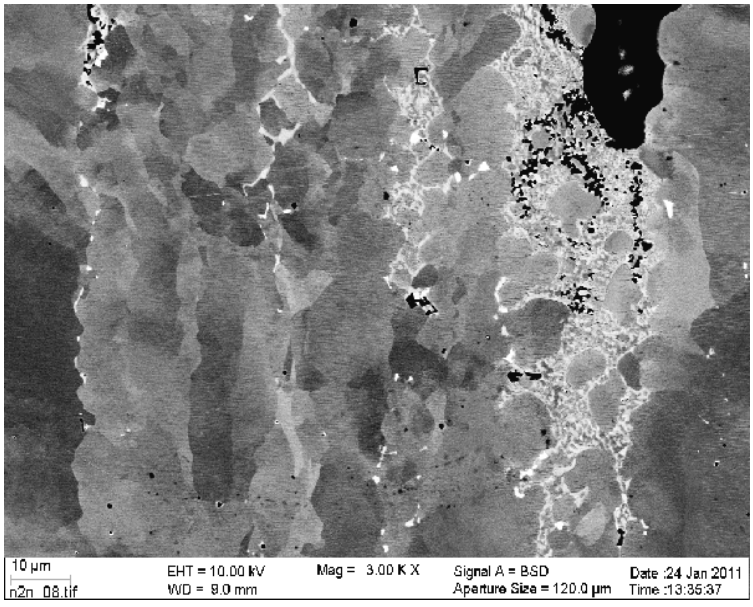

Figure 51. A channelling contrast backscattered image of an area with a large quantity of Laves phase. The clear cell structure in the base material between the Laves phase strings indicates a high degree of deformation in the base material close to the Laves phase.

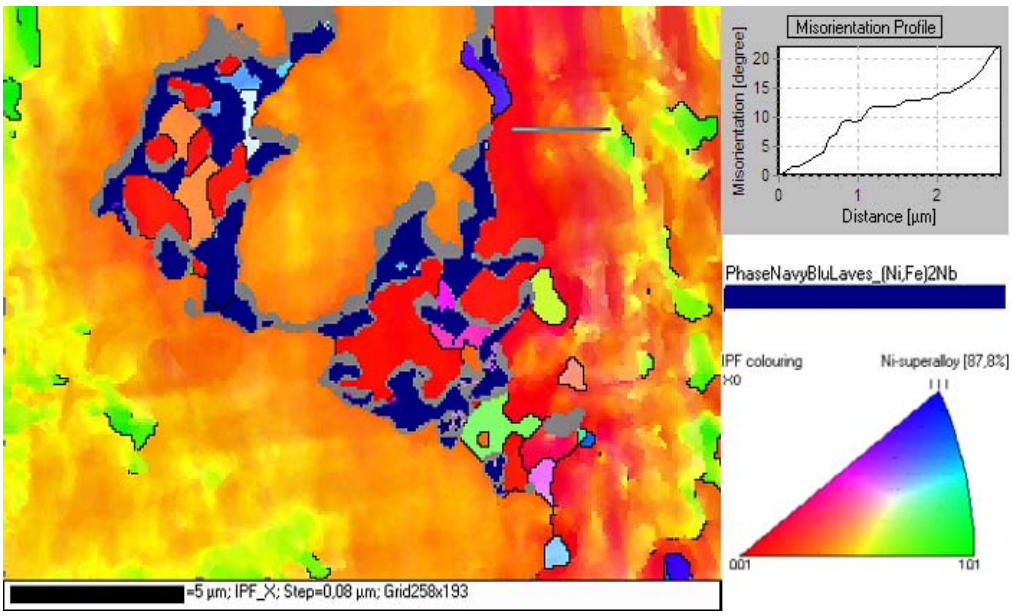

Figure 52. a) Inverse pole figure map of the base material with respect to x-direction and the Laves phase shown dark blue. The grain boundaries are marked by black lines. The misorientation line profile marked in the map shows a high degree of lattice rotation in the base material close to the Laves phase.

2.6 Residual stress measurements of the dissimilar metal weld mock-ups

The Contour method is a relatively new, nonstandardised method for measuring two-dimensional residual stress contours destructively. The method is based on measuring displacements caused by relaxation of residual stresses on a cut surface. For the measurement, the sample to be studied is carefully cut in two pieces (with a precise and low-stress cutting technique such as electric discharge machining). If the studied sample was free from residual stresses, the cut surfaces will retain their planarity. However, if residual stresses existed in the cut surface, those stresses are now relaxed by the cutting process and cause deviations from planarity on the cut surface. These deviations resulting from elastic relaxation of residual stresses can be measured, e.g., by coordinate measurement machine and analyzed to calculate the residual stress contours. The main advantages of this method are the attainable 2-dimensional stress contour of the full cross-section of the residual stress component normal to the cross-section and the robustness of solving the residual stresses from the measured surface displacements. The contour method is very useful for studying and mapping residual stresses in thick-wall fusion welds. The principle of the contour method is presented in Figure 53.

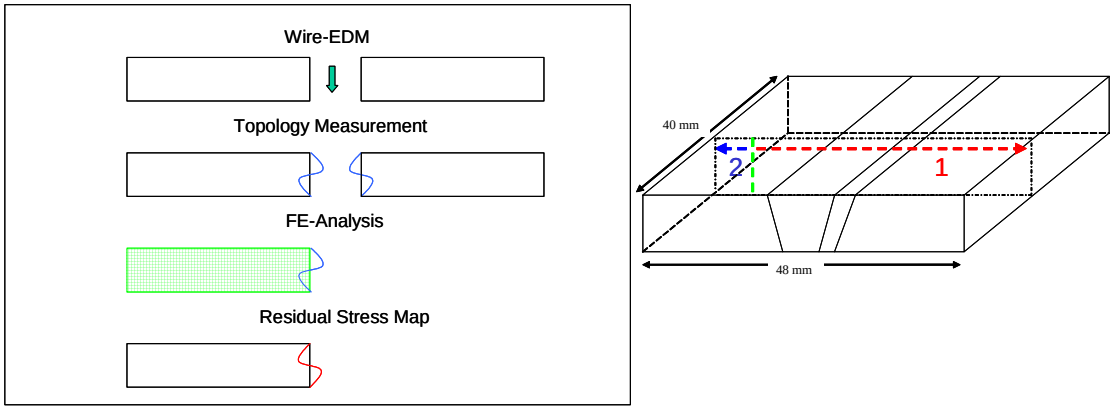

Figure 53. The contour method measures the 2-dimensional, cross-sectional residual stress map. First the part containing the residual stress is cut in two, and as residual stresses normal to the cut plane are released by the cut, the part is elastically deformed. Then the free surface created by the cut is forced back to its original flat shape. Assuming elasticity, superimposing the partially relaxed stress state with the change in stress (when forcing relaxed cut surface back to its flat shape) will give the original residual stress throughout the part. The superposition principle assumes elastic relaxation of the material and that the cutting process does not introduce stress that could affect the measured contour.

The method assumes, as with all relaxation techniques for residual stress measurement, that the relaxation of residual stresses occurs elastically and that the cutting does not induce stresses. In addition, because the displacements are measured directly from the cut surface, it is assumed that the cut occurs along a plane that was flat when the cutting started. This assumption requires that the sample is constrained from both sides, when the cut is made. The main error sources for this method are inadequate constraint during the cutting, and possible stresses caused by the cutting. A more detailed description of the contour method can be found online from (http://www.lanl.gov/contour/, [21]).

Dissimilar metal weld samples were WEDM cut and cut surfaces were measured by a coordinate measurement machine. The sample types are documented in more detail by Hänninen et al. [5, 6] (see also Figure 1) and the same sample designation is used here also. Measurement data from weld geometry and microstructure (metallographic examination) and cut samples were used for the residual stress analysis. The measurement data of cut samples had measurement anomalies near the starter hole used to start cutting. Consequently, the analysis was limited to the section of the measured surface to remove any effect of the starter hole.

The cut sample was meshed using ElmerGrid software (http://www.csc.fi/elmer). The measurement data was transferred to a finite element mesh by custom Trueflaw code. As is typical for the raw measurement data from an WEDM-cut surface, the data contained significant measurement scatter. This scatter includes the surface roughness induced by WEDM cutting as well as real measurement scatter. The scatter was removed prior to stress analysis in order to achieve reliable results. The micrographs from each sample were used for creating calculation mesh by tracing the material boundaries and geometry visible in the micrographs. The measurement data was then applied to the generated mesh and the residual stresses were solved.

The removal of the scatter was facilitated by calculating the node loads used in the stress analysis as an arithmetic average of all measurement dots within 2 mm of the node. This procedure has the effect of smoothing out the data and thus removing the measurement scatter. The side effect of this procedure is that the spatial resolution of the method is also decreased to a value corresponding approximately to the smoothing radius.

The finite element model was then solved using a custom-built version of the ELMER finite element code (http://www.csc.fi/elmer/). The material parameters used are given in Table 5.

Table 5. The material parameters used in the residual stress calculation made by the Contour method.

Material	E (GPa)	Poisson ratio
Inconel 600, Inconel 182, Inconel 82	**214**	**0.324**
Inconel 690, Inconel 152, Inconel 52	**207**	**0.30**
AISI 308, AISI 309, AISI 316	**190**	**0.30**
42CrMo4, SA508	**210**	**0.30**

Residual stress measurement of dissimilar metal weld samples by the Contour method was completed. The micrographs of the cut cross-sections, generated calculation meshes, and resolved residual stresses of each studied dissimilar metal weld mock-up sample are shown in Figures 54–58.

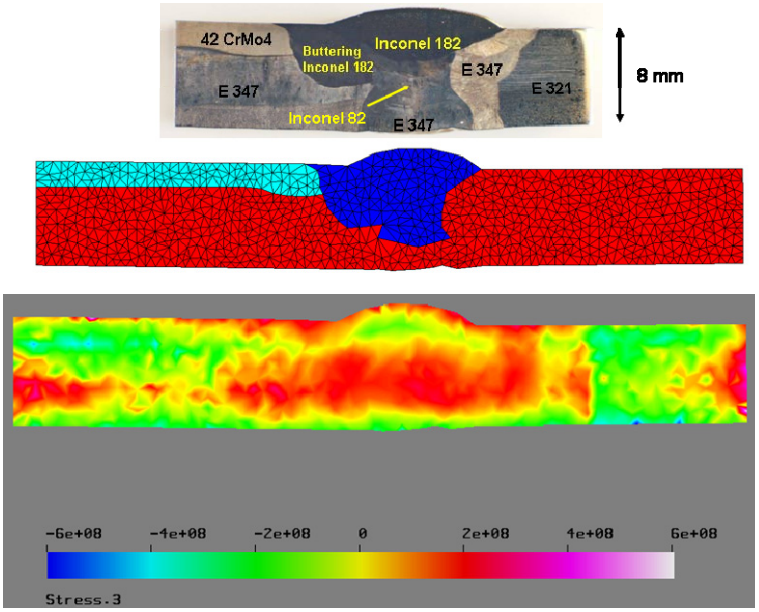

Figure 54. The cross-section micrograph, calculation mesh and resolved residual stresses of sample "Neste" made for ERIPARI project [5].

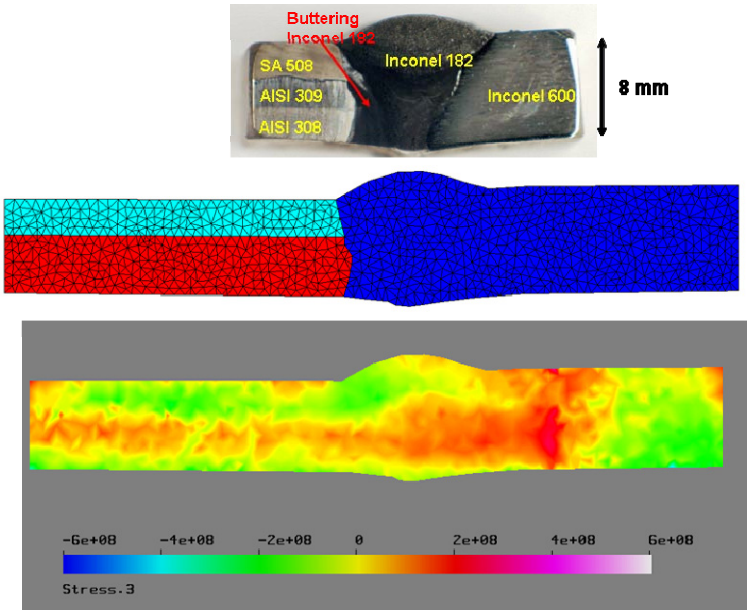

Figure 55. The cross-section micrograph, calculation mesh and resolved residual stresses of sample mock-up TV.

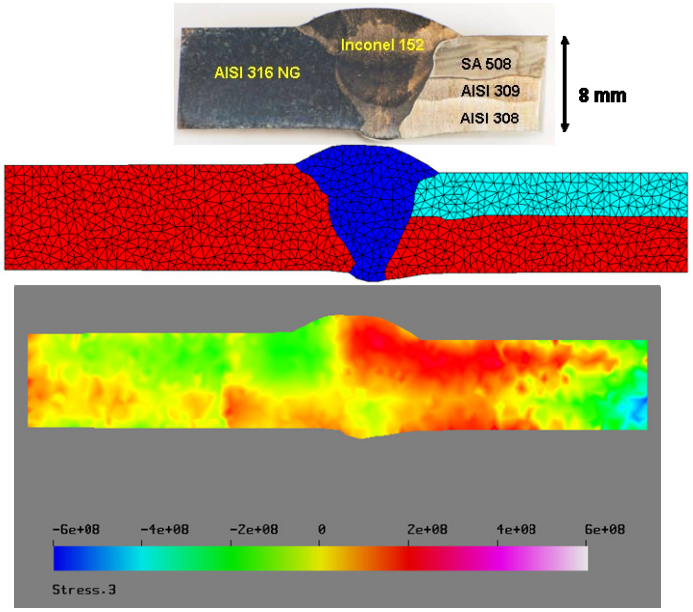

Figure 56. The cross-section micrograph, calculation mesh and resolved residual stresses of sample mock-up 1.

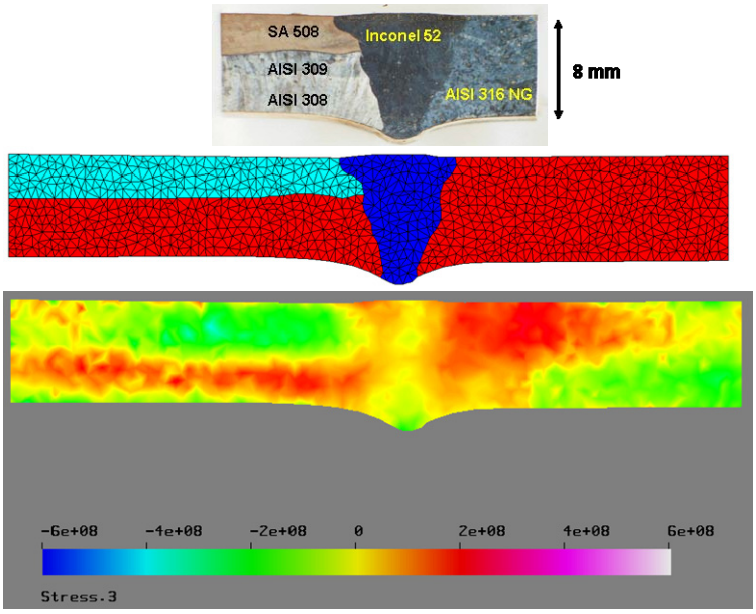

Figure 57. The cross-section micrograph, calculation mesh and resolved residual stresses of sample mock-up 2.

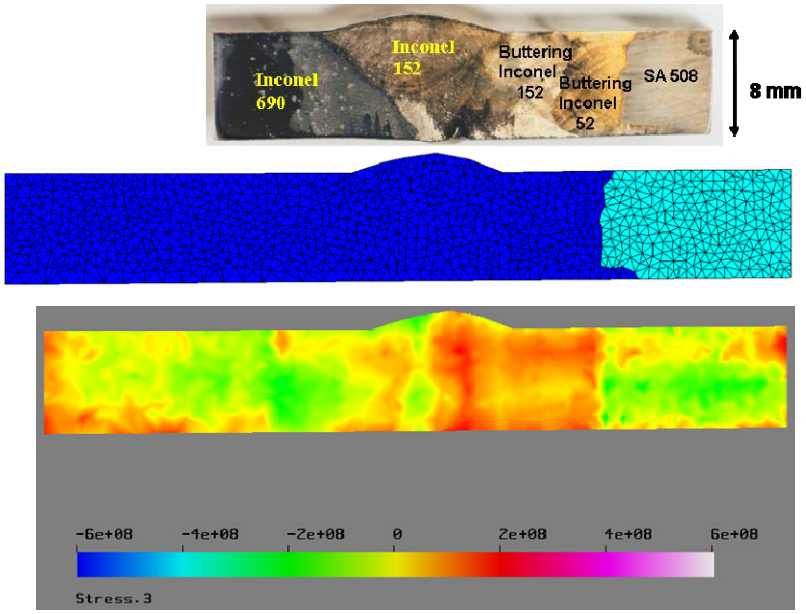

Figure 58. The cross-section micrograph, calculation mesh and resolved residual stresses of sample mock-up 3.

It is evident that the highest longitudinal residual stresses of the studied dissimilar metal welds are either in the nickel-based weld metal or very close in the heat-affected zone. In the weld mock-up "Neste," representing a typical dissimilar metal weld of an oil refinery, very high tensile residual stresses are present in the whole root region of the weld and also on the AISI 321 austenitic stainless

steel side of the DMW. Mock-up “TV,” representing a typical BWR DMW, shows the highest residual stresses in the HAZ of the safe end material, Alloy 600. High tensile residual stress is also present in the weld metal itself, but residual stresses in the buttering and the low alloy steel side are low. Alloy 152 and 52 DMWs show the highest tensile residual stresses on the top side of the weld, and in the heat-affected zones on both sides of the DMW. In the Alloy 152 mock-up where a thick buttering layer of Alloy 52/152 was present, the tensile residual stresses were the highest on the buttering side of the weld, and through the whole thick buttering layer.

3. Dynamic strain aging (DSA) of nickel-base alloy weld metals

3.1 Introduction

DSA is a material, strain rate and temperature dependent phenomenon. As its name implies, it occurs during the deformation process, and can lead to an inhomogeneous or serrated plastic flow during straining at elevated temperatures. It often results in a marked degradation of mechanical properties. DSA occurs in alloys containing solute atoms that can rapidly and strongly segregate to dislocations during plastic flow. In Ni-base alloys the occurrence of DSA has been previously reported for a wide range of temperatures and strain rates. In Alloy 600 and 690 DSA was observed in the temperature range of 150 – 600 ^{o}C at the strain rates from 10^{-6} to 10^{-3} s^{-1} [22–25]. In other Ni-base alloys, like Alloy 718, Alloy 720 and Ni – C alloys, DSA has also been reported for the similar temperature and strain rate ranges [26–32].

In different materials various solute atoms and a number of mechanisms can participate in the solute atom – mobile dislocation interactions. In nickel-base alloys and superalloys interstitial (H, C and N) and substitutional (Cr) solute atoms are usually responsible for the serrated flow [22–32].

It has been established that interstitials play a key role in DSA of pure Ni, which has been shown for Ni-C and Ni-H interstitial alloys [31, 32]. In Ni-C alloys the lower critical temperature of DSA occurrence had an activation enthalpy of about half of that for bulk diffusion of carbon, and it was associated with carbon diffusion in the dislocation core. Additionally it was observed that serrations were not affected by quenched-in vacancies [32]. By comparison of activation energies of the DSA occurrence in Ni-base alloys with activation energies of solute diffusion in Ni, it has been suggested that at lower temperatures, where type A and B serrations were observed, DSA is attributable to the interaction of dislocations with mobile interstitial atoms. But at higher temperatures, where DSA promotes serrations of type C, responsible solutes are most likely Cr or C-Cr and N-Cr complexes [29, 32].

The role of crack tip plastic deformation in the highly deformed material of the plastic zone in the EAC mechanisms was the key question of this study. The aim of the present investigation was to study and to compare the DSA phenomenon in base materials of Alloy 600 and 690 with that of weld metals of Alloy 182, 82, 152 and 52.

3.2 Experimental and materials

Two commercial Ni-base alloys Inconel Alloy 600 and 690 and the weld metals of Alloy 182, 82, 152 and 52 were studied. Chemical compositions of the materials are shown in Tables 6 and 7. The base materials of Alloy 600 and 690 were supplied as two metal plates in mill-annealed condition with average grain size of about 100 μm for Alloy 600 and about 30 μm for Alloy 690. The sample preparation procedure and the description of the materials of the studied Alloy 600 and 690 are reported elsewhere [24]. The material of the weld metals for the study was taken from the pre-fabricated welded blocks. These blocks of four different filler materials (Alloy 182, 82, 152 and 52) are presented in Figure 59. The base material was basic carbon steel plates that were attached in the shape of the cross.

Figure 59. Four welded Ni-base alloy blocks: from the left Alloy 82, 182, 52 and 152.

The corners of the cross were filled length-wise by multi-pass welding in sequence presented in Figure 60 a. An example of a cross-section of Alloy 152 block is shown in Figure 60 b. Welding methods were shielded metal arc welding (SMAW) for filler metals of Alloy 182 and 152 and gas tungsten arc welding (GTAW) for filler metals of Alloy 82 and 52, respectively.

Metallographic characterisation of weld defects and microstructure of the fabricated weld metals was performed by means of optical and scanning electron microscopy. The specimens for the metallographic characterisation were cut in the shape of rectangular bars with the cross-section of 10 x 10 mm and length of 25 mm by an abrasive disc-saw from the inner part of the corresponding weld metal blocks, near the interface area. The blue box in Figure 60 b indicates area where the specimens were cut from Alloy 152. The thickness of the weld metal over the interface area was not smaller than 5 mm. The specimens were polished from the side of the pure weld metal with emery paper down to 4000 grit, and completed with 1 μm diamond paste. The etching was performed using Kalling's no. 2 solution ($CuCl_2$ + HCl + C_2H_5OH). Examples of weld metal microstructures are shown in Figure 61. The typical large, elongated grains can be seen along with regions of fine grains with an average grain size of 85 μm for Alloy 182, 100 μm for Alloy 82, 87 μm for Alloy 152 and 90 μm for Alloy 52. Most of the possible indications of weld defects were small pores distributed randomly over the cross-

section of the metallographic sample, or arranged in lines along the grain boundaries or boundaries of the welding passes, which may also result from etched secondary phases, Figures 61 a, b, c. Typical weld defects such as short intergranular cracks and deep voids were found only in Alloy 52 along grain boundaries, Figure 61 d.

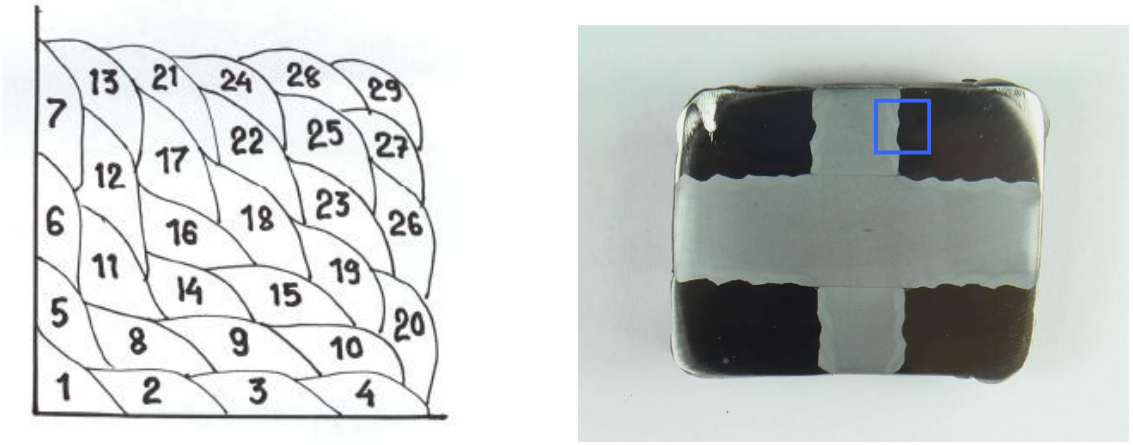

a) b)

Figure 60. Welding sequence (a) and an example of a cross-section of Alloy 152 block (b).

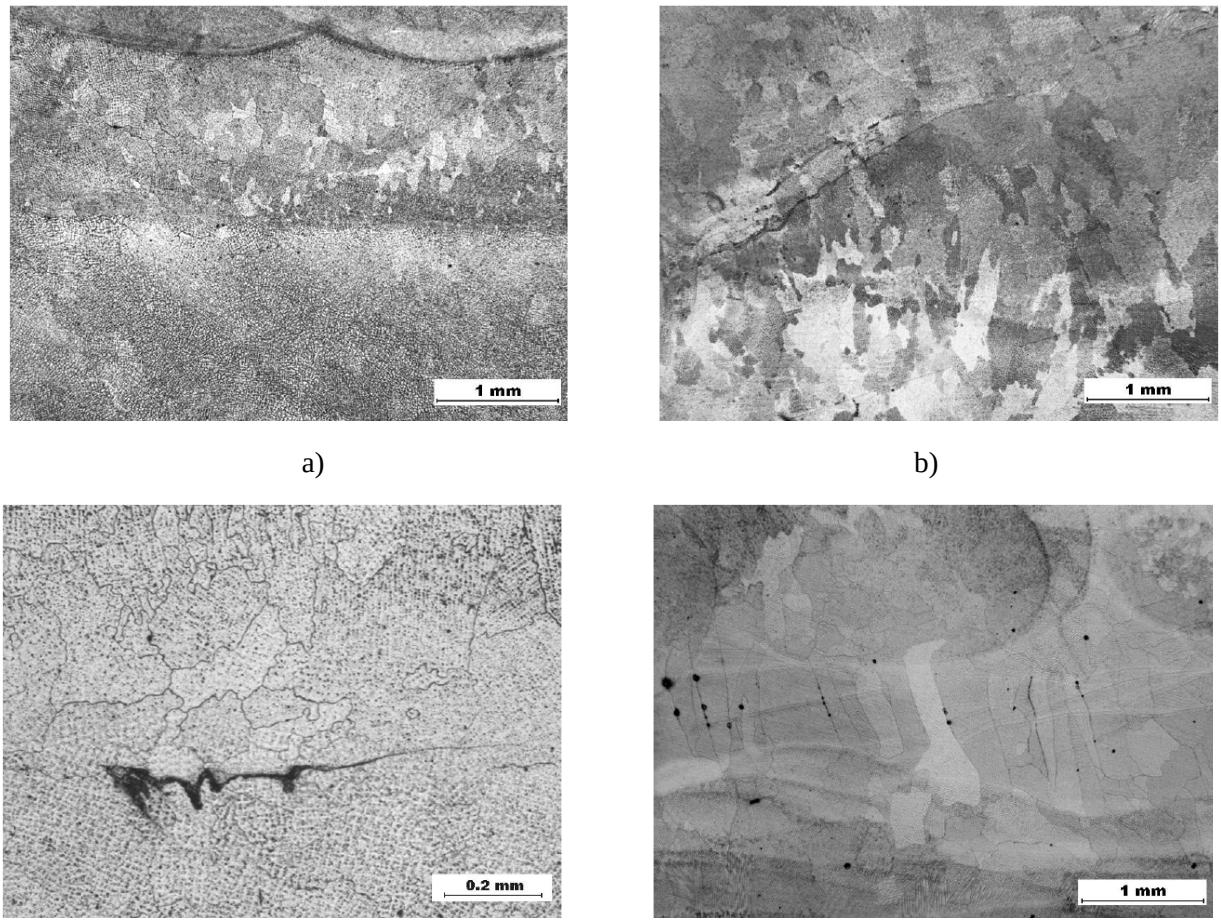

Figure 61. Microstructures and weld defects of the weld metals of Alloy 182 (a), 82 (b), 152 (c) and 52 (d) in as-welded condition.

Table 6. Chemical composition of the base material alloys used in DSA measurements in weight %.

Base mat.	Ni	Cr	Fe	Cu	Al	Co	Nb	Ti	Mn	Si	S	P	C
Alloy 600	bal.	16.1	8.1	0.01	0.17	0.29	0.01	0.16	0.22	0.32	<0.01	<0.01	0.04
Alloy 690	bal.	27.7	8.4	0.01	0.18	0.07	0.01	0.14	0.22	0.23	<0.01	<0.01	0.01

Table 7. Chemical composition of the weld metal alloys used in DSA measurements in weight %.

Weld met.	Ni	Cr	Fe	Cu	Al	Co	Nb	Mo	Ti	Mn	Si	S	P	C	O_2	N_2	H_2
Alloy 182	bal.	15.6	9.1	0.01	0.02	0.02	2.1	0.05	0.01	6.5	0.7	0.002	0.002	0.02	0.029	0.027	5.87 ppm
Alloy 82	bal.	19.5	4.0	0.01	0.06	0.01	2.9	0.02	0.20	3.6	0.13	0.002	0.002	0.02	0.015	0.020	2.27 ppm
Alloy 152	bal.	28.1	13.0	0.01	0.06	0.03	2.2	0.05	0.01	5.0	0.39	0.002	0.002	0.02	0.061	0.021	9.32 ppm
Alloy 52	bal.	28.7	10.3	0.01	0.84	0.04	0.04	0.03	0.58	0.33	0.22	0.002	0.002	0.02	0.010	0.007	1.83 ppm

Rectangular bars of the welds with cross-section dimensions of about 10 × 20 mm were cut from the corners of the block and then sliced to 2.1 mm thick plates in longitudinal direction of the welds by wire electro-discharge machining (WEDM). The sheet-type sub-size specimens for tensile tests (ASTM standard E8M) were shaped by WEDM with final surface polishing of the reduced section of the tensile specimen down to 1200 grit to remove surface defects. The final dimensions of cross-section of the reduced section were 2 × 6 mm. Tensile tests were performed according to the standards SFS-EN 1002-1 and ASTM E21 (Standard Test Method for Elevated Temperature Tension Tests of Metallic Materials) in air environment. Tensile tests were carried out using a 25 kN MTS 858 test machine equipped with a MTS High-Temperature Furnace 653.02 at strain rates in the range of 10^{-3}–10^{-6} s^{-1} and temperatures from 27 to 600°C. The strain rate sensitivity was measured using step-wise changes of the strain rate from 10^{-4} to 10^{-6} s^{-1} and in the reverse way during tensile testing, with the ratio of initial and subsequent strain rate ($\dot{\varepsilon}_1 / \dot{\varepsilon}_2$) equal to 100 or 0.01. The step-wise tests were performed at 27, 100, 200 and 300°C. To calculate the strain rate sensitivities in true stress – true strain coordinates a linear interpolation of each strain rate interval was performed.

The weld metals were studied using the internal friction (IF) technique. The IF specimens with typical size of about 0.5 × 2 × 35 mm were cut by an abrasive disc-saw from the 2 mm thick plates in longitudinal direction of the welds. All IF specimens were polished with emery paper down to 1200 grit to avoid surface effects. Temperature dependencies of internal friction Q^{-1} and natural frequency of the pendulum were measured in the temperature range from room temperature to 600 °C. The amplitude of the deformation in the torsion pendulum did not exceed 10^{-5}, and the natural frequency of the pendulum was changing in the range of 0.5–3.0 Hz. The heating rate of the specimens during IF measurements was kept at 2°C/min.

3.3 Results

3.3.1 Manifestations of DSA

Shifted segments of typical engineering stress-strain curves obtained for the weld metals of Alloy 182, 82, 152 and 52 at the strain rates of 10^{-5} and 10^{-6} s^{-1} and temperature of 300 ^{o}C are shown in Figure 62.

The tensile tests revealed that serrated plastic flow, which is one of the manifestations of DSA, is well established at 300^{o}C and strain rates of 10^{-5} and 10^{-6} s^{-1} in all the studied weld metals. From Figures 62 a and b, it is seen that serrations on stress-strain curves appear immediately when the plastic flow takes place. Development of serrated plastic flow with decreasing of strain rate from 10^{-5} to 10^{-6} s^{-1} can be observed from magnified parts of stress-strain curves on Figures 62 c and d. The serrated plastic flow observed at 10^{-5} s^{-1} corresponds to serrated flow of type A+B or A2+B according to previous studies on Alloy 600 [22–24], while at a strain rate of 10^{-6} s^{-1} the observed serrations conform to the well-known type B [33].

Fast Fourier transform (FFT) analysis was employed to obtain characteristic times between stress pulses on the flow stress signal from tensile tests, and to study the regularity of the observed serrated plastic flow. FFT spectra of the flow stress signal from CERT tests of the weld metals tested at the temperature of 300^{o}C and strain rates of 10^{-5} s^{-1} and 10^{-6} s^{-1} are shown in Figures 63 a and b, respectively. In the presence of mixed mode serrations of type A+B on the stress-strain curve at 300^{o}C and strain rate of 10^{-5} s^{-1}, two maxima at low and high values of frequency arise. Low frequency maxima are dominant in all the studied weld metals, Figure 63 a. When weld metals were strained at strain rate of 10^{-6} s^{-1}, Figure 63 b, from two to three well established maxima can be pointed out. Application of the Gaussian distribution to maxima of FFT spectra gives modal values of frequencies corresponding to characteristic times between stress oscillations shown in Figure 63. These characteristic times reflect repeated advancement of the Lüders band through the specimen.

The dependencies of strain rate sensitivity on flow stress in the temperature range of 27–300^{o}C were obtained by means of step-wise tensile tests for weld metal Alloy 182 and the base materials Alloy 600 and 690, Figure 64. Negative strain rate sensitivity is reported for the studied alloys at the temperatures where serrated flow was observed, which confirms that the serrated flow observed is caused by DSA.

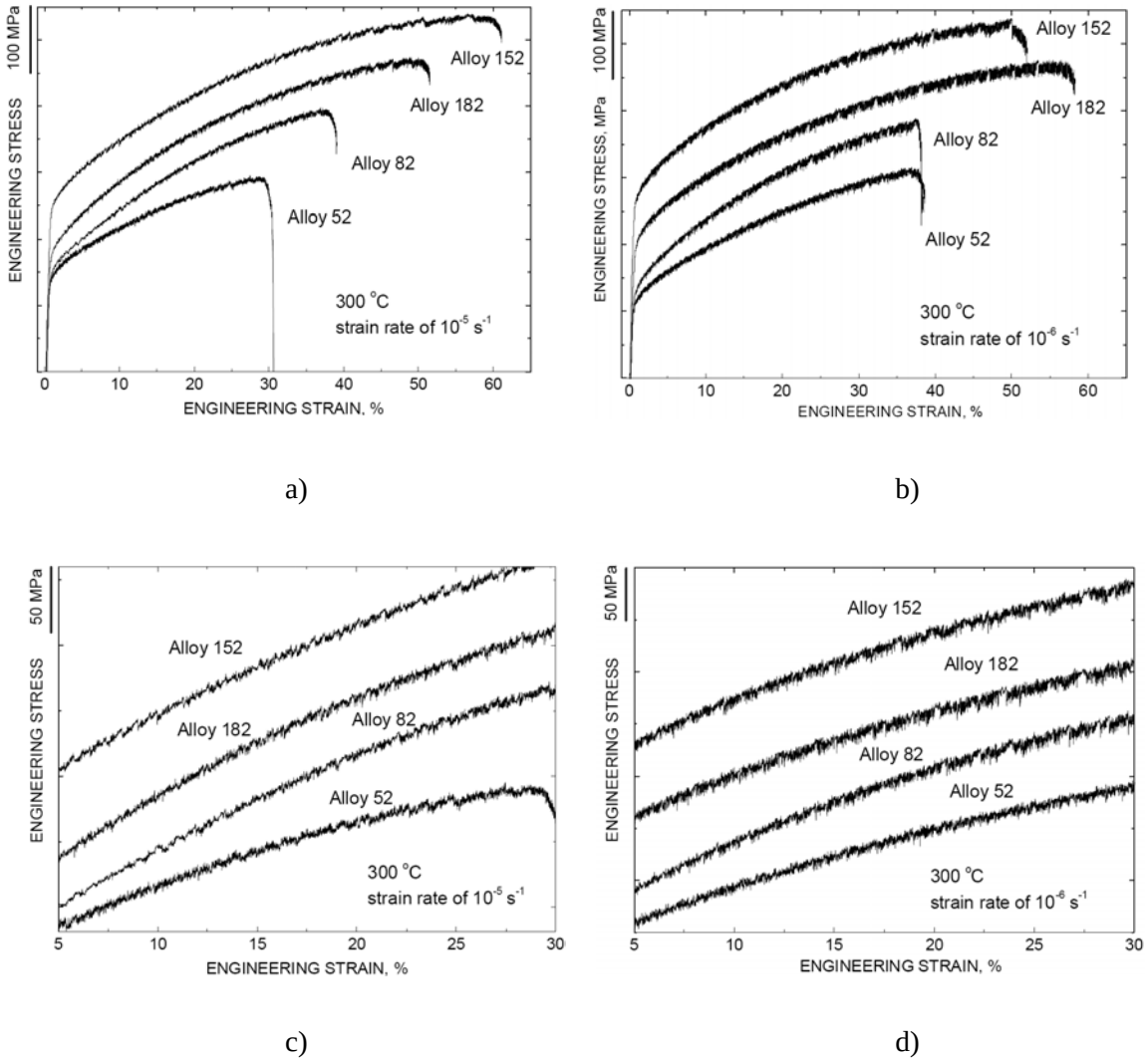

Figure 62. Shifted segments of engineering stress-strain curves obtained at 300°C and strain rate of 10^{-5} s^{-1} (a and c) and strain rate of 10^{-6} s^{-1} (b and d) for the weld metals Alloy 182, 82, 152 and 52. (c) and (d) are magnified parts of the engineering stress-strain curves showing serration appearance.

3. Dynamic strain aging (DSA) of nickel-base alloy weld metals

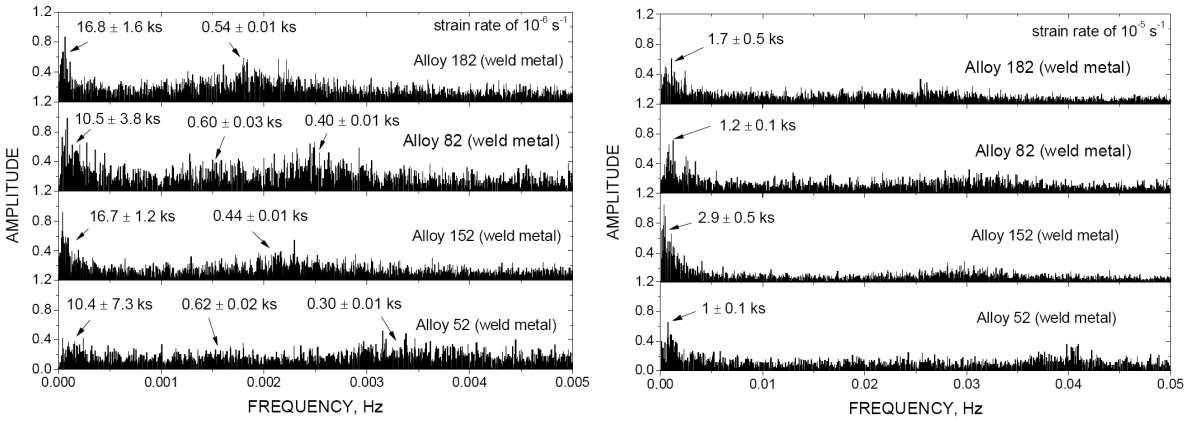

a) b)

Figure 63. Fourier transformation spectra of the flow stress signal from the tensile tests of the weld metals Alloys 182, 82, 152 and 52 strained at 300 °C and strain rate of 10^{-5} s^{-1} (a) and strain rate of 10^{-6} s^{-1} (b).

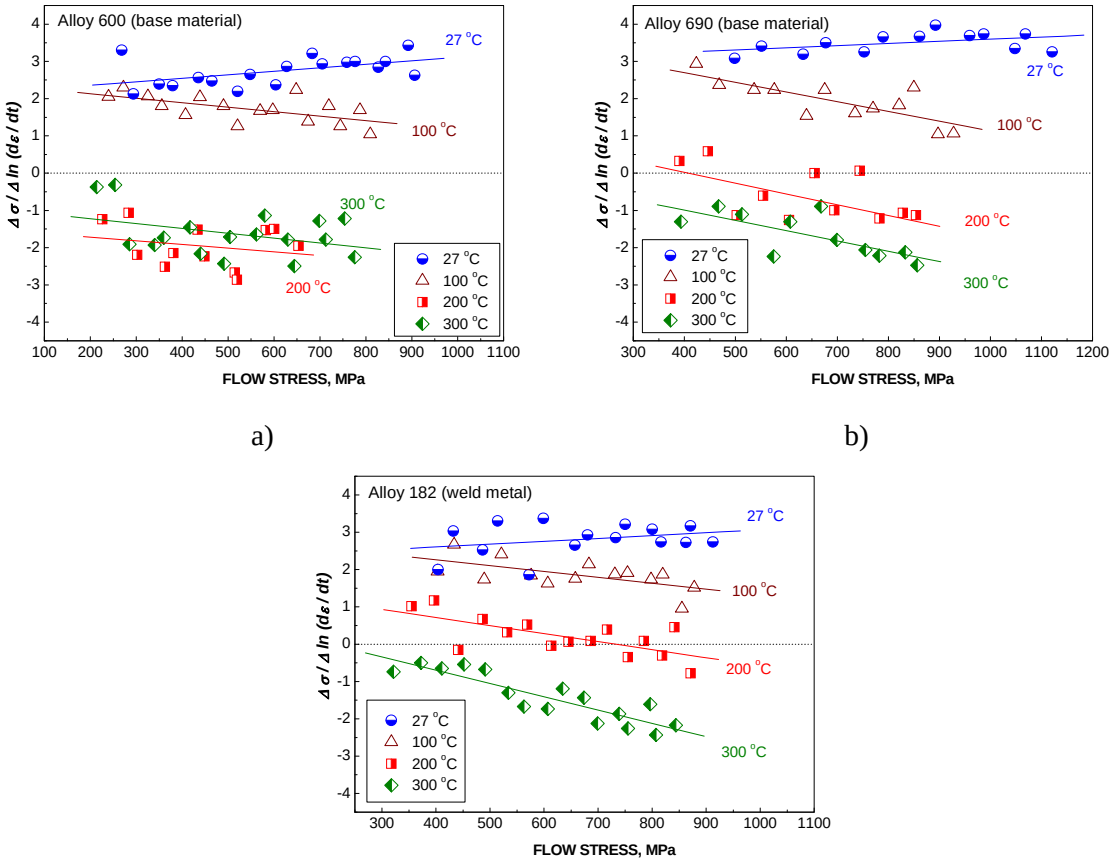

a) b)

c)

Figure 64. Dependence of strain rate sensitivity of base material Alloy 600 (a), base material Alloy 690 (b) and weld metal Alloy 182 (c).

In Figure 65, the dependency of the onset of DSA serrated flow on temperature and strain rate in weld metal Alloy 182 is compared to those of the base materials Alloy 600 and 690. The data summarizes the appearance of serrations on the stress-strain curves of the weld metal and the base materials at different strain rates and testing temperatures. In the figure, filled data points represent conditions where serrated flow was observed while open points indicate that no serrations were observed. The results of CERT tests performed at different temperatures and strain rates for Alloy 182 show that the appearance of DSA manifested by serrated flow fits well with the previously obtained map of the DSA appearance for the base materials Alloy 600 and 690.

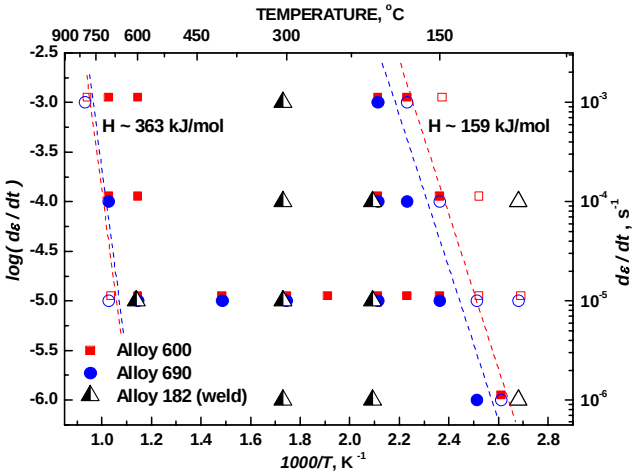

Figure 65. Dependence of the DSA serration appearance on temperature and strain rate for Alloy 600 and 690 shown by squares and circles, respectively. Data points shown by triangles correspond to weld metal Alloy 182. Filled data points correspond to strain rate and temperature values at which the DSA serrations occur on stress-strain curves and open points correspond to smooth flow. The dotted lines are the boundaries for the onset (or disappearance) of serrations.

3.3.2 Internal friction

Internal friction (IF) of the studied weld metals was mainly measured to check the presence of free interstitial carbon and nitrogen atoms in the crystal lattice. The Snoek-like IF peak is observed in FCC alloys with a maximum in the temperature range of 300–500°C, attributed to the relaxation process induced by re-distribution of interstitial carbon or nitrogen atoms in the solid solution [34]. It has been established that the height of the Snoek-like peak is proportional to amount of interstitial atoms that take part in the relaxation process [35]. Typical temperature dependencies of IF obtained for the weld metals Alloy 182, 82, 152 and 52 in the as-welded state are presented in Figure 66.

The carbon Snoek-like IF peak reported for Alloy 600, shown by dashed line in Figure 66, was not detected in the studied weld metals in the same manner as for Alloy 690 [25]. IF peak of small height with a maximum in the vicinity of -50°C was observed in all the studied weld metals except Alloy 52, and most probably corresponds to the Snoek-like IF peak induced by hydrogen, which was previously reported for hydrogen charged base material Alloy 600 [36].

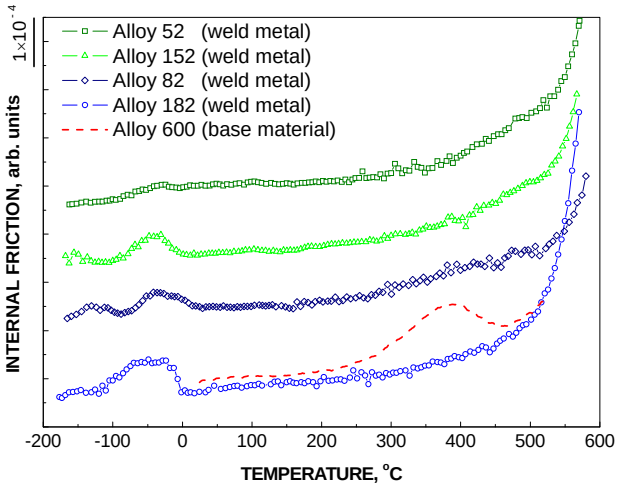

Figure 66. Temperature dependencies of internal friction for the weld metals Alloy 182, 82, 152 and 52 in as-welded condition and base material Alloy 600 in mill-annealed condition.

Pre-straining of the weld metal Alloy 182 to 5% of tensile strain at 27°C and 300°C, when DSA was evidenced by serrated flow, did not evoke carbon or nitrogen Snoek-like IF peak, Figure 67. The height of the hydrogen Snoek-like peak was slightly increased after pre-straining at 27°C, and a peak with the maximum in the vicinity of 100°C also arose, which is probably attributable to dislocation point defect interactions [36]. Pre-straining at 300°C and strain rate of 10^{-6} s^{-1} to 5% of tensile strain did not result in any pronounced peak except a minor hump where the peak attributed to dislocation point defect interactions was observed. The pre-straining at 300°C suppressed the hydrogen peak, due to hydrogen outgasing of the specimen during ~14 h exposure while pre-straining at 300°C.

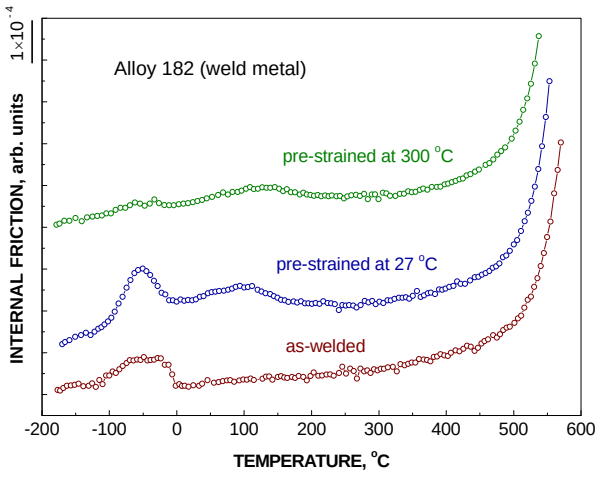

Figure 67. Effect of pre-straining to 5% of tensile strain at 27 and 300°C at strain rate of 10^{-6} s^{-1} on temperature dependencies of internal friction for the weld metal Alloy 182.

3.3.3 Mechanical properties

Yield strength, ultimate tensile strength, elongation to fracture and strain hardening coefficient for the studied weld metals tested at 27 and 300°C and different values of strain rate are summarized in Table 8.

Table 8. Summary of mechanical properties of the studied weld metals.

Weld metal	Strain rate, s^{-1}	Test temperature, °C	$R_{p0.2}$, MPa	R_m, MPa	A_t, %	n
Alloy 182	10^{-3}	27	376	637	40	0.47
Alloy 182	10^{-5}	300	307	610	51	0.55
Alloy 182	10^{-6}	300	309	587	58	0.56
Alloy 82	10^{-5}	27	389	590	26	0.42
Alloy 82	10^{-5}	300	303	558	39	0.51
Alloy 82	10^{-6}	300	260	518	38	0.53
Alloy 152	10^{-3}	27	385	648	48	0.50
Alloy 152	10^{-5}	300	252	544	61	0.58
Alloy 152	10^{-6}	300	297	570	52	0.51
Alloy 52	10^{-5}	27	390	562	38	0.41
Alloy 52	10^{-5}	300	333	486	31	0.38
Alloy 52	10^{-6}	300	228	441	39	0.54

3.4 Discussion

The type of serrated flow exhibited by the weld metals of this study, and the lack of a critical strain for the appearance of serrations in the stress strain curve at 300 °C and strain rates of 10^{-5} and 10^{-6} s^{-1}, conforms to the observations made previously for the corresponding base materials Alloy 600 and 690 [22–24]. The negative strain rate sensitivity observed for Alloy 600 and 690 and weld metal Alloy 182 at the temperatures where serrated flow was present on the stress-strain curves, confirms that the observed serrated flow is caused by DSA. A similar propagation of serrated flow with test temperature and strain rate, the same change in strain rate sensitivity, and a rather close characteristic times between stress pulses on the flow stress obtained by FFT analyses in the studied weld metals and their base materials, may suggest the same DSA mechanisms are occurring in these materials. At 300 °C DSA is attributable to the interaction of mobile dislocations with mobile interstitial carbon and nitrogen atoms [24, 25, 29]. Another supporting fact is that the appearance of DSA manifested as serrated flow in the weld metal Alloy 182 fits well with the previously obtained map of the DSA appearance for the base materials Alloy 600 and 690. One of the possible reasons for the absence of the carbon or nitrogen Snoek-like IF peak in the studied weld metals may be the low amount of free interstitial atoms (C and N) because of the formation of niobium and titanium carbides and nitrides. The weld metals Alloy 182, 82 and 152 contain niobium and Alloy 82 and 52 contain more titanium than the Alloy 600 and 690 base materials. Thus, the amount of interstitial carbon and nitrogen atoms in the solid

solution is not sufficient to be detected as a Snoek-like IF peak in these weld metals. The absence of the IF peak in the weld metals 152 and 52 can also be explained by the high chromium content, in the same manner as it has been explained for the base material Alloy 690 [24, 25]. The remaining part of interstitial carbon and nitrogen atoms, which are responsible for DSA, can be located in the interstitial sites with 6 Cr atoms at the vertices of an octahedron [37]. These interstitial atoms do not take part in the relaxation process, due to their cubic symmetry [38]. More detailed analyses of the Snoek-like peaks observed for Alloy 600 and 690 are reported elsewhere [24, 25].

Based on the mechanical test results of the studied weld metals, it seems that DSA does not significantly affect the studied mechanical properties, as the observed variation seems to be dependent mainly on the test sample, due to large variations in grain size and the presence of small weld defects, segregation and secondary phases. An effect of DSA on basic mechanical properties of the weld metals may be revealed more clearly by fracture mechanical testing.

One of the key parameters for classifying Ni-base alloys based on their susceptibility to IGSCC is their carbon content, and its distribution between solid solution and carbides. The beneficial effects of carbon in the solid solution on the resistance to IGSCC have been discussed in Refs. [39–41]. The influence of carbon was attributed to the improvement of the creep resistance by pinning of the mobile dislocations by carbon atoms and by delaying the recovery process of climb at the grain boundary thereby inhibiting grain boundary sliding and cavitation, thus, decreasing the creep rate. The conditions in the crack tip plastic zone, considering environmental effects in addition to DSA, were discussed in Refs. [39–41]. At the crack tip, oxidation reactions inject vacancies into the plastic zone and hydrogen uptake is also known to increase the local vacancy concentration [42]. Thus, metal vacancies at the crack tip plastic zone are most probably the key factor explaining the crack growth and controlling the crack tip strain rate, while DSA inhibits the plastic strain inside the plastic zone further away from the crack tip. The hardening effects from the DSA induce greater stress concentration at the crack tip by preventing the stress relaxation inside the plastic zone, which localizes the strain to the crack tip and increases the crack growth rate.

3.5 Conclusions

Dynamic strain aging (DSA) was observed for weld metals Alloy 182, 82, 152 and 52 at temperature of 300°C and strain rates of 10^{-5} and 10^{-6} s^{-1}. Serrated flow was analysed by standard fast Fourier transform analysis and characteristic times of abrupt changes of stress were obtained. The characteristic times of the weld metals were compared with those obtained for the corresponding base materials Alloy 600 and 690. Dependencies of strain rate sensitivity on flow stress in the temperature range of 27–300°C were obtained by means of step-wise tensile tests for weld metal Alloy 182 and the base materials Alloy 600 and 690. Negative strain rate sensitivity was reported for the studied alloys at the temperatures where serrated flow was observed, confirming that the serrated flow is caused by DSA. Internal friction studies revealed no detectable IF peak attributed to free interstitial carbon or nitrogen atoms in the FCC lattice of the studied weld metals, in the same manner as it was reported for base material Alloy 690. Pre-straining of weld metal Alloy 182 to 5% of tensile strain at 27°C and at 300°C did not evoke the IF peak either. A study of Alloy 182 by CERT tests in the temperature range of 27–

600°C at strain rates of 10^{-3}–10^{-6} s^{-1}, showed that the appearance of DSA manifested by serrated flow fits well with the previously obtained map of the DSA appearance for the base materials Alloy 600 and 690.

4. Environment-assisted crack initiation in doped steam test

The Ni-base alloy dissimilar metal welds are typically made using Alloy 182 and Alloy 82. Recently Alloy 52 has been used both in new constructions as well as in repair welding. The trend towards alloys with higher contents of chromium is driven by the observed environment-assisted cracking (EAC) in Alloy 182, and recently also in Alloy 82. One driving force towards the more EAC resistant alloys is also the challenges and costs related to non-destructive examination of dissimilar metal welds in nuclear power plant applications.

A limited amount of laboratory EAC test results is available for the new material combinations of dissimilar metal welds of nuclear power plants. A test has been developed to enhance cracking of Ni-base alloys and their weld metals at 400°C in hydrogenated steam doped with sodium sulphate, fluoride and chloride. According to Staehle and Gorman [43], the initiation time of low potential stress corrosion cracking (LPSCC) follows monotonic 1/T dependence from hydrogenated steam to water. This suggests that the mechanistic processes in water and steam are the same, at least for pure water. As crack initiation takes a very long time (years or decades) in actual LWR water at relevant operating temperatures, the accelerated tests have been conducted at 400°C in steam doped with hydrogen, chloride, sulphate and fluoride.

Jacko et al. [44] performed an accelerated laboratory test series in an environment consisting of hydrogenated 400°C steam doped with fluoride, chloride and sulphate anions. Comparison tests were performed using Alloy 600 and Alloy 182 weld metal. Alloy 52M welds, prepared to simulate the Ringhals 4 field repairs of the reactor pressure vessel outlet nozzle, exhibited complete resistance to stress corrosion crack initiation in laboratory exposure times exceeding 45 effective full-power years (EFPYs) equivalent service times. Stress corrosion cracks initiated in Alloy 182 welds in exposure times less than one-fifth of the total exposure time of the Alloy 52M specimens. Crack initiation was also observed in specimens of Alloy 600 CRDM nozzle material in the doped steam environment. The specimens used by Jacko et al. [44] were prepared as flat plates and they were bolt loaded in specially designed four-point bending fixtures. Analysis indicated that the degradation observed after 89000 effective full-power hours (EFPHs) at 317°C in Ringhals 4 was duplicated with 289 h exposure at 400°C to sulphate, chloride and fluoride doped hydrogenated steam. This translates to an acceleration factor of 308. For other temperatures Jacko et al. [44] adjusted the acceleration factor using an activation energy of Q = 55 kcal/mole. The activation energy was estimated by assuming an Arrhenius type dependence for cracking probability between Alloy 600 in Ringhals 4 and Alloy 600 in laboratory

tests at 400 °C in doped steam [45]. The approach of Jacko et al. [44] with some modifications was adopted for this investigation.

4.1 Doped steam test set-up

The crack initiation tests were performed in steam at 400°C and 150 bar. The steam was generated from de-ionized O_2 free water doped with 30 ppb SO_4^{2-} (added as Na_2SO_4), 30 ppb F^- (added as NaF) and 30 ppb Cl^- (added as NaCl). The target value for H_2 partial pressure was 0.56 bar, which, according to the Ellingham diagram, represents the Ni-NiO equilibrium at this temperature and steam pressure. The steam pressure was maintained using a high performance liquid chromatography (HPLC) pump feeding replacement water to the autoclave operated under constant pressure mode. The H_2 partial pressure was measured using a Pd-membrane sensor inside the autoclave. The H_2 partial pressure was controlled by a West 6100 PID controller connected to the pressure sensor and a high pressure solenoid valve connected to the tube between the autoclave and the hydrogen bottle. The autoclave temperature was controlled using a West 6100 PID controller and a commercial K-type thermocouple. A schematic picture of the test configuration is shown in Figure 68.

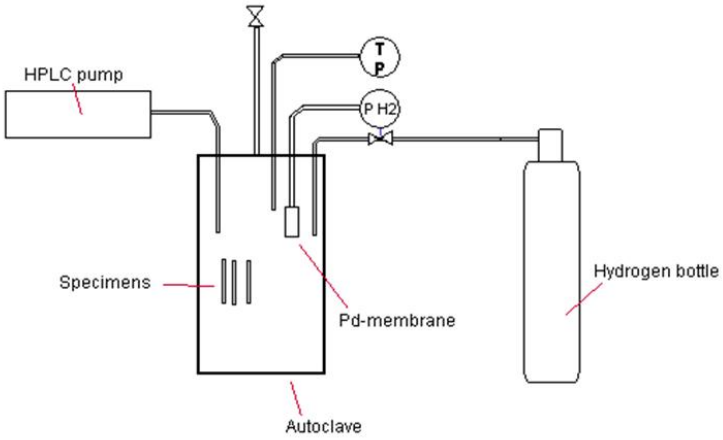

Figure 68. A schematic picture of the test equipment configuration [46].

The test implementation was performed as follows:

- the specimens were washed in de-mineralized water and ethanol,
- the specimens were installed into the autoclave,
- autoclave lid was closed,
- air was replaced by N_2 (pressure was raised to 3 bar, autoclave was emptied through a valve, and this cycle was repeated 10 times),
- the autoclave was heated to the test temperature,
- the autoclave was de-pressurized,

- doped water feeding was started,
- when the steam pressure was 150 bar, hydrogen feeding was started,
- 400 ^{o}C/150 bar steam pressure/0.56 bar H_2 pressure was maintained until the exposure time was complete,
- the temperature was decreased to room temperature,
- at the room temperature, the autoclave gases were replaced by N_2,
- the autoclave was opened, specimens were taken out and washed in de-mineralized water and ethanol,
- liquid penetrant test was performed for the specimens and the indications were inspected with an optical microscope.

4.2 Specimens for doped steam testing

The specimens were prepared by plane milling. A mechanical polishing by 600 grit emery paper was performed after milling in order to remove the roughness of the specimen surfaces. The specimens were bolt-loaded in four-point bend loading. Strain was calculated from the bending radius of a 3.5 mm thick plate and the target strain for the specimens was 1.1%. The total time of exposure is 2178 h performed in 240–250 h steps. In the earlier tests [5, 6] of dissimilar metal welds, the strain was calculated from the bending radius of a 3 mm thick plate and the nominal target strains for the specimens were 0.35 and 1%. The longest total time of exposure then was 1460 h, Table 9. The specimens were investigated repeatedly after each exposure step using a stereo microscope and liquid penetrant testing. All liquid penetrant indications were further studied using stereo and scanning electron microscopes. Some cracks were opened and specimens were sliced in order to study the crack propagation paths in the microstructure.

Four different dissimilar metal welds were studied. The weld geometries contained nickel-base weld metals Alloy 152 (mock-up TU1), 52 (mock-up TU2), both 52 and 152 (mock-up TU3), 182 (mock-up TV1) and of Alloy 182, 82, 152 and 52 pure weld metals i.e. all weld metals simulating weld repairs or overlays, Figure 69.

Table 9. Doped steam crack initiation test results of the previous study [5, 6].

Specimen code	Orien-tation	Strain, %	Total exposure time, h	First LP indication, h	Crack locations (post-test microscopy examination)	Number of cracks	Max. crack length, mm
TU1-1	T	1[a]	1460	507[b, d]			
TU1-2	T	0.35[a]	1460				
TU1-3	T	1	1172.5				
TU1-4	T	1	1172.5	734.5 [d]			
TU1-5	L	0.35	1460				
TU1-6	L	0.35	1460	507[b, d]			
TU1-7	L	1	1172.5	219.5[b, d]			
TU1-8	L	1	1172.5	734.5 [d]			
TU2-1	T	0.35	1460				
TU2-2	T	0.35	1460				
TU2-3	T	1	1172.5	219.5[b]	Weld	3	0.3
TU2-4	T	1	1172.5	455.5	Weld	1	3
TU2-5	L	0.35	1460	507[b, d]			
TU2-6	L	0.35	1460	1022 [d]			
TU2-7	L	1	1172.5	734.5	Weld	3	0.4
TU2-8	L	1	1172.5	219.5[b]	Weld	2	0.15
TU3-1	T	0.35	1460	507[b, d]			
TU3-2	T	0.35	1460	743	Weld	1	1
TU3-3	T	1	1172.5	219.5[b]	Weld, 52 butter	2	0.5
TU3-4	T	1	1172.5	734.5	52 butter	1	0.4
TU3-5	L	0.35	1460	507[b]	Weld	2	2
TU3-6	L	0.35	1460	743 [d]			
TU3-7	L	1	1172.5	219.5[b]	Weld	1	2
TU3-8	L	1	1172.5				
TV4-1	T	0.35	1460	1460	Weld, butter	>10	5
TV4-2	T	0.35	1460	1460	Weld, butter	>10	8
TV4-3	T	1	1172.5	734.5	Base (I600), weld, butter	>10	9
TV4-4	T	1	1172.5	219.5[b]	Base (I600), weld	>10	15
TV4-5	L	0.35	1460	743	Base (I 600), weld, butter	>10	1
TV4-6	L	0.35	1460	1460	Weld, butter	>10	1.5
TV4-7	L	1	1172.5	734.5	Base (I600), weld, butter	>10	4
TV4-8	L	1	1172.5	1172.5 [d]			
TV4K-1	T	1	438				
TV4K-2	T	1	438	438 [d]			
TU1C1	T	0.01 mm[c]	953	Not relevant			
TU2C1	T	0.01 mm[c]	953	Not relevant			
TU3C1	T	0.01 mm[c]	953	Not relevant			

[a] The specimen pair TU1-1 and TU1-2 was bent unevenly.
[b] Liquid penetrant test performed for the first time.
[c] Crack mouth opening displacement (CMOD).
[d] No cracks observed in microscopy examination.

The mock-up specimens were 80 x 15 x 3.5 mm^3 plates cut from the root side of the welds. The specimen dimensions and cutting location are shown schematically in Figure 70 (mock-up TU2 weld as an example). The dissimilar metal weld was in the middle of the specimen with its orientation transverse to the longitudinal axis of the specimen (see welding parameters in Hänninen et al. [5, 6]). The test

block welding procedure for pure weld metal specimens is shown in Figures 70–72 and the test samples (80 x 15 x 3.5 mm^3 plates as well as the mock-up specimens) were cut so that the pure weld metal was transverse in the middle of the sample, Figure 72.

Some of the specimens were thermally aged in order to simulate long term (~30–50 years) exposure to the operating temperature of 325°C. The ageing was performed in the same autoclave where the doped steam testing was performed. The ageing temperature was 420°C and the duration was 2000 h. The specimens were protected from oxidation by an N_2 gas atmosphere.

The specimens with hot cracks were produced by Varestraint testing with an augmented strain of 4%. Then the samples were cut so that either the dissimilar metal weld or the pure weld metal was transverse to the loading axis.

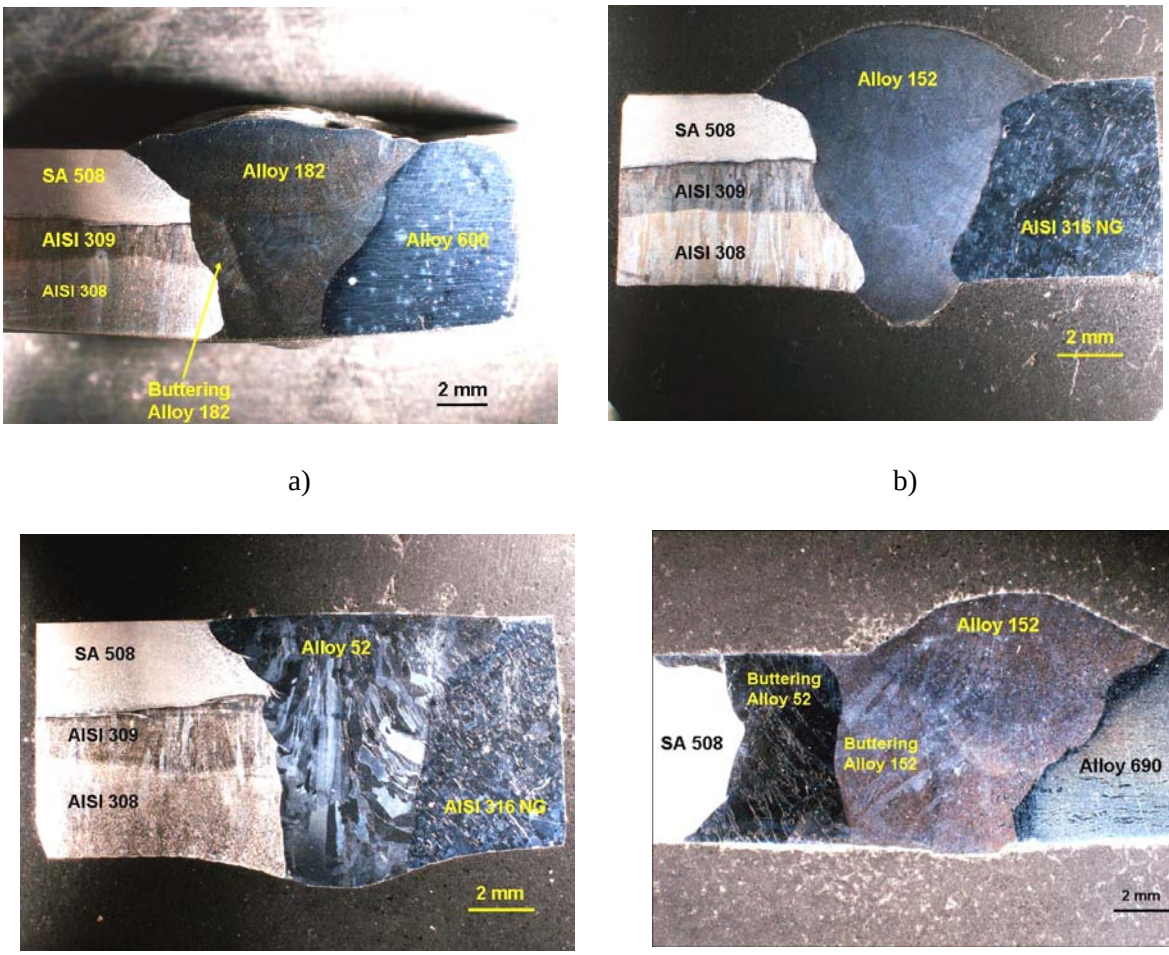

Figure 69. Materials and cross-sections of a) mock-up TV1, b) mock-up TU1, c) mock-up TU2 and d) mock-up TU3 dissimilar metal welds.

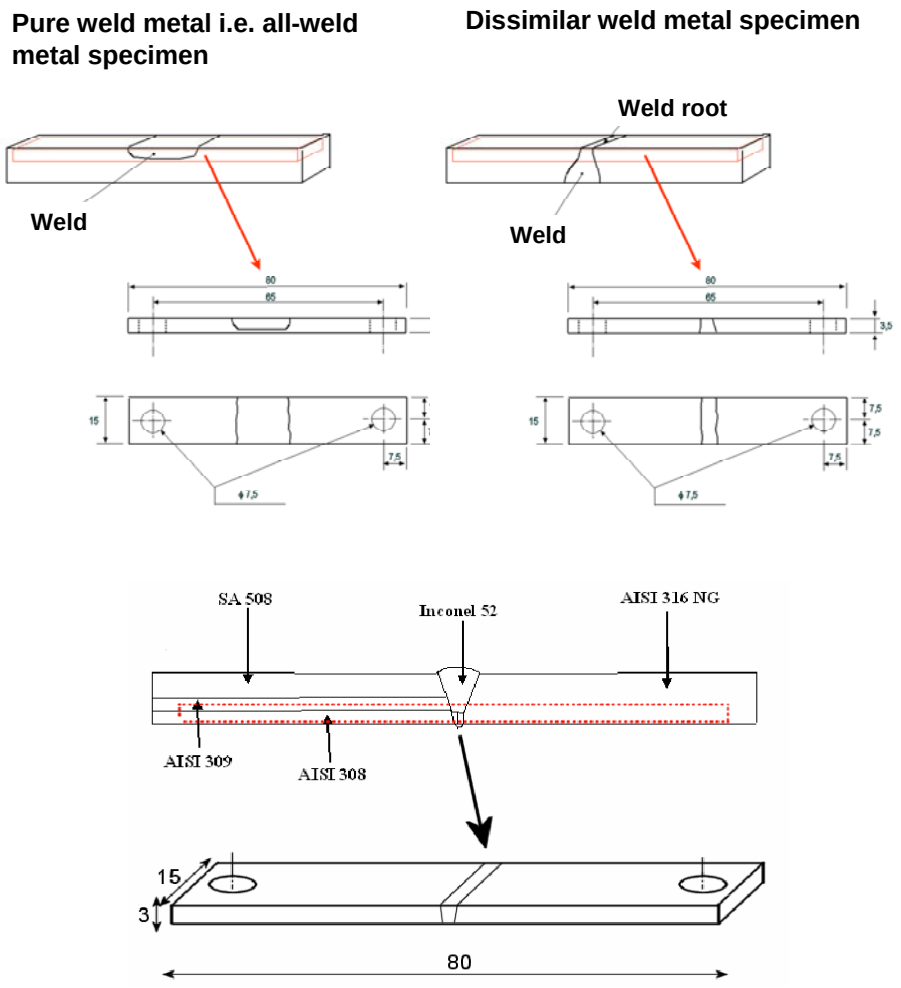

Figure 70. Schematic EAC specimen cutting location (transverse orientation) and specimen dimensions.

The specimens containing hot cracks were then loaded under an optical stereomicroscope until the crack mouth opening of some of the cracks was in the range of 0.02 mm. Higher loading would have resulted in strain localization and kinking of the specimens. The test surface containing the hot cracks produced by Varestraint testing was not machined at any point after welding. These specimens were also thicker than the mock-up and pure weld specimens, i.e., in the range of 4.5 mm.

Three specimens (in parenthesis in Table 10) showed cracks visually after being left loaded in air for a few days before their exposure to the doped steam. These specimens were not exposed in the doped steam tests, and subsequent metallographic study revealed large slag inclusions that most likely caused the cracking in air under the pre-load (see Figures 31 and 32, weld defects).

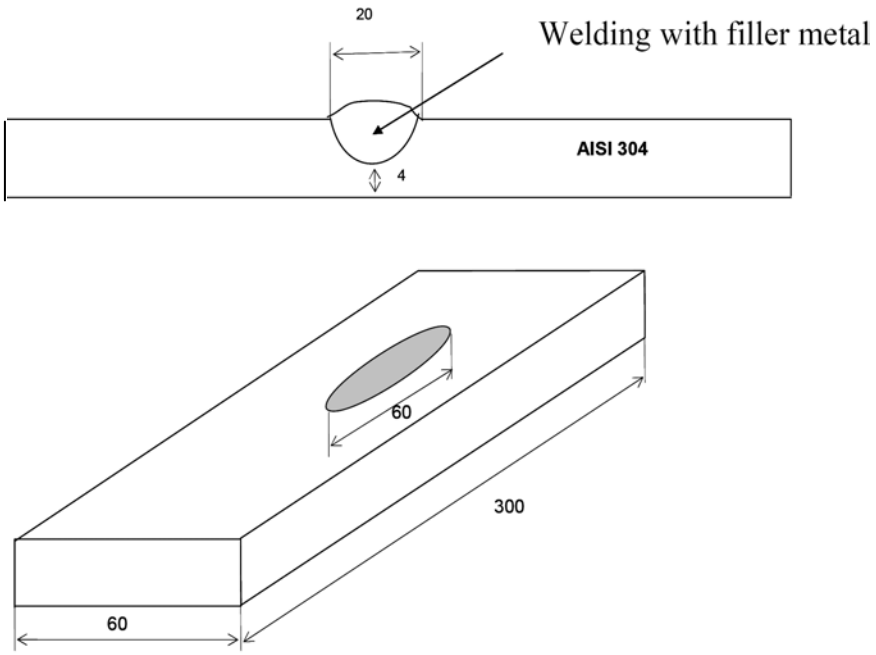

a)

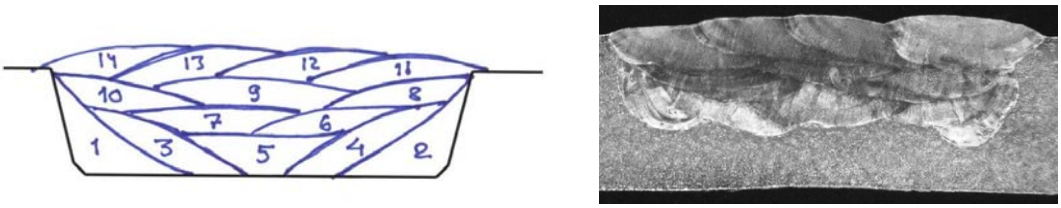

b)

Figure 71. Test piece of pure weld metals (plain) a) and b) weld pass sequence of the test specimen welded with Alloy 82 filler metal.

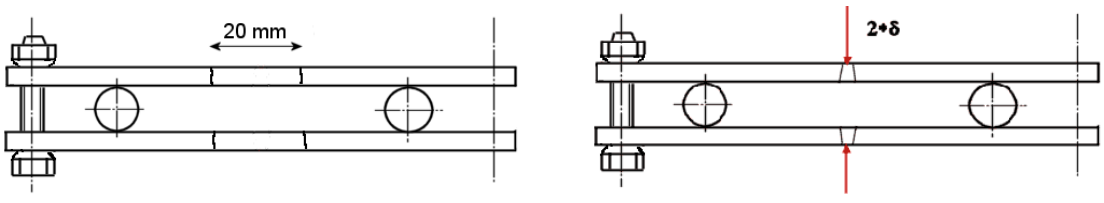

a) b)

Figure 72. Loading geometry with displacement measurement location indicated by two red arrows of pure weld metal (a) and dissimilar weld metal mock-up (b) samples.

Table 10. Test matrix and test results after 2178 h testing.

Spec. No. /spec. ID	Weld	Heat treatment	Strain, %	Time to cracking, h
1-4 / P182	182 (plain)	-	1,1	750/750/240/750
5-6 / P182A	182 (plain)	Aged	1,1	750/750
7-10 / P82	82 (plain)	-	1,1	240/240/240/240
11-12 / P82A	82 (plain)	Aged	1,1	750/240
13-16 / P152	152 (plain)	-	1,1	-/-/-/-
17-18 / P152A	152 (plain)	Aged	1,1	-/-
19-22 / P52	52 (plain)	-	1,1	-/-/-/-
23-24 / P52A	52 (plain)	Aged	1,1	-/-
25-(26) / TU1A	TU1	Aged	1,1	-/(-)
27-28 / TU2A	TU2	Aged	1,1	-/-
29-30 / TU3A	TU3	Aged	1,1	990/-
(31)-32 / TVA	TV1	Aged	1,1	(-)/750
33-(34) / NA	Neste /5/	Aged	1,1	-/(-)
35 / P182C	182 (plain)	Hot cracked	CMOD ~0.02 mm	-
36 / P82C	82 (plain)	Hot cracked	CMOD ~0.02 mm	-
37 / P152C	152 (plain)	Hot cracked	CMOD ~0.02 mm	-
38 / P52C	52 (plain)	Hot cracked	CMOD ~0.02 mm	-
39 / TU1C	TU1	Hot cracked	CMOD ~0.02 mm	-
40 / TU2C	TU2	Hot cracked	CMOD ~0.02 mm	-
41 / TU3C	TU3	Hot cracked	CMOD ~0.02 mm	-
42 / TV4C	TV4	Hot cracked	CMOD ~0.02 mm	-
43 / TV1C	TV1	Hot cracked	CMOD ~0.02 mm	-

Aged = thermal ageing at 420°C for 2000 h, represents ~ 50 years at 325°C.

4.3 Results from doped steam testing

The first samples from the doped steam testing were cracked already after the first exposure period (240 h). After about 480 h and 750 h testing time the pure weld metal Alloy 82 samples and Alloy 182 samples, respectively, have cracked completely (see examples in Figure 73 and 74). The test results are shown in Table 10.

The cracks were in the middle of the welds in pure Alloy 82 and 182 weld metal specimens, except for one case in which the cracking took place in the diluted zone of the weld metal ~1–2 mm from the fusion line. In the Alloy 182 weld mock-up (specimen No. 32) the crack was also in the middle of the

fusion weld (i.e., not in the buttering weld). The small weld defects on the sample surfaces were not initiating the EAC cracks in any of the Alloy 182 or 82 samples.

No crack extension was observed on the outer surfaces of the specimens in any of the hot cracked specimens after about 2178 h total exposure time. After test termination the largest hot cracks were opened for fractography, and their cross-sections were prepared for metallography of the corrosion products inside the hot cracks, and determination of possible extension of the hot cracks by an EAC mechanism. A liquid penetrant indication was observed in one TU3 mock-up specimen (Alloy 52 + 152 buttering and Alloy 152 fusion weld) (see Table 10). The indication was at the interface of the Alloy 52 weld butter and SA 508 low alloy steel. This was discovered to be an artefact resulting from the edge of the thick oxide layer on the low alloy steel.

Detailed fractography of broken pure Alloy 182 and 82 specimens showed that the outer surface and fracture surface were covered with an oxide layer. However, on the fracture surface a metallic Ni film formed on the top of the oxide layer, and covered the fracture surface almost completely close to the outer surface, Figure 75 and Figure 76. In the middle of the fracture surface the formation of NiO was also observed as small particles growing laterally on the oxide covered surface, together with larger Fe-rich spinel oxide particles (Figure 76). Close to the crack tip no metallic Ni or NiO was observed, and the fracture surface was covered only by a thin Cr-rich oxide layer. In the cross-sections of the cracks the intergranular propagation of the fracture is clear (Figure 82).

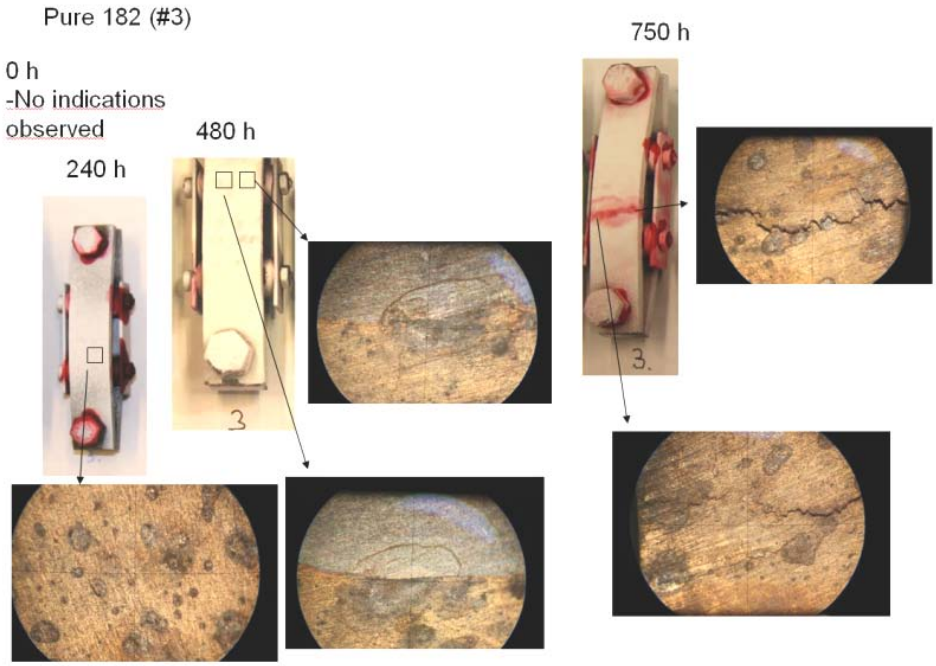

a)

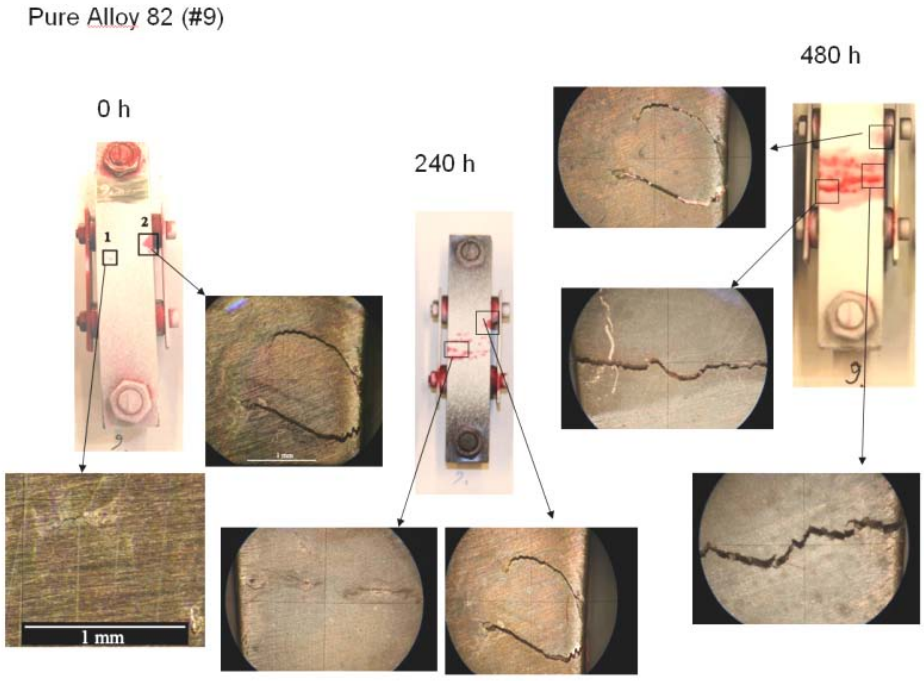

b)

Figure 73. Pure Alloy 182 (specimen No. 3) (a) and pure Alloy 82 (specimen No. 9) (b) cracking after various exposure times. Note that neither in Alloy 182 nor in Alloy 82 the opened weld defects do not grow further and final fracture takes place in the middle of the specimens.

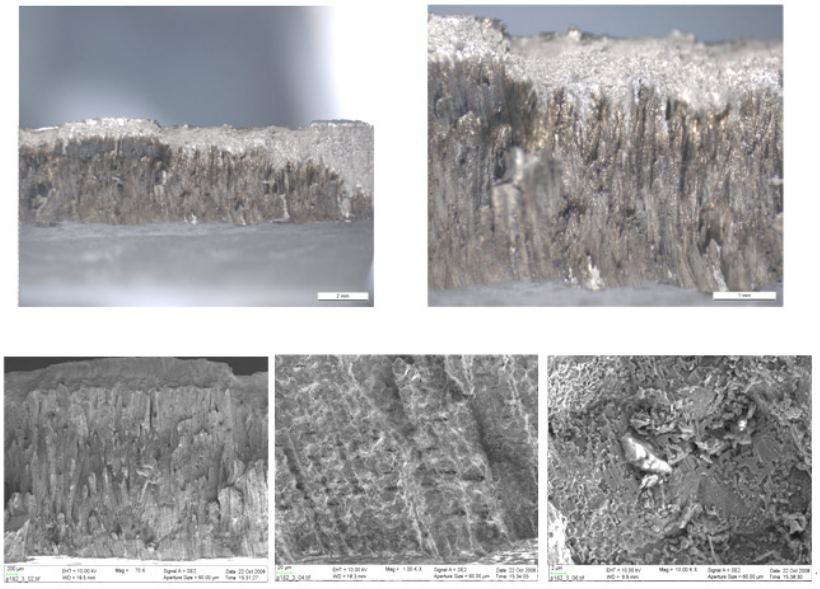

a)

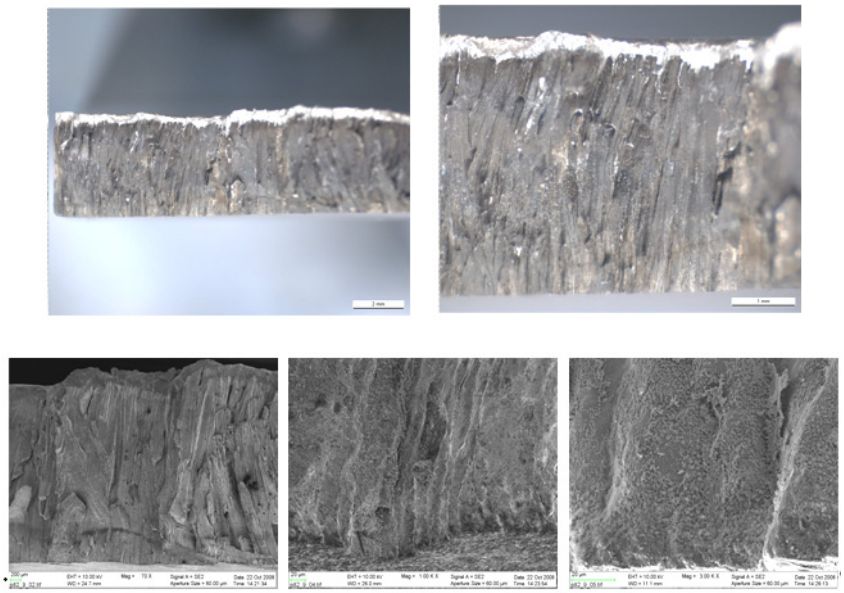

b)

Figure 74. Pure Alloy 182 (specimen No. 3) (a) and Alloy 82 (specimen No. 9) (b) fracture surface after 750 h and 480 h exposure time, respectively.

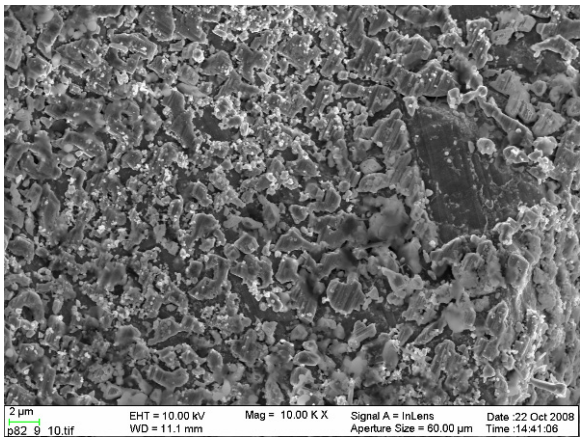

a)

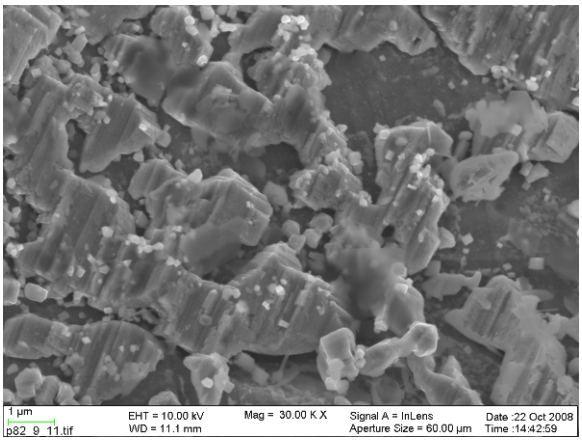

b)

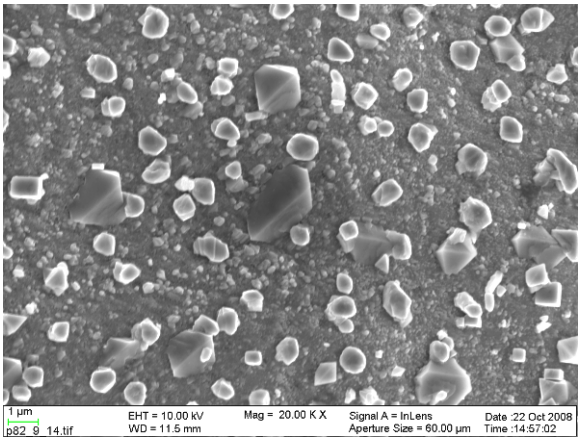

c)

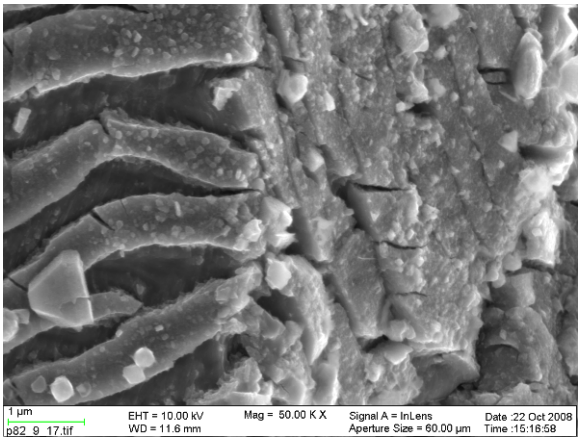

d)

Figure 75. Pure Alloy 82 (specimen No. 9) fracture surface after 480 h exposure time. (a and b) Metallic Ni deposit layer close to the crack mouth. (c) NiO and Fe-rich spinel oxide particles on the fracture surface close to the crack tip. (d) Cracked Cr-rich oxide film due to bending the crack open at the crack tip.

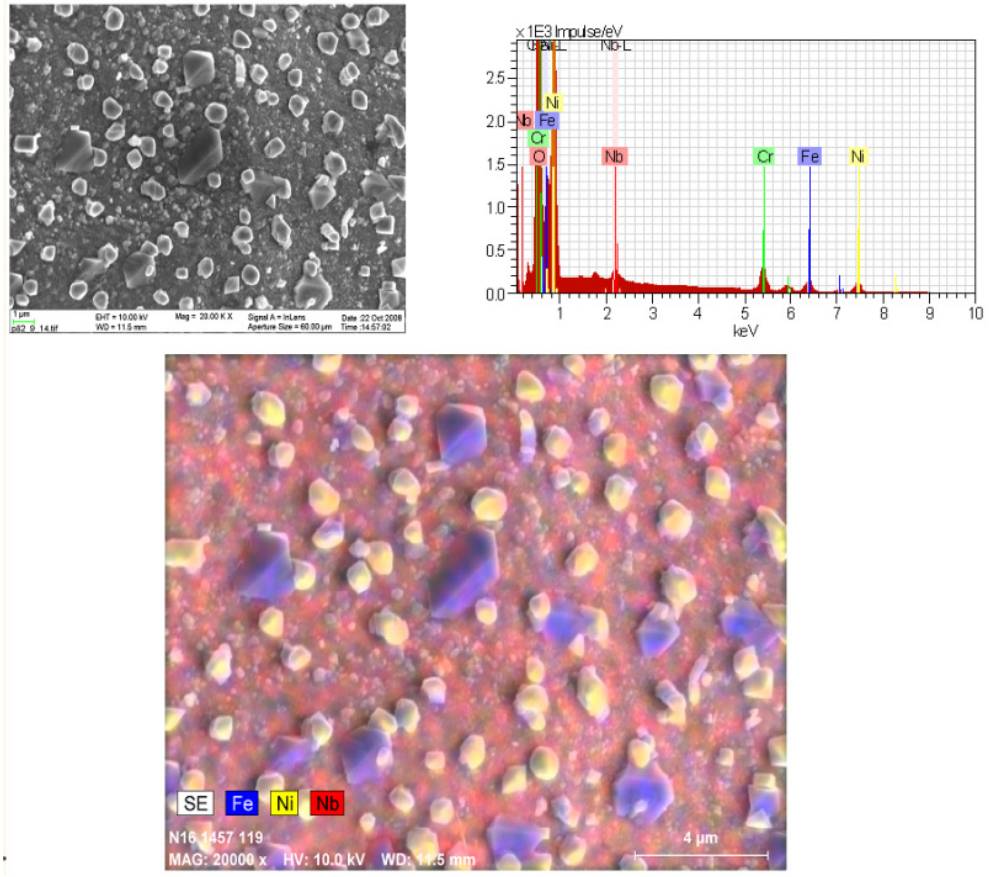

Figure 76. Chemistry of the particles on the fracture surface close to the crack tip of Alloy 82 specimen No. 9.

In order to analyse the thicknesses of the various films forming inside the cracks and on the outer surfaces of the specimens cross-sections of the cracked samples were made. Figures 77–82 show details of these cross-sections indicating that the metallic Ni film is in the middle of the cracks extending almost up to the crack tip. The metallic Ni deposit in the middle of the crack is surrounded on both sides by a Cr-rich oxide layer which grows into the metal matrix and extends to the crack tip. During the oxide growth nickel diffuses through the Cr-rich oxide film and deposits on the top of the Cr-rich oxide layer as metallic Ni. Typical for Alloy 182 are the Nb-rich phases along the dendrite boundaries. However, the Nb-rich phase does not seem to dissolve quickly in these test conditions as shown by Figure 80. The Nb-rich phases are closely connected to the hot cracking behaviour of Nb-alloyed Ni-base alloy weld metals and this observation may explain why hot cracks of Alloy 182 and 82 are not preferably extending during EAC testing.

Metallic Ni-deposits are also forming in the fine scale inside the Cr-rich oxide films on the outer surface of the specimens, Figure 81. Additionally, on the outer surface larger metallic Ni deposit particles are present. Inside the Cr-rich oxide film metallic Ni deposits form spike like structures in areas of deeper penetration of the oxide film into the metal matrix.

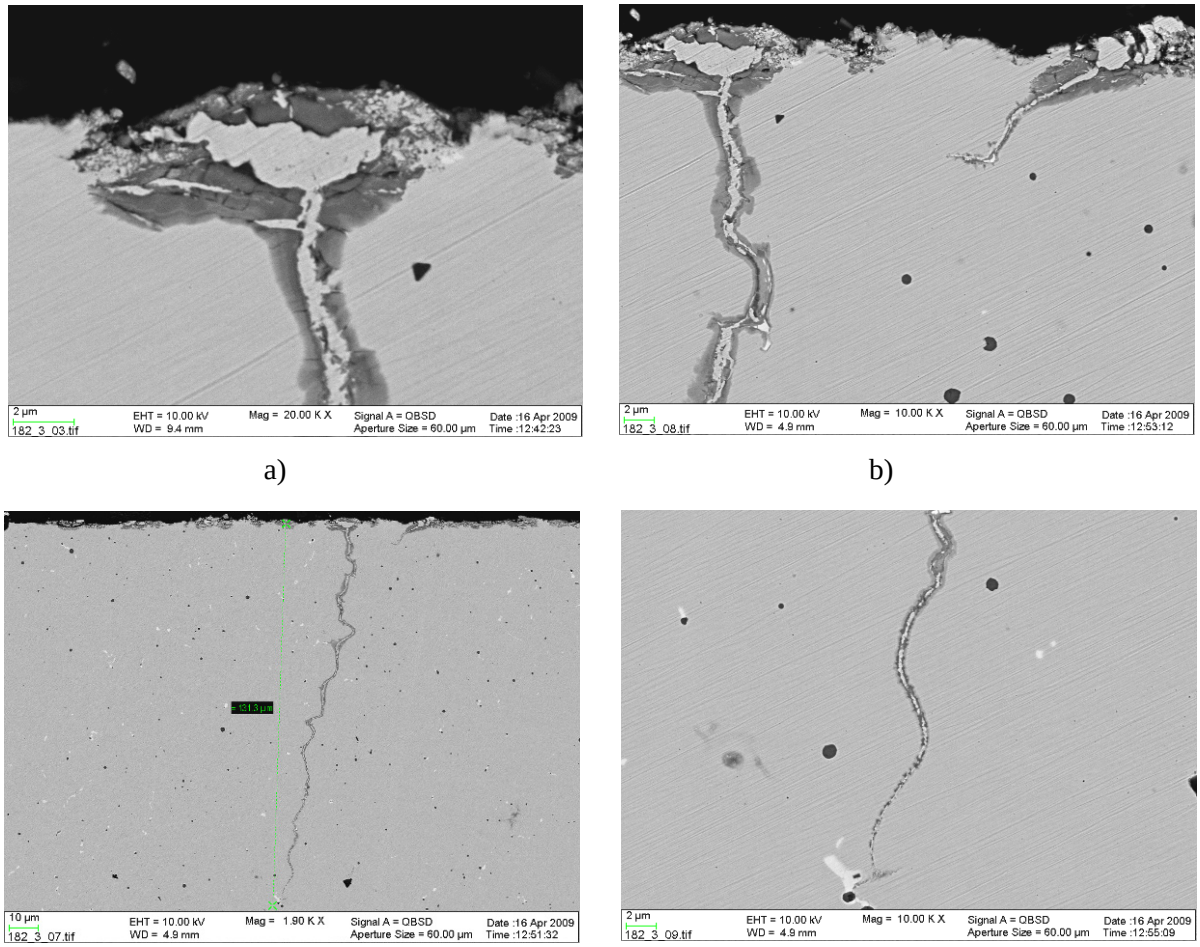

Figure 77. Cross-section of a crack in Alloy 182 pure weld metal specimen No. 3. Note the formation of metallic Ni deposit layer in the middle of the crack surrounded by Cr-rich oxide layers on both sides. The metallic Ni deposit layer extends almost up to the crack tip in (d).

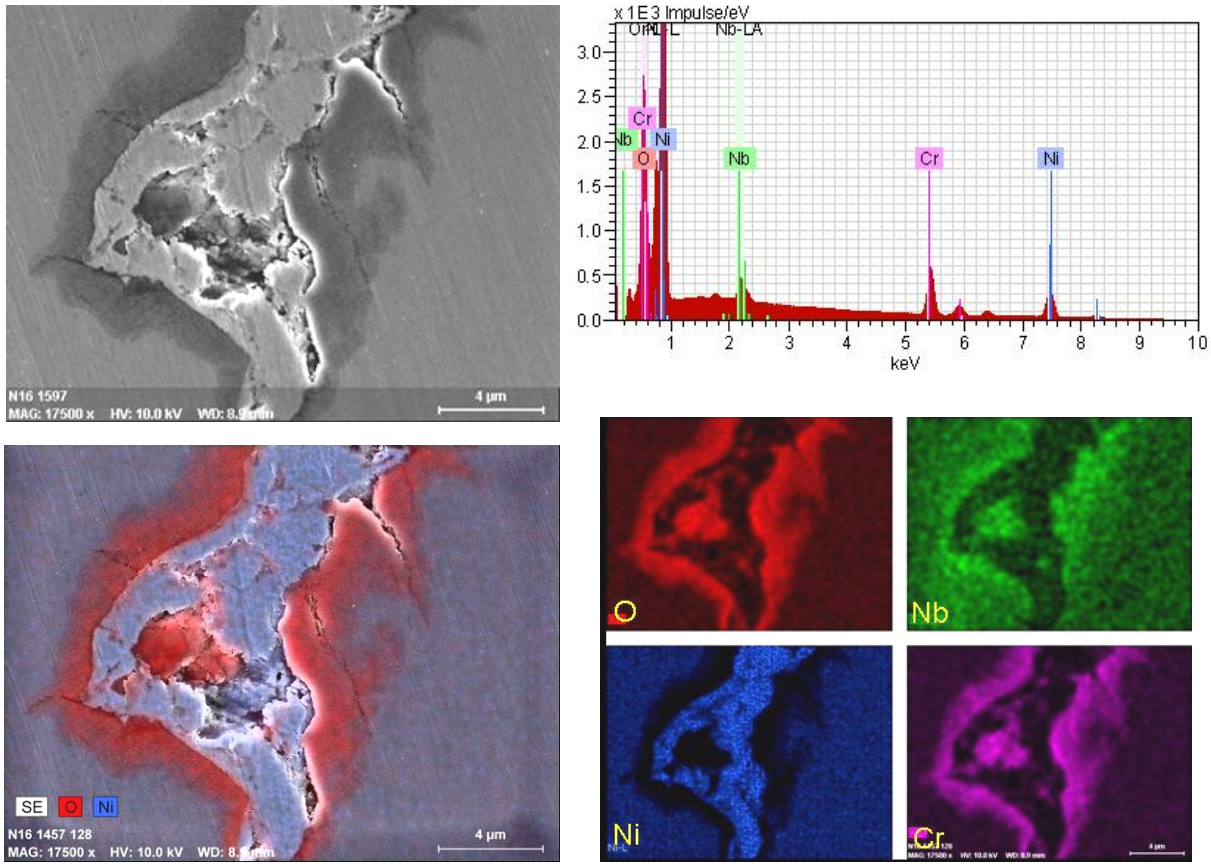

Figure 78. Detail of the cross-section of a crack in Alloy 82 pure weld metal specimen No. 9. Note the formation of metallic Ni deposit layer in the middle of the crack surrounded by Cr-rich oxide layers on both sides. The metallic Ni deposit layer seems to be porous and very brittle.

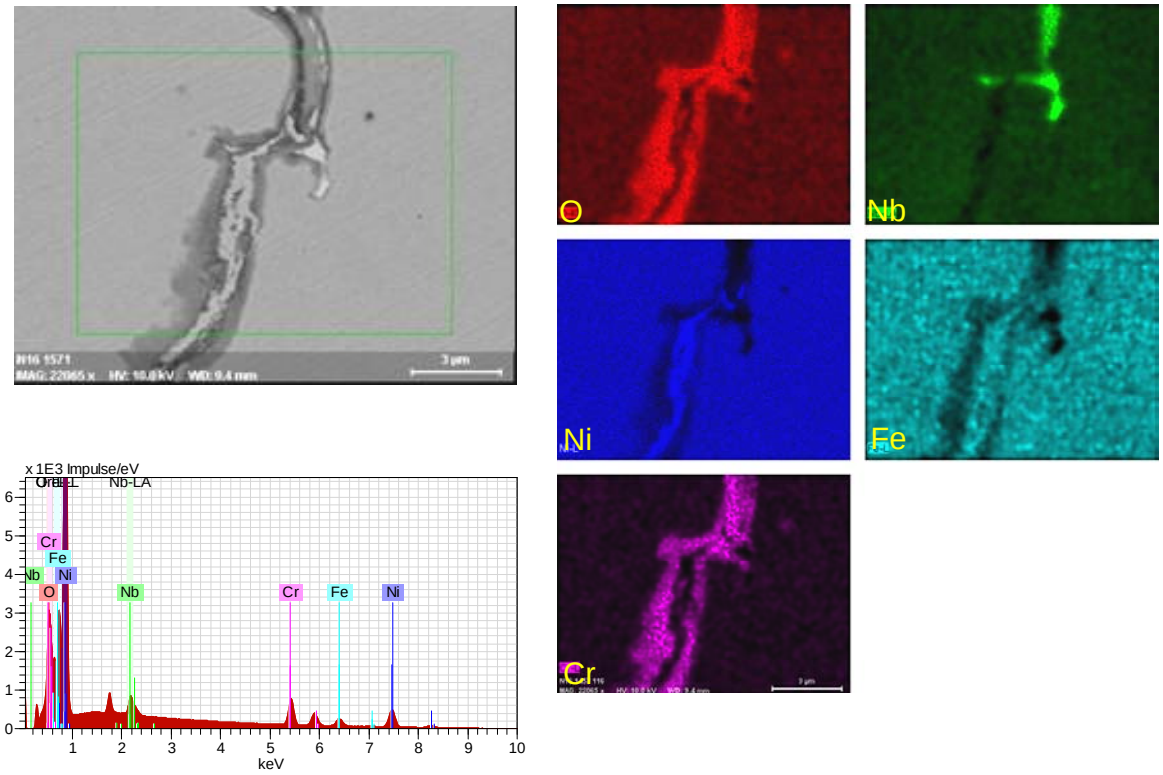

Figure 79. Detail of a cross-section of a crack in Alloy 182 pure weld metal specimen No. 3.

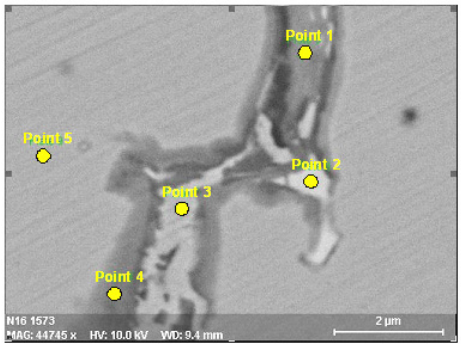

Element	Si	Cr	Mn	Fe	Ni	Nb	O	Ti
Point 1 (wt.-%)	0,9	4,1	24,4	13,4	5,7	35,1	15,2	-
Point 2 (wt.-%)	-	7,2	2,6	3,9	2,5	78,4	-	2,3
Point 3 (wt.-%)	-	-	-	-	94,2	-	5,8	-
Point 4 (wt.-%)	1,5	21,5	11	9,7	40,5	2,6	11,6	-
Point 5 (wt.-%)	1	16,3	9,3	13,3	57,4	1,7	-	-

Figure 80. EDS point analysis of Alloy 182 pure weld metal specimen No. 3. Note the formation of metallic Ni deposit layer in the middle of the crack surrounded by Cr-rich oxide layers on both sides. Point 2 represents the Nb-rich phase typical for Alloy 182 weld metal which has not oxidized during the crack growth. However, in Point 1 Nb- and Mn-rich oxide is present representing another type of Nb-rich phase, which is oxidized.

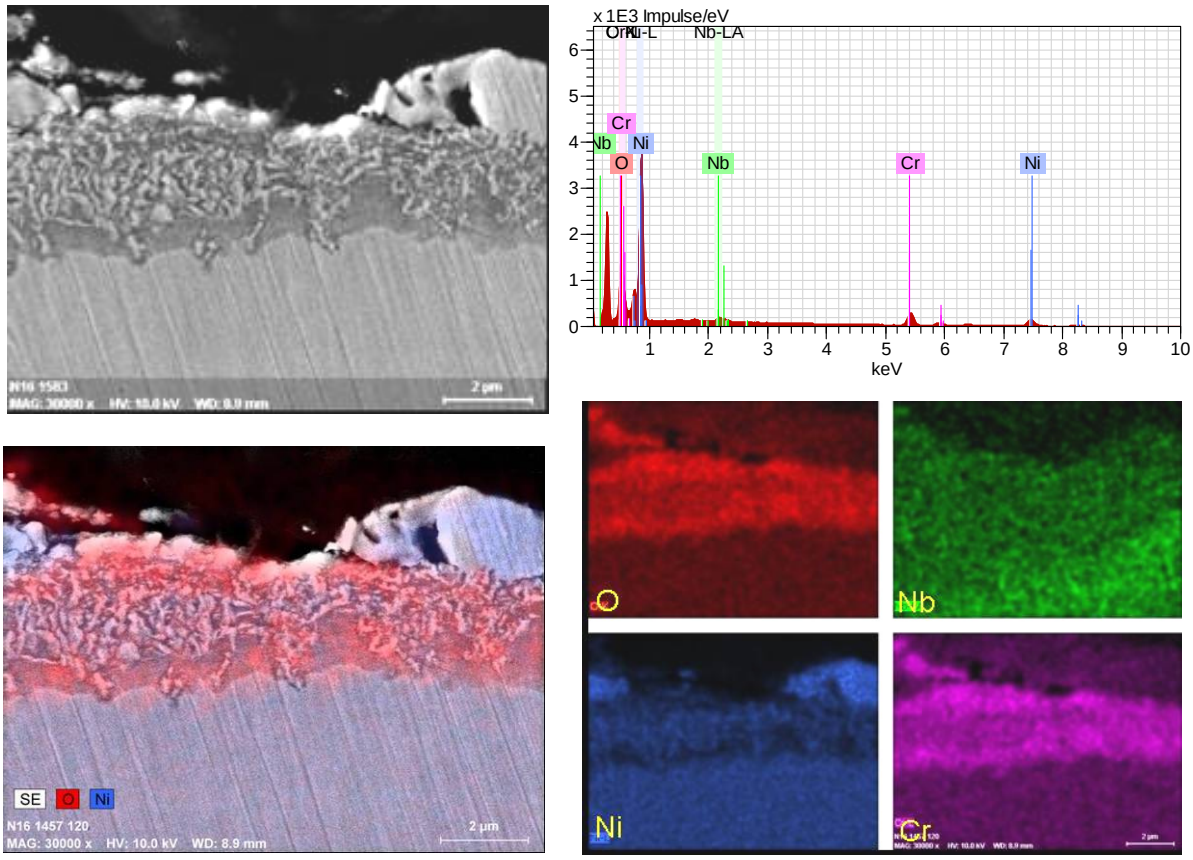

Figure 81. Detail of a cross-section of the outer surface oxide film on cracked Alloy 82 pure weld metal specimen No. 9. Note the formation of fine metallic Ni deposits inside the Cr-rich oxide layer.

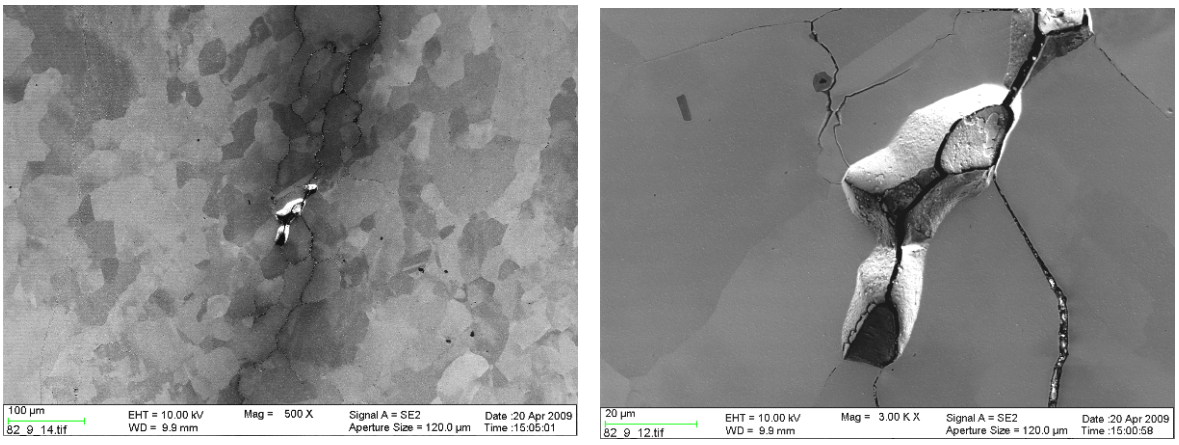

a) b)

Figure 82. Cross-section of a crack in Alloy 82 pure weld metal specimen No. 9. Note the fully inter-granular propagation of the cracks.

In Alloy 182 and 82 samples, even after various exposure times, the opened small weld defects did not grow further, and the EAC crack initiation and the final fracture took place in the middle of the specimens without any observable weld defect interaction (Figure 73). Figure 83 shows that the same was also true for the aged Alloy 82 samples. Alloy 152 and 52 samples also showed small weld defects that opened enough under loading to give small liquid penetrant test indications. None of these small indications were observed to grow during the autoclave testing, and nor did either alloy show any signs of EAC crack initiation in the durations of exposures carried out, Figure 84.

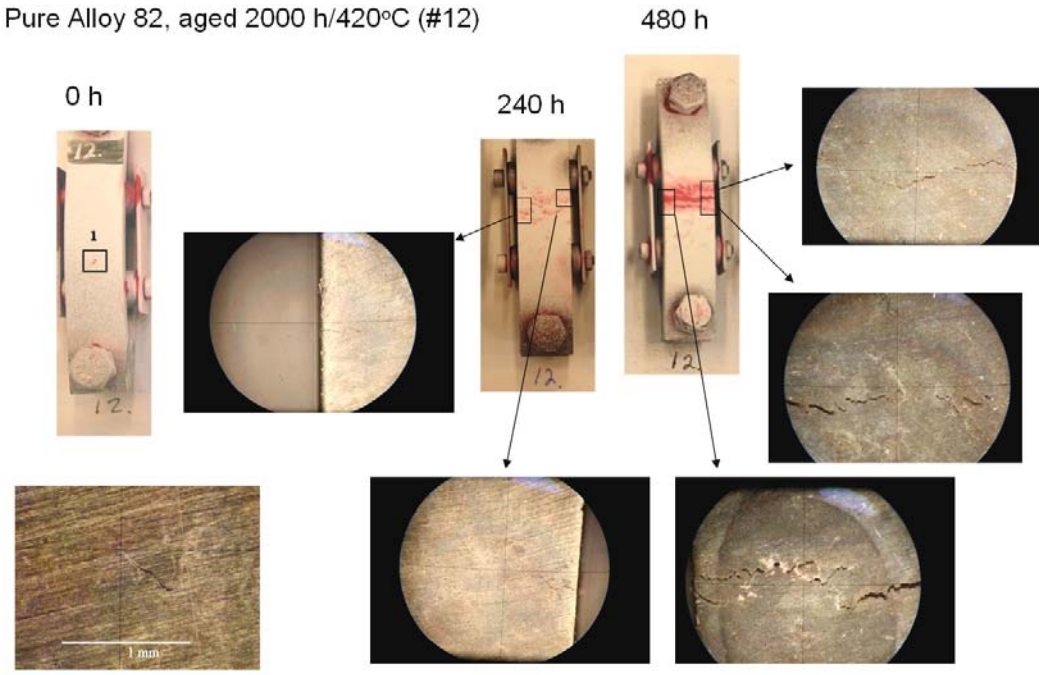

Figure 83. Aged (2000 h/420°C) pure Alloy 82 (specimen No. 12). Cracking after various exposure times was not related to the small weld defects. Note that the opened weld defect did not grow further, and final fracture took place in the middle of the specimen.

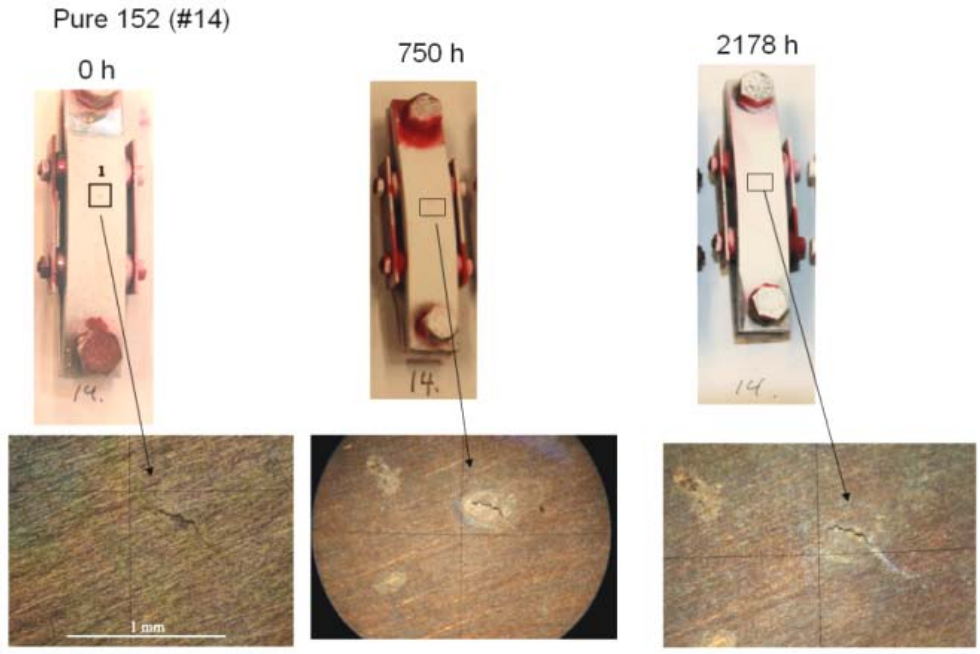

a)

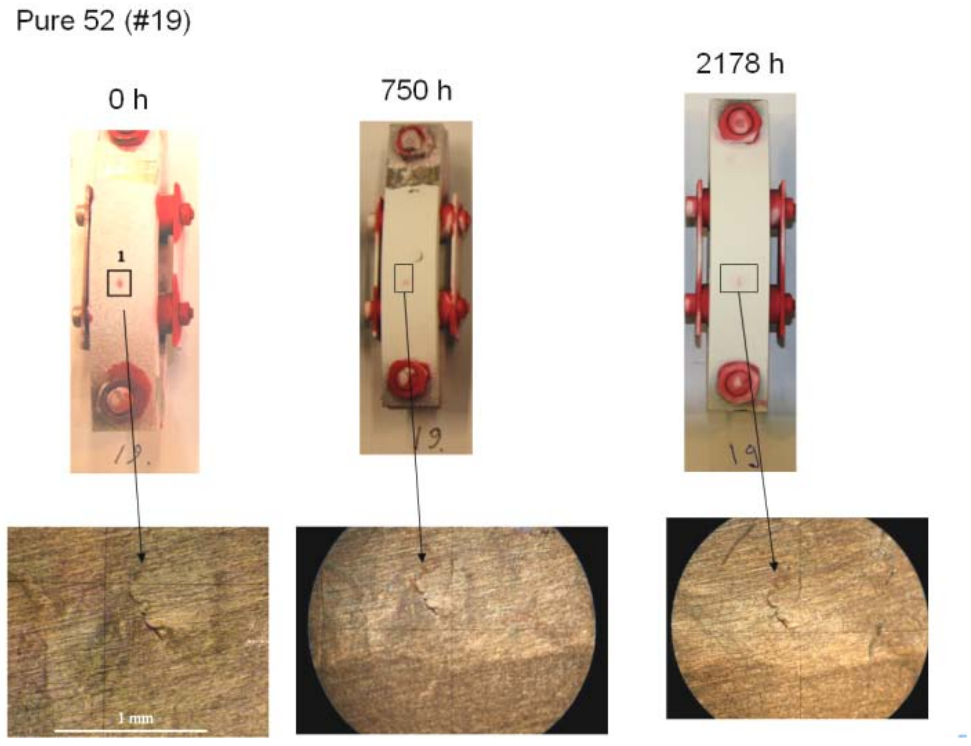

a)

Figure 84. Pure Alloy 152 (specimen No. 14) (a) and pure Alloy 52 (specimen No. 19) (b) after various exposure times. Note that in neither Alloy 152 nor Alloy 52 did the opened small weld defects grow any further, nor did the alloys show any EAC crack initiation after any of the exposure times.

Effects of hot cracks on EAC crack initiation and growth in the studied nickel-base alloy weld metals were studied according to Table 10. Crack extension on the outer surface was monitored during the test interruptions, and at the end of the 2178 h exposure test the largest hot cracks were opened for fractography and their cross-sections were prepared for metallography of the corrosion products inside the hot cracks, and possible extension of the hot cracks by an EAC mechanism. Figure 85 shows the hot cracks before the exposure and after certain exposure time (750 h) to doped steam. No crack extension was observed on the outer surfaces in any of the hot cracked specimens after 2178 h total exposure time. Figures 86–92 show the sample surfaces after test termination, and the cross-sections of the samples as well as the fractography of the largest hot cracks. In all samples, inside the hot cracks porous metal debris was observed that was obviously related to the final melt that solidified inside the opening hot cracks, and mainly dropped to the hot crack tip area. This porous debris showed almost the same chemical composition as the weld metal, and did not show marked oxidation (only a thin Cr-rich oxide film was present on the debris as well as on the hot crack surfaces). Only in one case was local selective oxidation observed inside the hot cracks, as shown in Figure 88 b, where selective dissolution of Ni has taken place and Cr and Mn have enriched in the oxide phase. Typical for the hot crack samples was that in all the weld metals in addition to solidification cracking, marked liquation cracking had occurred below the weld bead where the hot cracks were intended to form. When the cracks were opened for fractography, it was clear that no EAC type of crack extension was present in any of the studied specimens at their hot crack tips. In the Alloy 152 sample some of the hot cracks terminated in areas of extensive Laves phase formation, but here also no crack extension by EAC was observed, Figure 88 c.

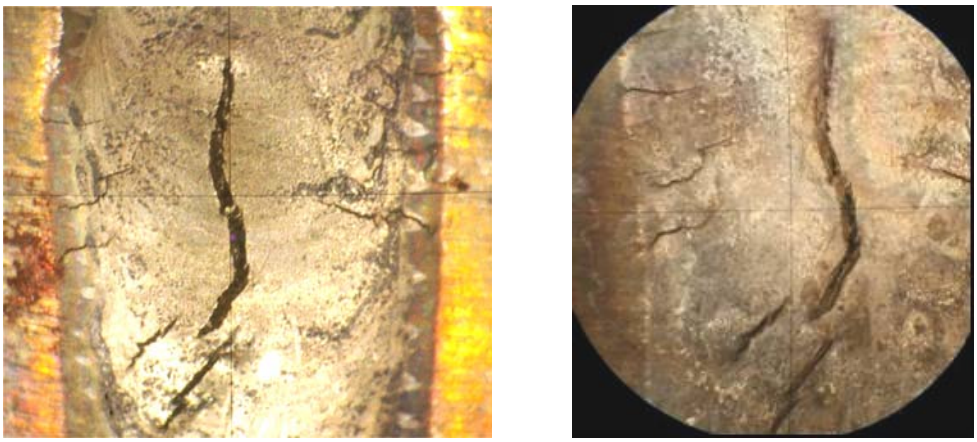

a)

4. Environment-assisted crack initiation in doped steam test

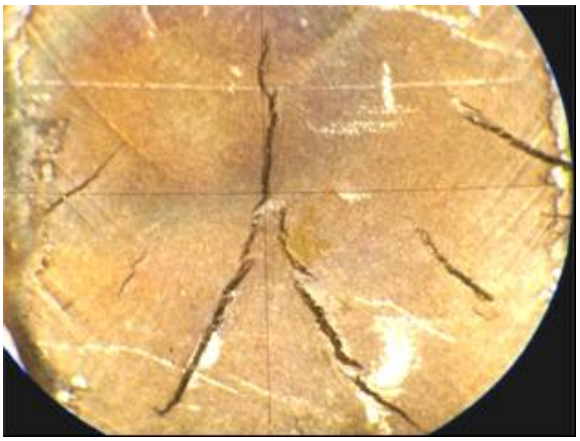

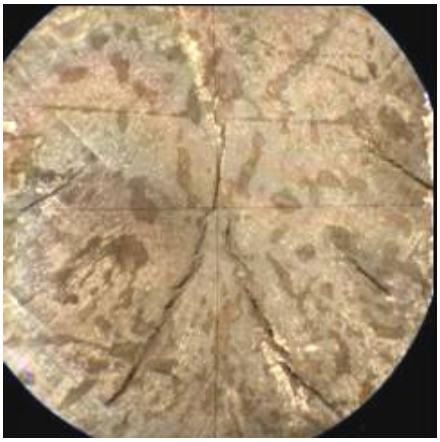

b)

c)

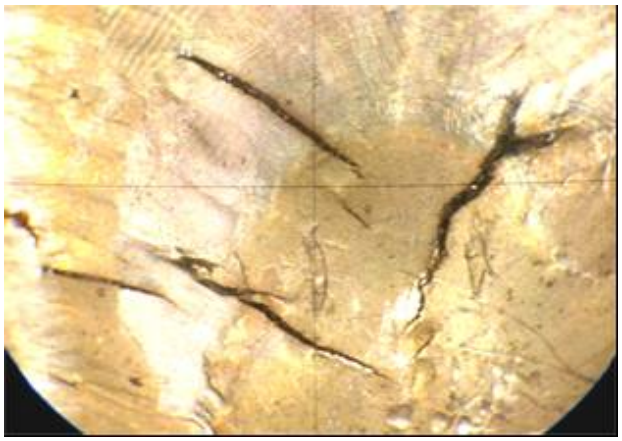

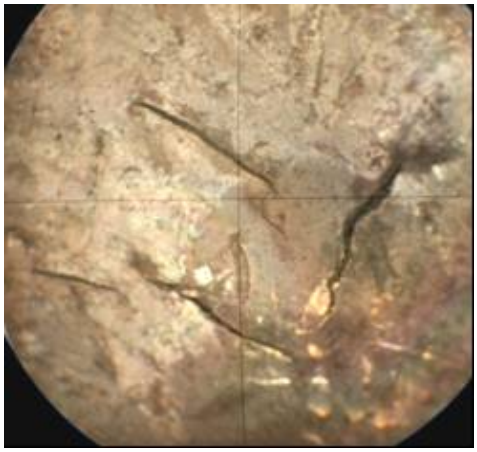

d)

Figure 85. Pure alloy welds after hot cracking in Varestraint test and after 750 h testing in doped steam. a) Alloy 182 (specimen No. 35), b) Alloy 82 (specimen No. 36), Alloy 152 (specimen No. 37), and d) Alloy 52 (specimen No. 38).

a)

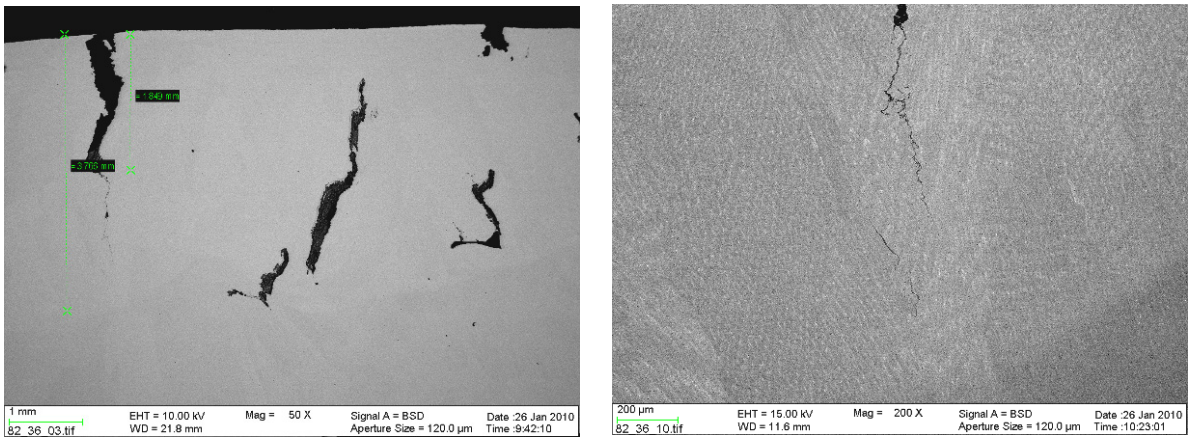

b)

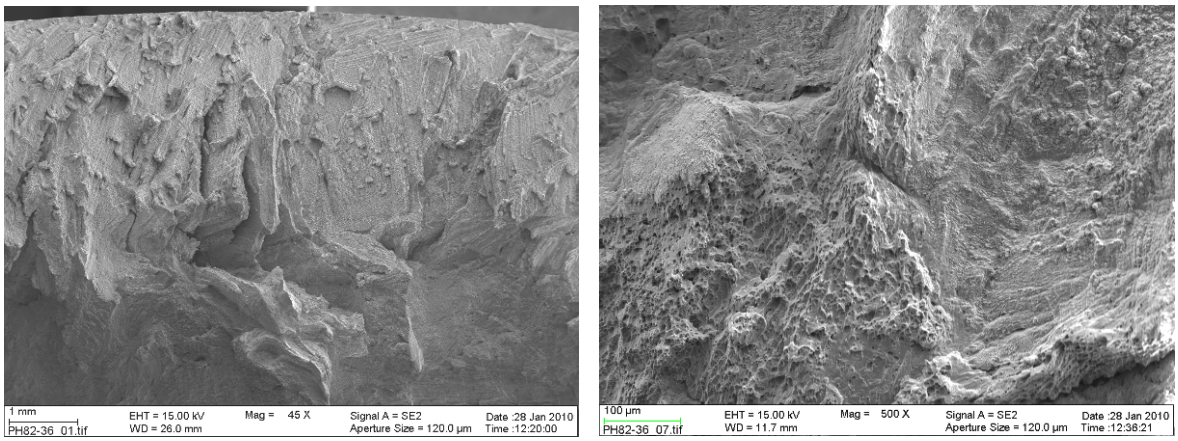

c)

Figure 86. Pure Alloy 82 weld (specimen No. 36) after hot cracking in the Varestraint test and subsequent exposure in doped steam for 2178 h. a) Outer surface and cross-sections of the main hot cracks. b) Cross-sections of the hot cracks and liquation cracking below the weld bead. c) Fracture surface of the opened hot crack.

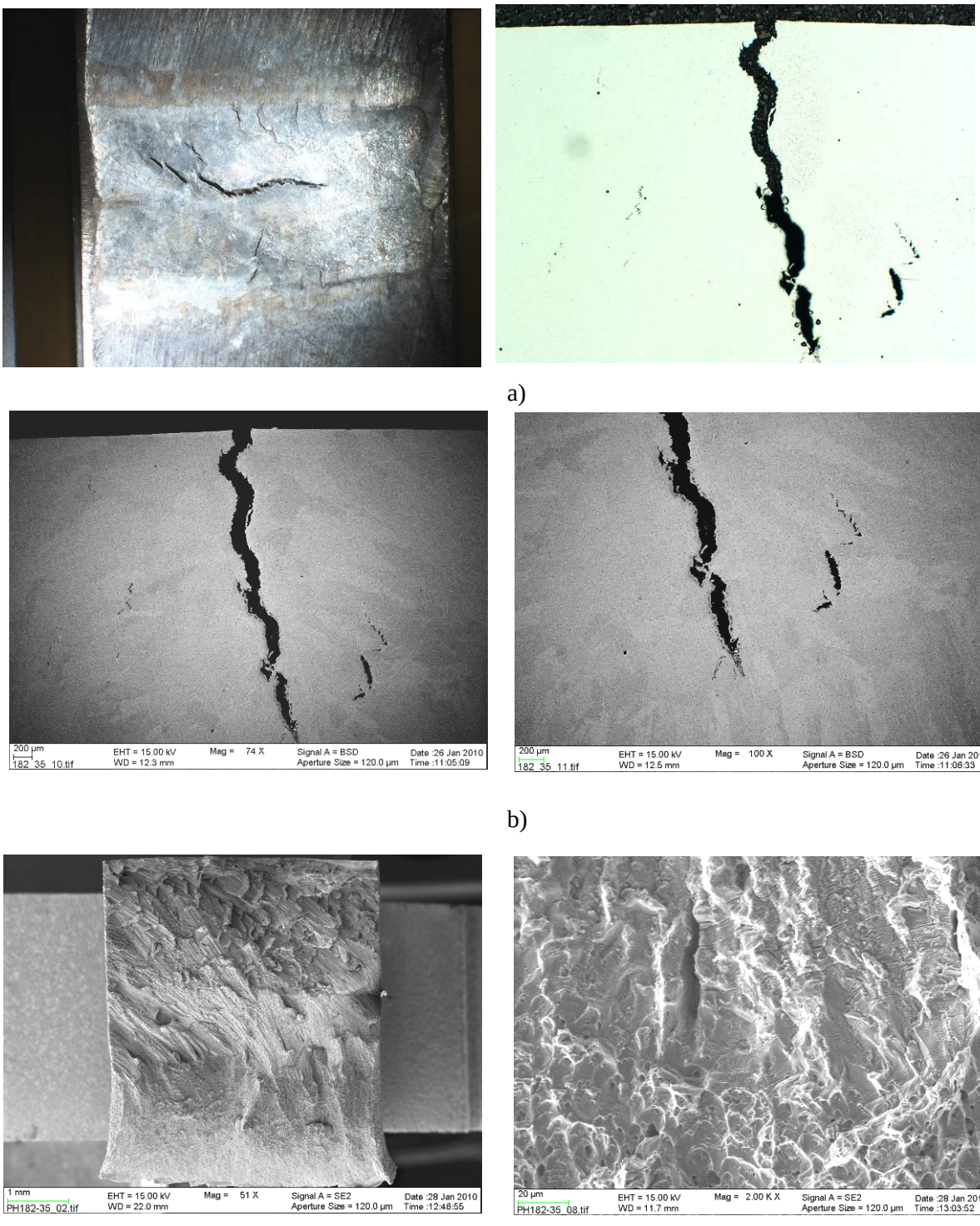

Figure 87. Pure Alloy 182 weld (specimen No. 35) after hot cracking in the Varestraint test and subsequent testing in doped steam 2178 h. a) Outer surface and cross-sections of the main hot cracks. b) Cross-sections of the hot cracks and liquation cracking below the weld bead. c) Fracture surface of the opened hot crack.

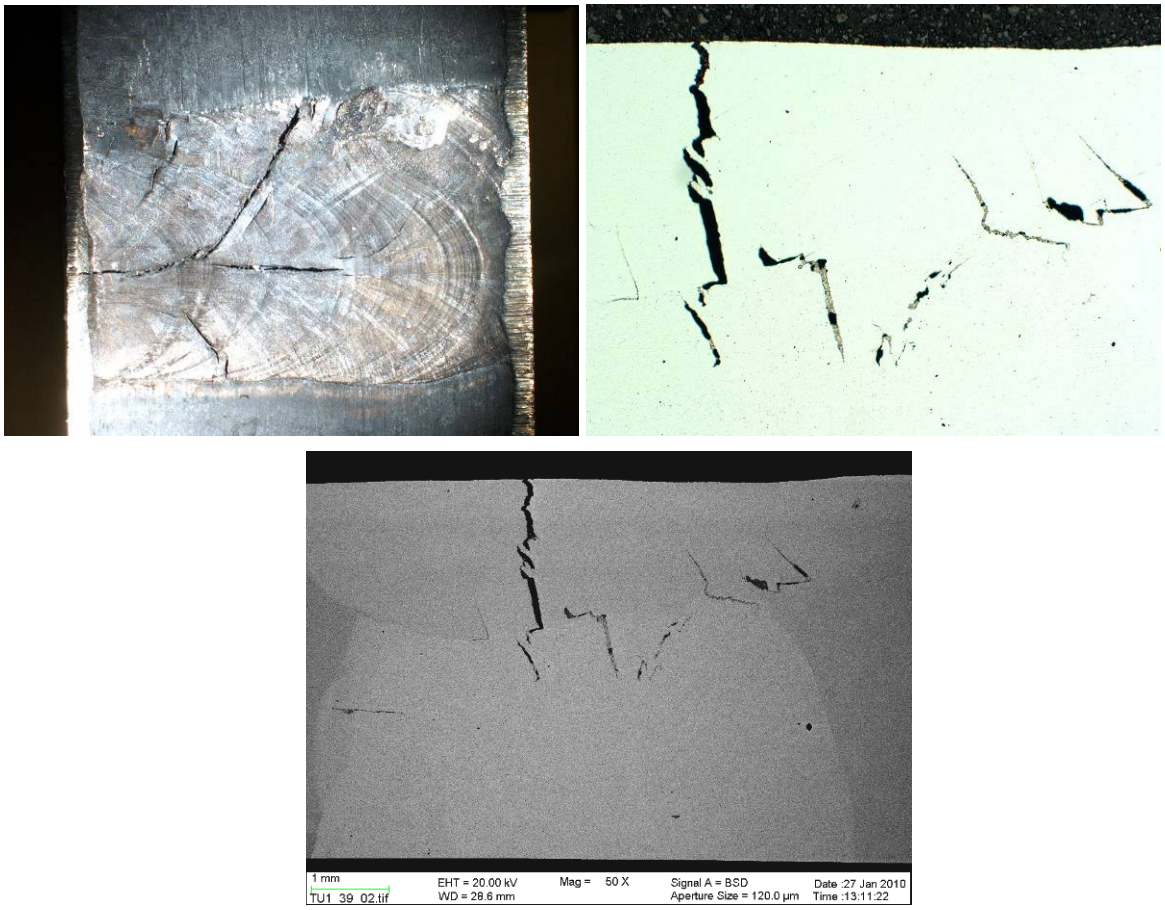
1 mm
TU1_39_02.tif
EHT = 20.00 kV
WD = 28.6 mm
Mag = 50 X
Signal A = BSD
Aperture Size = 120.0 µm
Date :27 Jan 2010
Time :13:11:22

a)

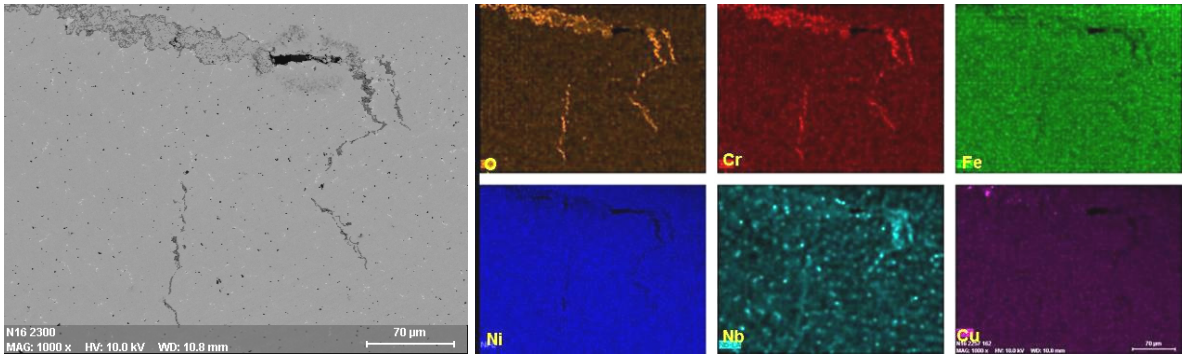
N16 2300
MAG: 1000 x HV: 10.0 kV WD: 10.8 mm
70 µm
O
Cr
Fe
Ni
Nb
Cu

b)

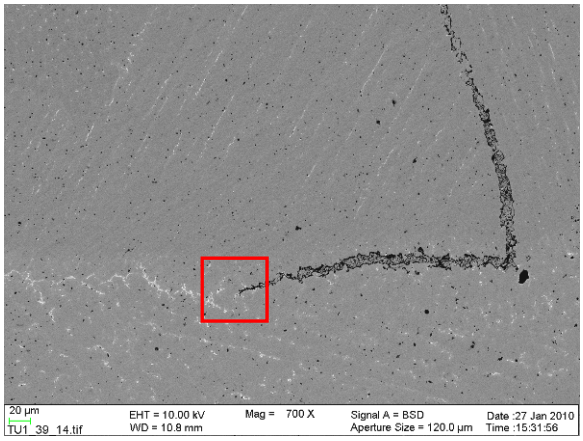

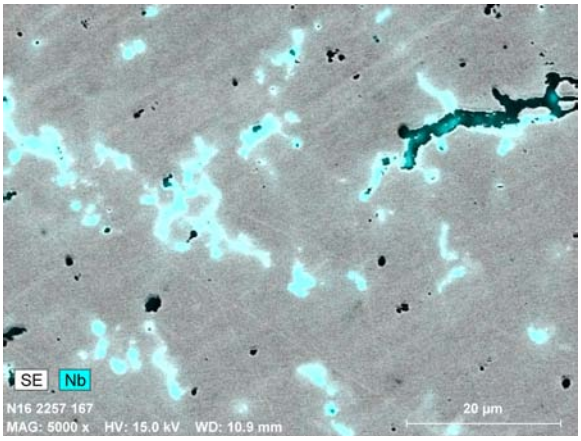

c)

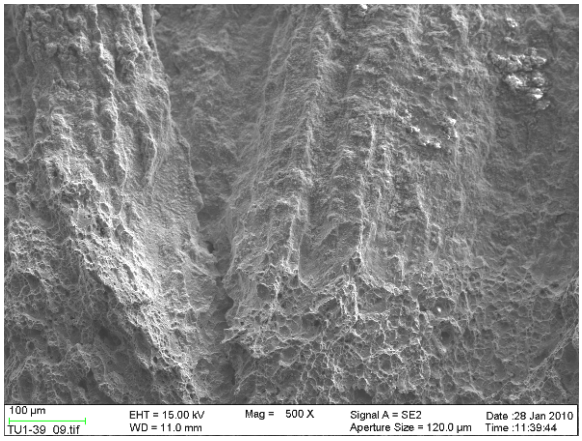

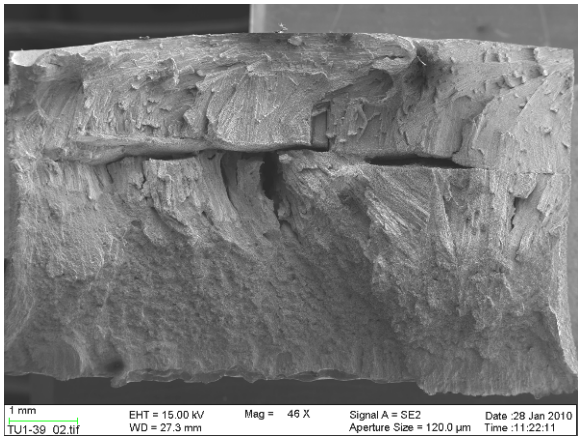

d)

Figure 88. Pure Alloy 152 weld (specimen No. 39) after hot cracking in Varestraint test and after 2178 h testing in doped steam. a) Outer surface and cross-sections of the main hot cracks and the liquation cracking below the weld bead. b) Cross-section of the hot crack tip showing minor oxidation of the hot crack fracture surfaces. c) Hot crack tip in the region of Laves phase. d) Fracture surface of the opened hot crack.

a)

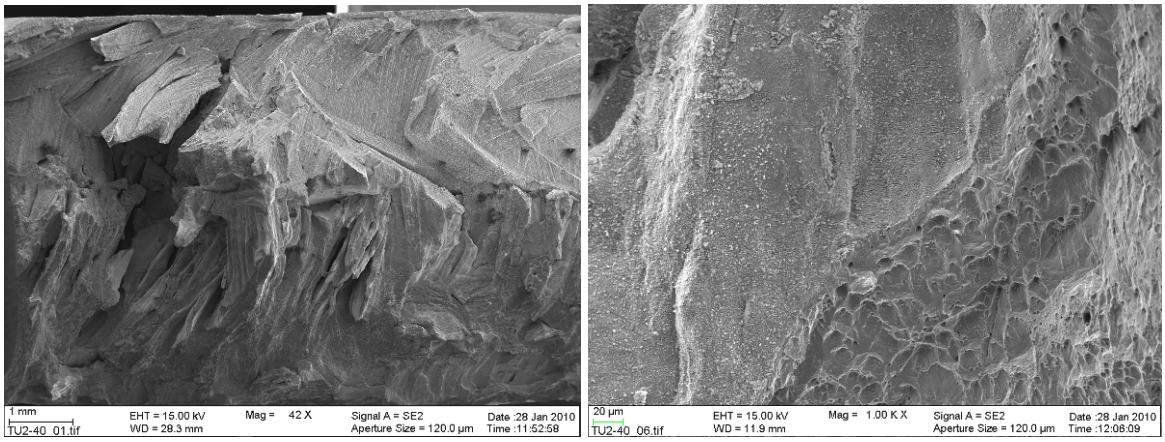

b)

Figure 89. Pure Alloy 52 weld (specimen No. 40) after hot cracking in Varestraint test and after 2178 h testing in doped steam. a) Outer surface and cross-sections of the main hot cracks and liquation cracking below the weld bead. b) Fracture surface of the opened hot crack.

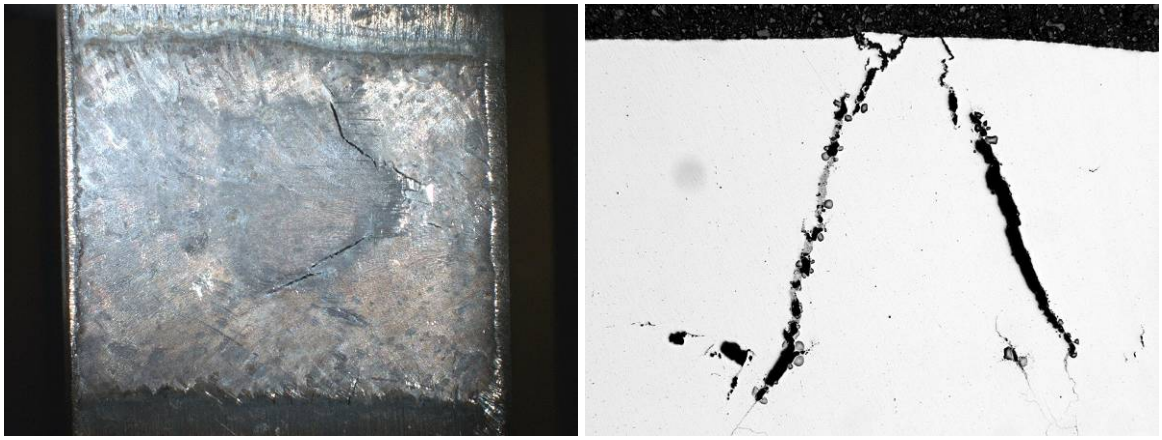

a)

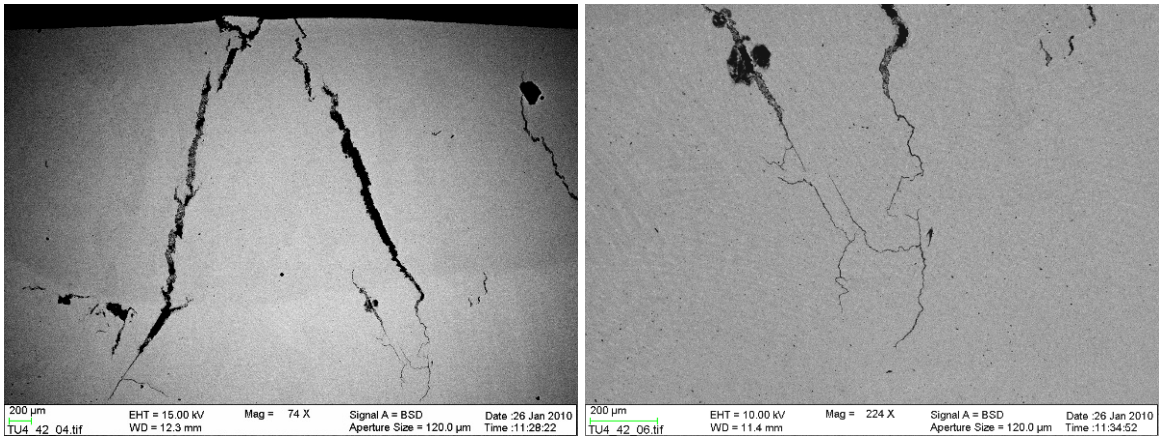

b)

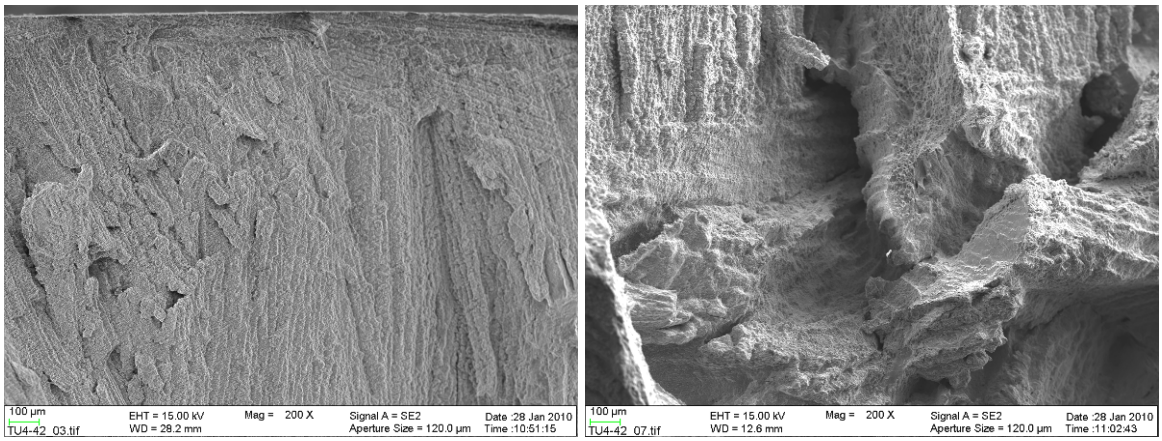

c)

Figure 90. Mock-up TV Alloy 182 weld (specimen No. 42) after hot cracking in Varestraint test and after 2178 h testing in doped steam. a) Outer surface and cross-sections of the main hot cracks. b) Cross-sections of the hot cracks and liquation cracking below the weld bead. c) Fracture surface of the opened hot crack.

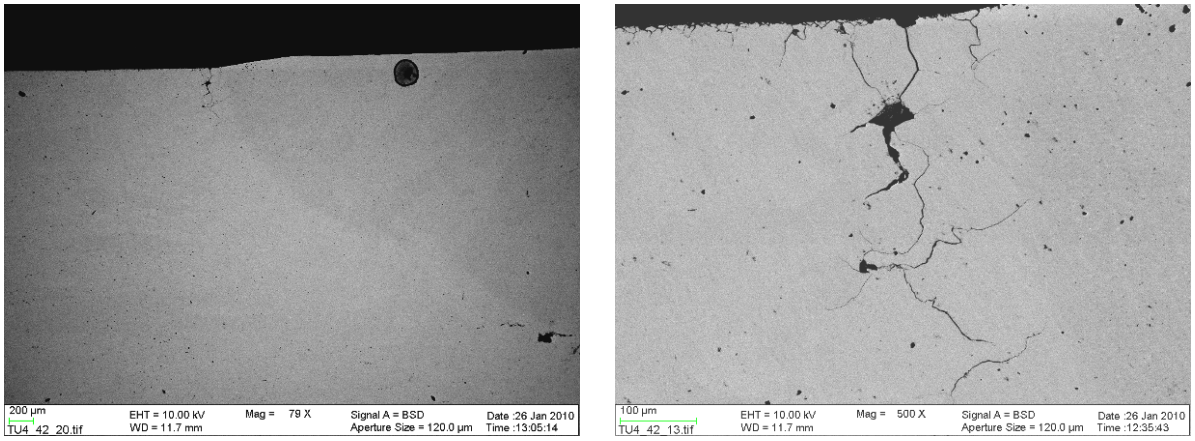

a)

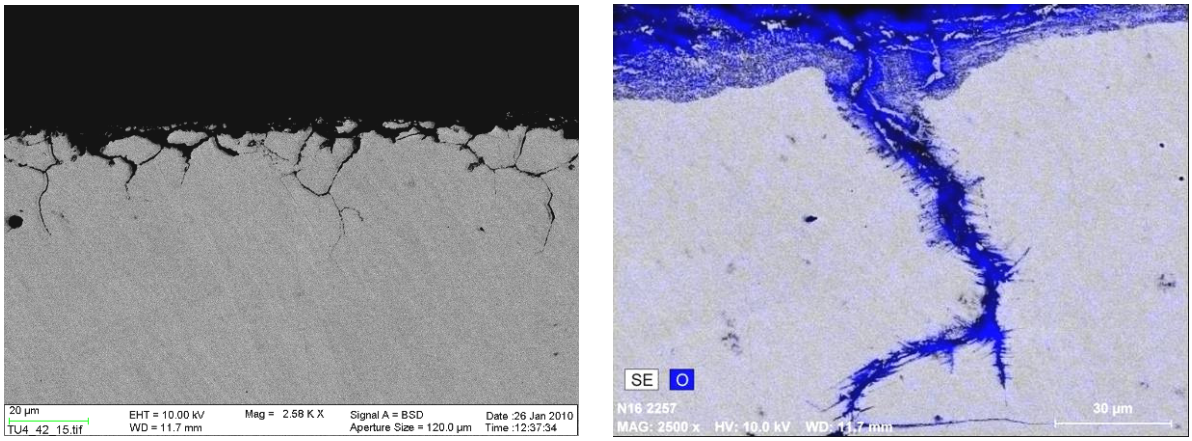

b)

Figure 91. Alloy 600 base metal cracking (specimen No. 42) after 2178 h testing in doped steam. a) Cross-sections of the EAC cracks on the outer surface of the Alloy 600 part of the specimen. b) Cross-section of an EAC crack showing oxidation of the fracture surfaces and the outer surface of Alloy 600 base metal.

In a couple of dissimilar metal weld samples wrought Alloy 600 safe end material was present, and extensive EAC cracking had occurred in the Ni-base alloy base metal, Figures 91 and 92. Typical for Alloy 600 in this test was the strong oxidation of the outer surface and the fracture surfaces inside the EAC cracks. Oxidation penetrated along the crystallographic slip planes deep inside grains from the intergranular fracture surfaces. The penetrative oxidation was highly selective, with the oxide structure becoming Cr-rich while metallic nickel dissolved selectively from the Alloy 600 base metal and deposited in the middle of the EAC cracks, and on the outer surface of the samples, as was shown previously for Alloy 182 and 82 weld metals. EAC fracture in Alloy 600 base metal was fully intergranular.

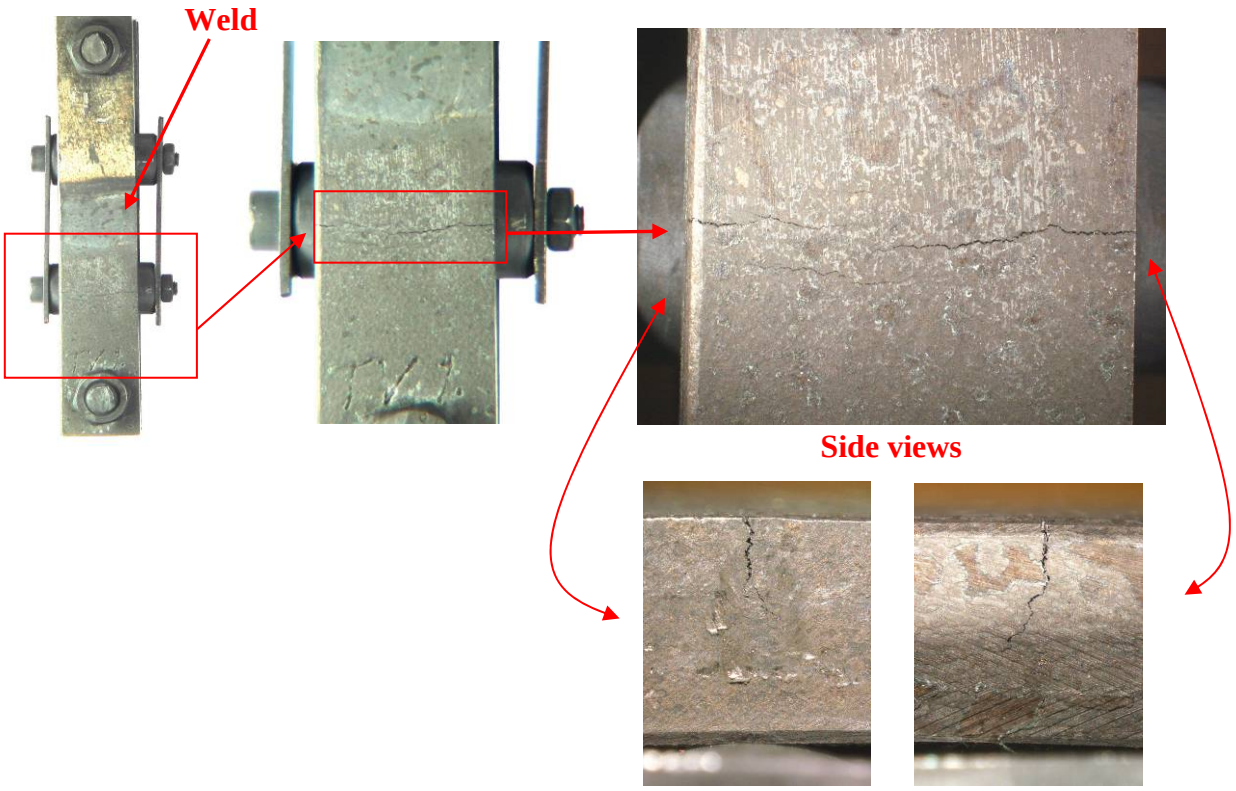
Weld
Side views

a)

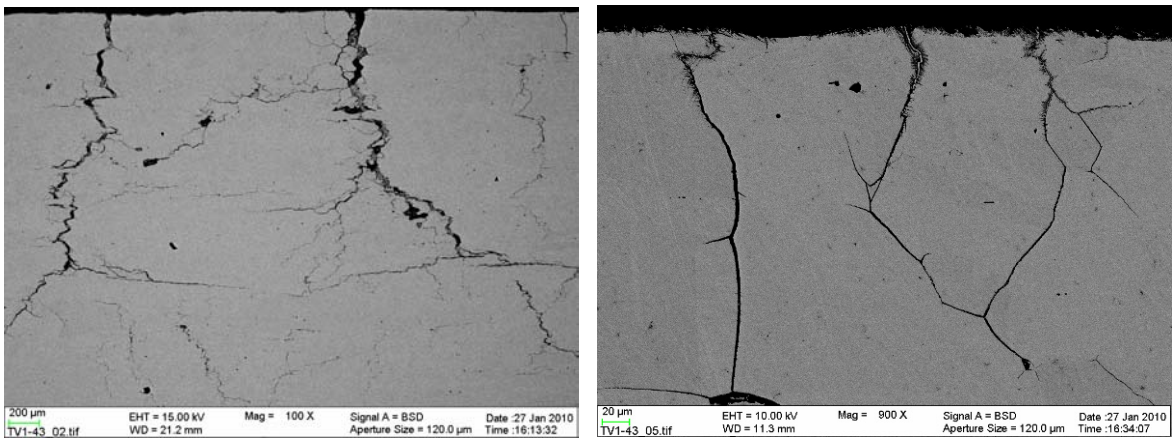
200 µm
TV1-43_02.tif
EHT = 15.00 kV
WD = 21.2 mm
Mag = 100 X
Signal A = BSD
Aperture Size = 120.0 µm
Date :27 Jan 2010
Time :16:13:32
20 µm
TV1-43_05.tif
EHT = 10.00 kV
WD = 11.3 mm
Mag = 900 X
Signal A = BSD
Aperture Size = 120.0 µm
Date :27 Jan 2010
Time :16:34:07

b)

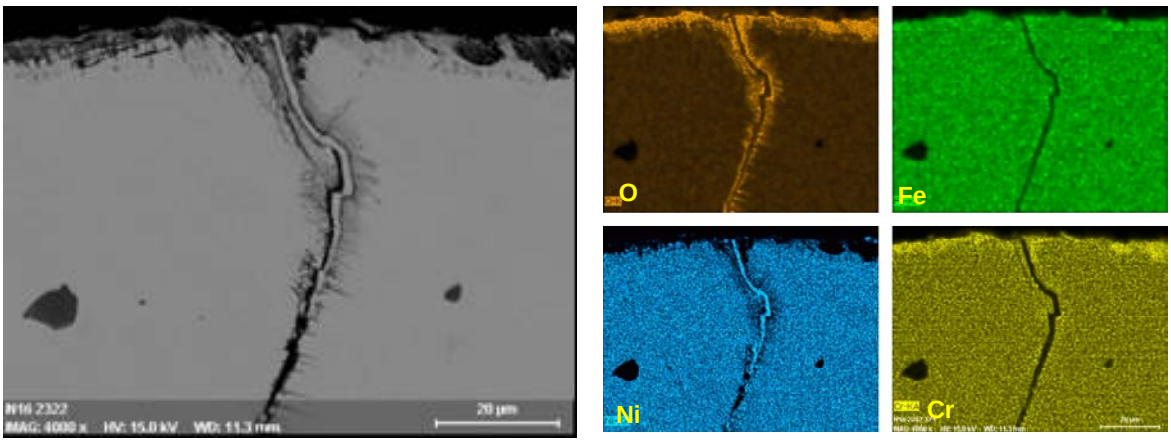

c)

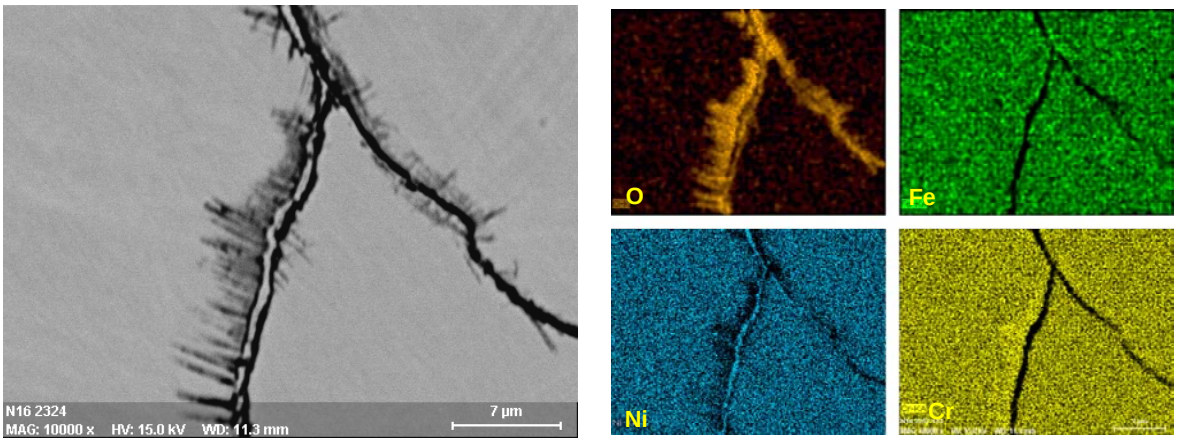

d)

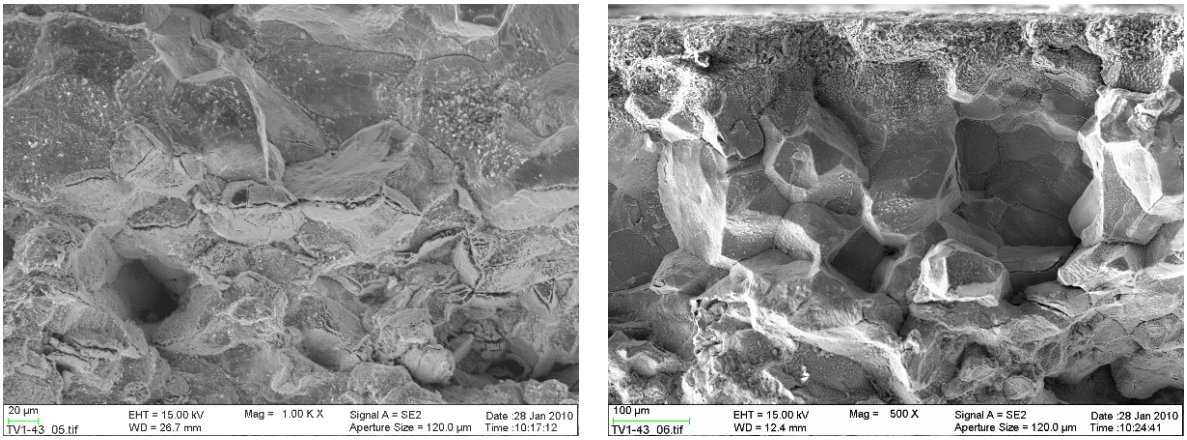

e)

Figure 92. Alloy 600 base metal cracking (specimen No. 43) after 2178 h testing in doped steam. a) Outer surface and side views of the main EAC cracks. b) Cross-sections of the EAC cracks. c) and d) Cross-sections of EAC cracks showing oxidation of the fracture surfaces and the outer surface of Alloy 600 base metal. e) Fracture surface of the opened EAC crack in Alloy 600 base metal.

4.4 EAC of nickel-base alloy dissimilar metal welds

In the earlier test series (Table 9 and [5, 6]), liquid penetrant indications after EAC testing in doped steam environment were found in specimens fabricated from all the studied weld combinations: mock-up 1 (Alloy 152) specimens showed indications in 5 of the 8 specimens, in mock-up 2 specimens (Alloy 52) indications were present in 6 of 8 specimens, in mock-up 3 specimens (Alloy 152/52) in 7 of 8 specimens and in every mock-up TV weld specimen (Alloy 182). In the repair welded (Alloy 82) mock-up specimens (Table 9, specimens TV4K-1 and TV4K-2) indications were present in one of the two tested specimens after short exposure time. All indications in Alloy 152/52 weld metals were caused by small weld defects, and they did not show any extension during the testing. The small defects on specimen surfaces were probably present from the beginning (loading), but unfortunately liquid penetrant testing was not made before the first exposure.

Mock-up TV weld (Alloy 182) was apparently the most susceptible of the studied welds. In one of the specimens (1% strain, 1172 h test duration) the main crack extended almost through the specimen (Figure 93). In addition to the weld metal itself, cracks were observed in Alloy 182 buttering and also in Alloy 600 base metal. No exact features to which the cracks or their initiation could be associated were observed.

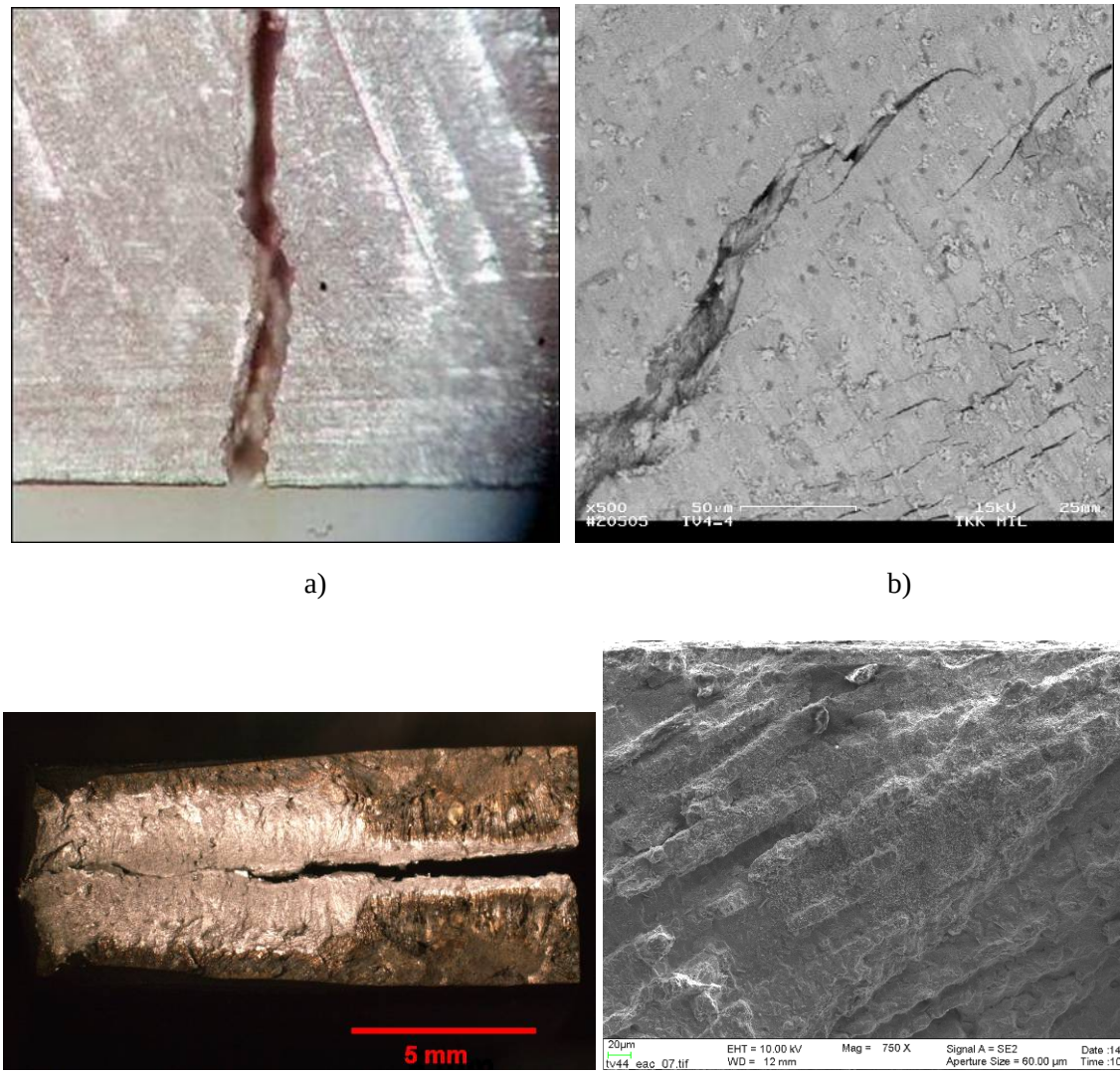

a) b)

c) d)

Figure 93. a) Optical microscope image of the main crack. b) An SEM (BSE) photograph from an area of a secondary crack. A number of small cracks can be seen in Alloy 182 weld metal and also in Alloy 182 buttering. c) Opened fracture surface. d) An SEM photograph showing the interdendritic nature of EAC cracking.

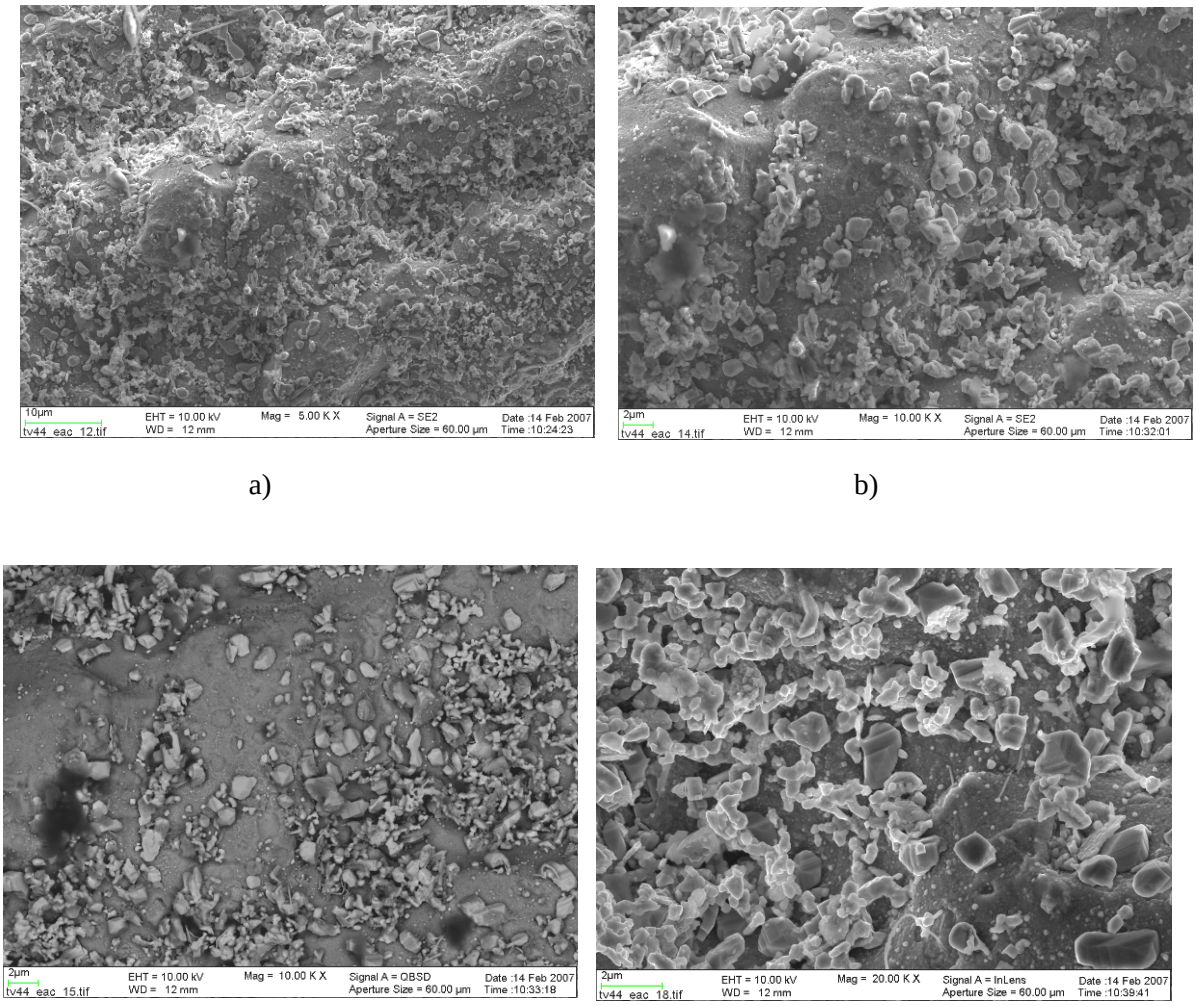

Figure 94. Fracture surface of the main EAC crack of Alloy 182 close to the outer surface is covered by NiO particles.

While considering the EAC susceptibility of the other alloys, which were much more resistant to EAC than Alloy 182 samples, the average number of cracks of the specimens is a better parameter in benchmarking of the different welds than the number of liquid penetrant test indications. The differences between mock-ups 2 and 3 were small. Cracks or crack-like features (less than 500 µm in size) were observed in specimens prepared from both mock-ups, but the number of cracks in them is clearly smaller than that in specimens prepared from the mock-up TV weld (Alloy 182 weld with Alloy 182 buttering). An example of the kind of cracks found in mock-up 2 and 3 welds is shown in Figure 96, where a mock-up 2 (Alloy 52) specimen is shown (1% strain, 1172 h test duration). These cracks were too small for a proper fractography study. The most resistant weld was mock-up 1, as no cracks nor crack-like features were observed by SEM or stereomicroscope, regardless of the liquid penetrant indications. (see more details in [5, 6]).

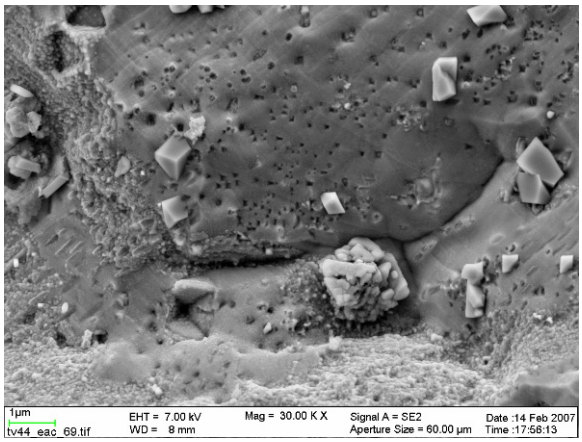

a)

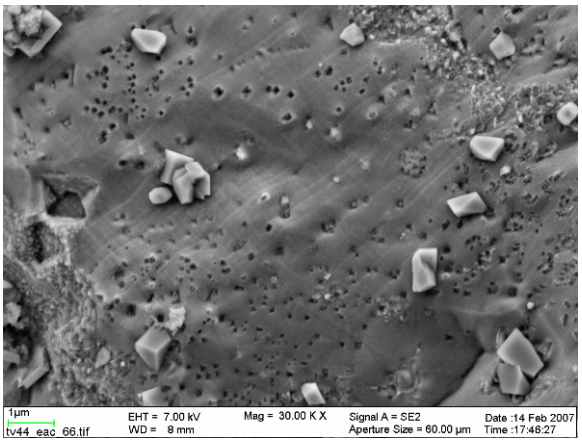

b)

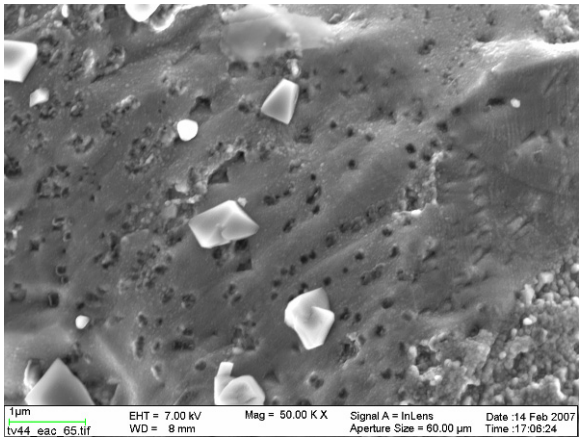

c)

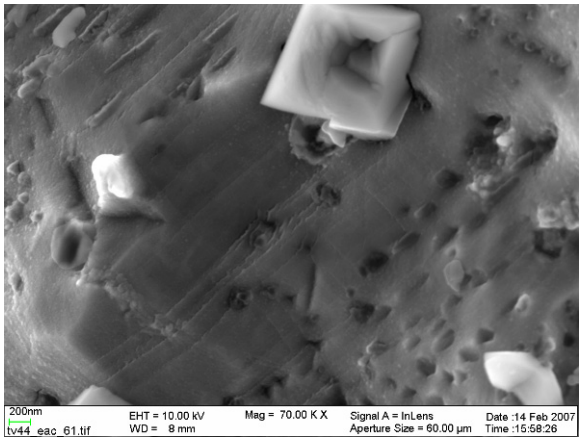

d)

Figure 95. Fracture surface of the main EAC crack of Alloy 182 close to the crack tip shows smooth intergranular fracture with large Nb(C, N) particles and a large amount of small precipitates, probably $M_{23}C_6$.

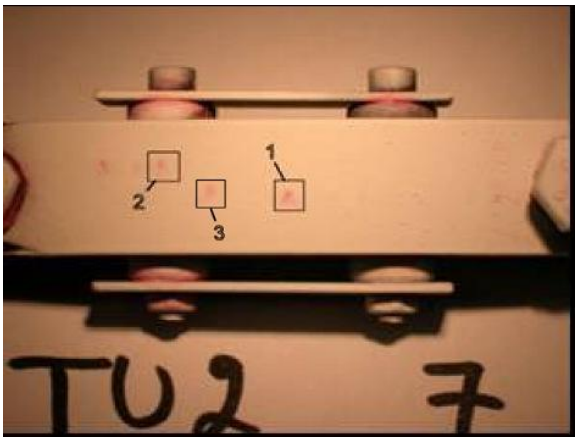

a)

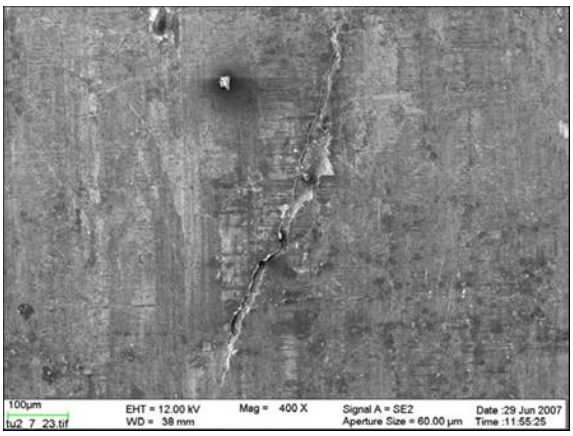

b)

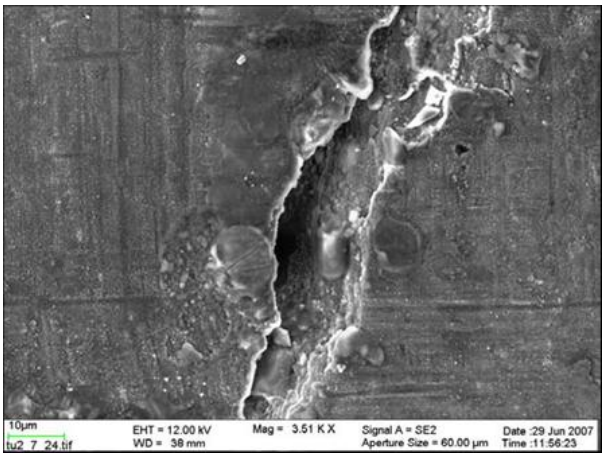

c)

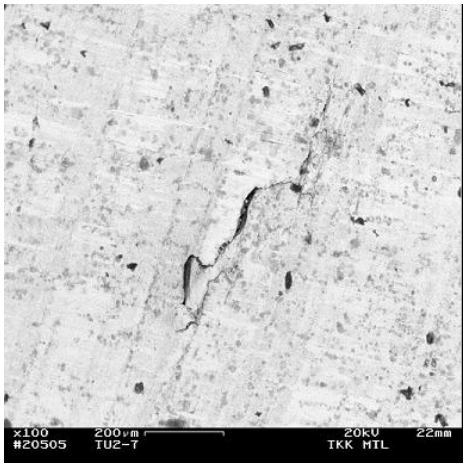

d)

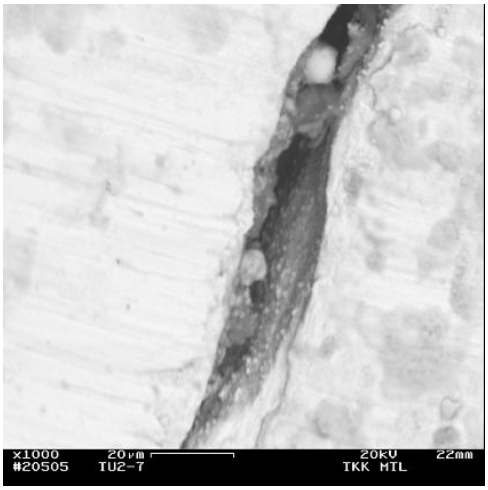

e)

Figure 96. a) Post-test liquid penetrant indications in a mock-up 2 specimen. b) An SEM (SEI) photograph taken from location 2. c) A higher magnification SEM (SEI) photograph from the same location as b) showing a small crack. d) An SEM (BSE) photograph taken from location 3. e) A higher magnification SEM (BSE) photograph taken from the same location as d) showing the crack-like appearance of the indication.

Fractography of the Alloy 182 specimen showed that the outer surface and fracture surface after EAC testing in doped steam environment were covered with an oxide layer where NiO forms on the top of the thinner oxide layer and covers the fracture surface close to the outer surface. Close to the crack tip no NiO particles were observed, and the fracture surface was covered only by a very thin oxide layer. Close to the crack tip the intergranular nature of the EAC fracture surface is clear (see Figure 95) and its morphology is quite different from the interdendritic morphology of the hot crack fracture surface, where the wavy structure of the solidified final melt is also visible. The differences in the fracture

mechanisms are marked; hot cracks form by separation in the liquid phase and EAC occurs by fracture in the solid phase. Close to the EAC crack tip of Alloy 182 the dual occurence of carbonitrides is present on the fracture surface, i.e. large blocky Nb(C, N) particles together with small particles, which are probably $M_{23}C_6$ carbides. The images of the small $M_{23}C_6$ particles indicate that they may have started dissolving or oxidizing, since their appearance changes and they are not clearly observed by FEG-SEM further away from the crack tip. Presence of the Laves phase on the fracture surface was especially studied, but only weak indications of the possible lamellar Laves phase, clearly visible on the fracture surfaces of the hot cracks, were observed. The studied features were rich in P, Mn and O (and depleted in Ni, Cr and Fe), but no enrichment of Nb or Si was observed.

4.4.1 ATEM study of EAC cracks

To complement the ATEM examinations of hot-cracks in Alloy 182 weld metal mock-up, a study was also conducted of EAC cracks formed in welds of a similar structure after exposure to the four-point bend testing in doped steam. While the complete results are reported separately in [47], they are summarized here.

The material of this study came from the doped steam four-point-bend test series (see previous chapter of this report and [5, 6] on the materials combination “Mock-up TV”). Mock-up TV4 was comprised of Alloy 182 weld metal joining the Alloy 600 safe end and the Alloy 182 buttering of stainless steel clad pressure vessel steel. The nominal composition of the weld metal (wt.%) was 68 Ni, 16 Cr, 6.7 Fe, 6.5 Mn, 1.8 Nb, 0.8 Si. Three different example cracks were extracted from one of the four-point bend test bars (TV4-7 with 1% of strain and 1172 h test time in doped steam environment [5, 6]), two from near the tips of deep cracks (Cracks A and C), and one shallow, surface crack (Crack B).

In order to target particular regions and to preserve the integrity of the oxides within the cracks, the cracks were back-filled with low-viscosity M-Bond epoxy, and then cross-section specimens of the oxide-filled cracks were fabricated by a process of mechanical thinning of the blanks, avoiding conventional electrolytic techniques. A slice of the region of interest was first ground down to about 0.1 mm thickness, and then trimmed to the appropriate 3 mm size to fit the TEM specimen holder. A Gatan Dimpler was used to gently grind and polish a small dimple in one side of the specimen, targeting the region of interest (generally the crack tip). This was followed by ion milling to electron transparency with a Gatan Pips ion mill.

Examinations focused on three different cracks, each having similarities and differences. Crack A was a deep, branched crack that appeared to be filled with a fairly uniform oxide all the way to its relatively blunt tip. As shown in Figure 97 a), some globular particles existed within the crack at its narrowest point. For comparison, Crack B was a shallow, surface crack, as shown in Figure 97 b). It had a rather wide mouth that quickly tapered to a narrow, oxide-filled crack. The oxide in that crack also tended to be fairly uniform in appearance. Finally, Figure 98 a) shows a portion of Crack C, which was actually the wake of a long, branched, oxide-filled crack. That oxide appeared to be comprised of blocky particles adjacent to the base material, with the rest of the crack filled by a more uniform-looking phase. As shown at higher magnification in Figure 98 b), the oxide adjacent to the metal

in Crack C was quite heterogeneous in geometry, with both light areas and dark areas, in both faceted shapes and more globular forms.

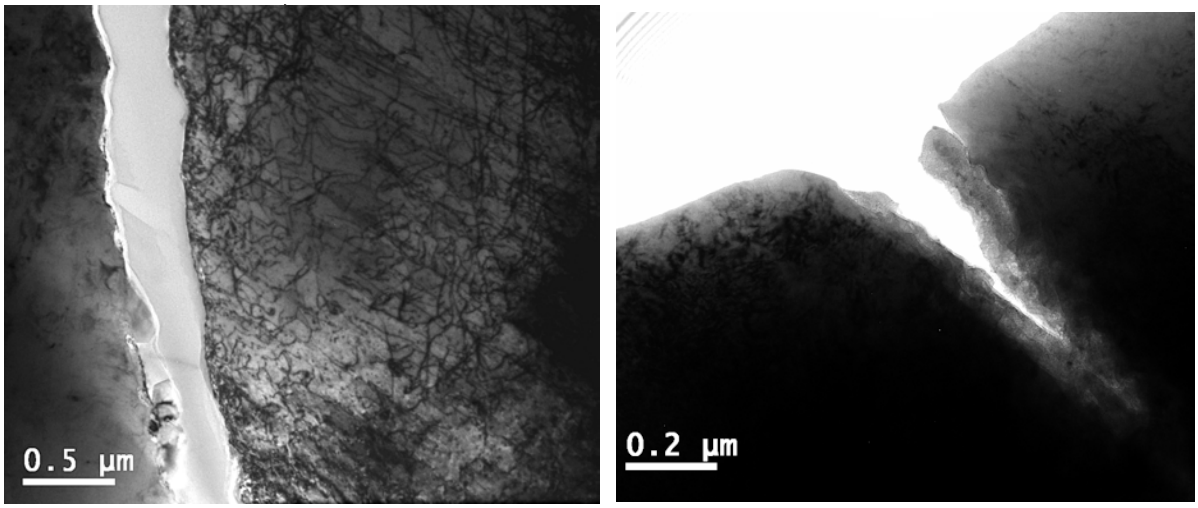

a) b)

Figure 97. Crack A was a deep, branched crack that appeared to be filled with a fairly uniform oxide all the way to its relatively blunt tip. As shown in a) some globular particles also existed within Crack A at its narrowest point. For comparison, Crack B was a shallow surface crack b), and had a rather wide mouth that quickly tapered to a narrow, oxide-filled crack.

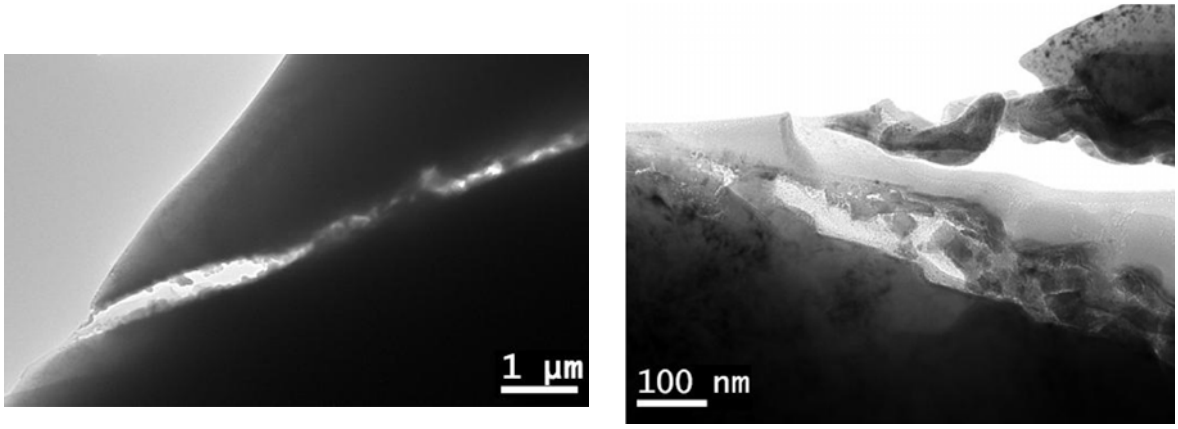

a) b)

Figure 98. Crack C was actually the wake of a long, branched, oxide-filled crack. a) The oxide appeared to be comprised of blocky particles adjacent to the base material, with the rest of the crack filled by a more uniform-looking phase. As shown at higher magnification in b), the oxide adjacent to the metal in Crack C was quite heterogeneous in geometry, with both light areas and dark areas, in both faceted shapes and more globular forms.

Energy dispersive X-ray spectroscopy (EDS) and selected area diffraction (SAD) results for the three different crack examples suggested that two kinds of oxides were present, arranged as an inner layer immediately adjacent to the crack wall with an outer layer filling the rest of the crack. The SAD analyses indicated that the oxides may take on either a diamond-cubic spinel structure or a face-centered cubic NiO type structure, in some cases having a slightly smaller lattice parameter than the pure counterpart. The EDS analyses indicated that the inner layer was richer in Cr and Fe than the outer layer, but the oxide was still predominately Ni-rich.

An element profile of Crack A is shown in Figure 99. For comparison, Figure 100 shows profiles measured from Crack B, particularly focused on the region adjacent the crack wall. The profiles for both cracks exhibited a fluctuation in Cr near the crack wall, with its peak occurring in a region about 20–30 nm wide close to the substrate. The Ni content seemed to mainly reflect the inverse of the O trend, with the exception of the higher Cr region. Particularly interesting in the profiles of Crack B, however, was the presence of Cl. The Cl content was high, particularly on either side of the higher Cr region. Some F and S were also detected in that oxide, though at much lower levels than the Cl. The presence of Cl, F and S was evident only in shallow surface Crack B, and was not found in deep Crack A or Crack C. Meanwhile, the oxide structure in Crack C was much more heterogeneous than in Crack A and Crack B. Some example trends for each element as a function of distance from the apparent metal/oxide interface are shown in Figure 101, collated from miscellaneous exploratory spot analyses. Since the interface was not distinct nor uniform, the precision of the collection locations was only about ±10 nm. Despite the heterogeneity, the composition appeared to fluctuate in a manner similar to that of Crack A and Crack B, clearly displaying the Cr-rich region at the crack wall. However, Crack C exhibited much more Cr enrichment than Crack A or Crack B, while its O profile no longer followed the inverse of the Ni content so closely in the oxide region. Also apparent from the trends was the similarity in behaviour between Fe, Cr and Mn, while the Ni fluctuated more independently.

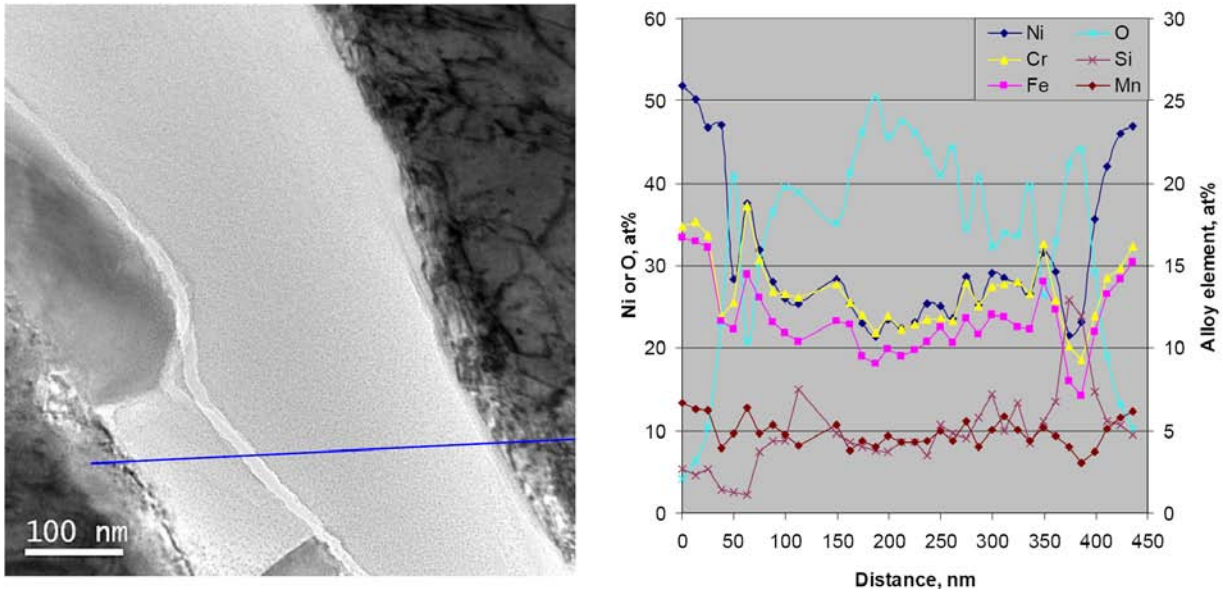

Figure 99. Composition profile in atom percent for a narrow portion of Crack A, along the blue line shown in the image. The large grey particles visible on the left and bottom of the image are niobium and manganese rich.

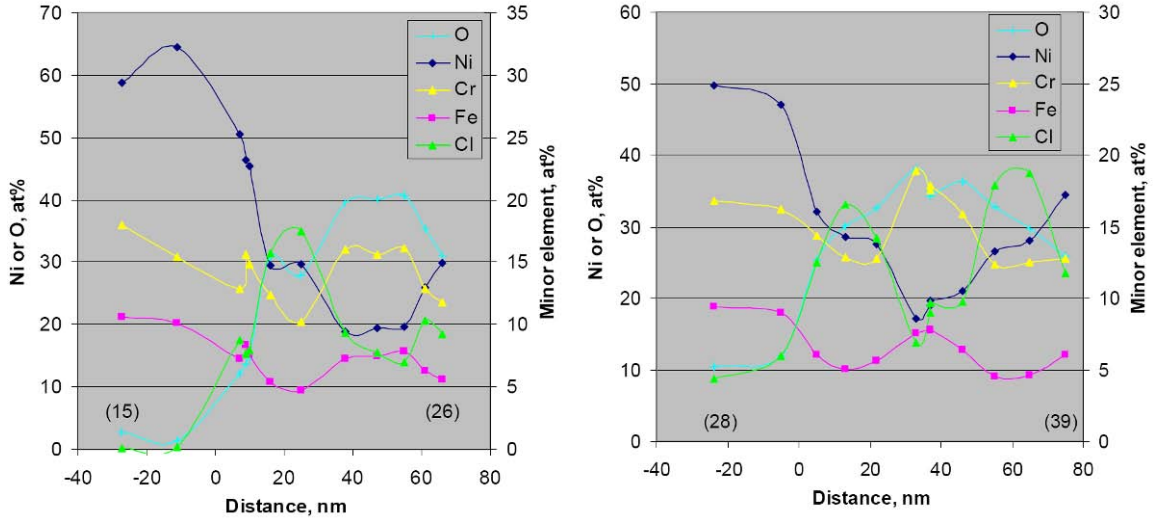

Figure 100. Composition profiles in atom percent for two different portions of the Crack B oxide, focused on the region closest to the substrate (i.e. crack wall). There is a chromium-rich inner layer occurring in a region about 20–30 nm wide. Of particular interest is the presence of chlorine, particularly located on either side of the Cr-rich region. Fluorine and sulphur were also detected in Crack B oxide, though at lower amounts than the Cl.

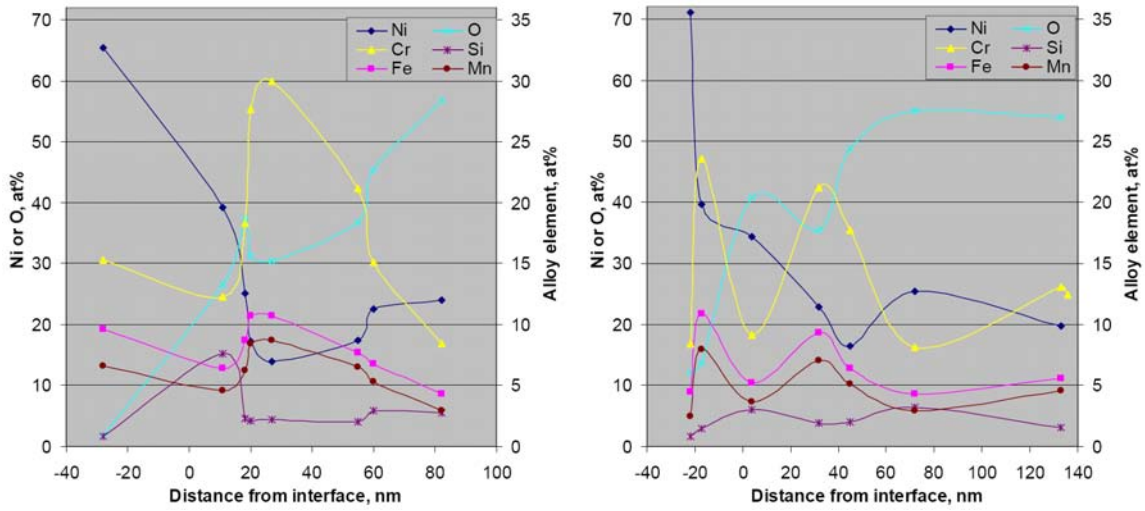

Figure 101. Composition profiles in atom percent for the oxide of Crack C, compiled from miscellaneous spot analyses. The figures clearly show a Cr-rich region a few tens of nm wide at the crack wall, in this case showing much more Cr enrichment as compared to that in Crack A or Crack B. In these cases the O profile no longer follows the inverse of the Ni content so closely in the oxide region.

Although electron diffraction was utilized to try to better understand the structure of the oxides, in general it was found that even the smallest selected area aperture was still too large to permit any clear structural differentiation between the Cr-rich inner portion of the oxide and the outer oxide filling the cracks. Instead the SAD patterns were often populated by a conglomeration of what were probably a number of different diffraction patterns for different grains and structure types simultaneously, preventing unambiguous identification of individual regions.

Nonetheless, Figure 102 shows one of the best SAD pattern examples found, which was recorded from the more uniform oxide in the middle of Crack C. The ring-type SAD pattern containing discrete spots indicates that the structure is nano-crystalline, with randomly oriented grains diffracting simultaneously. The distribution of the rings as a particular series of pairs and singular rings of specific diameters suggests that the structure is face-centered cubic (FCC). Calculations based on the measured diameters of those rings indicated that the oxide had a lattice parameter of a_o = 3.905 Å. For comparison, a NiO type of oxide also has a FCC structure, but in pure form its lattice parameter is a_o = 4.179 Å. That would produce a SAD ring pattern having the same ring periodicity, but of slightly smaller diameter.

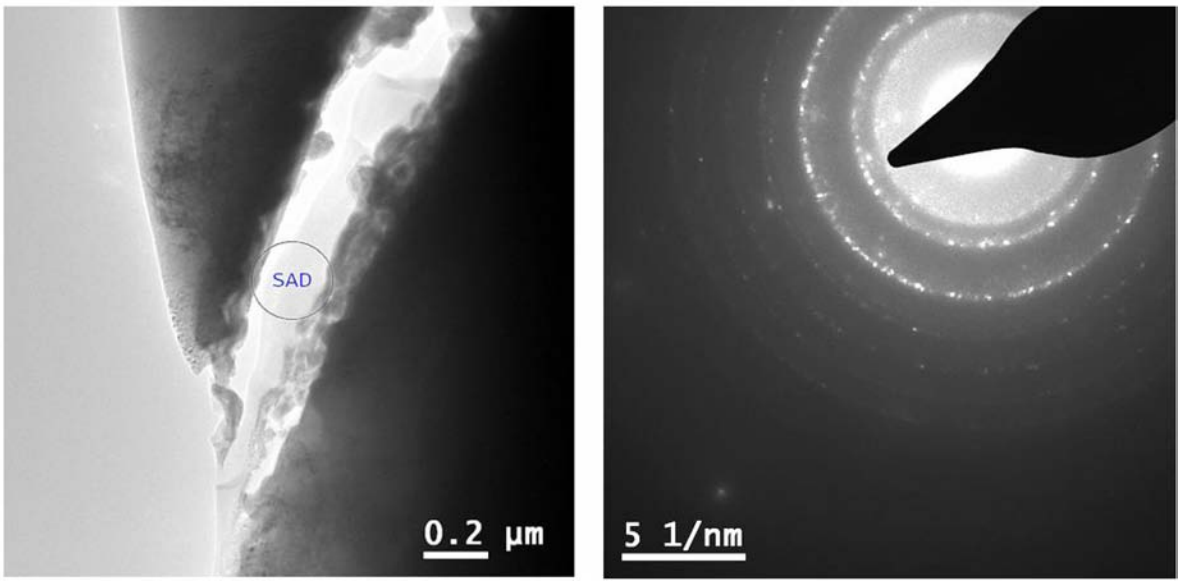

Figure 102. An example of a SAD ring pattern from the more homogeneous oxide in the middle of Crack C (location indicated in left hand image) suggested a face-centered cubic (FCC) structure having a lattice parameter a_o = 3.905 Å.

On the other hand, the EDS analyses consistently indicated the presence of Cr and Fe (and often Mn as well). Such mixed-composition oxides often take on the form of a diamond-cubic structured spinel oxide, having a version of the stoichiometry AB_2O_4, where A is a divalent Ni (or Fe) ion and B is a trivalent Cr or Fe ion [48]. In its pure form, a chromium oxide spinel has a lattice parameter of a_o = 8.36 Å, and would exhibit diamond-cubic ring periodicity in SAD. When such a ring pattern was superimposed on a diffraction pattern composed mostly from the more heterogeneous inner layer of the oxide of Crack C, a reasonable fit was achieved, as shown in Figure 103. It may be that the model ring pattern is slightly smaller than that of the actual ring pattern of the image, which would suggest a slightly smaller lattice parameter in the actual oxide. However, the poor quality of the diffraction pattern prevented such a calculation from being satisfactorily achieved. The fact that some of the spots along the rings are much brighter than others indicates some preferential orientation in some particular directions, possibly in relation to the substrate metal.

The oxide of Crack B was also examined with SAD. Though the result was much less clear, it seemed that the spinel oxide ring pattern was a better fit than that of an idealized NiO or of the FCC oxide identified in Figure 102.

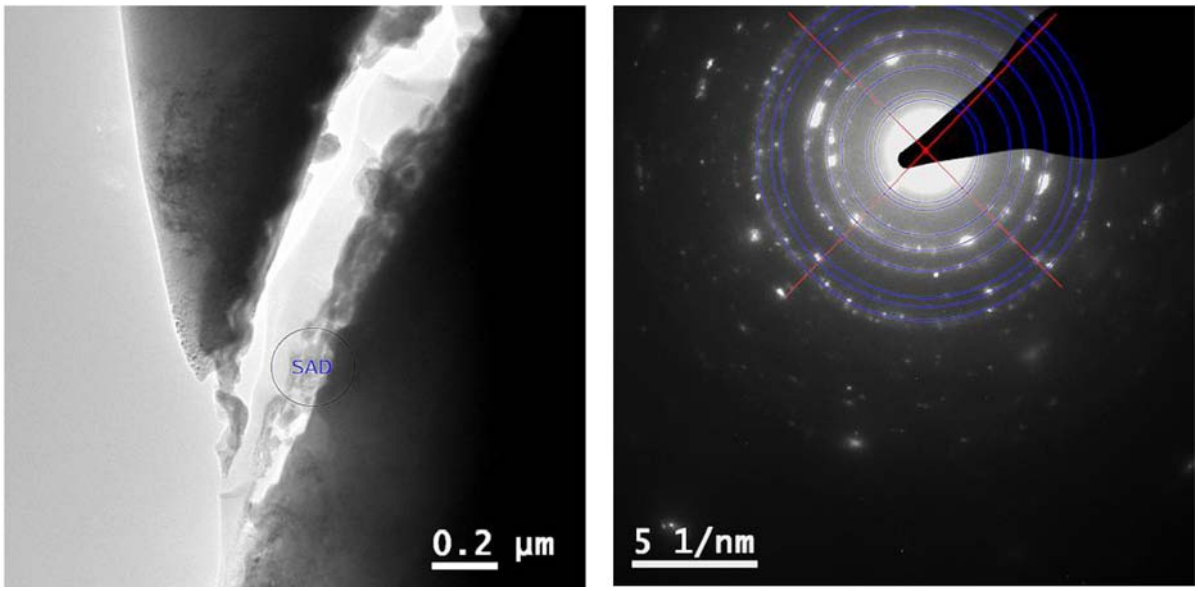

Figure 103. An example of a SAD ring pattern from the heterogeneous oxide at the crack wall of Crack C (location indicated in left hand image) suggested a diamond cubic structure similar to the idealized version of a spinel oxide having a_0 = 8.36 Å (overlay rings in right hand image).

Crack A offered an opportunity to examine the relationship between the oxide and the matrix, as shown in the series of images in Figure 104. The SAD patterns indicated an epitaxial NiO formed in a distinct orientation relationship with the matrix. While SAD32 is comprised principally of the Ni alloy matrix spots with only a minor presence of a ring of NiO spots, SAD30 mostly indicates an almost amorphous NiO, with the pair of bright spots from the Ni alloy matrix only faintly visible. However, SAD31 shows more predominant NiO rings, with greater crystallinity indicated by the rings of equally spaced, but separate spots. The Ni alloy matrix spots are much more evident in SAD31 as well, and the orientation relationship between the two phases is apparent as the inner ring of spots is enclosed by a square of matrix spots (a pair of primary spots and a pair of spots resulting from double diffraction with the oxide). Noteworthy is that the lattice parameter in this case is closer to that expected for pure NiO. The amorphous character in the outer oxide may be an artefact of the ion-milling, which is known to produce a thin amorphous layer, which would then be more apparent in extremely thin regions like that of SAD30.

In summary, EDS and selected area diffraction SAD results indicated that two main kinds of oxides were present, containing mostly nickel, but arranged as a 30–50 nm wide Cr- and Fe-rich inner layer showing spinel structure, and an outer layer having NiO type structure filling the rest of the crack. Based on the observation of an epitaxial relation between the NiO and the matrix, as well as the relative thicknesses and composition variations in the different oxide layers, it would seem that both in crack initiation and growth the formation of the NiO is dominant. The Cr-rich spinel inner layer subsequently grew at the interface with the matrix, becoming thicker and more Cr- and Fe-rich as it evolved, perhaps promoting the transport of Ni ions towards the outer oxide surface. Such behaviour is also typically expected for PWR environments, but at this moment the real conditions existing in the crack during doped steam testing are unknown, so the crack oxide evolution in the doped steam is not

yet evident. In this test series only NiO was also observed in the FEG-SEM studies inside the EAC cracks (see previous chapter of this report and [5, 6]). However, in the other test series metallic Ni dominated inside the EAC cracks indicating how sensitive is the balance between NiO and metallic Ni when operating close to the Ni stability line, which is close to the H_2-H_2O line in high temperature water.

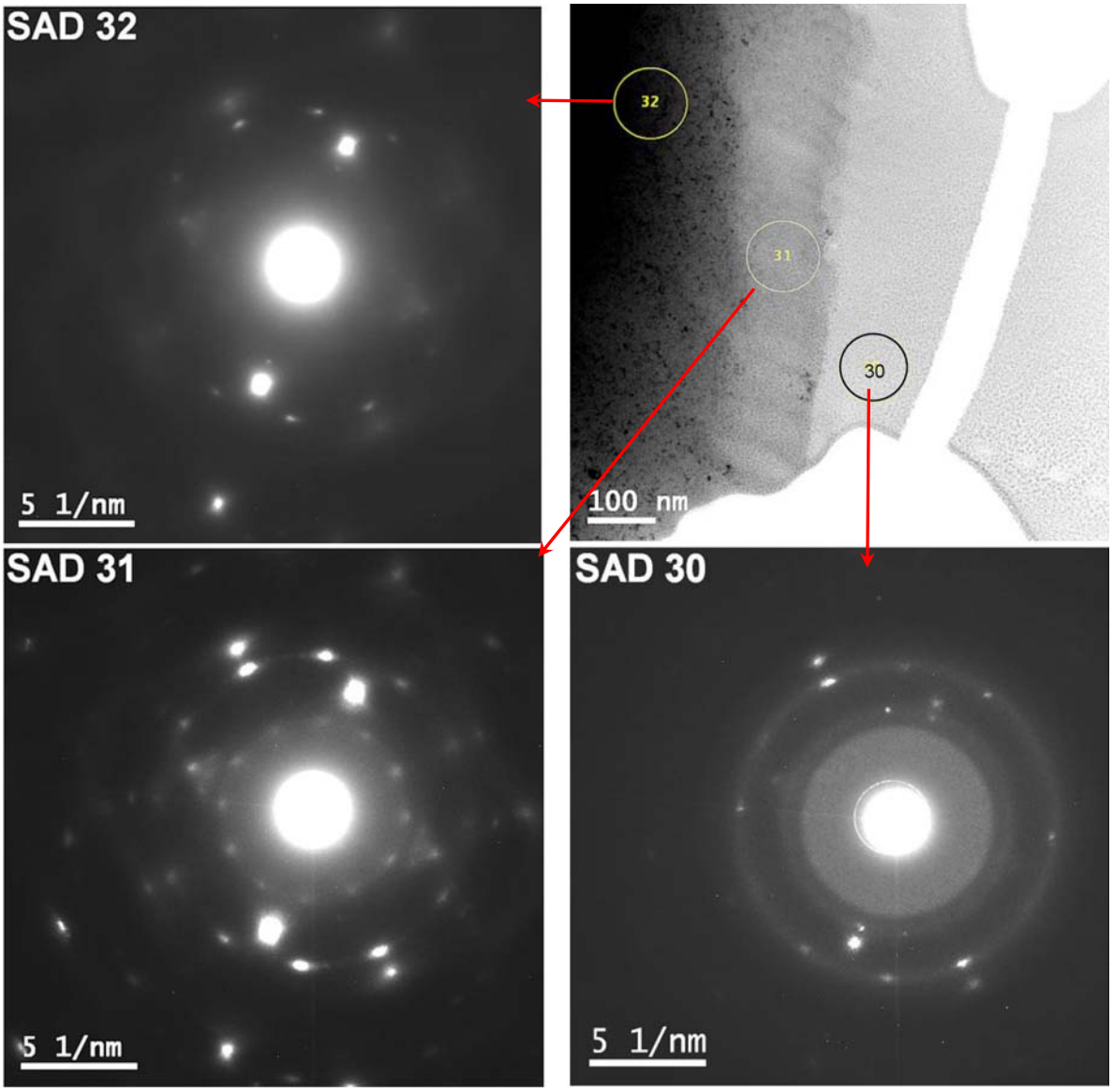

Figure 104. SAD patterns of three oxide/matrix regions in Crack A, showing an apparent epitaxial oxide formation. SAD30 mostly indicates an almost amorphous NiO, with a couple of bright spots from the Ni alloy matrix. SAD31 shows much more predominant NiO with greater crystallinity indicated by the rings of equally spaced, but separate spots. The Ni alloy matrix spots are much more evident as well, and the two phases share an orientation relationship. Finally, SAD32 is comprised principally of the dominant pair of Ni alloy matrix spots, with only a minor presence of the larger ring of oxide spots, and no inner ring of spots.

5. Specimens for EAC crack growth testing in PWR primary water

When it was observed that EAC crack initiation does not take place from the pre-existing hot cracks in the doped steam testing, it was decided to also perform crack growth testing with the samples containing hot cracks, in order to see how crack growth behavior is affected by the presence of hot cracks in the material. The weld metals selected for testing were Alloys 182 and 152, which were welded on Alloy 600 base metal. The specimen manufacturing procedure was developed based on the Varestraint test technique. The procedure is schematically presented in Figure 105.

1. **Normal welding up to 2 passes remaining**

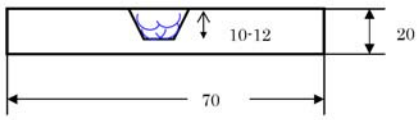

2. **Removal of backside by machining**

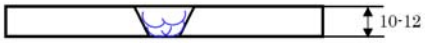

3. **Introduction of hot cracks by trans-Varestraint testing**

4. **Welding of the filling passes to obtain the surface level**

Weld defects are ca. 2 mm beneath the top surface level

Figure 105. Schematic procedure for sample preparation where buried hot cracks are present in the weld metal.

The actual samples are shown in Figures 106–109. First preparations were made by WEDM machining on Alloy 600 base material plate (20 mm thickness) and then normal manual metal arc (MMA) welding was performed.

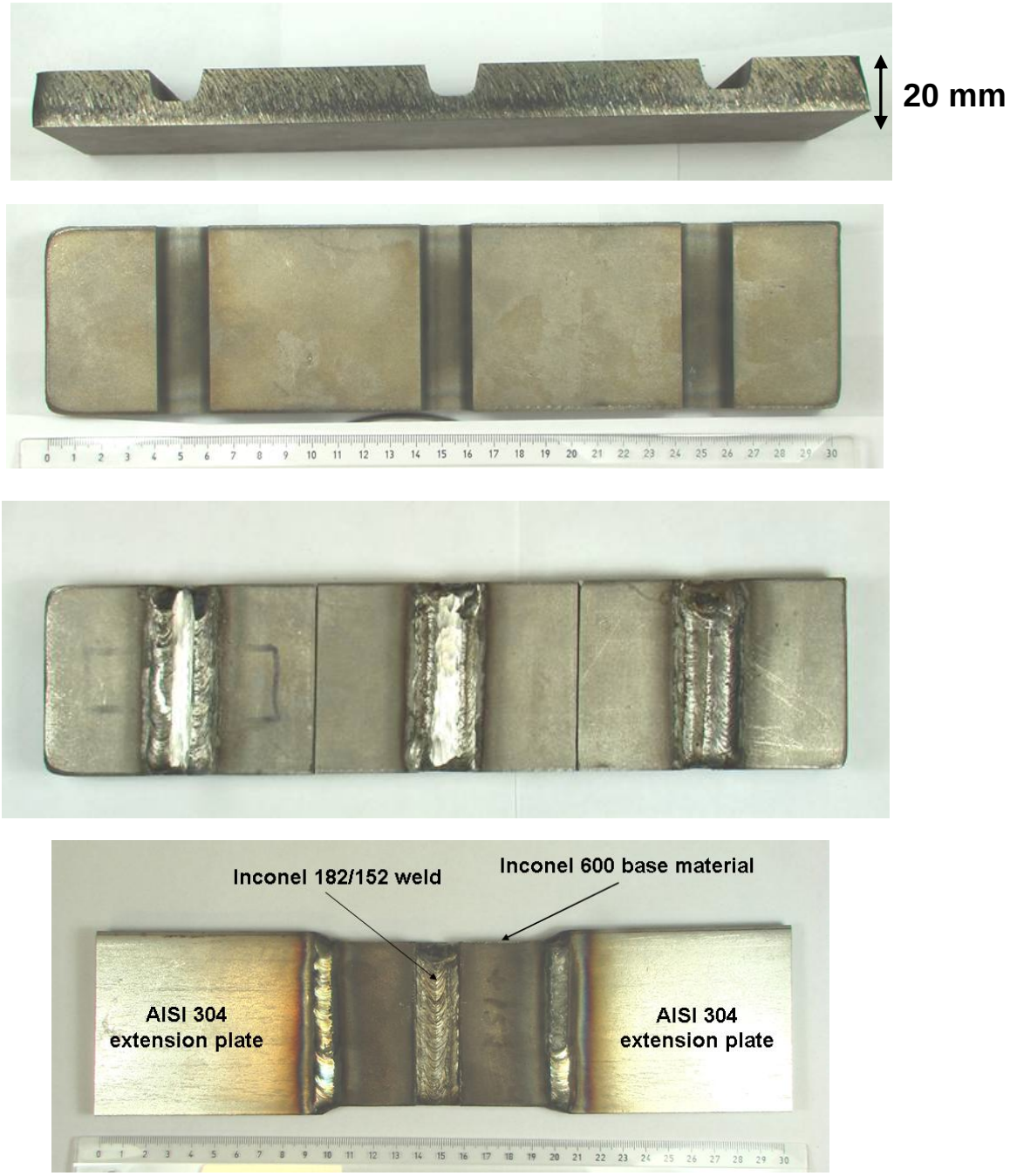

Figure 106. WEDM machining and welding of the preparations on Alloy 600 base metal plates for trans-Varestraint tests.

When the weld groove was almost filled, the trans-Varestraint test was performed with autogeneous gas tungsten arc (GTA) welding as shown in Figure 107. During Varestraint testing a small augmented strain (about 2%) was introduced, which was enough to produce the hot cracks in the weld bead.

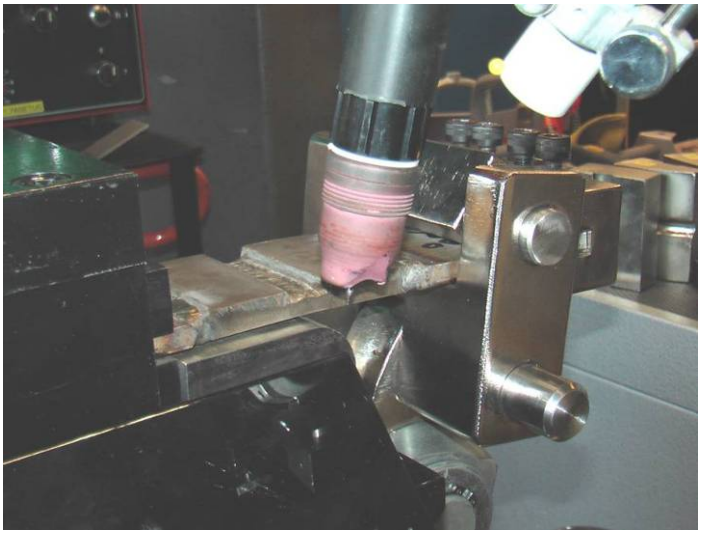

Trans-Varestraint test parameters

Welding current:	250 A
Welding voltage:	12,5 V
Welding speed:	12 cm/min
Heat input:	9,4 kJ/cm
Bending speed:	16 mm/s
Augmented strain:	ca. 2 %

Figure 107. Trans-Varestraint testing of the test sample with almost filled weld metal. The Varestraint testing parameters are shown as an insert in the figure.

The final MMA welding was made with normal welding parameters for filling the preparation and finalising the welding. In this phase the bent samples were straightened and flat samples were obtained containing hot cracks buried inside the weld metal, as intended, Figure 108. The estimated sizes of the buried hot cracks in the different specimens are ca. 3 mm in length.

The plate samples of Alloy 182 and 152 welds containing buried hot cracks were then used for manufacturing CDCB specimens, as shown schematically in Figure 109. For each of the two weld metals, 4 specimens were prepared, 2 with cracks and 2 without cracks.

5. Specimens for EAC crack growth testing in PWR primary water

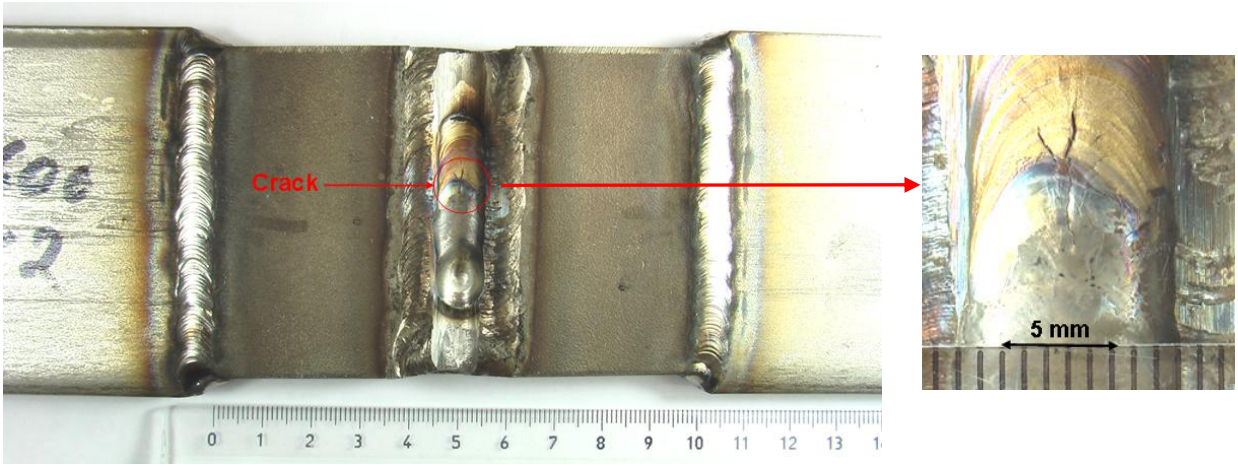

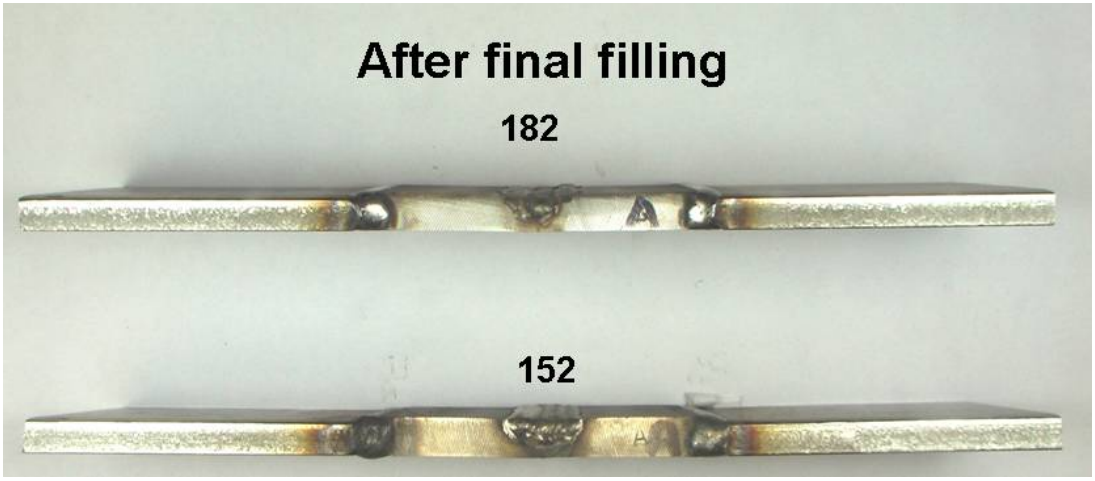

Figure 108. The specimens after trans-Varestraint testing for producing the hot cracks, and the final filling of the preparation resulting in flat specimens with hot cracks buried inside the weld metal.

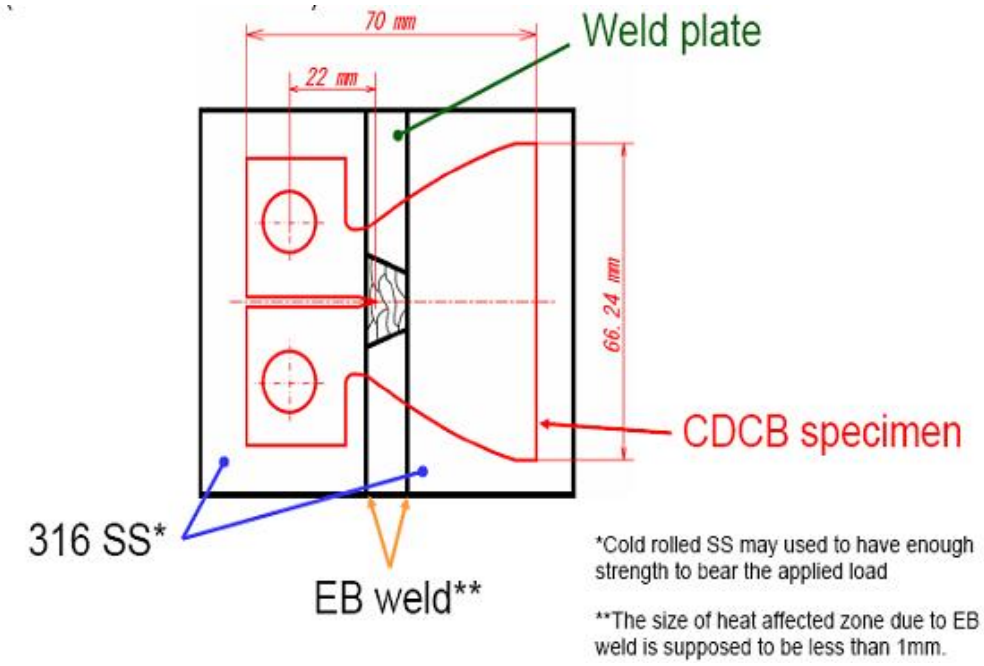

Figure 109. The manufacturing of the composite CDCB specimens by using EB welding, where the manufactured plates having hot cracks buried inside the weld metal are inserted between the cold-worked AISI 316 austenitic stainless steel plates and EB welded, so that the HAZ is less than 1 mm wide.

The welded plate samples are inserted in the middle of two pieces of cold-worked AISI 316 metal plate and EB welded together so that the HAZ is less than 1 mm wide. After the EB welding, the final CDCB specimens are machined. Then the samples are precracked by fatigue so that there is still a ligament for crack extension before crossing over the buried hot cracks in the insert. For Alloy 182 constant load testing is made and Alloy 152 may require cyclic crack growth testing in order to have some crack propagation for crossing over the hot crack region of the samples. The crack growth rate testing of the final samples will be made at Tohoku University, Japan. The purpose of the testing is to find out if the hot cracks will enhance the crack extension, or if they have a decreasing effect on the crack growth rate.

The same weld samples with hot cracks are also used for making of the Auger electron spectroscopy (AES) samples, as shown in Figure 110.

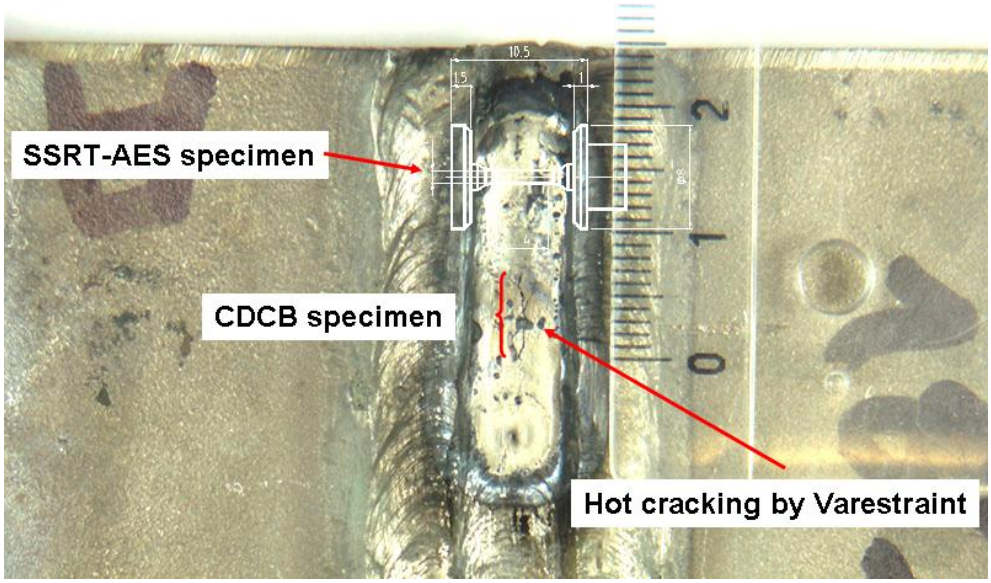

Figure 110. From the plate samples, crack tips of the hot cracks are used for sample preparation for Auger electron spectroscopy. The Auger spectroscopy sample is shown schematically, as well as its cutting location.

The samples are prepared from the tips of the hot cracks so that the hot crack tip is in the gauge length region of the sample, which will be fractured inside the vacuum chamber of the Auger electron microscope. The purpose is to study both the hot crack fracture surface as well as the microstructure along the dendrite boundary ahead of the hot crack tip, where marked segregation is expected to be present. The Auger electron microscopy results will bring additional information on the dendrite boundary segregation and hot cracking mechanism of these alloys to complement the FEG-SEM and ATEM results.

6. Mechanism of environment-assisted cracking of nickel-base alloy weld metals

In the earlier studies [5, 6] in the doped steam conditions the Ni-base weld metal mock-up specimens showed indications but much less fracture (Table 9) than the pure weld metal specimens of Alloy 182 and 82 (Table 10), which cracked quickly in the testing conducted in the current study. In the earlier mock-up tests, Alloy 182 was apparently the most susceptible of the studied mock-up welds. However, in the present study the pure weld metals of Alloy 182 and 82 seemed to be equally susceptible. Aging at 420 °C for 2000 h did not seem to affect the cracking susceptibility in these test conditions. Specimens containing hot cracks did not show any crack extension in either pure weld metal samples or in mock-up samples after exposure to doped steam for 2178 h. Also, the hot crack surfaces showed little oxidation and no selective oxidation processes were observed on the hot crack fracture surfaces as compared to the fracture surfaces of the EAC cracks in the same conditions. This may indicate that the local microchemistry and microstructures on the dendrite boundaries ahead of the hot crack tips are not inherently susceptible to EAC. Typical for Nb-containing alloys is that Nb-rich phases are present in the hot cracks, and the adjacent austenite has heavy segregated of Nb (up to 10%). But in Alloy 52, where no Nb alloying is present, TiN phase is associated with hot cracking [5, 6]. Additionally, dendrite boundaries exhibit high dislocation densities (residual strain) together with segregation and second phase particles.

Fractography of Alloy 182 and 82 pure weld metal specimens after EAC testing in doped steam environment showed that the outer surfaces and fracture surfaces are covered with a Cr-rich oxide layer. Metallic Ni deposits or a NiO layer forms on the top of the Cr-rich oxide layer, and covers the fracture surface close to the outer surface. Metallic Ni deposits also form on the outer surface of the specimens, and on a finer scale, inside the outer surface oxide film. Close to the crack tip, NiO and Fe-rich spinel oxide particles are also observed when metallic Ni is present, and the fracture surface is covered by a thin Cr-rich oxide layer up to the crack tip. Thus, in the doped steam test the oxides forming a two-layer oxide structure on the crack walls and outer surface of the specimens are similar to those forming in normal reactor conditions [49–51]. In the doped steam test, however, the phases are larger and thicker, and more clearly separated, allowing them to be studied much more easily. The intergranular nature of the EAC fracture is evident, and its morphology is quite different from the interdendritic morphology of the hot crack fracture surface [5, 6].

Selective oxidation leading to separation of Cr-rich oxide and metallic Ni or NiO layer is occurring in the initiation and propagation of IGSCC in the doped steam test. A Cr-rich oxide layer forms on the crack walls and extends to the crack tip. Precipitation of a metallic Ni layer or formation of NiO behind the crack tip on top of the Cr-rich oxide layer occurs inside the cracks and on the outer surface. With the resolution of the present equipment it was not possible to clarify whether the entire alloy is oxidising and the elements undergo hydrolysis, except Ni, which is transferred through the oxide layer and re-plated, or if the other elements dissolve selectively and a porous Ni-rich sponge is left close to interface, or if both mechanisms operate at the same time. The details of the metallic Ni layer, multilayer Cr-rich oxide corrosion product, and possible corrosion sponge at Cr-depleted/Ni-enriched base material interface, as well as possible vacancy clusters (nanovoids) in the base material, should all be studied in the future, e.g., by atom probe techniques. The role of hydrogen in cracking should be separately studied, and it may be related more to the enhancement of oxidation and stabilization of vacancies rather than to the hydrogen-induced brittle cracking at 400 °C.

When viewed as a function of potential and pH, The Ni stability region is close to the H_2–H_2O line in high temperature water, while the stability regions of Fe and Cr are below the line, Figure 111. The critical H_2 fugacity varies with temperature, and increasing the H_2 fugacity causes the corrosion potential to decrease into the Ni stability region. The hydrolysis reaction of metal ions (Cr, Fe, etc.) produces additional H^+/H_2. Inside the cracks the increased H_2 fugacity lowers the Ni^{2+} and NiO stability, and metallic Ni can be deposited. In the two test series performed, targeting the hydrogen content of the environment to the Ni/NiO stability line showed that in the first test series NiO layers formed inside the cracks, while in the second test series, where cracks formed also much more quickly, the cracks were filled by a metallic Ni deposit layer. This indicates that the two test series have been exposed to the different sides of the Ni/NiO stability line.

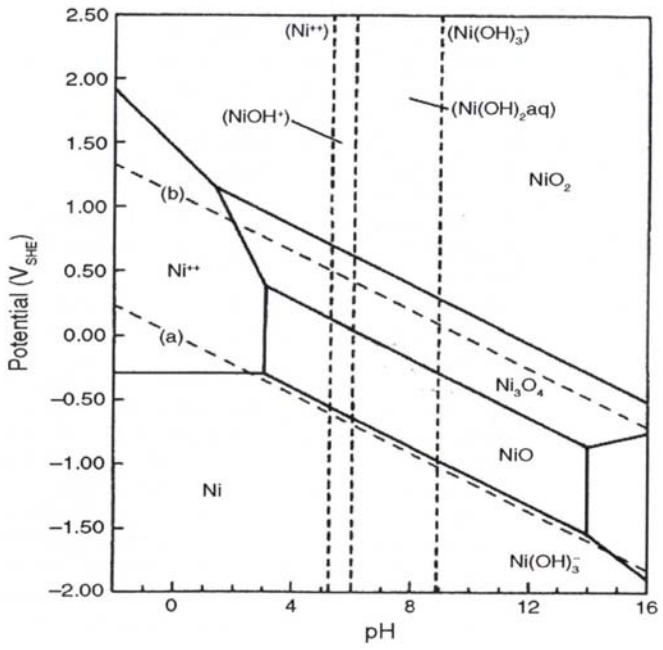

Figure 111. Pourbaix diagram of Ni–H_2O at 300°C.

The mechanism of cracking of Ni-base alloys in doped steam test can be explained by the Selective Dissolution – Vacancy Creep (SDVC) model for SCC [42]. Cracking takes place by a selective oxidation mechanism where Cr and Fe are hydrolyzed and Ni is transferred through the oxide film and deposited on the film in the metallic form or NiO outer layer forms. Vacancy injection into the base material is expected to take place, and to enhance the creep rate at the crack tip. The mechanistic processes in steam and high temperature water are thought to be the same, and they are described in Figure 112.

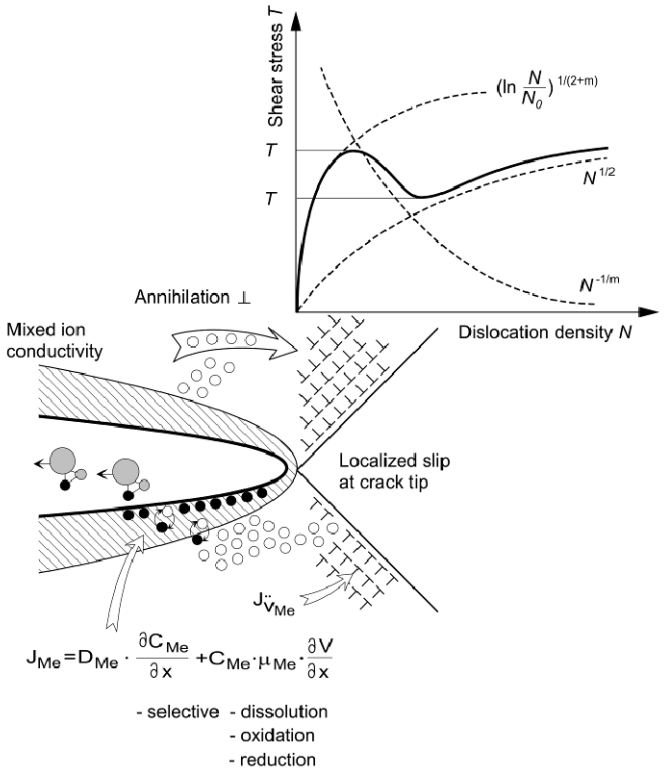

Figure 112. Selective Dissolution – Vacancy Creep (SDVC) model for SCC [42].

7. Summary

The following conclusions can be drawn based on the results of this study:

- Dissimilar metal weld joints of Ni-base weld metals show marked segregation in their microstructures, especially of Nb to the dendrite boundaries. In the Nb-bearing alloys eutectic Laves and Nb(C, N) phases form along the dendrite boundaries, and in Ti-alloyed Alloy 52 TiN(C) phase forms, respectively. These segregated structures and second phases play and important role in hot cracking, but were not found to enhance EAC in the doped steam test.

- The differences in the EAC susceptibility between different weld geometries and weld metals can be distinguished by the doped steam test method. Pure weld metals of Alloy 182 and 82 were clearly more susceptible to EAC than pure weld metals of Alloy 152 and 52, which did not show any crack initiation. The mock-up welds with diluted microstructures were less susceptible than the pure weld metals of Alloy 182 and 82. Aging at 420 °C for 2000 h did not seem to affect the cracking susceptibility in these test conditions.

- The accelerated doped steam test for Ni-base alloys results in a high acceleration factor for cracking, and because of the high temperature, the test conditions led to enhanced growth of oxide layer structures and clear separation of different phases.

- In the first test series, two main kinds of oxides were present on the fracture surfaces, containing mostly Ni, but arranged as a 30–50 nm thick Cr-rich inner layer showing spinel structure, and an outer layer having NiO type structure filling the rest of the crack.

- In the second test series, metallic Ni formed a continuous layer in the middle of the cracks surrounded by the Cr-rich oxide layer (locally also Nb-rich oxide may be present) in contact with the base material. On the outer surface islands of deposited Ni were also present.

- Cracking is consistent with a selective oxidation mechanism where vacancy injection into the base material is expected to enhance the creep rate at the crack tip. The mechanistic processes in steam and high temperature water are thought to be the same, at least for pure water.

- Dynamic strain aging is present in the studied weld metals of Alloy 182, 82, 152 and 52. Negative strain rate sensitivity observed for weld metal of Alloy 182 corresponds to tensile test temperatures and strain rates where serrated plastic flow was observed. Appearance of DSA manifested by serrated flow in weld metal of Alloy 182 fits well with the previously obtained map of the DSA appearance for the base materials of Alloy 600 and 690. Internal friction studies did not reveal any detectable IF peak attributed to free interstitial carbon or nitrogen atoms in FCC lattice of the studied weld metals in the same manner as it has earlier been reported for base material of Alloy 690.

- Specimens containing small weld defects or hot cracks did not show any crack extension in the doped steam test, either in pure weld metal samples or in mock-up samples after 2178 h. Also the hot crack surfaces showed little oxidation and no selective oxidation processes were observed on the hot crack fracture surfaces as compared to the fracture surfaces of the EAC cracks in the same exposure conditions. This indicates that the local microchemistry and microstructures on the dendrite boundaries ahead of the hot crack tips are not inherently susceptible to EAC.

Acknowledgements

The project PERDI (Performance and ageing of dissimilar metal joints), launched in 2006, deals with dissimilar metal weld issues in nuclear power and the oil refinery industry. The three-year project was funded by Tekes, TVO, Fortum Nuclear Services Oy, Metso Minerals Oy, Neste Oil Oyj, Posiva Oy, Forsmarks Kraftgrupp AB, OKG Aktiebolag, Aalto University School of Engineering and VTT, which is gratefully acknowledged. The objectives of the project were to develop reliable methods to measure and evaluate the manufacturing, properties and performance of new dissimilar metal welds. A main objective was also to understand the aging of Ni-base weld metals and the failure mechanisms of dissimilar metal welds in nuclear power plants, and to develop non-destructive examination techniques for DMW structures. The help of Dr. Iikka Virkkunen (Trueflaw Co.) in analysing the DMW residual stresses by the contour method is gratefully acknowledged.

References

1. Ritamäki, P. Non-destructive inspection of dissimilar metal welds between stainless steel and heat-resisting steel (Ruostumattoman ja kuumalujan teräksen hitsatun eripariliitoksen mikrorakenne ja ultraäänitarkastettavuus). M.Sc. Thesis, Helsinki University of Technology, Espoo, Finland, 2008. 137 p. + app. 10 p.

2. Morra, M. and all laboratories that participated in the Alloy 182 Round Robin. Final results from Alloy 182 round robin. ICG-EAC meeting, Båstad, Sweden, 20–25 April 2008.

3. Cumblidge, S. E., Doctor, S. R., Heasler, P. G. & Taylor, T. T. Results of the program for the inspection of nickel alloy components. NUREG/CR-7019, Rev. 1. U.S. Nuclear Regulatory Commission, Washington DC, USA, 2010, 576 p. http://www.nrc.gov/reading-rm/doc-collections/nuregs/contract/cr7019/r1/cr7019r1.pdf.

4. Aaltonen, P., Toivonen, A. & Hänninen, H. Applicability of HIP for reactor components. VTT Technical Research Centre of Finland, Espoo, Finland, 2009. VTT Research Report VTT-R-00714-09. 27 p.

5. Hänninen, H., Brederholm, A., Saukkonen, T., Gripenberg, H., Toivonen, A., Ehrnstén, U. & Aaltonen, P. Hot cracking and environment-assisted cracking susceptibility of dissimilar metal welds. VTT Technical Research Centre of Finland, Espoo, Finland, 2008. VTT Research Notes 2399. 177 p.

6. Hänninen, H., Toivonen, A., Brederholm, A., Saukkonen, T., Ehrnstén, U. & Aaltonen, P. Environment-assisted cracking and hot cracking of Ni-base alloy dissimilar metal welds. Proceedings of the 13th International Conference on Environmental Degradation of Materials in Nuclear Systems – Water Reactors, Whistler, British Columbia, Canada, 19–23 August, 2007. CD-ROM, 19 p.

7. Hood, B. & Lin, W. Weldability testing of Inconel filler materials. Seventh International Symposium on Environmental Degradation of Materials in Nuclear Power Systems – Water Reactors, Breckenridge, Colorado, USA, 7–10 August, 1995. Pp. 69–79.

8. Wu, W. & Tsai, C. Hot cracking susceptibility of fillers 52 and 82 in Alloy 690. Met. Mat. Trans., 1999. Vol. 30A, pp. 417–426.

9. Collins, M. & Lippold, J. An investigation of ductility dip cracking in nickel-based filler materials – Parts I–III. Welding Journal, 2003. Vol. 82, No. 10, pp. 288–295.

10. Nissley, N., Collins, M., Guaytima, G. & Lippold, J. Development of the strain to fracture test for evaluating ductility dip cracking in austenitic stainless steels and Ni-base alloys. Welding in the World, 2002. Vol. 46, Iss. 7/8, pp. 32–40.

11. Knorovsky, G. A., Cieslak, M. J., Headley, T. J., Romig Jr., A. D. & Hammetter, W. F. Inconel 718: A solidification diagram. Metallurgical Transactions, 1989. Vol. 20A, Iss. 10, pp. 2149–2158.

12. Cieslak, M. J., Headley, T. J., Kollie, T. & Romig, A. D. Jr. A melting and solidification study of Alloy 625. Metallurgical Transactions, 1988. Vol. 19A, Iss. 9, pp. 2319–2331.

13. Dupont, J. N. Solidification of an Alloy 625 weld overlay. Metallurgical Transactions, 1996. Vol. 27A, Iss. 11, pp. 3612–3620.

14. Dupont, J. N., Robino, C. V. & Marder, A. R. Solidification and weldability of Nb-bearing superalloys. Welding Journal, 1998. Vol. 77, pp. 417–431.

15. Young, G. A., Hackett, M. J., Tucker, J. D. & Pyle. J. M. Ni-Cr weld characterization. EPRI Alloy 690/152/52 Expert Panel Meeting, 2–3 December 2009, Tampa, Florida, USA. 25 p.

16. Aoh, J. & Yang, C. Cracking susceptibility study of Inconel 600 alloy using Varestraint and hot ductility test. 6th International Trends in Welding Research Proceedings. ASM International, Pine Mountain, GA, USA, 2003. Pp. 597–602.

17. Nissley, N. E. & Lippold, J. C. Ductility-dip cracking susceptibility of nickel-based weld metals: Part 1: Strain-to-fracture testing. Welding Journal, 2008. Vol. 87, No.10, pp. 257–264.

18. Asanoi, S. & Ishidat, S. Magnetism and crystal structure of Laves phase compounds. Journal of Physics F: Metal Physics, 1988. Vol. 18, pp. 501–515.

19. Zhu, J. H., Liu, C. T. & Liaw, P. K. Phase stability and mechanical behavior of $NbCr_2$-based Laves phases. Intermetallics, 1999. Vol. 7, pp. 1011–1016.

20. Machado, I. F. & Padilha, A. F. The occurrence of Laves phase in Fe-15%Cr-15%Ni austenitic stainless steels containing niobium. Acta Microscopica, 2003. Vol. 12, No.1, pp. 111–114.

21. Prime, M. B. & Kastengren, A. L. The contour method cutting assumption: error minimization and correction. Report LA-UR-10-01605, 2010 (http://www.lanl.gov/contour/).

22. Mulford, R. A. & Kocks, U. F. New observations on the mechanisms of dynamic strain aging and of jerky flow. Acta Metallurgica, 1979. Vol. 27, pp. 1125–1134.

23. Hong, S. H., Kim, H. Y., Jang, J. S. & Kuk, I. H. Dynamic strain aging behavior of Inconel 600 alloy. Superalloys 1996: Proceedings of the Eight International Symposium on Superalloys, Seven Springs Mountain Resort, Champion, Pennsylvania, USA, 22–26 September, 1996. Pp. 401–407.

24. Hänninen, H., Ivanchenko, M., Yagodzinskyy, Y., Nevdacha, V., Ehrnstén, U. & Aaltonen, P. Dynamic strain aging of Ni-base alloys Inconel 600 and 690. Proceedings of the 12th International Conference on Environmental Degradation of Materials in Nuclear Power System – Water Reactors. Salt Lake City, Utah, USA, 14–18 August 2005. Pp. 1423–1430.

25. Ivanchenko, M., Nevdacha, V., Yagodzinskyy, Y. & Hänninen, H. Internal friction studies of carbon and its redistribution kinetics in Inconel 600 and 690 alloys under dynamic strain aging conditions. Materials Science and Engineering A, 2006. Vol. 442, pp. 458–461.

26. Rao, K.B.S., Kalluri, S., Halford, G. R. & McGaw, M. A. Serrated flow and deformation substructure at room temperature in Inconel 718 superalloy during strain controlled fatigue. Scripta Metallurgica et Materialia, 1995. Vol. 32, pp. 493–498.

27. Chen, W. & Chaturvedi, M. C. On the mechanism of serrated deformation in aged Inconel 718. Materials Science and Engineering A, 1997. Vol. 229, pp. 163–168.

28. Fournier, L. Delafosse, D. & Magnin, T. Oxidation induced intergranular cracking and Portevin – Le Chatelier effect in nickel base superalloy 718. Materials Science and Engineering A, 2001. Vol. 316, pp. 166–173.

29. Hale, C. L., Rollings, W. S. & Weaver, M. L. Activation energy calculations for discontinuous yielding in Inconel 718SPF. Materials Science and Engineering A, 2001. Vol. 300, pp. 153–164.

30. Gopinath, K., Gogia, A. K., Kamat, S. V. & Ramamurty, U. Dynamic strain ageing in Ni-base superalloy 720Li. Acta Materialia, 2009. Vol. 57, pp. 12431–253.

31. Kimura, A. & Birnbaum, H. K. Anomalous strain rate dependence of the serrated flow in Ni-H and Ni-C-H alloys. Acta Metallurgica, 1990. Vol. 38, pp. 1343–1348.

32. Nakada, Y. & Keh, A. S. Serrated flow in Ni-C alloys. Acta Metallurgica, 1970. Vol. 18, pp. 437–443.

33. Rodriguez, P. Serrated plastic flow. Bulletin of Materials Science, 1984. Vol. 6, pp. 653–663.

34. Blanter, M. S., Golovin, I. S., Neuhäuser, H. & Sinning, H.-R. Internal friction in metallic materials. In: Hull, R., Osgood, R.M., Parisi, J. & Warlimont, H. (Eds). Springer Verlag, Berlin, Heidelberg, 2001. Pp. 28–30.

35. Verner, V. D. Nature of the internal friction peak in face-centered cubic interstitial solid solutions. Soviet Physics – Solid State (USA), 1965. Vol. 7, pp. 1874–1880.

36. Aaltonen, P., Yagodzinski, Yu., Tarasenko, A., Smouk, S. & Hänninen, H. Study of Snoek-type relaxation in hydrogenated Inconel 600. Philosophical Magazine A, 1998. Vol. 78, pp. 979–994.

37. Grujicic, M. & Owen, W. Models of short-range order in a face-centered cubic Fe-Ni-Cr alloy with a high concentration of nitrogen. Acta Metallurgica et Materialia, 1995. Vol. 43, pp. 4201–4211.

38. Nowick, A. S. & Berry, B. S. Anelastic relaxation in crystalline solids. In: Alper, A. M., Margave, J. L. & Nowick, A. S. (Eds). Academic Press, New York and London, 1972. Pp. 176–246.

39. Hertzberg, J. L. & Was, G. S. The effect of carbon on grain boundary diffusivity in Ni-16Cr-9Fe alloys. Scripta Metallurgica et Materialia, 1995. Vol. 33, pp. 1193–1199.

40. Hertzberg, J. L. & Was, G.S. Isolation of carbon and grain boundary carbide effects on the creep and intergranular stress corrosion cracking behavior of Ni-16Cr-9Fe-xC alloys in

360°C primary water. Metallurgical and Materials Transactions A, 1998. Vol. 29, pp. 1035–1046.

41. Stiller, K., Nilsson, J.-O. & Norring, K. Structure, chemistry, and stress corrosion cracking of grain boundaries in Alloys 600 and 690. Metallurgical and Materials Transactions A, 1996. Vol. 27, pp. 327–341.

42. Aaltonen, P., Saario, T., Karjalainen-Roikonen, P., Piippo, J., Tähtinen, S., Itäaho, M. & Hänninen, H. Vacancy-creep model for EAC of metallic materials in high temperature water. Corrosion 96, Colorado, Denver, USA, 25–28 March 1996. Paper No. 96081. 12 p.

43. Staehle, R. W. & Gorman, J. A. Quantitative assessment of submodes of stress corrosion cracking on the secondary side of steam generator tubing in pressurized water reactors: Part 2. Corrosion, 2004. Vol. 60, No. 1, pp. 5–63.

44. Jacko, R. J., Gold, R. E. & Kroes, A. Accelerated corrosion testing of Alloy 52M and Alloy 182 weldments. Proceedings of the 11th International Conference on Environmental Degradation of Materials in Nuclear Systems – Water Reactors, Stevenson, WA, USA, 10–14 August, 2003. CD-ROM.

45. Rao, G. V., Jacko, R. J. & McIlree, A. R. An assesment of the CRDM Alloy 600 reactor vessel head penetration PWSCC remedial techniques. Proceedings of Fontevraud 5, Contribution of Materials Investigation to the Resolution of Problems Encountered in Pressurized Water Reactors. SFEN, Fontevraud, France, 23–27 September, 2002. CD-ROM.

46. Hänninen, H., Toivonen, A., Saukkonen, T., Brederholm, A., Aaltonen, P. & Ehrnstén, U. EAC crack initiation in nickel-based dissimilar metal welds using doped steam test. Proceedings of the 14th International Conference on Environmental Degradation of Materials in Nuclear Systems – Water Reactors, Hilton Virginia Beach, Virginia Beach, VA, USA, 23–27 August 2009. CD-ROM. Pp. 333–343.

47. Karlsen, W. & Pakarinen, J. TEM investigation of cracks in dissimilar metal weld Inconel 182 following doped steam testing. VTT Technical Research Centre of Finland, Espoo, Finland, 2009. VTT Research Report VTT-R-05722-09. 29 p.

48. Ziemniak, S. E. & Hanson, M. Corrosion behaviour of NiCrFe Alloy 600 in high temperature, hydrogenated water. Corrosion Science, 2006. Vol. 48, pp. 498–521.

49. Scott, P. M. An overview of internal oxidation as a possible explanation of intergranular stress corrosion cracking of Alloy 600 in PWRs. Proceedings of the 9th International Symposium on Environmental Degradation of Materials in Nuclear Systems – Water Reactors, Newport Beach, CA, USA, 1–5 August, 1999. Pp. 3–14.

50. Thomas, L. E. & Bruemmer, S. M. Insights into environmental degradation mechanisms from analytical transmission electron microscopy of SCC cracks. Proceedings of the 9th International Symposium on Environmental Degradation of Materials in Nuclear Systems – Water Reactors, Newport Beach, CA, USA, 1–5 August, 1999. Pp. 41–47.

51. Scenini, F., Newman, R. C., Cottis, R. A. & Jacko, R. J. Effect of surface preparation on intergranular stress corrosion cracking of Alloy 600 in hydrogenated steam. Corrosion, 2008. Vol. 64**,** No. 11, pp. 824–835.

Series title, number and
report code of publication

VTT Research Notes 2582
VTT-TIED-2582

Author(s)

Hannu Hänninen, Anssi Brederholm, Tapio Saukkonen, Mykola Ivanchenko, Aki Toivonen, Wade Karlsen, Ulla Ehrnstén and Pertti Aaltonen

Title

Environment-assisted cracking and hot cracking susceptibility of nickel-base alloy weld metals

Abstract

The operating experience of major nuclear power plant (NPP) pressure boundary components has recently shown that dissimilar metal weld joints can markedly affect the plant availability and safety because of increased incidences of environment-assisted cracking (EAC, PWSCC) of Alloy 600 and corresponding weld metals (Alloys 182/82). Alloy 690 and associated weld metals (Alloys 152/52) are widely used for repair and replacement of the affected thick-section components. The selection of new materials relies mainly on laboratory results and short-term service experience. The long-term behavior of these materials and their performance in the plant has still to be demonstrated.

Weldability and susceptibility to hot cracking of the studied nickel-base materials was evaluated based on the Varestraint test results obtained with weld metals of different chromium contents. Weld metal solidification and melting temperature ranges were determined by scanning DSC experiments. The microstructures and microchemistry of the multi-pass nickel-base alloy welds were studied by FEG-SEM/EDS/EBSD and ATEM techniques and the highly segregated weld microstructures were found to be very different from those of the wrought and recrystallized nickel-base materials. Additionally, the weld residual stresses were measured and analyzed by a novel Contour method suitable for through-thickness residual stress determination. EBSD method revealed the distribution residual strain in the weld metals and the heat-affected zones of the welds.

The studied nickel-base material welds were exposed to doped steam test environment at 400°C and crack initiation susceptibility of them was studied. The differences in the EAC susceptibility between different weld geometries and weld metals was distinguished: pure weld metals of Alloy 182 and 82 were clearly more susceptible to EAC than pure weld metals of Alloy 152 and 52, which did not show any crack initiation. The mock-up welds with diluted microstructures were less susceptible than the pure weld metals of Alloy 182 and 82. Specimens containing small weld defects or hot cracks did not show any crack extension in the doped steam test either in pure weld metal samples or in mock-up samples. The hot crack surfaces showed little oxidation and no selective oxidation processes were observed on the hot crack fracture surfaces as compared to the fracture surfaces of the EAC cracks in the same exposure conditions. This indicates that the local microchemistry and microstructures on the dendrite boundaries ahead of the hot crack tips are not inherently susceptible to EAC. The mechanism of EAC was examined both by FEG-SEM/EDS and ATEM techniques and cracking is consistent with a selective oxidation mechanism. The mechanistic processes in steam and high temperature water are thought to be the same, at least for pure water.

ISBN
978-951-38-7709-5 (soft back ed.)
978-951-38-7710-1 (URL: http://www.vtt.fi/publications/index.jsp)

Series title and ISSN	Project number
VTT Tiedotteita – Research Notes 1235-0605 (soft back ed.) 1455-0865 (URL: http://www.vtt.fi/publications/index.jsp)	12420

Date	Language	Pages
May 2011	English	152 p.

Name of project	Commissioned by
Performance and ageing of dissimilar metal joints (PERDI)	Tekes, TVO, Fortum Nuclear Services Oy, Metso Minerals Oy, Neste Oil Oyj, Posiva Oy, Forsmarks Kraftgrupp AB, OKG Aktiebolag, Aalto University School of Engineering and VTT

Keywords	Publisher
Nickel-base alloys, weld metal, hot cracking, environment-assisted cracking, electron microscopy, dynamic strain aging, differential scanning calorimetry, residual stress	VTT Technical Research Centre of Finland P.O. Box 1000, FI-02044 VTT, Finland Phone internat. +358 20 722 4520 Fax +358 20 722 4374

The operating experience of major nuclear power plant pressure boundary components has recently shown that dissimilar metal weld (DMW) joints can markedly affect the plant availability and safety because of increased incidences of environment-assisted cracking (EAC, PWSCC) of Alloy 600 and corresponding weld metals (Alloys 182/82). Alloy 690 and associated weld metals (Alloys 152/52) are widely used for repair and replacement of the affected thick-section components. Weldability of the nickel-base materials was evaluated based on the Varestraint test results as well as detailed electron microscopy and differential thermal analysis. In addition to the susceptibility to hot cracking in welding, EAC susceptibility in the doped steam test at 400°C was evaluated based on the metallurgical properties of the nickel-base alloy weld metals. Weld residual stresses and strains of DMWs were measured and analyzed with the Contour and EBSD methods, respectively.

ISBN 978-951-38-7709-5 (soft back ed.)
ISSN 1235-0605 (soft back ed.)
ISBN 978-951-38-7710-1 (URL: http://www.vtt.fi/publications/index.jsp)
ISSN 1455-0865 (URL: http://www.vtt.fi/publications/index.jsp)